Tridimensional Estimation of Turbulent Fluid Velocity

Ioana Barbu

N° d'ordre : ANNÉE 2014

UNIVERSITÉ DE RENNES 1

THÈSE / UNIVERSITÉ DE RENNES 1
sous le sceau de l'Université Européenne de Bretagne

pour le grade de

DOCTEUR DE L'UNIVERSITÉ DE RENNES 1

Mention : Traitement du signal et télécommunications

École doctorale Matisse

présentée par

Ioana Barbu

préparée à l'unité de recherche Inria
Centre Inria Rennes — Bretagne Atlantique
Université de Rennes 1

Tridimensional Estimation of Turbulent Fluid Velocity

Thèse soutenue à Rennes
15 décembre 2014

devant le jury composé de :

Charles SOUSSEN
Maître de Conférences, U. de Lorraine / rapporteur

Frédéric CHAMPAGNAT
Directeur de recherche, ONERA / rapporteur

Rémi GRIBONVAL
Directeur de recherche, INRIA / examinateur

Benjamin LECLAIRE
Ingénieur de recherche, ONERA / examinateur

Laurent DAVID
Professeur, Institut PPrime / examinateur

Cédric HERZET
Chargé de recherche, INRIA / co-directeur de thèse

Étienne MÉMIN
Directeur de recherche, INRIA / directeur de thèse

Pour Roseti Avram,
poétesse des chiffres, tricoteuse de mots,
allez-vous, de là-haut,
mettre les chahuteurs dans le même banc
et nous réciter un vers entre deux équations ?

Contents

Remerciements vii

List of figures viii

Notations and Acronyms xi

Résumé en français xix

Introduction xxxiii

1 Experimental Fluid Mechanics 1
- 1.1 Passive Tracers . . . 3
- 1.2 Measurements in Flows . . . 4
- 1.3 From Planar to tridimensional (3D) Measurements . . . 5
- 1.4 Conclusion . . . 10

2 TomoPIV: Settings and Models 11
- 2.1 Experimental Setup . . . 13
  - 2.1.1 Volume Illumination . . . 14
  - 2.1.2 Particles . . . 15
    - 2.1.2.1 Dynamics . . . 16
    - 2.1.2.2 Light scattering . . . 17
  - 2.1.3 Sensors . . . 20
  - 2.1.4 Small Particles' Imaging . . . 22
  - 2.1.5 System Calibration . . . 25
  - 2.1.6 Summary . . . 26
- 2.2 Related Model . . . 26
  - 2.2.1 General Assumptions . . . 26
  - 2.2.2 Continuous frame . . . 27
    - 2.2.2.1 Density Function and Transport Assumption . . . 27
    - 2.2.2.2 Physical-Based Continuous Model . . . 29
    - 2.2.2.3 Approximated Continuous Model . . . 30
  - 2.2.3 Digitized frame . . . 31
    - 2.2.3.1 Preliminary Notations . . . 32
    - 2.2.3.2 Blob-Based Density Function . . . 32
    - 2.2.3.3 Particle-Based Density Function . . . 33
    - 2.2.3.4 Image Formation . . . 34
    - 2.2.3.5 Transport Model . . . 37
  - 2.2.4 Summary . . . 38

3 Volume Reconstruction **39**
3.1 System Features . . . 42
3.2 Notations . . . 43
3.3 Standard Procedures for Tomographic PIV (tomoPIV) Volume Reconstruction . . . 43
3.4 Inverse Problem . . . 46
3.4.1 Choices of the Cost Function on the Signal . . . 48
3.4.2 Choices on the Function Penalizing the Prediction-Observation Discrepancy . . . 50
3.5 Beyond (M)ART with Proximal Methods . . . 52
3.5.1 The Gradient Project Method (GPM) and Variants . . . 52
3.5.2 Proximal Gradient Method (PGM) Applied to Tomo-PIV Problem (3.18) . . . 55
3.5.3 Nonlinear GPM Applied to Tomo-PIV Problem (3.19) . . . 56
3.6 Tomo-PIV Reconstruction based on the Alternating Direction Method of Multipliers . . . 57
3.6.1 Alternating Direction Method of Multipliers (ADMM) . . . 57
3.6.2 Application to Tomo-PIV Problem (3.17) . . . 58
3.7 Other Computational Methods for Sparse Linear Solutions . . . 59
3.8 Guarantees Related to the ℓ_0- and ℓ_1-norms . . . 62
3.9 Pruning . . . 64
3.10 Assessement . . . 67
3.10.1 Synthetic Setting . . . 67
3.10.2 Description of Evaluation Criteria . . . 68
3.10.3 Nomenclature . . . 70
3.10.4 Pruning Assessement . . . 71
3.10.5 Volume Reconstruction Assessement . . . 72
3.11 Summary . . . 77

4 Velocity Estimation **89**
4.1 Features . . . 89
4.2 Classical Motion Estimation Methods . . . 91
4.3 Joint Local Method . . . 96
4.4 Assessement . . . 99
4.4.1 Synthetic Setting . . . 99
4.4.2 Description of Evaluation Criteria . . . 100
4.4.3 Nomenclature . . . 101
4.4.4 Velocity Reconstruction Assessement . . . 101
4.5 Summary . . . 103

5 Conclusion and Perspectives **117**

A Lagrangian and Eulerian Specification of the Flow Field **121**

B Mie Scattering Coefficients **123**

C Synthetic Configuration of the Imaging System **127**

D Implementation of (2.39) **131**

E The Proximal Operator **133**

Bibliography **146**

Remerciements

Je tiens à remercier l'ensemble des personnes ayant apporté leur contribution à ce travail. Merci à mes directeurs de m'avoir transmis un pan de leur savoir et de m'avoir prodigué des étalons d'exigence et de tenue scientifiques. Merci aux membres du jury pour leur lecture attentive et leur retour constructif. Merci à Huguette Béchu pour l'enveloppe administrative et plus. Merci à la DGA pour le co-financement de cette thèse. Enfin, merci à ma famille pour son soutien.

List of Figures

1 Performances des algorithmes de reconstruction volumique dans un scénario idéal sans bruits. . . . xxix
2 Comparaison de l'amplitude du mouvement estimé par quatre méthodes dans un volume ensemencé avec $ppp = 0.2$ lors d'un scénario bruité. . . . xxx

1.1 Visualization of the three functioning regimes of the fluid flow: **laminar**, **transitional** and **turbulent** . . . 2
1.2 Rendition of flow pattern depending on the nature of the particle tracer . . . 4
1.3 Experimental arrangement for particle image velocimetry in a wind tunnel. . . . 6
1.4 PIV Chronicle . . . 8

2.1 Working principle of tomoPIV . . . 12
2.2 Sketches of different optical setups . . . 14
2.3 Time response of oil particles with different diameters in a decelerating air flow. . . . 17
2.4 $S_{11}(\theta^c, d_p)$ . . . 20
2.5 $S_{11}(\theta^c)$ . . . 21
2.6 Axes . . . 23
2.7 Airy patterns . . . 23
2.8 Image formation from a volumetric projection . . . 24
2.9 Representation of the incident intensity at the surface of a particle and its blob-description counterpart . . . 34
2.10 2D Scheme of a 4-voxels cuboid in focus of two 4-pixel cameras; each voxel in $\mathcal{V}$ is divided into 4×4 subvoxels; the cone-of-sight Ω_2^1 passing through the 2^{nd} pixel of the first camera intersects subvoxels in $\mathcal{V}$, comprised within the blue lines. . . . 36

3.1 Fully discrete model of tomoPIV . . . 40
3.2 ℓ_p and $-ent$ balls . . . 51
3.3 Roc curve for the pruning procedures . . . 78
3.4 Positive Predictive Value (PPV)/True Positive Rate (TPR) curves for the pruning procedures . . . 79
3.5 Original ideal distribution . . . 79
3.6 Estimated ideal distribution . . . 80
3.7 Oracle curve **Test Case 1(a)** . . . 80
3.8 The ratio between the number of observations and the unknowns output by theFeasible Reduced Set (FRS) pruning for all test cases . . . 81
3.9 ARTs assessment for **Test Case 1(a)** . . . 82
3.10 SMARTs assessment for **Test Case 1(a)** . . . 82
3.11 Accelerated techniques assessment for **Test Case 1(a)** . . . 83
3.12 Assessement for **Test Case 1(a)** . . . 83
3.13 Computational time for all algorithms for **Test Case 1(a)** . . . 84
3.14 Assessement for **Test Case 1(b)** . . . 85
3.15 Assessement for **Test Case 2(a)** . . . 85

3.16 Assessement for **Test Case 2(b)** . . . 86
3.17 Assessement for **Test Case 3(a)** . . . 86
3.18 Assessement for **Test Case 3(b)** . . . 87
3.19 Convergence for **Test Case 1** . . . 87
3.20 Convergence for **Test Case 2** . . . 88
3.21 Convergence for **Test Case 3** . . . 88

4.1 OFC . . . 91
4.2 Aperture problem . . . 92
4.3 Magnitude of the ground truth velocity . . . 103
4.4 Magnitude of the reconstructed velocity fields, for $particlesperpixel$(ppp) = 0.34 in **Test Case 1(b)** . . . 104
4.5 Ground truth and estimated volumetric densities at consecutive time frames for ppp = 0.34 in **Test Case 1(b)** . . . 105
4.6 MSE for ppp = 0.34 in **Test Case 1(b)** . . . 106
4.7 ASE for ppp = 0.34 in **Test Case 1(b)** . . . 107
4.8 Magnitude of the reconstructed velocity fields, for ppp = 0.2 in **Test Case 1(b)** . . . 108
4.9 Ground truth and estimated volumetric densities at consecutive time frames for ppp = 0.2 in **Test Case 1(b)** . . . 109
4.10 MSE for ppp = 0.2 in **Test Case 1(b)** . . . 110
4.11 ASE for ppp = 0.2 in **Test Case 1(b)** . . . 111
4.12 Magnitude of the reconstructed velocity fields, for ppp = 0.2 in **Test Case 3(b)** . . . 112
4.13 Ground truth and estimated volumetric densities at consecutive time frames for ppp = 0.2 in **Test Case 3(b)** . . . 113
4.14 MSE for ppp = 0.2 in **Test Case 3(b)** . . . 114
4.15 ASE for ppp = 0.2 in **Test Case 3(b)** . . . 115

A.1 Eulerian and Lagrangian specifications of the fluid flow . . . 122

B.1 Definition of the incident coordinates system and of the scattering plane. . . . 124

C.1 Synthetic System Calibration . . . 129

Notations and Acronyms

Mathematical Conventions and Nomenclature

For better readability, we follow throughout the whole manuscript, unless otherwise stated, the following conventions:

Ensembles

$\mathbb{N}$	the set of natural numbers
$\mathbb{R}$	the set of real numbers
$\mathbb{R}_+$	the set of positive real numbers
$\mathbb{R}_+^\star$	the set of strictly positive real numbers
$\mathcal{S}$	a set of elements
$\mathcal{S}^C$	the complement set of $\mathcal{S}$
$Int(\mathcal{S})$	an open subset of $\mathcal{S}$
s^i	the i^{th} element of a set $\mathcal{S} = \{s^1, \ldots, s^n\}$
$\sup(\mathcal{S})$	the supremum of a subset $\mathcal{S}$

Order Relations

$x \sim f(x)$	x is distributed according to $f(x)$
$x \approx y$	x is approximately equal to y
$x \triangleq y$	x is defined as y
$x \ll y$	x is much smaller than y

Vectors and Matrices

$\mathbf{x}$	a vector
$\mathbf{x}^T$	the transpose of vector $\mathbf{x}$
$\mathbf{x}^\star$	an estimate of vector $\mathbf{x}$
x_i	the i^{th} element of vector $\mathbf{x}$
$\mathbf{x}_\mathcal{S}$	a subvector of $\mathbf{x}$ indexed by $\mathcal{S}$
$\|\mathbf{x}\|_p$	ℓ_p-norm of $\mathbf{x}$: $\|\mathbf{x}\|_p = (\sum_{i=1}^M \|x_i\|^p)^{\frac{1}{p}}$, if $0 < p < \infty$
$\langle \mathbf{x}, \mathbf{y} \rangle$	scalar product of vectors $\mathbf{x}$ and $\mathbf{y}$
$\mathbf{0}_n$	the zero column vector of size n
$\mathbf{1}_n$	the one column vector of size n
$\mathbf{D}$	a matrix

$\mathbf{D}^T$	the transpose of matrix $\mathbf{D}$
$\mathbf{D}^{-1}$	the inverse of matrix $\mathbf{D}$
$\mathbf{D}^\dagger$	Moore-Penrose pseudo-inverse of matrix $\mathbf{D}$
d_{ij}	the element at row i and column j of matrix $\mathbf{D}$
$\mathbf{d}_{\bullet j}$	the j^{th} column of matrix $\mathbf{D}$
$\mathbf{D}_{\mathcal{SP}}$	the submatrix of $\mathbf{D}$ with rows and columns indexed by $\mathcal{S}$ and $\mathcal{P}$, respectively
$\mathbf{I}_N$	identity matrix of dimensions $N \times N$
$\text{diag}(a_1, \cdots, a_n)$	the diagonal matrix of size $n \times n$ collecting the elements $a_1, \cdots, a_n$ on its diagonal

Functions and Operators

$\mathcal{N}(m, \sigma)$	the normal distribution with mean m and variance σ
$\Pi(\cdot)$	the gate function
$\text{Vol}(\cdot)$	the volume function
div	the divergence operator
curl	the curl operator
$\arg\min_x f(x)$	the value of x that minimizes $f(x)$
$\nabla f(x)$	the gradient of $f(x)$
$\mathbf{1}_{\mathcal{X}}(x)$	the indicator function which takes 1 if $x \in \mathcal{X}$ and 0 otherwise
$\mathbb{I}_{\mathcal{X}}(x)$	the **characteristic** function which takes 0 if $x \in \mathcal{X}$ and $+\infty$ otherwise; as an **abuse of language** we will also refer to it as the indicator function

Coordinate System

An orthogonal coordinate frame F is defined as a n-tuple $(\mathbf{o}, \mathbf{x}_1, \ldots, \mathbf{x}_{n-1})$ formed by the origin $\mathbf{o}$ and the basis vectors $\mathbf{x}_1, \ldots, \mathbf{x}_{n-1}$, all $\in \mathbb{R}^{n-1}$, with $n \in \mathbb{N}\backslash\{1\}$. The coordinates of a point $\mathbf{m}$ in F are defined as the lengths of its orthogonal projections onto the vectors basis vectors and write:

$$\begin{cases} m_1 = \langle \mathbf{m}, \mathbf{x}_1 \rangle \\ \cdots \\ m_{n-1} = \langle \mathbf{m}, \mathbf{x}_{n-1} \rangle. \end{cases}$$

Therefore, the coordinates of a point expressed with respect to F is the column vector $\mathbf{m} = \begin{bmatrix} m_1 & \cdots & m_{n-1} \end{bmatrix}^T \in \mathbb{R}^{n-1}$. For completeness in the formalization of elements of analytic euclidean geometry used in computer vision, the reader should refer to [150].

Nomenclature

M	number of seeded particles
N_c	number of cameras
$\bullet^c$	super-scripted camera index
n	total number of pixels for all the sensors
f	the focal distance of a camera

$\begin{bmatrix}\tilde{n}_1 & \tilde{n}_2\end{bmatrix}^T$	the dimensions of the screen of a camera
$\begin{bmatrix}n_1 & n_2\end{bmatrix}^T$	the number of pixels per dimension of a camera
$f_\sharp$	the f-number of a camera
Mag	the magnification factor
d_a	the diameter of the aperture of a camera
d_{diff}	the diameter of the diffraction spot
d_{est}	the diameter of the particle image spot
$\bullet_t$	sub-scripted temporal index
m	total number of voxels
$\tilde{m}$	total number of subvoxels
$\mathcal{J}$	the ensemble of the indices of voxels
$\mathcal{Z}$	the ensemble of the indices of subvoxels
ζ^j	the j^{th} voxel
ξ^{ij}	the i^{th} subvoxel of the j^{th} voxel
$\mathcal{V}$	the volumetric space of interest defined as a set of voxels $\zeta^j, \forall j \in \mathcal{I}$
$\begin{bmatrix}L_1 & L_2 & L_3\end{bmatrix}^T$	the dimensions of $\mathcal{V}$
$\mathcal{P}$	the image projection screen discretized into a set of pixels
$\mathbf{y}$	the vector of 2D observations
$\mathbf{w}$	the vector of the 3D intensity signal
$\mathbf{D}$	the interaction dictionary between pixels and voxels
$\mathbf{G}$	the interaction dictionary between voxels and subvoxels
$\mathrm{F_w} : (\mathbf{o}, \mathbf{x}_w, \mathbf{y}_w, \mathbf{z}_w)$	the world frame coordinate system
$\mathrm{F^c_{cam}} : (\mathbf{o}^c_{\mathrm{cam}}, \mathbf{x}^c_{\mathrm{cam}}, \mathbf{y}^c_{\mathrm{cam}}, \mathbf{z}^c_{\mathrm{cam}})$	the coordinate system of a camera indexed by c
$\mathrm{F^c_{img}} : (\mathbf{o}^c_{\mathrm{img}}, \mathbf{x}^c_{\mathrm{img}}, \mathbf{y}^c_{\mathrm{img}})$	the coordinate system of the image plane of the camera indexed by c
$\tilde{i}$	the intensity function of the laser pulsation
$l(\cdot)$	the shading intensity profile in $\mathcal{V}$, assumed to be Gaussian
σ_f	the standard deviation of $\tilde{l}$
d_p	the diameter of a particle
$h(t)$	the position of a particle in a fluid at time t
$u_h(t)$	velocity of a particle in a fluid
$u(\mathbf{h}, t)$	the Eulerian description of the velocity of the fluid at an instant t at a location $\mathbf{h} \in \mathbb{R}^3$
$H(\mathbf{h}_0, t)$	the Lagrangian description of the velocity of the fluid which gives the position at time t of a parcel of fluid labeled by its initial position $\mathbf{h}_0 \in \mathbb{R}^3$ at time $t = 0$
τ_p	response time of a particle in a fluid
μ	dynamic viscosity of the fluid
λ	the wavelength of the laser light

d_q	the normalized diameter of a particle
$\mathcal{N}(\cdot)$	the function that expresses the coordinates of a point in the world frame with respect to the camera frame
$\mathcal{M}(\cdot)$	the function that expresses the projection of a point in the camera frame into the image frame
$\mathcal{W}(\cdot)$	the function that projects a point in the world frame into the image frame of a camera

Acronyms

2D two-dimensional xxxiii

3D tridimensional v

3C three-component

arb. u. arbitrary units 27

ART Algebraic Reconstruction Technique xxii

ADMM Alternating Direction Method of Multipliers vi

CCD Charge Coupled Device 20

CFD Computational Fluid Dynamics 2

CMOS complementary metal-oxide-semiconductor 21

CS Compressed Sensing 60

DDPIV Digital Defocusing PIV 7

DFD Displaced Frame Difference 90

DHPIV Digital HPIV 7

DNS Direct Numerical Simulation . . . 2

DFD Displacement Frame Difference . . . 90

FRS Feasible Reduced Set . . . ix

GPM Gradient Project Method . . . vi

OFC Optical Flow Constraint . . . 90

OLS Orthogonal Least Squares . . . 60

HPIV Holographic PIV . . . 7

ISTA Iterative Shrinkage-Thresholding Algoritm . . . xxvi

IHT Iterative Hard Thresholding . . . 60

JVVE Joint Volume Velocity Estimation . . . 98

FISTA Fast Iterative Shrinkage-Thresholding Algoritm . . . xxvi

LES Large Eddy Simulation . . . 2

LASSO Least Absolute Shrinkage and Selection Operator . . . 61

MART Multiplicative Algebraic Reconstruction Technique . . . xxiii

MFG Multiplicative First Guess . . . 66

MLOS Multiplicative Line of Sight . . . 66

MP Matching Pursuit . . . 60

LocM MLOS Local Maxima . . . 66

MTE Motion enhancement technique 98

NP-hard Non-deterministic Polynomial-time hard 63

OMP Orthogonal MP 60

PGM Proximal Gradient Method vi

PIV Particle Image Velocity xxxiii

ppp particles per pixel x

PSF Point Spread Function 23

PTV Particle Tracking Velocity 5

RIP Restricted Isometry Property 63

SAPIV Synthetic Aperture PIV 7

SART Simultaneous Algebraic Reconstruction Technique xxii

SIRT Simultaneous Iterative Reconstruction Technique xxii

SMART Simultaneous Multiplicative Algebraic Reconstruction Technique xxiii

FSMART Fast Simultaneous Multiplicative Algebraic Reconstruction Technique xxvi

SLS Scanning Light Sheet 7

SNR signal-to-noise ratio 15

SR sparse representation 49

StOMP Stagewise Orthogonal MP 60

SP Subspace Pursuit 60

SBR Single Best Replacement 60

TR time-resolved

tomoPIV Tomographic PIV vi

CoSaMP Compressed Sensing Matching Pursuit 60

KL Kullback-Leibler xxiii

LK Lucas-Kanade xxix

TP True Positive 69

FP False Positive 69

FN False Negative 69

TN True Negative 69

TPR True Positive Rate ix

FPR False Positive Rate 69

ROC Receiver Operating Characteristic 70

PPV Positive Predictive Value ix

Résumé en français

Mesurer avec précision le mouvement de fluides turbulents en 3 dimensions (3D) est l'un des problèmes fondamentaux de l'étude de la dynamique des fluides. Il est en effet intéressant à plus d'un titre : sur le plan théorique, il reste l'un des problèmes majeurs en physique, et sur le plan pratique, il présente de nombreuses applications prometteuses en ingénierie.

L'accès à une information quantitative de la turbulence en 3 dimensions peut être réalisé par des techniques dites de "simulation numérique directe" (SND). Cette approche consiste à résoudre numériquement les équations de Navier-Stokes, gouvernant le mouvement du fluide. Malheureusement, la SND se révèle impossible à mettre en œuvre pour des fluides turbulents, puisque dans ce cas, la gamme des échelles physiques devant être résolues augmente de façon significative.

Pour surmonter ce problème, de nouvelles technologies basées sur l'analyse de séquences d'images ont été récemment proposées (cf. [56]). Leur méthodologie repose sur la conjugaison des approches issues de la communauté Vision par Ordinateur avec des modèles issus de la physique des fluides afin d'obtenir des estimateurs précis du champ de mouvement. Mais voilà, la plupart de ces procédures sont formalisées dans un contexte bidimensionnel (2D) dans le sens où elles reconstruisent un champ 2D à partir des deux images consécutives 2D. Le cas 3D est généralement beaucoup plus complexe à traiter (cf. par exemple, [14, 74]). Dans le travail fondateur de *Elsinga et al.* [74] de la mesure de Tomographie PIV (tomoPIV), les champs de vitesse sont reconstruits à partir des distributions volumiques d'intensité préalablement estimées. Une amélioration de ce dernier, décrite dans [134], s'inscrit dans les efforts de la communauté d'aller vers une estimation jointe de ces deux quantités inconnues. En effet, les auteurs rajoutent au paradigme classique de reconstruction un chemin d'initialisation des distributions volumiques qui prend en considération les deux instants successifs de la scène. La technique, nommée Motion Tracking Advancement (MTE), s'avère être plus performante en terme de qualité du signal estimé tout en respectant la topologie des particules suivies.

Motivés par ces développements, nous proposons dans cet étude une alternative aux schéma joint déjà présent dans la littérature. A cette fin, nous nous intéressons aux formulations qui prennent en compte les particularités notables propres au système de TomoPIV. Cette étude est organisée comme suit : nous présentons d'abord une abstraction

mathématique de l'application tomographique à la mécanique des fluides expérimentale. Ensuite, nous nous penchons sur le problème de reconstruction volumique et nous proposons des schémas de faible complexité qui prennent en compte des *a priori* connus sur le système, plus particulièrement la **non-négativité** et la **parcimonie** du signal inhérents aux applications de tomoPIV. Une nouvelle formulation du problème d'estimation de champs de vitesses est proposée par la suite. Cette-dernière prend en compte la structure **jointe** des volumes et des vitesses dans un contexte bruité.

Modélisation

Nous posons le cadre mathématique du scénario décrit ci-dessus. Pour ceci, nous nous intéressons d'abord au modèle qui relie le signal physique continu aux observations. Ensuite, nous présentons leur interaction dans une formulation discrète reliant les images 2D à la densité de particules dans l'espace 3D.

Modèle continu

Soit $\tilde{i}_t$ la valeur de l'intensité volumique définie aux centres des particules passives suspendues dans le fluide, que nous supposons constante dans le volume. Suivant [4], une particule dans l'espace a des dimensions physiques négligeables. Toutefois, selon les propriétés d'un système de visualisation à partir des caméras Charge Coupled Device (CCD), sa projection sur l'image impacte un agrégat de pixels dont l'intensité varie selon une fonction de répartition évanescente sur les deux dimensions. Afin d'approximer la formation des images, nous modélisons la fonction d'intensité 3D comme une somme de fonctions gaussiennes pondérées, au temps t :

$$w_t(\mathbf{k}) = \tilde{i}_t \sum_{j=1}^{M} g\left(\mathbf{k} - \mathbf{h}^j\right), \forall \mathbf{k} \in \mathbb{R}^3, \tag{1}$$

avec :

$$g\left(\mathbf{k}\right) = \exp\left[-\frac{\|\mathbf{k}\|_2^2}{2\sigma_{\text{psf}}^2}\right], \forall \mathbf{k} \in \mathbb{R}^3, \tag{2}$$

où $\sigma_{\text{psf}}^2 \in \mathbb{R}_+^\star$ est un scalaire modélisant la variance des spots Gaussiens dont les centres sont positionnés en $\mathbf{h}^j$ avec $j = \{1, \ldots, M\}$, où M est le nombre total des particules ensemencées. Les particules passives vont suivre le mouvement du fluide et seront, en conséquence, portées par une fonction de déplacement. Nous notons par $u(\mathbf{k}, t) \in \mathbb{R}^3$ le déplacement entre l'instant t et $t+1$ d'un traceur situé à la position $\mathbf{k} \in \mathbb{R}^3$ à l'instant t. Sous l'hypothèse que la fonction de densité est invariable selon la trajectoire de la particule, nous obtenons que :

$$w_{t+1}(\mathbf{k} + u(\mathbf{k}, t)) = w_t(\mathbf{k}), \forall \mathbf{k} \in \mathbb{R}^3. \tag{3}$$

A chaque instant, le signal 3D se projette simultanément sur l'ensemble des plans 2D correspondants à chaque caméra. Chaque pixel i à l'instant t représente l'intégration de la densité d'intensité 3D selon le cône de vue qui a son origine dans le centre optique de la caméra en question et passant par la surface du pixel, comme ci-dessus :

$$y_{i,t} \approx \int_{\Omega_i} w_t(\mathbf{k}) \mathrm{d}\mathbf{k}, \forall i, t, \tag{4}$$

où Ω_i est le cône de vue passant par le $i^{\text{ème}}$ pixel d'une caméra.

Modèle discret

Soit $\mathcal{V} \in \mathbb{R}^3$ un cuboïde dans l'espace tridimensionnel. Ce dernier est défini comme une grille cartésienne composée de m voxels centrés sur de positions $\mathbf{k}^j, \forall j \in \{1, \ldots, m\}$. Nous supposons que la densité continue volumique peut être numérisée sur le domaine $\mathcal{V}$ à l'instant t par une fonction polynomiale par morceaux telle que :

$$x_t(\mathbf{k}) \approx \sum_{j=1}^{m} w_t\left(\mathbf{k}^j\right) b^j(\mathbf{k}), \forall \mathbf{k} \in \mathbb{R}^3, \tag{5}$$

où $\left\{b^j(\mathbf{k})\right\}_{j\in\{1,\ldots,m\}}$ est un polynôme de Lagrange continu par morceau. Utilisant l'équivalence décrite par (5) et en l'insérant dans le modèle défini par (4), il est aisé de constater que la projection s'écrit, pour toute caméra, comme $y_{i,t} = \sum_j^m w_t\left(\mathbf{k}^j\right) d_{ij}$, où d_{ij} représente le poids de contribution de l'intensité du $j^{\text{ème}}$ voxel à l'énergie mesurée dans le cône de vue passant par $i^{\text{ème}}$ pixel. Dans une forme matricielle, on obtient :

$$\mathbf{y}_t = \mathbf{D}\mathbf{w}_t, \tag{6}$$

où $\mathbf{y}_t \in \mathbb{R}^n$ collecte les observation de toutes les caméras, $\mathbf{w}_t \in \mathbb{R}^m$ recueille, à chaque instant, l'intensité volumique sur les points de la grille, tandis que la matrice $\mathbf{D} \in \mathbb{R}^{n\times m}$ assemble les éléments d_{ij} décrits auparavant. En notant $\mathbf{u}_t \triangleq \begin{bmatrix} u\left(\mathbf{k}^1, t\right) & \cdots & u\left(\mathbf{k}^m, t\right) \end{bmatrix}^T$ et $\mathbf{w}_{t+1}(\mathbf{u}_t) \triangleq \left[w_{t+1}\left(\mathbf{k}^j + \mathbf{u}_{t,j}\right)\right]^T_{j\in\{1,\ldots,m\}}$, il en découle, en utilisant des propriétés algébriques simples, que :

$$\mathbf{w}_t = I(\mathbf{u}_t)\mathbf{w}_{t+1}, \tag{7}$$

où $I(\cdot)$ est un opérateur d'interpolation qui dépend explicitement des polynômes utilisé.

On note que l'on peut, de manière alternative, construire une approximation de (6) qui modélise la projection des particules appartenant à une grille fine, que l'on dénote $\mathcal{R} \in \mathbb{R}^3$ assemblant p^3m sous-voxels sur l'espace des blobs, qui est $\mathcal{V}$. Le modèle résultant écrit :

$$\mathbf{w}_t = \tilde{i}_t \mathbf{G}\mathbf{s}_t, \tag{8}$$

où $\mathbf{G} \in \mathbb{R}^{m(p^3\times m)}$ est créé tel qu'il contient sur la $j^{\text{ème}}$ colonne les coefficients gaussiens de convolution $g\left(\mathbf{k}^i\right)$ définis dans (2), $\forall \mathbf{k}^i \in \mathbb{R}^3, \forall i \in \{1, \ldots, p^3m\}$ et $\mathbf{s}_t$ un vecteur colonne de taille $p^3 \times m$ dont le $i^{\text{ème}}$ élément appartient à $\{0, 1\}^{p^3m}$ et prend 1 si une particule est centré sur le sous-voxel correspondant et 0 sinon.

Particularités notables

Des méthodes standards dans la communauté tomoPIV cherchent une solution aux systèmes (6) et (8) (nous mentionnons que, par souci de concision, on discutera plutôt du système (6) dans la suite). Cependant, ce dernier est souvent sous-déterminé, c.à.d. $n \ll m$. Si, de plus, $\mathbf{D}$ est de rang plein, (6) a une infinité de solutions. En pratique, nous devons exploiter de l'information *a priori* sur le système afin de distinguer parmi ces solutions : *(i)*

les éléments de $\mathbf{w}$ correspondent à une intensité et doivent donc être positifs ; *(ii)* le vecteur recherché $\mathbf{w}$ est typiquement parcimonieux, c.à.d. il contient plus d'éléments nuls que de coefficients non-nuls (fait lié à l'ensemencement physique de la scène avec des particules).

Procédures standard

Depuis l'avènement de la tomoPIV, plusieurs techniques de reconstruction volumique ont été proposées dans la littérature. Les méthodologies les plus courantes font partie de la classe « Row-Action Methods », cf. [45], préférées dans la communauté par leur faible niveau de complexité et de stockage. L'idée sousjacente de ces techniques consiste dans la recherche d'une solution de (6) (avec, éventuellement de contraintes de positivité) par la projection itérative d'une estimée courante (selon une certaine fonction « distance ») sur des sous-ensembles convexes qui définissent l'ensemble de solutions admissibles. Nous nous intéressons ci-dessous à deux telles familles. Pour homogénéiser les noms des algorithmes avec le reste du manuscrit et la littérature, nous allons référencer cer derniers selon leur appellation anglaise.

Techniques algébriques

Une solution de (6) se trouve à l'intersection de n hyperplans définis par les lignes de $\mathbf{D}$. Ceci est réalisé en suivant l'itération :

$$\mathbf{w}^{(k+1)} = \mathbf{w}^{(k)} + \gamma \frac{y_i - \mathbf{d}_{i,\bullet}\mathbf{w}^{(k)}}{\|\mathbf{d}_{i,\bullet}\|_2^2}\mathbf{d}_{i,\bullet}^T, \; i = k \mod n, \tag{9}$$

où $\mathbf{d}_{i,\bullet}$ est la $i^{\text{ème}}$ ligne de $\mathbf{D}$. Lorque $\gamma \in (0, 2)$, l'itération (9) décrit l'algorithme « Kaczmarz » [104], plus couramment sous le nom de Algebraic Reconstruction Technique (ART).

Si ART projette l'estimée courante sur **un** hyperplan à la fois, les techniques appelées Simultaneous Iterative Reconstruction Technique (SIRT)s exploitent **tous** les hyperplans à la fois. L'itération qui les régit, formalisée de manière générale, s'écrit :

$$\mathbf{w}^{(k+1)} = \mathbf{w}^{(k)} + \alpha^{(k)}\mathbf{W}\mathbf{D}^T\mathbf{\Gamma}(\mathbf{y} - \mathbf{D}\mathbf{w}^{(k)}), \tag{10}$$

où $\alpha^{(k)} > 0$ et $\mathbf{W}$, $\mathbf{\Gamma}$ sont des matrices définies positives. La formulation de (10) correspond au cas où $\mathbf{W}$ and $\mathbf{\Gamma}$ sont des matrices diagonales. Les algorithmes de :« Cimmino » [53] où « Simultaneous Algebraic Reconstruction Technique (SART) » [8] sont les exemples les plus connus de SIRTs.

Finalement, nous mentionnons que des variantes de ART et SIRT on été proposées pour chercher des solutions *non-négatives* au problème (6), [182, Chapter 9]. Ces variantes, nommées « ART+ » et « SIRT+ » dans la suite, prennent respectivement les formes :

$$\mathbf{w}^{(k+1)} = \Pi_{\mathbb{R}_+}^m \left(\mathbf{w}^{(k)} \left(1 + \gamma \frac{y_i - \mathbf{d}_{i,\bullet}^T\mathbf{w}^{(k)}}{\|\mathbf{d}_{i,\bullet}\|_2^2}\mathbf{d}_{i,\bullet} \right) \right), \quad i = k \mod n, \tag{11}$$

$$\mathbf{w}^{(k+1)} = \Pi_{\mathbb{R}_+}^m \left(\mathbf{w}^{(k)} + \alpha^{(k)}\mathbf{W}\mathbf{D}^T\mathbf{\Gamma}(\mathbf{y} - \mathbf{D}\mathbf{w}^{(k)}) \right), \tag{12}$$

où $\Pi_{\mathbb{R}_+}(\cdot)$ formalise l'opérateur de projection sur l'orthant positif et $\mathbf{\Gamma}$ et $\mathbf{W}$ sont des matrices diagonales, définies positives.

Techniques algébriques multiplicatives

Les technique algébriques **multiplicatives** sont bâties sur le même principe que les ART, à la différence qu'elles réalisent les projections selon une distance Kullback-Leibler (KL) [112]. Nous remarquons que l'usage de la distance KL impose implicitement la contrainte $\mathbf{w} \geq 0$. La méthode la plus simple appartenant à cette famille obéit à la récursion [95] :

$$w_j^{(k+1)} = w_j^{(k)} \left(\frac{y_i}{\mathbf{d}_{i,\bullet}^T \mathbf{w}^{(k)}} \right)^{\gamma d_{ij}}, \tag{13}$$

avec $\gamma \leq \min\{\mathbf{d}_{\bullet,j}\}$, $\forall j$ choisi tel que les observations y_i sont strictement positives, $\forall j$ choisi tel que la matrice $\mathbf{D}$ contient que des éléments positifs. Cette procédure est connue dans la littérature comme « Multiplicative Algebraic Reconstruction Technique (MART) ».

Une variante de MART qui projette sur tous les hyperplans dans une seule itération a été proposée dans [40] et s'écrit :

$$w_j^{(k+1)} = w_j^{(k)} \prod_{i=1}^{n} \left(\frac{y_i}{\mathbf{d}_{i,\bullet}^T \mathbf{w}^{(k)}} \right)^{\gamma d_{ij}}. \tag{14}$$

Cette procédure est connue sous le nom de « Simultaneous Multiplicative Algebraic Reconstruction Technique (SMART) » dans la littérature. Il s'agit de la technique la plus populaire dans la littérature tomoPIV.

La tomoPIV : un problème d'optimisation convexe

Nous avons établi précédemment que, afin d'isoler une bonne solution parmi l'infinité de solutions possibles, nous devons exploiter de l'information *a priori* sur le signal recherché. Si nous avons vu dans la section antérieure que la positivité est facile à prendre en compte, la parcimonie est moins triviale à imposer à notre solution. Pour pallier à ce problème, nous considérons un problème d'optimisation de la forme :

$$(P^{\varepsilon}) : \mathbf{w}^{\star} = \arg\min_{\mathbf{w}} l_r(\mathbf{w}) \text{ sous contrainte } \begin{cases} l_d(\mathbf{D}\mathbf{w}, \mathbf{y}) \leq \varepsilon, \\ \mathbf{w} \geq 0, \end{cases} \tag{15}$$

où $\varepsilon \geq 0$, $l_d(\cdot,\cdot)$ est une fonction de type « distance » qui mesure l'écart entre les observations et le modèle (6), et $l_r(\cdot)$ est une fonction renforçant des particularités notables sur le signal recherché. Pour ceci, nous devons résoudre un problème qui minimise une fonction encourageant la parcimonie. Nous observons que ce modèle nous permet de prendre en compte des contextes bruitées (par exemple, du bruit de mesure ou d'approximation). Lorsque $l_d(\mathbf{y}, \mathbf{D}\mathbf{w}) = \|\mathbf{y} - \mathbf{D}\mathbf{w}\|_2^2$, on considère un bruit Gaussien sur les observations ; quand $l_d(\mathbf{y}, \mathbf{D}\mathbf{w}) = \mathrm{KL}(\mathbf{y}, \mathbf{D}\mathbf{w})$, nous supposons que le bruit est de type Poisson. Nous nous référons au problème (P^0) lorsque l'on considère un contexte sans bruit.

La non-négativité et la parcimonie du signal peuvent être pris en compte par un choix approprié de la fonction $l_r(\cdot)$. Un choix idéal pour renforcer la parcimonie est le choix de la norme ℓ_0, c.à.d. $l_r(\mathbf{w}) = \|\mathbf{w}\|_0$, qui compte le nombre de coefficients non-nuls du signal. Malheureusement, cette dernière fonction n'est pas convexe et le problème résultant peut être insoluble en temps raisonnable. Dans la pratique, la norme ℓ_1

$$l_r(\mathbf{w}) = \|w\|_1 = \sum_j |w_j|, \tag{16}$$

est souvent préférée comme substitut convexe à la norme ℓ_0. D'autre part, les contraintes de non-négativité peuvent être prises en compte en considérant, en guise de fonction de régularisation, la fonction indicatrice de l'orthant positif :

$$l_r(\mathbf{w}) = \mathbb{I}_{\mathbb{R}^m_+}(\mathbf{w}). \tag{17}$$

Finalement, en combinant (16) et (17) on obtient une fonction encourageant la parcimonie **et** la positivité sur le signal recherché, qui s'écrit :

$$l_r(\mathbf{w}) = \|\mathbf{w}\|_1 + \mathbb{I}_{\mathbb{R}^m_+}(\mathbf{w}) = \mathbf{1}^T\mathbf{w} + \mathbb{I}_{\mathbb{R}^m_+}(\mathbf{w}). \tag{18}$$

Avant de procéder à la résolution des problème, on note qu'il existe de formalisations équivalentes à (15), notamment

$$\begin{aligned} (R) : \mathbf{w}^\star = \arg\min_{\mathbf{w}} l_d(\mathbf{D}\mathbf{w}, \mathbf{y}) + r l_r(\mathbf{w}), \\ \text{such that } \mathbf{w} \geq 0. \end{aligned} \tag{19}$$

$\forall r > 0$.

Le problème (15) peut également être écrit comme ci-dessous :

$$(A) : \mathbf{w}^\star = \arg\min_{\mathbf{w}} l_d(\mathbf{D}\mathbf{w}, \mathbf{y}) \text{ such that } \begin{cases} l_r(\mathbf{w}) \leq a, \\ \mathbf{w} \geq 0. \end{cases} \tag{20}$$

$\forall a > 0$.

Au-delà de (M)ART avec des procédures proximales

Même si au niveau conceptuel les algorithmes algébriques standards pour la résolution du problème tomoPIV sont intéressants, ils souffrent néanmoins de quelques inconvénients. Entre autres, ces méthodes : *(i)* ne permettent pas la prise en compte de la parcimonie du signal ; *(ii)* leur comportement dans un scénario bruité n'est pas toujours connu. Nous nous proposons d'aller vers des méthodes pour l'optimisation (convexe) qui répondent aux même pré-requis en terme de complexité et stockage que les méthodes algébriques et qui permettent la prise en compte de la parcimonie. Pour cela, nous nous orientons vers les méthodes de gradient projeté et leur généralisation proximale. Plus particulièrement, nous cherchons à résoudre un problème du type $\min_{\mathbf{w}\in\mathcal{W}} f(\mathbf{w})$, où $\mathcal{W} \subset \mathbb{R}^m$ est un ensemble convexe et $f : \mathbb{R}^m \to \mathbb{R}$ est une fonction convexe différentiable et continue. La descente de

gradient projeté obéit à la récursion :

$$\mathbf{w}^{(k+1)} = \Pi_{\mathcal{W}} \left(\mathbf{w}^{(k)} - \alpha^{(k)} \nabla f(\mathbf{w}^{(k)}) \right), \tag{21}$$

où $\alpha^{(k)} > 0$ est un pas réglable, $\nabla f(\mathbf{w}^{(k)})$ est le gradient de $f(\mathbf{w})$ évalué à $\mathbf{w}^{(k)}$ et $\Pi_{\mathcal{W}}(\mathbf{v})$ est la projection Euclidienne (orthogonale) de $\mathbf{v}$ sur $\mathcal{W}$. Quelques variantes de cet algorithme ont été proposées dans la littérature.

La méthode du gradient projeté non-linéaire s'écrit :

$$\mathbf{w}^{(k+1)} = \arg \min_{\mathbf{w} \in \mathcal{W}} \left\{ \nabla f(\mathbf{w}^{(k)})^T \mathbf{w} + \frac{1}{\alpha^{(k)}} \mathrm{D}(\mathbf{w}, \mathbf{w}^{(k)}) \right\}, \tag{22}$$

où $\mathrm{D}(\mathbf{u}, \mathbf{v}) : \mathbb{R}^m \times \mathbb{R}^m \to \mathbb{R}_+$ est un terme « de proximité » qui peut être choisi, par exemple, comme une distance de Bregman [36] (dans le sens de [23]).

Une autre extension de la méthode du gradient projeté s'adresse aux problèmes de type $\min_{\mathbf{w}} f(\mathbf{w}) + g(\mathbf{w})$, où $f : \mathbb{R}^m \to \mathbb{R}$ and $g : \mathbb{R}^m \to \mathbb{R}$ sont des fonctions fermées, convexes et f est différentiable. La récursion des méthodes de gradient proximal [136] s'écrit :

$$\mathbf{w}^{(k+1)} = \mathrm{prox}_g(\mathbf{w}^{(k)} - \alpha^{(k)} \nabla f(\mathbf{w}^{(k)})), \tag{23}$$

où $\mathrm{prox}_g(\cdot)$ est l'opérateur proximal de g, cf. Annexe E.

Nous mentionnons que nous pouvons accélérer les schémas de gradient proximal (cf. [24]) par la « première méthode de Nesterov » [132], comme suit :

$$\begin{aligned} \mathbf{z}^{(k+1)} &= \mathbf{w}^{(k)} + \omega^{(k)}(\mathbf{w}^{(k)} - \mathbf{w}^{(k-1)}) \\ \mathbf{w}^{(k+1)} &= \mathrm{prox}_g(\mathbf{z}^{(k+1)} - \alpha^{(k)} \nabla f(\mathbf{z}^{(k+1)})) \end{aligned} \tag{24}$$

avec $\omega^{(k)} \in [0, 1)$. De manière évidente, la récursion (24) est similaire à (23), à la différence qu'un pas d'interpolation supplémentaire est effectué avant l'application du gradient proximal. Pour la simplicité, nous allons préfixer les méthodes ainsi accélérées par F(ast).

La méthode du gradient proximal appliquée au problème (19)

Soient $f(\mathbf{w}) = l_d(\mathbf{y}, \mathbf{D}\mathbf{w})$ et $g(\mathbf{w}) = rl_r(\mathbf{w})$, la récursion (23) particularisée au problème (19) s'écrit

$$\mathbf{w}^{(k+1)} = \mathrm{prox}_{rl_r} \left(\mathbf{w}^{(k)} - \alpha^{(k)} \nabla l_d(\mathbf{y}, \mathbf{D}\mathbf{w}^{(k)}) \right) \tag{25}$$

avec $\nabla l_d(\mathbf{y}, \mathbf{D}\mathbf{w}) = -\mathbf{D}^T(\mathbf{y} - \mathbf{D}\mathbf{w})$ pour $l_d(\mathbf{y}, \mathbf{D}\mathbf{w}) = \frac{1}{2}\|\mathbf{y} - \mathbf{D}\mathbf{w}\|_2^2$ et l'opérateur $\mathrm{prox}_{rl_r}(\cdot)$ qui dépend de la définition de $l_r(\mathbf{w})$. Nous rappelons que les formules analytiques pour $\mathrm{prox}_{rl_r}(\cdot)$ pour $l_r(\mathbf{w})$ définies par (16)-(18) sont définies dans l'Annexe E. Nous attirons l'attention sur le fait que certains algorithmes standard de la littérature tomoPIV peuvent être considérés comme des cas particuliers de la méthode de gradient projeté pour des choix

particuliers de $l_d(\cdot,\cdot)$ et $l_r(\cdot)$. Par exemple, pour $l_d(\mathbf{y},\mathbf{Dw}) = \frac{1}{2}\|\mathbf{y}-\mathbf{Dw}\|_2^2$ et $l_r(\mathbf{w}) = 1$, la récursion (25) revient à l'itération de SIRT dans laquelle $\mathbf{W} = \mathbf{I}$ et $\mathbf{\Gamma} = \mathbf{I}$. D'une manière similaire on obtient la même équivalentce pour SIRT+. Dans la suite, nous appellerons les algorithmes de gradient proximal par Iterative Shrinkage-Thresholding Algoritm (ISTA), suffixé par la contrainte un terme correspondant à la contrainte $l_r(\cdot)$ que l'on lui impose.

Nous faisons deux remarques. Premièrement, comme le suggère l'itération (25), ISTA/ISTA+ peuvent être étendus de manière à prendre en compte la parcimonie sur la solution recherchée en faisant des choix judicieux pour la fonction $l_r(\cdot)$, cf. Annexe E pour les formes analytiques correspondantes pour les fonctions régularisant la parcimonie. Deuxièmement, puisque ISTA/ISTA+ sont exprimés comme des méthodes de gradient proximal, ils peuvent être accélérés par des schémas de Nesterov, cf. (24). On référera les algorithmes qui en découle comme Fast Iterative Shrinkage-Thresholding Algoritm (FISTA), FISTA+, FISTAℓ_1+, ...

Le gradient projeté non-linéaire appliqué au problème (20)

Nous nous intéressons au problème (20) - où l'on considère pas, pour de raisons de simplicité, la contrainte « $\|\mathbf{w}\|_1 \leq a$ »- que nous résolvons avec une approche basée sur le gradient projeté non-linéaire. Pour $f(\mathbf{w}) = l_d(\mathbf{y},\mathbf{Dw})$, $\mathcal{W} = \mathbb{R}_+^m$ et la distance KL comme opérateur de proximité (cf. (22)), nous obtenons

$$\mathbf{w}^{(k+1)} = \operatorname{diag}(e^{-\alpha^{(k)}\nabla l(\mathbf{y},\mathbf{Dw}^{(k)})})\,\mathbf{w}^{(k)}, \tag{26}$$

où $\operatorname{diag}(\mathbf{v}) \in \mathbb{R}^{m\times m}$ est une matrice carrée dont les éléments diagonaux sont collectés dans le vecteur $\mathbf{v} \in \mathbb{R}^m$. De manière intéressante, si nous considérons $l_d(\mathbf{y},\mathbf{Dw}) = \mathrm{KL}(\mathbf{y},\mathbf{Dw})$, la récursion (26) se réduit à celle de SMART, cf. (14). Nous pouvons, de manière alternative, nous intéresser au problème (19) afin de résoudre un problème contraint par la parcimonie du signal avec une méthode gradient projeté non-linéaire. Nous référerons à ces problèmes comme SMARTℓ_1 ... De plus, en accélérant ces méthodes avec les schémas de Nesterov, nous obtenons leur correspondants rapides, cf. « Fast Simultaneous Multiplicative Algebraic Reconstruction Technique (FSMART) », FSMARTℓ_1. Notons qu'une variante de FSMART a déjà été proposée dans [142].

Nouvelle technique de reconstruction pour la tomoPIV basée sur l'ADMM

Nous nous intéressons, dans cette section, à une nouvelle méthodologie innovante dans la communauté du traitement du signal, cf. « Alternating Direction Method of Multipliers (ADMM) ». En effet, cette procédure se focalise sur le problème suivant :

$$\begin{aligned} &\min_{\mathbf{w}} f(\mathbf{w}) + g(\mathbf{z}) \\ &\text{subject to } \mathbf{Aw} + \mathbf{z} = 0 \end{aligned} \tag{27}$$

où $f : \mathbb{R}^m \to \mathbb{R}$, $g : \mathbb{R}^n \to \mathbb{R}$ sont des fonctions fermées et convexes. Nous nous intéressons à ce type de techniques de part leur conditions souples sur les fonctions $f(\cdot)$ et $g(\cdot)$ (qui ne doivent pas nécessairement être différentiables) et les garanties de convergence sous des

conditions assez générales (cf. [34]).

Dans le contexte de notre application, nous abordons le problème (15) avec $l_d(\mathbf{y}, \mathbf{Dw}) = \|\mathbf{y} - \mathbf{Dw}\|_2$ et $l_r(\mathbf{w})$ définis comme dans (16), (17) et (18). Le problème (15) peut être ré-écrit de manière équivalente :

$$\min_{\mathbf{w},\mathbf{z}_1,\mathbf{z}_2} l_r(\mathbf{z}_1) + \mathbb{I}_{\mathcal{B}(\mathbf{y},\epsilon)}(\mathbf{z}_2) \quad \text{subject to} \begin{cases} \mathbf{z}_1 = \mathbf{w} \\ \mathbf{z}_2 = \mathbf{Dw} \end{cases}, \tag{28}$$

où $\mathcal{B}(\mathbf{y}, \epsilon) = \{\mathbf{v} \in \mathbb{R}^n \,|\, \|\mathbf{y} - \mathbf{v}\|_2 \leq \epsilon\}$ est la boule ℓ_2 de rayon ϵ centrée sur $\mathbf{y}$. Pour souci de concision, nous ne développons pas ici nos dérivations appliquées au problème tomoPIV. Nous retenons tout de même que ces dernières ont été inspirées par l'algorithme « C-SALSA » proposée en [7]. Nous référerons aux algorithmes qui en découlent, selon le choix de la fonction $l_r(\cdot)$, comme bpADMM+, bpADMMℓ_1, bpADMMℓ_1+, ...

Estimation jointe des volumes et des vitesse

L'estimation du mouvement pour la tomoPIV se fait, de manière quasi-uniforme dans la littérature, en appliquant des traitements a posteriori à deux distributions consécutives volumiques, précédemment estimées, afin d'accéder au champ de déplacements qui les relie [74]. Même si au niveau conceptuel l'estimation séquentielle est intéressante, elle souffre de certaines faiblesses. De manière plus réaliste, la distribution volumique au cours de la séquence temporelle peut être modélisée comme une entité déformée par le mouvement du fluide. Dès lors, l'estimation indépendante des deux quantités ne respecte pas la vérité physique du système. En outre, les imprécisions sur le modèle (qui peuvent être dues à une calibration inexacte, au faible nombre d'observations) ne sont pas prises en compte dans les méthodes actuelles. La netteté des champs de vitesse reconstruits peut être donc améliorée par leur intégration dans les algorithmes d'estimation.

Récemment, *Novara et al.* [134] ont proposé une approche qui respecte la structure jointe des volumes et des vitesses. En effet, les auteurs mettent en place une heuristique dans le but d'initialiser l'algorithme MART avec une quantité prenant en compte deux vues successives de la scène. Cette technique accélère la reconstruction et affine la précision de la reconstruction. Nous formalisons, dans le même esprit d'estimation jointe, un critère global qui exprime la connexion entre les densités volumiques instantanées consécutives et les vitesses qui les rattachent. En particulier, nous nous proposons de résoudre le problème suivant :

$$\begin{aligned} &\min_{\mathbf{w}_t,\mathbf{w}_{t+1},\mathbf{u}_t} f_d(\mathbf{w}_t, \mathbf{w}_{t+1}, \mathbf{u}_t) + \lambda \left[\|\mathbf{w}_t - \mathbf{w}_t^\star\|_2^2 + \|\mathbf{w}_{t+1} - \mathbf{w}_{t+1}^\star\|_2^2 \right], \\ &\text{sous contrainte } f_r(\mathbf{u}_t) = 0. \end{aligned} \tag{29}$$

où $\mathbf{w}_t^\star, \mathbf{w}_{t+1}^\star$ résolvent respectivement le problème (20) et le paramètre $\lambda > 0$ modélise un rapport entre les bruits qui peuvent découler des imperfections sur le modèle de transport et des reconstructions inexactes volumiques. Les fonctions $f_d(\cdot)$ et $f_r(\cdot)$ modélisent respectivement le terme d'attache aux données qui prend en compte des particularités photométriques sur la séquence temporelle d'images et un *a priori* sur le champ de déplacement. Des choix particuliers de ces-dernières nous mènent à une formulation

spécifique du problème. Plus particulièrement, la fonction $f_d(\cdot)$ est dictée par l'hypothèse de conservation de la luminance de la scène dans le temps décrite par l'équation (7). Quant au terme *a priori* sur le champ de vitesse, en posant $f_r(\mathbf{u}_t, \boldsymbol{\Theta}) = \sum_j \mathbb{I}_{\{\boldsymbol{\Theta}\}}(u(\mathbf{k}, t))$, où $\mathbb{I}$ est la fonction indicatrice et $\boldsymbol{\Theta}$ un vecteur de paramètres, nous imposons à ce dernier d'être **localement** constant sur un petit voisinage autour de $\mathbf{k}$. Nous obtenons l'expression analytique d'une nouvelle fonctionnelle à minimiser :

$$\begin{aligned} f_j\left(\mathbf{w}_t(\mathbf{k}), \mathbf{w}_{t+1}(\mathbf{k}), \boldsymbol{\Theta}\right) = &\left\|\mathbf{w}_t(\mathbf{k}) - I(\boldsymbol{\Theta})\mathbf{w}_{t+1}(\mathbf{k})\right\|_2^2 + \\ &\lambda\left[\left\|\mathbf{w}_t(\mathbf{k}) - \mathbf{w}_t^\star(\mathbf{k})\right\|_2^2 + \left\|\mathbf{w}_{t+1}(\mathbf{k}) - \mathbf{w}_{t+1}^\star(\mathbf{k})\right\|_2^2\right], \end{aligned} \tag{30}$$

où $\mathbf{w}_t(\mathbf{k}), \mathbf{w}_t^\star(\mathbf{k})$ collectent les densités volumiques $\mathbf{w}_t, \mathbf{w}_t^\star$ sur le voisinage considéré autour de $\mathbf{k}$. Nous accédons au minimum de (30) par une procédure itérative de descente de gradient.

Résultats

Nous avons validé nos approches dans un contexte synthétique destiné à reproduire les particularités d'un système réel de tomoPIV. Pour ceci, nous avons considéré un cuboïde discrétisé dans une grille cartésienne de $61 \times 61 \times 19$ voxels, dont l'unité de voxel est établie à 1 (adimensionnel). Nous obtenons, à partir d'un système de 4 caméras et après la calibration de ce dernier, le dictionnaire d'encodage $\mathbf{D} \in \mathbb{R}^{14884\times 70699}$ et le dictionnaire de décodage $\mathbf{B} \in \mathbb{R}^{14884\times 565592}$, pour $p = 2$. Nous ensemençons ce volume avec des densités croissantes correspondantes à des ppp allant de 0.0263 à 0.4222.

Nous procédons d'abord à une étude comparative dans le cadre décrit des algorithmes standards contre les algorithmes d'optimisation présentés ci-dessus, tout d'abord lors d'un scénario idéal (non-bruité), ensuite en aggravant le contexte de manière incrémentale (en y rajoutant du bruit de modèle et/ou du bruit de mesure). La Figure 1 illustre une telle comparaison dans le cas idéal (les particules sont placées idéalement aux centres des voxels et les observations ne sont pas perturbées). Nous remarquons en particulier que l'omniprésent SMART est surpassé en performance de reconstruction par ses variantes proximales (c.à.d., les FSMART) et par les autres approches pour l'optimisation convexe (c.à.d., FISTA, ADMM). Par ailleurs, les schémas ADMM pour l'optimisation convexe engendrent des estimations dont le facteur de qualité est proche de 1 même pour des hautes valeurs d'ensemencement ; ceci est dû à une grande vitesse de convergence en milieu idéal. Nos expériences en milieu bruité nous mènent à des conclusions similaires ; plus précisément, les méthodes FSMART et les procédures ADMM pour l'optimisation convexe devancent immuablement en terme de qualité de reconstruction les procédures plus courantes dans la littérature (nous pensons à SMART dans la tomoPIV et à FISTA dans le communauté de traitement de signal), pour des exigences en complexité et stockage comparables.

Nous simulons ensuite un écoulement de cisaillement dans notre cuboïde afin valider l'intérêt de notre approche d'estimation de mouvement. Nous nous plaçons dans un scénario plus proche de la scène tomoPIV originale en rajoutant du bruit de modèle (c.à.d., les particules ont de positions aléatoires dans le cuboïde et les observations sont perturbées par un bruit Gaussien de variance 0.01). La Figure 2 montre les résultats obtenus pour une sous-grille du volume considéré, à une valeur de profondeur fixée, dans un volume

correspondant à un ensemencement ppp $= 0.2$, à partir des volumes préalablement estimés avec bpADMM+. Nous remarquons en particulier que l'utilisation de l'approche jointe permet d'enlever les pics d'erreurs qui peuvent apparaître localement avec l'approche séquentielle basée sur la méthode Lucas-Kanade (LK) itérative ; cependant, lorsque l'espace est peu résolu, elle propage, de manière légère, certains imprécisions sur les solutions qui restent néanmoins inférieures à celles résultantes par l'approche séquentielle. Nos autres expériences nous mènent aux mêmes déductions : globalement, l'approche jointe gère mieux les indéterminations liées à une mauvaise reconstruction volumique ou à une faible résolution de l'espace 3D. Toutefois, une étude comparative dans un scénario expérimental est nécessaire afin d'établir, de manière quantitative dans un milieu réaliste, l'intérêt de nos méthodes.

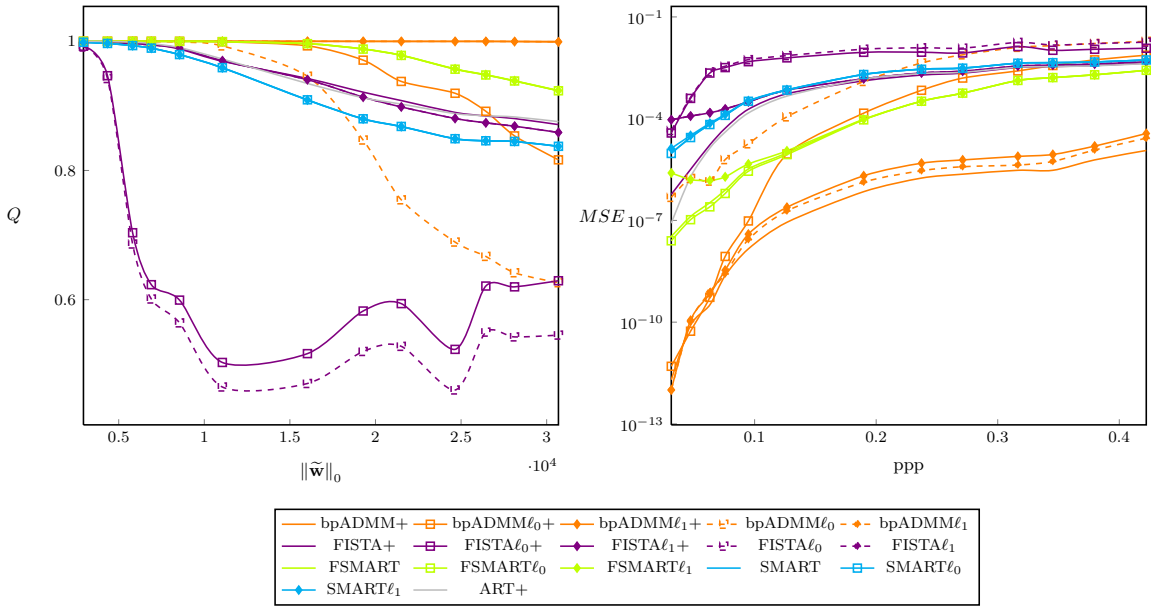

FIGURE 1: Performances des algorithmes de reconstruction volumique dans un scénario idéal sans bruits par comparaison du vecteur estimé $\mathbf{w}^\star$ avec la vérité terrain $\widetilde{\mathbf{w}}$. A gauche : l'évaluation de la mesure de qualité de reconstruction $Q = \frac{\widetilde{\mathbf{w}}^T}{\|\widetilde{\mathbf{w}}\|_2}\frac{\mathbf{w}^\star}{\|\mathbf{w}^\star\|_2}$; à droite : l'évaluation de l'erreur quadratique moyenne $MSE = \frac{\|\widetilde{\mathbf{w}} - \mathbf{w}^\star\|_2^2}{\|\widetilde{\mathbf{w}}\|_0}$.

Organisation du document

Outre cette synthèse en français et une courte introduction, ce document est organisé en cinq chapitres. Le Chapitre 1 présente le contexte expérimental de cette thèse. Nous mettons l'accent sur les principales difficultés liées à la compréhension du mouvement tridimensionnel du fluide turbulent. Nous décrivons les approches classiques de mesure dans le contexte de la mécanique du fluide expérimentale et nous justifions notre choix de se vouer à un système de tomoPIV. Le Chapitre 2 porte sur la formalisation du modèle de projection de l'espace 3D sur le plan bidimensionnel des images et du modèle de transport

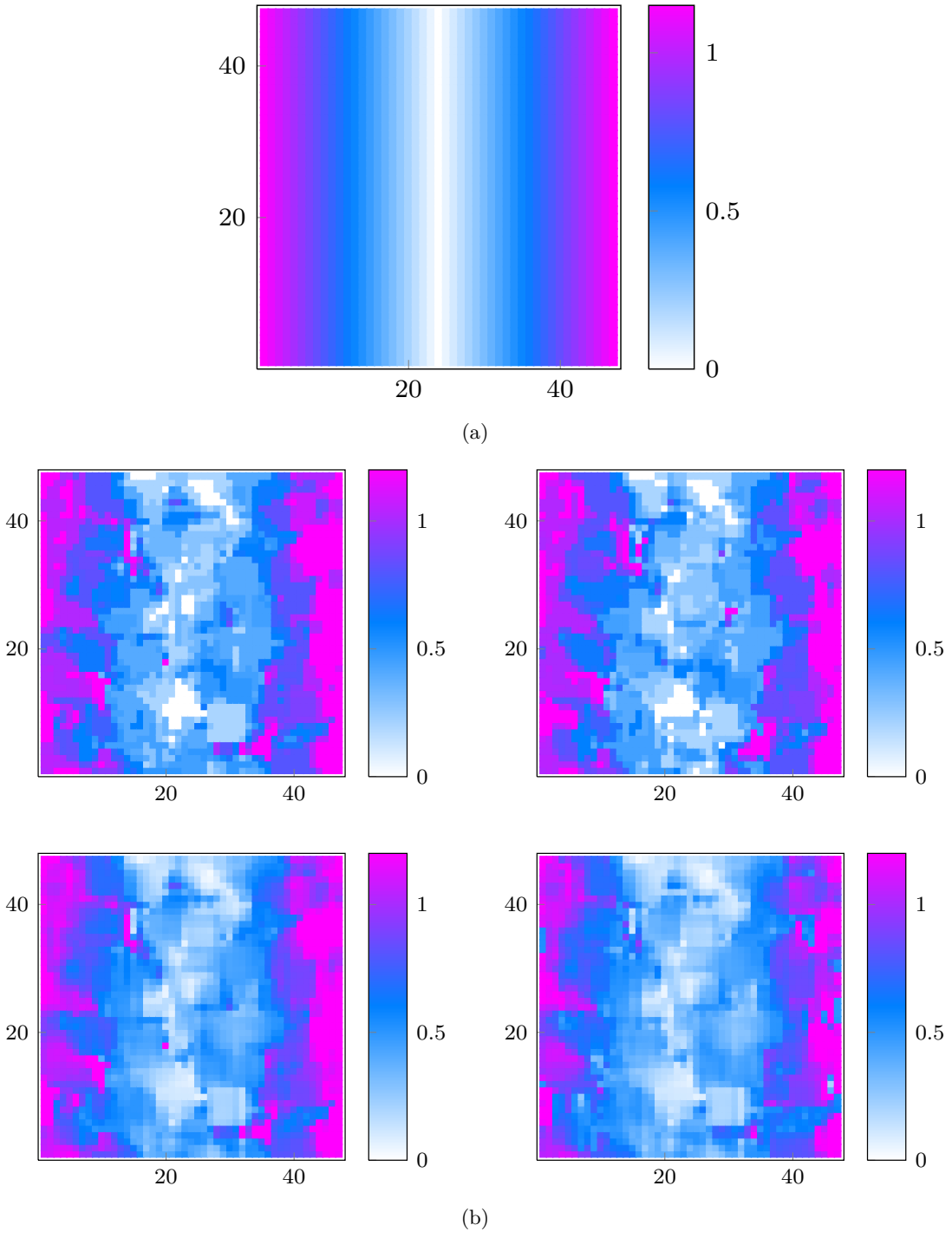

FIGURE 2: Comparaison de l'amplitude du mouvement estimé par quatre méthodes dans un volume ensemencé avec $ppp = 0.2$ lors d'un scénario bruité. (a) : Vérité terrain. (b) : Ligne supérieure, de gauche à droite : Lucas-Kanade (LK)-discret et Corrélations 3D ; ligne inférieure, de gauche à droite : LK itératif et notre méthode.

du fluide. Ce travail est structuré en deux parties : dans un premier temps, nous décrivons xxx

les particularités physiques nous ayant mené à une formalisation des modèles continus de notre application ; ensuite, nous proposons des schémas de discrétisation de ces derniers. Le Chapitre 3 présente le cadre général d'optimisation que nous proposons pour l'estimation du problème de reconstruction volumiques. Plus précisément, nous faisons des connexions intéressantes entre les procédures standards pour la tomoPIV et des méthodes proximales et nous introduisons dans la littérature tomoPIV les méthodes innovantes ADMM. L'intérêt de basculer vers de telles nouvelles approches est mis en évidence lors d'une étude numérique. Le Chapitre 4 présente notre méthode d'estimation jointe des volumes et de vitesse ; en particulier, nous montrons que contraignant le terme d'attache aux données permet d'enlever des indéterminations liées à une reconstruction volumique médiocre. Finalement, le Chapitre 5 résume les approches proposées et présente des perspectives à considérer dans un travail futur.

Introduction

Measuring with precision the tridimensional velocity of the turbulent flows constitutes one of the fundamental problems of fluid dynamics. Understanding the motion of turbulent fluids impacts at both a practical and theoretical level: while it represents one of the greatest conundrums in theoretical physics, the stakes of fathoming it out are high for various engineering applications.

Accessing to a fine information on tridimensional (3D) turbulent flows is typically a complex tasks that standard theoretical developments or numerical simulations fail in solving. Therefore, a popular alternative to theoretical developments and numerical simulations is Particle Image Velocity (PIV). This approach consists in resolving the motion of fluid by coupling **computer vision** techniques with **experimental fluid mechanics** to produce observations, further submitted to **signal processing** tools. Unfortunately, classical PIV literature mainly addresses bidimensional scenarios (*e.g.*, the fluid is assumed to be confined in a two-dimensional (2D) layer), whereas turbulent flows typically encountered in practice are highly tridimensional. It is not until recently that the focus of PIV community turned to the tridimensional case, giving birth to a novel measuring technique, coined Tomographic PIV (tomoPIV). If successful simple 3D motion estimation techniques to solve the observations produced by a tomoPIV system are already available, there is room for progress in terms of understanding of the visualized system, modeling it accurately and inserting physically-sound priors into the reconstruction schemes.

Objective of this thesis

The overall objective of this thesis aims at the creation of new approaches allowing for an effective and efficient study of the tridimensional flows from multiple synchronized sequences of bidimensional images. The challenge of solving the inherent estimation problems encompasses numerous bottlenecks of the current technology, yet to be overcome. We give hereafter a description of the problems that will be addressed in the current manuscript and the corresponding objectives.

Volumetric Image Reconstruction

Modern measurements in fluid dynamics are enabled by seeding the fluid with passive tracers. In the current literature, state-of-the-art procedures belonging to the *algebraic family* have gained a lot of interest. Although conceptually interesting and effective in

terms of storage and computational loads, the latter suffer from a certain number of caveats. On a theoretical level, their behavior in presence of noisy data is still an open question. Furthermore, such procedures do not fully exploit physical knowledge of the scene (*i.e.*, *non-negativity* and *sparsity*). In practice, these state-of-the-art techniques can only accurately recover a limited number of particle positions from the available observations. The latter shortcoming directly affects the subsequent fluid motion estimation, which depends on the density of particles of the fluid: the higher the density of the particles the better the resolution of the fluid movement at fine scales.

The goal of the volumetric reconstruction task is to devise novel procedures robust to noise to estimate the distribution of a moderate-to-high number of passive tracers with high accuracy. We propose to achieve this goal by *(i)* fully exploiting the physical constraints on the signal; *(ii)* working out faster schemes with the same or lower storage requisites.

Towards Joint Volume-Velocity Reconstruction:

Current state-of-the-art procedures for 3D fluid-motion estimation generally proceed in two steps: *(i)* the 3D volume is first reconstructed at each time instant from the observations of the corresponding 2D images; *(ii)* the fluid motion is then estimated from the decision made on the volume at the first step. Although its implementation is straightforward and it yields satisfying results, this two-step procedure is suboptimal in terms of achievable performance. In fact, the volume reconstruction is performed separately at each instant, disregarding the velocity field that links the two consecutive estimated quantities. Moreover, the current schemes do not account for the possible reconstruction errors on the volumetric reconstruction.

The objective of this joint volume-velocity task is to develop methods of 3D motion estimation directly from 2D images. We propose to achieve this goal by designing a novel formulation of the problem accounting for the nexus between the volume and the velocity.

What This Thesis Is Not About

The goal of this thesis is providing a theoretical understanding of the scene and at designing tools with great physical underpinning prone to be easily applied in practice. However, our work must not be understood as an experimental assessment of proposed methods within the Tomographic PIV (tomoPIV) context. We aim, on the flip side, at bridging the gap between theoretical signal processing and experimental fluid mechanics by devising theoretical tools accounting for physical knowledge of the scene convenient for high complexity systems and destined to be assessed on a real-world tomoPIV benchmark.

Contributions

To respond to first task, we recast the tomoPIV problem within a general optimization framework. First, we emphasize that both physical constraints (*i.e.*, non-negativity, sparsity) and noisy observations can be handled by properly defining an optimization problem. Then, we exploit the general framework of proximal methods to show that

procedures with the same computational and storage features as standard methods can be derived. In particular, we show that some standard algebraic methods can be seen as particular cases of proximal methods. Assessment in a realistic synthetic scenario show a considerable enhancement in reconstruction accuracy for moderate-to-high seeding concentrations of regularized proximal methods versus their unconstrained counterparts.

The second task is addressed by formalizating a novel functional that accounts for noisy settings and for the linked structure between two instantaneous volume reconstructions and alternatively seeking for the respective quantities via a descent procedure. A similar assessment campaign in a realistic synthetic scenario validates the interest of formally defining the nexus between the two reconstruction problems as a joint optimization problem.

Outline and Organization

This thesis is organized as follows. Chapter 1 presents the experimental context of this thesis. The main challenges related to the understanding of the 3D turbulent fluid motion are delineated. Classical tools enabling the retrieval of probes of the fluid motion are depicted, with focus on 3D techniques. Finally, the choice of relying on a tomoPIV setting within our work is motivated.

Chapter 2 formalizes the 2D-3D projection and the fluid transport models. The first part of the chapter unravels the physical knowledge leading to a continuous formulation of the two problems. The second part proposes discrete counterparts of the latter. In particular, we propose a novel projection model offering the advantages of **structuring** the sparsity in the context of volume estimation problem and of backpedaling to its smoothed (denser) counterpart for the velocity estimation problem.

Chapter 3 exposes the framework we propose to handle the issue of volume reconstruction. In particular, we make interesting connections between state-of-the-art procedures and proximal algorithms. In a second part of the chapter, we emphasize on the importance of reducing the dimensionality of the initial problem by formalizing a general framework for all state-of-the-art pruning procedure within the tomoPIV context. The performance is assessed, for both the volume reconstruction problem and the pruning procedures, on various realistic tomoPIV scenarios.

In chapter 4, we present our method to address the problem of velocity estimation of the turbulent fluid. This chapter provides the technical aspects, as well as performance assessment on various realistic tomoPIV scenarios.

Finally, chapter 5 recaps the proposed approaches and the obtained results, and some future perspective are suggested.

With the partial support of DGA, this thesis has evolved in the Fluminance team at INRIA Rennes, whose aim is providing in the one hand image sequence methods devoted to the analysis and description of fluid flows and in the other hand physically consistent models and operational tools to extract meaningful features characterizing or describing the

observed flow and enabling decisions or action.

Chapter 1. Experimental Fluid Mechanics

In my early adolescence, I would discover French literature by Jacques Prévert's "Déjeuner du matin", that I would read over and over again until visualizing each frame of the scene in its bare simplicity. The character would pour the coffee into a mug, then add a drop of milk to it. Then, he would abidingly stir the whole with a tea-spoon, while he lightened a cigarette with his other hand. He would next linger in front of his mug, where small whirlpools were spiraling, blowing smoke rings. Later on, as I persisted deeper in my science studies, I would grow up to translate this matinal ceremony in terms of signal processing and fluid mechanics. Moreover, I would take this example whenever someone asked me to explain in a very simplistic way my thesis' subject.

In fact, we all empirically know that stirring the composition with a spoon increases the homogenization rate of the two liquids (coffee and milk). The fluids become **turbulent** and streams of liquid start interacting with each other, which speeds up the mixing process (contrary to the viscosity, which slows it down). The smoke rising from a cigarette resting in an ashtray is an excellent descriptor of the fluid behavior based upon its velocity profile. For the first few centimeters, the flow is smooth, regular and fluid streams are rising, parallel and unmixed, with a moderate speed: the flow is **laminar**. Then, as the velocity of the plume increases, the flow is twisted into eddies and irregular paths, **transitioning** from a laminar regime to a **turbulent** one (see Figure 1.1 for a visualization of the three regimes).

On top of being at stake for the theoretical comprehension of common domestic habits, the study of turbulent fluid flow represents a discipline of far-reaching interest in a large panel of scientific domains. Indeed, a good knowledge of its behavior would be of great contribution in myriads of engineering fields, such as aerodynamic shape design, oil recovery from an underground reservoir, or multiphase/multicomponent flows in furnaces, heat exchangers, and chemical reactors.

Turbulent flows are described by the *Navier-Stokes* equations, stemmed from *Newton*'s laws of motion in an hydrodynamical context and presented here for an *incompressible* fluid:

$$\frac{\partial u(\mathbf{h},t)}{\partial t} - \mu \nabla u(\mathbf{h},t) + (u(\mathbf{h}),t) \cdot \nabla)\, u(\mathbf{h},t) + \nabla p = \mathbf{f}, \tag{1.1}$$

$$\nabla \cdot u(\mathbf{h},t) = 0, \tag{1.2}$$

Figure 1.1: Buoyant plumes of smoke. Their visualization demonstrates three types of fluid flow: **laminar**, **transitional**, and **turbulent**. At the bottom of the photo, the plumes are smooth and orderly, as is typical for **laminar flow**. Despite the quiescent air, tiny perturbations sneak into the flow causing periodical vortical whorls, as we can observe mostly on the first plume; the flow is in **transition**. Then, disturbances in the plume get amplified and break down into **turbulence**; near the top of the image, we observe the smoke's movement: chaotic and intermittent, full of turbulent eddies. (Photo credit: Gizmodo Shooting Challenge)

where $u(\mathbf{h}, t)$ stands for the Eulerian velocity of the fluid at time t at a position $\mathbf{h} = \begin{bmatrix} h_1 & h_2 & h_3 \end{bmatrix}^T \in \mathbb{R}^3$ expressed in a canonical system of coordinates, p for the pressure, $\mathbf{f}$ is the sum of exterior forces and μ is the viscosity of the fluid, inversely proportional to the *Reynolds number*. The appearance of the convection term $(u(\mathbf{h}, t) \cdot \nabla)\, u(\mathbf{h}, t)$, which depicts the non-linearities in the flow, is at the origin of the difficulties encountered in the resolution of the system. Appendix A elucidates the two main approaches to address the fluid motion description. Despite more than a century of theoretical research, the analytical resolution of *Navier-Stokes* equations remains one of the most challenging conundrums in physics. It is thus indispensable to resort to alternative strategies in order to access to noteworthy solutions relevant for the industries.

Computational Fluid Dynamics (CFD) uses numerical methods and algorithms to solve and analyze the system upper-mentioned. *The Reynolds number* is the control parameter of *Navier-Stokes* equations. A generally accepted rule-of-thumb is that *Reynolds number* values less than 2000 will probably be laminar, while values in excess of 10000 will probably be turbulent. Numerical simulations - such as Direct Numerical Simulation (DNS), Large Eddy Simulation (LES) - of the flow are a valuable tool providing a complete description of the flow structure in the turbulent regime. The reader should refer to [105] for a detailed review skimming through recent developments in numerical simulation. Having said that,

these methods are quickly restricted by the substantial number of parameters to handle which evolves with respect to the *Reynolds number* and are thus confined to moderate values of the latter.

Going back to Prévert's example, one can notice how I was able to draw conclusions on the 3D nature of the flow, whether it was a liquid or a gas. In fact, as the white color of the milk clashes against the deep brown color of the coffee, we can visualize the milk's flow pattern as it mixes with the coffee. Had Prevert's character not have added milk, the foam at the surface of the coffee would have also given valuable information on the flow pattern. The buoyant plumes rising from the cigarette are an even better visualization tool, provided its grey color is in contrast with its environment, as the smoke uplifts unconstrained to the ceiling. Moreover, the information we are given is 3D since our brain naturally produces the depth perception out of the two different views given by our two eyes. This is a very simple example of a flow visualization system.

Flow visualization techniques have emerged in parallel to CFD as an effort to understanding flow phenomenon. They consist in employing certain techniques so that the flow velocity is being made visible. Therefore, by observing flow patterns, one can derive qualitative data from the obtained flow picture and deduct informations about the flow field. Other, more conventional flow measurement techniques involving experimental systems (Pitot tubes, hot-wire anemometers, vane anemometers) were available, but only provided point-wise flow statistics. With the arrival of quantitative velocity measurements (which are to be developed in Section 1.2) estimated velocity distribution became accessible and allowed from then on the computation of global statistics within the turbulent glow.

This situation where we intend to find the nature of phenomenon based on observations of its effects is commonly known in the Signal Processing Community as an **inverse problem**. Its resolution relies on a **modelling** of the **direct problem** which is a close representation of the actual measuring system. These steps are detailed in Chapters 3 and 4.

For now, we aim at non-exhaustively overviewing a large panel of visualization techniques with emphasis on techniques allowing for 3D measurements. For doing so, we first describe in section 1.1 means of rendering the transparent media of the flow visible by the use of passive tracers. Then, we move forward to general visualization techniques used in experimental fluid mechanics, that we briefly enumerate in section 1.2. Finally, we present in section 1.3 a PIV measurement chronicle and its historical evolution toward 3D probes.

1.1 Passive Tracers

Most fluids, gaseous or liquid, are transparent media. As a consequence, their motion remains invisible to human eye during direct observation, unless a technique allowing for the visualization of the flow is applied. If in the earlier example flowing fluid was visible *naturally* (turbulent coffee or plumes of smoke) is because of the unscripted occurrence of means equivalent to the experimental methods of flow visualization described in the following section. The literature on flow visualization covers anthologies of remarkable flow scenes picture [130, 180].

Certain flow measurements techniques involve the use of neutrally buoyant markers immersed in the fluid which follow its movements. The flow becomes *seeded* with *passive* particles which, given their nature, do not perturb the flow. If one resolves the light scattered from these tracer particles, a quantitative study is rendered possible by measuring the velocity of the scatterers. These particles are chosen, depending on the measurement task, based on their mean size, shape, width, surface characteristics and refractive index. Gas is commonly seeded with smoke, whereas in liquid flows the choice lies between dye, bubbles, ash, hollow glass spheres, polyamide, fluorescent or phosphorescent particles (Figure 1.2 shows rendition of flows depending on particle media). Other visualization techniques register the evolution of certain passive scalar components, such as dye concentration, water vapor concentration or sea surface temperature and allow for **qualitative** measurements. However, in this thesis, we are interested in **quantitative** measurements allowing for velocity estimation. Insights on methods for the generation and the seeding of fluids with passive tracers can be found in [123], [107].

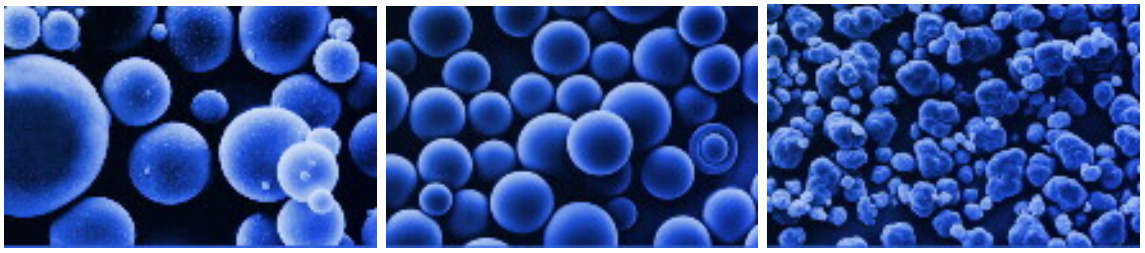

(a) (b) (c)

Figure 1.2: Rendition of flow pattern depending on the nature of the particle tracer. From left to right: polyamide seeding particles, silver-coated hollow glass spheres, fluorescent polymer particles. (Photo credit: Dantec Dynamics)

1.2 Measurements in Flows

In experimental fluid mechanics, we count for three flow visualization techniques:

Surface flow visualization : Visualization of flow patterns very close to or at the body surface is a key element in measuring the rates of shear or pressure forces exerted by a fluid as it approaches a solid surface. Commonly, visible information is made possible by the application of colored oil. The information derived concerns quantities as flow direction, mass transfer to the obstacle, the obstacle's temperature. A literature survey can be found in [69].

Optical methods : These category of methods, among which we mention Shadowgraph and Interferometry, produce a natural, easily-interpretable image of refractive-index-gradient fields. Optical methods do not require any intrusion in the fluid and prevents any modifications of the considered flow. They can thus be implemented to undertake full scale measurements and outdoor experiments [164].

Particle tracer methods : The most common images issued by flow visualization techniques rely on the use of particle tracers presented in the previous section. The seeded fluid is illuminated and the scattered light is captured by numerical cameras. The goal of this procedure is to measure the velocity of the flow and the techniques employed fall into the fields of Particle Image Velocity (PIV) or Particle Tracking Velocity (PTV) methodologies.

A comprehensive description of each technique can be found in Merzkirch's classic text [125]. Whatever the method, it is through the interpretation of images it produces that one gains an understanding of the physics of the flow field. We are interested in the retrieval of measurements allowing to deduct information on the velocity fields of the turbulent fluid at any given point. While the first method enables solely for surface statistics, the second allows for motion retrieval with the cost of having recourse to a non-trivial acquisition model [11]. For the above considerations, particle tracer methods are the most appropriate for the present study.

1.3 From Planar to 3D Measurements

Turbulent flows exhibit complex and highly 3D motions over a wide range of scales and amplitudes. Given the highly tridimensional nature of fluid velocity under certain regimes, planar measurement systems quickly evolved towards systems allowing for the retrieval of the three components of the velocity fields. This section depicts the evolution of planar tracer methods toward 3D probes. We intent, by the present overview, to bring forth certain theoretical and practical tools indispensable for the comprehension of the manuscript. For thorough descriptions of this evolution, the reader should start by addressing the bibliography of PIV by Adrian [3] which covers exhaustive early references on PIV starting with Meynart's articles released during his Ph.D. thesis [126, 127] - marking the introduction of PIV- and scanning up to succeeding developments until 1995. Later on, the same author flags the 20 years since the term was first coined by pointing out important milestones until the early 3D developments thought **stereoscopic-PIV** [2]. More recently, book chapter [13] and article [155] review techniques for turning PIV into a 3D velocimetry procedure. Likewise, in [156] a brief survey of the advancement with respect to dimensionality is depicted, together with working principles of the 3D probes. The reader should refer to [153] and [4] for complete theoretical comprehension of the signal processing underpinning particle tracer velocimetry.

A PIV system is historically a quantitative measurement allowing for the retrieval of velocity vectors in a planar domain. Figure 1.3 depicts the standard progression of steps towards these measurements. First, light passive tracers are immersed in the flow with respect to its nature. A camera faces the volume of interest. Then, a light sheet of the latter is illuminated at high frequency by a laser such that the light scattered by the particles is captured on the camera's plane at each period. These consecutive recordings are then post-processed by means of motion retrieval techniques, provided the particles follow the fluid's movements, in order to compute the velocity fields within the illuminated plane.

Highlights of PIV development have been marked by the arrival of **digital** cameras - allowing for recordings at very high frequencies ([187]) - and of **high-power pulsed**

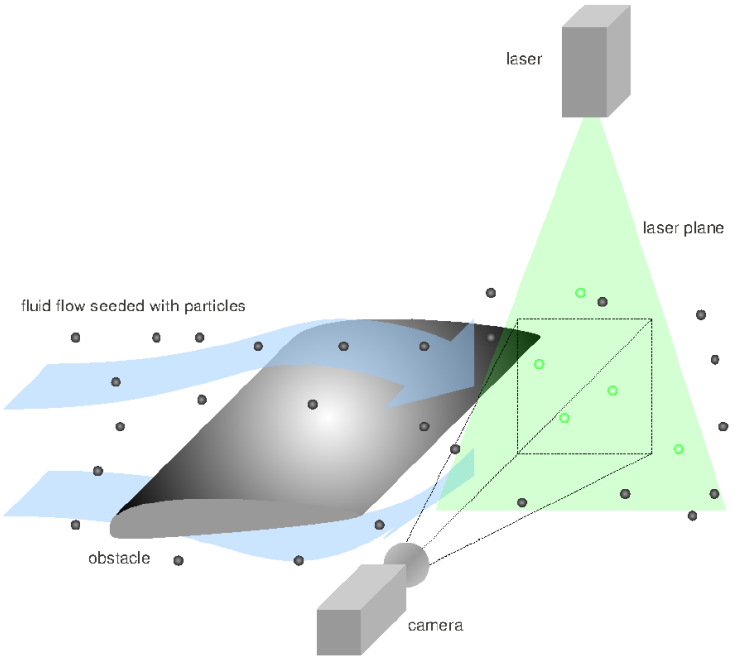

Figure 1.3: Experimental arrangement for particle image velocimetry in a wind tunnel. The flow behind an ostacle is seeded with tracer particles. A light sheet within the flow is periodically illuminated by means of a laser. The light scattered by the tracer particles is recorded at each illumination by a high frequency numerical camera. (Photo credit: taken from [25]).

lasers which enabled for more accurate measurements within larger volumes of interest. However, along with important technological milestones, one should dwell on progress in the understanding of the mathematical underpinning particle tracer measurements. In fact, theoretical knowledge on the system gives the means for a pertinent model of the latter, which dramatically improves the accuracy of reconstructed velocity fields. Moreover, a good comprehension of the physical framework provides neat estimations of parameters fitted for the layout of the system. These theoretical aspects will be detailed in Chapter 2.

Despite great progress in PIV, its planar limitations soon lead to a turning point in flow visualization techniques. As pointed out earlier, the full understanding of turbulent fluids requires the access to 3D measurements. A first step towards this direction was made by the emergence of stereoscopic adjustments to planar PIV, enabling though epipolar geometry for 3C measurements ([12], [186]). Further on, stereoscopic configurations were enhanced by the illumination of two or more parallel sheets in the volume, allowing for the computation of the complete velocity gradient tensor over a planar domain (**dual-plan stereoscopic-PIV**, **multiple-plan PIV**, [106]). However, extended planar techniques are limited by the discontinuous nature of the planar snapshots captured. One cannot draw quantitative statistics on intricate vortex interactions out of uncorrelated measurements. The study of the 3D organization of unsteady flow must thus be extracted out of measurements acquired in the 3D space.

Numerous techniques dedicated to the measurement of three-dimensional unsteady flow in whole-field studies have emerged starting in early 1990. The latter seem to fall into four categories:

- **internal optics alteration**: Scanning Light Sheet (SLS) [37];
- **holography**: Holographic PIV (HPIV) [100], Digital HPIV (DHPIV) [54];
- **multiple viewpoints**: 3D PTV [118], Digital Defocusing PIV (DDPIV) [138], Synthetic Aperture PIV (SAPIV) [26], tomoPIV [76,77];
- **plenoptic**: plenoptic PIV [10,80,117,172], which can also fall into multiple viewpoints classification [113].

Figure 1.4 shows the classification of upper-mentioned techniques with respect to the space of measurements, to the space of solved solution and to time.

A direct extension of multiple-plan PIV is the **SLS** technique [37], which consists in illuminating a set of approximately equally spaced, discrete light-sheets successive in time. This implies that the scanning pace must be very high with respect to the variation of the particles' positions in time. If this procedure has raised interest by demonstrating great assessments in fluids of low speed, it cannot be applied to flows with velocity exceeding 1m/s [39], thus being considered as a quasi-instantaneous measuring technique.

HPIV received particular attention [100], being considered the preferred approach for the description of volumetric structures in the flow. The interference pattern of a reference light beam with the light scattered by particles is recorded on a photographic plate or, more recently, directly on CCD screens (DHPIV - [54]). The latter is then used to determine the particles' location in depth. An extensive review of both provide an extensive review both film of digital techniques can be found in [124]. If HPIV has not become mainstream it is because of the difficulties of extracting quantitative measurements from film photography. A comparative study between HPIV and multiple viewpoint technique shows that the latter outperforms the holographic procedure in terms of spatial resolution, visibility of particle tracers and inherent measurable turbulence characteristics [160]. In contrast, DHPIV attains higher spatial resolutions, but it is constrained to smaller volumes of interest (and thus, to lower seeding concentrations), which corresponds to configurations where the optical system is most accurate [124].

Plenoptic PIV has recently emerged in the PIV community [10,80,117,172]. Its inception brings together two most up-to-date features in their respective communities by merging methods pertaining to light field imaging with concepts that drive experimental fluid mechanics. The developments in plenoptic cameras began with [1] and were recently improved by [85]. The latest breakthroughs involve the establishment of the **plenoptic function**, which writes a five dimensional complete description of rays of light in space with respect to their positions and angles of propagation. The combination of both the recorded spatial and angular information enables the three-dimensional reconstruction. Unfortunately single camera plenoptic PIV measurements suffer from the same problems as does HPIV due to the low angular resolution. In [113], the authors submit a novel proposal

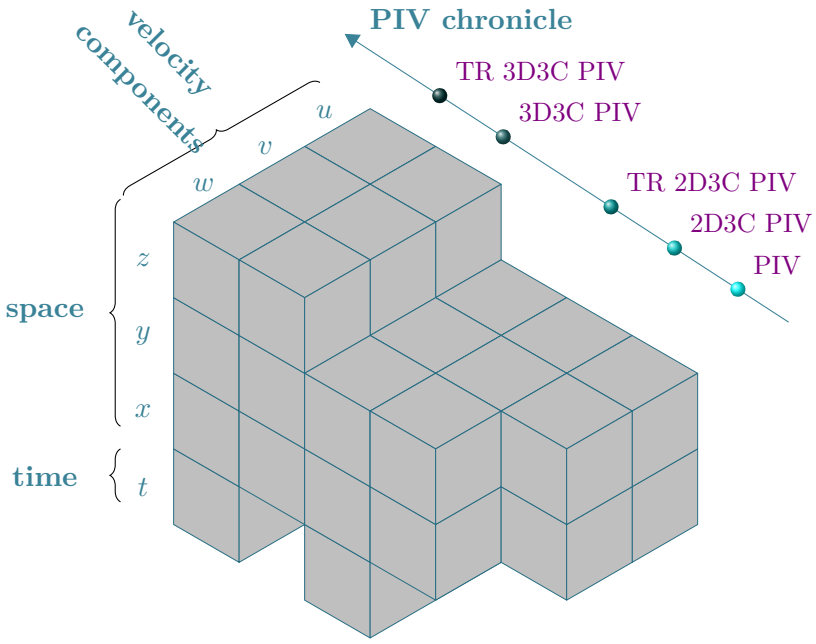

- PIV
- 2D3C PIV
- TR 2D3C PIV : stereoscopic-PIV, dual-plan stereoscopic-PIV, multiple-plan PIV
- 3D3C PIV
- TR 3D3C PIV: SLS, DDPIV, 3D PTV, HPIV, DHPIV, SAPIV, plenoptic PIV, tomoPIV

Figure 1.4: PIV chronicle depicting the evolution of PIV towards time-resolved (TR) tridimensional (3D) measurements. Let $\{u, w, v\} \subset \mathbb{R}^3$ be the space where the three-component (3C) velocity fields are sought and $\{t\}, \forall t \in \mathbb{N}$ the ensemble collecting the time resolution of a TR temporal sequence. Consequently, TR-X denotes time-resolved measurement techniques. With the exception of the SLS procedure, limited to a low velocity range due to its technicality, every X is a TR-X. (Adapted from: [156] and [99]).

which exploits the advantages of Plenoptic PIV in a nowadays standard framework for flow visualization which involves the use of three or more cameras. Although benefits over classical multiple cameras reconstructions have been shown under specific configurations in a simulated scenario, an experimental assessment has not yet been performed at our knowledge. Nevertheless, this technique deserves, in our belief, a close follow-up due to its applicability to large volumes of interest with the use of a lower number of cameras than in standard measurements.

Within velocimetry techniques making use of multiple viewpoints, 3D-PTV [118] and DDPIV [138] rely on the identification of individual particles in the PIV recordings. In 3D-PTV, the coverage of the third dimension of the space field is accessed by combining the output from (typically) four cameras stereoscopic reconstruction and exploring approaches from photogrammetry (particle tracking, cross-correlation) to extract particle trajectories. The reconstruction strongly relies on a good knowledge of both the intrinsic and extrinsic parameters of the cameras and allows for low calibration errors. The DDPIV is based on the defocused blur of the seeding particles by placing an aperture with a defined pattern (usually pinholes arranged as an equilateral triangle) before the lens and thus forming a coded aperture imaging. A single particle is therefore mapped to multiple areas representing its blurred image, whose mutual distance is closely related to the distance of the plane of focus of the camera. The position of the particles are then solved by searching in the superimposed projections from all cameras the patterns which form equilateral triangles [90, 108]. In both techniques, extracting features from the images planes limits the seeding values to moderate values in order to avoid overlapping of particles and implicitly, false matches between different views around the volume of interest. This impedes measurements in volumes with high spatial resolution, for high number of particles.

SAPIV uses methods from previously described light-field imagery in order to digitally refocus a 3D flow field at arbitrary focal planes throughout a volume [26]. An array of synchronized CCD cameras is placed around the volume of interest such that the fields of view overlap. The projections are then recombined using appropriate light field imaging algorithms to obtain different planes of focus. The 3D light field intensity is acquired by refocusing the images throughout the entire volume. Finally, the velocity fields are computed out of successive intensity fields by means of standards 3D cross-correlation. Despite the fact that the technique is adapted to solve large volumes with high seeding densities, the high order of the camera array (up to eight) currently limits the practical use. In [10] the authors explain how this drawback can be overcome by replacing the camera array with a single plenoptic sensor.

Tomographic PIV falls into the multiple viewpoints techniques classification and the imaging principles are similar to that of previously described 3D-PTV. Its novelty consist mostly in the reconstruction of the instantaneous 3D object. The working principles along with applications were first introduced by *Elsinga et al.* in [76, 77] and detailed in seminal paper [74]. Along with the innovative concept, experiments demonstrated the possibility of working at the highest seeding levels in the literature (up to 0.05 in synthetic scenarios and attaining values in the range of $0.02 - 0.08$ ppp in experimental settings [79, 158]). Ever since its arrival, most attention was devoted to understanding and optimizing its properties for the retrieval of 3D instantaneous pattern of the coherent structures in the flow. In fact,

the apprehension of tridimensional objects opened from then on the way to the possibility of unraveling the intricate anatomy of flows in a turbulent regime. In a nutshell, theoretical developments include work on the 3D calibration technique [184]), essential to the control and correction of the mapping between images planes and the discrete volume of interest. Early developments include theoretical studies on tomographic reconstruction with great mathematical underpinning [143, 145]. Later on, initial acceleration schemes of the volume reconstruction procedure have been proposed ([15, 188]), while other digital techniques to accelerate the reconstruction have been investigated [61]. Progress includes analysis of the bias errors induced by the formation of ghost particles during the reconstruction [78] and more recently, improvements on the enhancement of the reconstruction accuracy after their the reduction of their number [75,165]. A step towards joint reconstruction of the volume and the velocity fields has been achieved in [134]. This latter achievement constitutes a milestone in the development of tomoPIV because it respects the nexus between the fluid trajectory and the static volumetric intensity distributions. Principles, limitations and arising tomoPIV model will be detailed in the next chapter.

1.4 Conclusion

Our present study has been motivated by the great spread of the tomoPIV technique since its first occurrence. Its great impact on the community soon lead to myriads of theoretical and experimental studies. Its adaptability to access 3D fields measurements and its performance at high seeding number constitute, on one hand, technical advantages of the measurement procedure. On the other hand, our interest was aroused by already established achievements taking into consideration the physical anatomy of the scene. The latter concerns the spatial distribution of the seeded particles in the scene ([144]) and the joint reconstruction of volume and velocity [134]. This framework motivated us to develop the joint procedure proposed in Chapter 4, which is the main contribution of the present manuscript.

Chapter 2. TomoPIV: Settings and Models

We have presented, in chapter 1, a survey on flow visualization methods with emphasis on optical methods. We have justified our choice of studying the fluid flow estimation problem out of measurements acquired by a tomoPIV system. A thorough comprehension of the intricacies related to the latter is of paramount importance for the development of theoretical tools which solve for the velocity fields of the turbulent fluid visualized within this framework. The goal of this chapter is to elucidate pivotal aspects that can provide optimization guidelines for the inverse problems announced in chapter 1 and detailed in chapters 3 and 4. Firstly, the general measurement principle is detailed. This gives us an entry point to both physical and theoretical understanding of the scene. Since reconstruction quality is impacted by diverse practical factors closely linked to the experimental setting, we overview aspects such as volume illumination, passive tracers related properties and optical system layout. A noteworthy entry point for the specifications of the system is available in the literature [153]. Further on, a mathematical abstraction of the described scenario is formulated both in continuous and discrete case with the goal of closely depicting the physical truth of the context. This representation will subsequently be utilized throughout the whole manuscript.

Working Principles

In a nutshell, the tomoPIV technique aims at synchronously imaging lightly seeded particles at very high update rates from a finite number of different views. The figure 2.1 faithfully illustrates its working principle, briefly described here below:

1. A measurement volume is defined, then illuminated by a thick laser beam;
2. Passive tracer particles are immersed in the region of interest, while the latter is pulsely illuminated by the upper-mentioned laser source;
3. The light scattered by the particles is projected onto the image planes of the cameras disposed around the illuminated volume;
4. A volumetric discrete rendition of the region of interest is then sought. This is made possible by defining a well-established projection model between the 3D and 2D space based upon the results of the calibration procedure. The latter representation describes

a direct problem and we solve for its inverse by seeking the nature of the object in the space out of its planar projections (*i.e.*, the images collected at each time frame from simultaneous different views);

5. A transport model is further defined. The last-mentioned exploits constraints on the volume intensity distributions between successive time frames. In an analogous way as above, the velocity regime is fathomed as an inverse problem out of the transport model by means of estimation programs;

6. Since the inception of tomoPIV, the two last-mentioned inverse problems have been tackled separately. Recently, new techniques have emerged which treat the two latter as a sole estimation problem and jointly solve for both volumetric intensity distributions at successive instants and for the velocity fields that rely them.

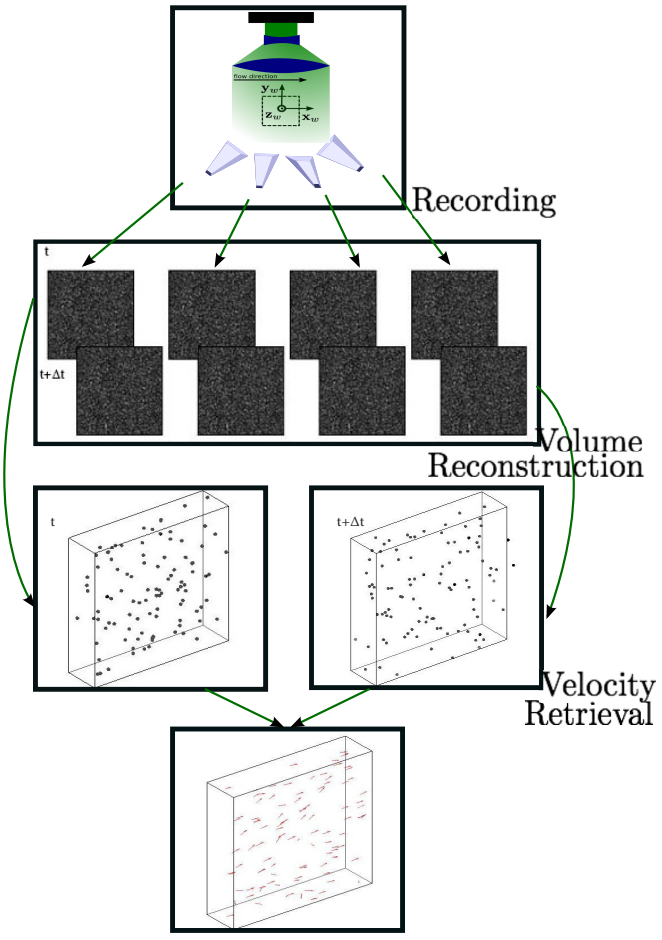

Figure 2.1: Working principle of tomoPIV.

We present, in section 2.1, the different experimental aspects closely linked to the working principle. In fact, each one of the features briefly itemized beforehand plays a distinct role in the rendering of the scene. **Volume illumination** can be determinant of the images' accuracy, as it will be further described in section 2.1.1, the **tracer particles**

need to respond to a number of requirements in order to enable good measurements, as depicted in section 2.2.2, and optic-related settings such as **particle imaging** and **camera-system calibration** are of prime importance in creating the direct observation model, as detailed in sections 2.1.4 and 2.1.5, respectively. We give, for each aspect, its mathematical transcription. Finally, we formulate, in section 2.2, the direct models depicting the projections of the volumetric space on the images and the transport of the particles, respectively, by taking into account the considerations related to the experimental setting.

2.1 Experimental Setup

Although our present study does not evolve, to a large extent, in an experimental context, we believe that a good knowledge of the implications ensued from the nature of physical parameters corresponding to a particular assessment is at stake for a sensible representation of the flow visualization system. In fact, an educated choice of the illumination system and of the tracer particles, as well as a good calibration are determinant for the accuracy of the quantitative diagnostic obtained over the corresponding measured data sets. In addition, the reader tangentially familiarized with experimental fluid mechanics will find here references allowing to deftly access insights into the specifics of the system settings.

Preliminaries

We mention that all the physical quantities intrinsically linked to a spatial position are expressed, unless otherwise stated, with respect to the world reference frame; the latter is a Cartesian system of coordinates defined by:

$$\mathrm{F_w} : (\mathbf{o}, \mathbf{x}_w, \mathbf{y}_w, \mathbf{z}_w), \tag{2.1}$$

where $\mathbf{o} = \begin{bmatrix} 0 & 0 & 0 \end{bmatrix}^T$, $\mathbf{x}_w = \begin{bmatrix} 1 & 0 & 0 \end{bmatrix}^T$, $\mathbf{y}_w = \begin{bmatrix} 0 & 1 & 0 \end{bmatrix}^T$ and $\mathbf{z}_w = \begin{bmatrix} 0 & 0 & 1 \end{bmatrix}^T$.

We introduce, as a useful contrivance purposed to be employed throughout the whole manuscript, the nomenclature defining the position of the center of a particle, that reads:

$$\mathbf{h} = \begin{bmatrix} h_1 & h_2 & h_3 \end{bmatrix}^T \in \mathbb{R}^3, \tag{2.2}$$

which is 3D point expressed with respect to the world frame system $\mathrm{F_w}$. If we refer to an element belonging to a set of particle centers, the latter will be upper-scripted as follows: $\mathbf{h}^j$.

We recall that the velocity of the fluid is designated here by its Eulerian representation, *i.e.*, by a function of time as the flow passes through fixed spatial locations, defined here by the following function:

$$u(\mathbf{h}, t).$$

For further detail on flow specifications and visual representation, the reader should refer to Appendix A.

2.1.1 Volume Illumination

As pointed out earlier, the illumination of the volume is enabled by means of laser lighting. The preceding planar PIV techniques need a thin sheet of light aligned to the planes of the captors and parallel to the direction of the flow; there are at most two cameras placed in a stereoscopic configuration (thus very close together); the beam is thinned out by using an intricate system made out of cylindrical lenses and the alignment is realized in order to avoid out-of-plane motion. Concurrently, the volumetric techniques rely on the illumination of a bigger region, ideally uniformly spread on the three dimensions of the space. As a result, there is no need to focus the light on a single sheet; on the contrary, the latter is widened by the use of a beam expander. We give, in this section, the description of the volume illumination profile in the physical scene and a mathematical model which accounts for its behavior.

In a typical optical setup (cf. Figure 2.2 (a)) the light intensity decreases throughout the volume inversely proportional to the square of the distance from the light source. Let the direction of the source light be taken as the $-\mathbf{y}_w = \begin{bmatrix} 0 & -1 & 0 \end{bmatrix}^T$ axis as depicted by the Figure 2.2. We can model this radial intensity profile along the region of interest as a Gaussian function in the $\mathbf{x}_w = \begin{bmatrix} 1 & 0 & 0 \end{bmatrix}^T$ direction. Let $l : \mathbb{R}^3 \to \mathbb{R}$ be the function depicting the evanescent behavior of the light in the scene at an instant t. The shading intensity function in a point $\mathbf{h} \in \mathbb{R}^3$ then writes:

$$l(\mathbf{h}) = \tilde{i}_t \exp\left[-\frac{(h_1)^2}{2\sigma_f^2}\right], \tag{2.3}$$

where $\sigma_f^2 \in \mathbb{R}_+$ is the variance accounting for the **forward** energy dissipation and $\tilde{i}_t$ stands for the intensity of the laser pulsation at instant t.

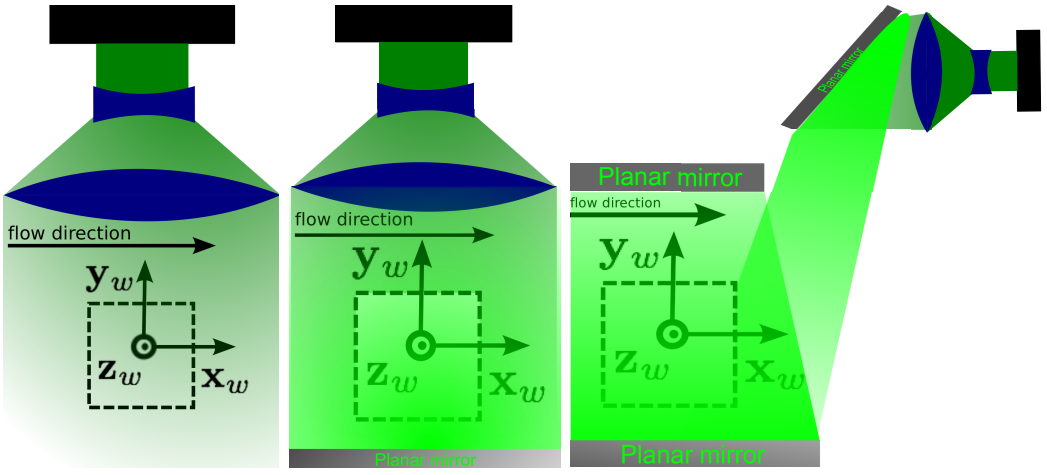

(a) (b) (c)

Figure 2.2: Sketches of different optical setups. From left to right: standard illumination setting for TomoPIV, double-pass illumination [158], multi-pass illumination [87].

Experimental assessment revealed that in certain TR configurations the amount of light produced in a typical lightning configuration was not sufficient to cover the requirements of the scene. As a further matter, recent developments in experimental tomoPIV focused on adapting the visualization system such that the power of the intensity during the pulse duration of the laser source is boosted. A first improvement relies on the introduction of a mirror on the opposite side of the light source; the **double-pass** light amplification system was established and exploited in [158]. Its functioning regime is portrayed in figure 2.2(b). A more complex development - the **multi-pass** light amplification system - has been proposed in [87, 163]. In the latter, the laser beam is directed with an angle towards a couple of high reflecting mirrors placed one in front of the other. Therefore, the laser ray is reflected back and forth within the mirrors multiple times increasing the light amplification. One can refer to figure 2.2(c) for an illustration of the this principle. Experiments revealed an amplification effect up to a factor of 5 in comparison with the double-pass system and up to 7 times if compared with the single-pass configuration.

Regardless of the illumination scheme implemented experimentally, one should keep in mind that any light recorded on the images that is outside of the region of interest (demarcated within dashed lines on figures 2.2(a-c)) will be included in the reconstructed object and will, therefore, contribute to a diminishment of the signal-to-noise ratio (SNR) of the density volumetric function standing for the intensity of the particle tracers in the volume at a given frame. This source of noise will be further taken into account in the observation volume formalized in section 2.2.

2.1.2 Particles

Physical properties of the particles suspended in the flow are crucial to a good visualization system. Good measurements are enabled by several fundamental properties of the tracers. First of all, PIV probes rely on tracers following with precision the movement of the flow without altering its properties. On top of that, accurate PIV renditions are enabled by the ability of the particles to scatter the incident light received from the laser source in the directions of the observing cameras. The fact that flow tracking demands small particles and light scattering improves with increasing particle size already suggests the need of a compromise when choosing tracer particles. Finally, factors such as the particles' concentration and shape are to be studied when designing a tomoPIV visualization system in order to guarantee uniformity of the probes over the measurement domain.

We will insist, in the succeeding sections, on the upper mentioned properties in order to formalize a pertinent observation model for the passive tracers. We discuss, in section 2.1.2.1, imprecisions on the tracing abilities of a particle based on its diameter size. Next, we describe, in section 2.1.2.2, a refinement of the lightning model depicted in section 2.1.1 with regard to the particles' anatomy and of their position and show further along, in section 2.2, how this a priori information can be added to the observation model in order to account for the light scattering angle with respect to each camera. For further reading, a comprehensive study of the most important properties of the tracer particles related to the specifics of the experimental scene can be found in [4, 153, 174].

2.1.2.1 Dynamics

The principle of **particle tracer** velocity estimation methods relies on the assumption that the diameter of a particle is smaller than the finest scale of the fluid motion [4]. The smallest fluid length scale is called the Kolmogorov length scale and it is related to the size of the smallest eddy. We consider a spherical particle of diameter d_p; its position is represented at each instant t by its Langrangian specification $H(\mathbf{h}_0, t)$, further outlined in Appendix A by the expression (A.1); the parcel corresponding to the studied particle is labeled by the position of its center at $t = 0$, that is $\mathbf{h}_0 = \begin{bmatrix} h_{1,0} & h_{2,0} & h_{3,0} \end{bmatrix}^T \in \mathbb{R}^3$. We denote by $u_h(t) : \mathbb{R}^3 \to \mathbb{R}^3$ the velocity of this so-labeled particle in the fluid. The latter is computed as follows:

$$u_h(t) \triangleq \frac{\partial H}{\partial t}(\mathbf{h}_0, t). \tag{2.4}$$

We designate the velocity of the fluid at the center of the particle specified by its Eulerian representation by $u(\mathbf{h}, t), \forall \mathbf{h} \in \mathbb{R}^3$, as established in Appendix A by the expression A.2. We point out that the term **passive** is inaccurately employed as it reckons on the hypothesis that the velocity of the particles $u_h(t)$ is equated to the velocity of the fluid at the center of the particle such that;

$$u_h(t) = u\left(H\left(\mathbf{h}_0, t\right), t\right). \tag{2.5}$$

The latter assumption implies that the velocity field is uniform over the diameter of the particle.

There are however discrepancies between the particles' and the fluid's motion and the most important source of such errors comes from the difference between the fluid's and the particles' densities, ρ_f and ρ_p, respectively. This discrepancy induces a velocity lag which is computed as the the difference between the velocities of the particle and of the fluid probed in the center of the particle.

Under certain reductive hypotheses (*i.e.*, acceleration of the fluid is constant, $\rho_p \gg \rho_f$), it is shown in [106] that the step response of $u_h(t)$ follows an exponential decay law which writes:

$$u_h(t) = u\left(H\left(\mathbf{h}_0, t\right), t\right)\left[1 - \exp\left(-\frac{t}{\tau_p}\right)\right], \tag{2.6}$$

where τ_p is the relaxation time approximated by $\approx \frac{d_p^2}{\mu}$. We mention that the latter generally constitutes a reliable measure which shows the ability of the particles to attain equilibrium within the flows. Equation (2.6) demonstrates that the particles' diameter must be small in order to ensure the reduction of the velocity lag. The result of (2.6) is shown in figure 2.3, where the time response of particles with different diameters is shown for a strong deceleration in an air flow. The curve highlights the strong dependency between the particle's size and its quick response to the velocity of the flow. Nevertheless, as we will see in the following section, if the particle's diameter is not sufficiently large it will not scatter the light properly and therefore, will bias the measurements.

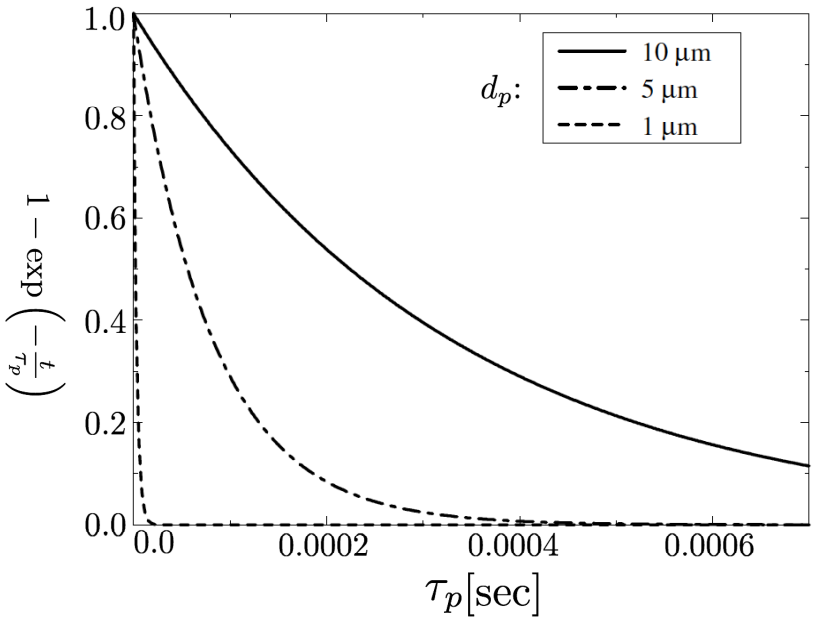

Figure 2.3: Time response of oil particles with different diameters across a planar shock wave. The velocity profile is extracted perpendicular to the shock wave along the direction of the flow in order to quantify the particle velocity downstream of the shock wave. Adapted from [153, 157].

2.1.2.2 Light scattering

The lightning model of the scene described in 2.1.1 can be further refined by taking into account the light scattered model by the seeding particles. In a nutshell, we call the scattered light the part of the incident laser light which is imaged by the particles onto the detectors. Consequently, it is the scattered information which duly enables access to the information on the velocity flow. A sensible choice of the nature of the particles will impact on the quality of the measurements. In fact, the more powerful is the scattered energy, the more contrasted are the images and thus, they will constitute more discriminant assessment. We begin our section by making a small introduction on general notions related to the scattering of the light; next, we present an entry point into the Mie scattering theory adapted for the tomoPIV setting; finally, we formalize related models in order to take into account the scattering of the light by the passive tracers into the experimental scene.

General Notions on Light Scattering

Fundamental notions about light scattering can be found in [6, 33, 179]. The study of the phenomenon is restrained based on several a priori knowledge and assumptions. Let us draw a list based on information compiled from previously cited publications. First of all, the scattering is elastic: the frequency of the scattered light is the same as that of the incident light. Secondly, particles are rarely solely represented in a scene; one particle usually belongs to a collection populating the volume of interest. Implicitly, they are electromagnetically coupled, thus each particle is excited by the resultant field scattered by all the other particles and by the exterior field. The simplification in order assumes single scattering: the number of particles is sufficiently small and their separation sufficiently

large that, in the neighborhood of any particle, the total field scattered by all the particles is small compared with the external field. Moreover, we assume **incoherent** scattering assuming that the separation between the scatterers is random; this implies that there is no consistency in the relation among the phases of the waves scattered by the individual particles.

The scattering behavior of the light varies with regard to the obstacles encountered by the latter on its way to the sensors. In [189], a review of elastic light scattering theories is provided based on the specifications of the physical scene. The author states that the theory to compute or approximate the scattered light power should be a function of the obstacle's shape, its composition and refractive index and its size relative to the wavelength of the incident wave.

Light Scattering for Small Particles

We address the light scattering problem for our specific optical setting. As outlined in section 2.1.1 when the scene is illuminated with a laser source, the distribution of this energy over the light beam leads to a relatively low energy density. If enhancements to the classical scheme have been brought, the efficiency of the particle scattering is still of utmost importance to the intensification of their projections on the recordings. As discussed in the previous section, we model the particles as spheres with small diameters (*e.g.*, up to 10 microns, for air flows experiments). Given the ratio between the radius of a particle and the wavelength λ of the illumination source, we embrace the thesis that the scattering of light by these particles occurs in the so-called Mie regime. The latter can be characterized by the normalized diameter d_q defined as a function of the particle's diameter d_p and the wavelength of the laser source λ such that:

$$d_q = \frac{\pi d_p}{\lambda}. \tag{2.7}$$

The Mie scattering model has been fully described by Bohren and Huffman [33]. The problem has been addressed for a linear, homogeneous, isotropic particles in chapter 4 of their book. The authors express the direct problem, which consists in the computation of the field of intensity at any point in the scene, given the precise description of the optical elements of the scene. Based on their breakthroughs, we are interested, in this section, in faithfully modeling the experimental scene, with regard to physical consideration such as d_p, λ and N_p, where N_p is the refractive index of the particles.

The study of the light scattering of a particle within the tomoPIV context has not received, to our knowledge, high attention when designing the observation model of the scene. The toolbox implemented by Mätzler [121] is based on the model formalized in [33] and computes the scattered intensity with respect to the wavelength of the laser beam λ, to the refractive index of the particles N_p and to the particle's diameter d_p. The toolbox developed by Schäfer during his PhD thesis [159] also relies on the model proposed by [33], but approximates the scattering of the light with respect to the same parameters as above and with respect to the so-called scattering angle; the latter is defined as the angle between the incoming light source and the sensor's direction in the scattering plane of the particle. This further development allows us to account for a smooth scaling factor in the image

formation with regard to the position of the sensor on the scene. In [60], the Mie scattering is accounted for by **approximating** an angular scattering function for typical PIV parameters based on the first described toolbox. The authors use however an inexact mode to determine the smoothing scale factor for all the cameras by performing a parametric estimation out of images generated using the Phong reflection model [149]. In [51], the authors perform a parametric study showing the behavior of the scattering function with respect to polydispersion and scattering angles. Further developments including taking into account the scattering behavior into the observation model are stated as future work in the upper-mentioned article and have not been integrated, to our knowledge, at this date.

Related Light Scattering Models

We will consider two choices for approximating the scattered intensity. As noted in [153], the average intensity over a range of observation angles roughly increases with d_q^2, where d_q is the normalized diameter expressed in equation (2.7). This leads to a first estimate, which considers the scattered light from a particle centered on $\mathbf{h} \in \mathbb{R}^3$ as proportional to its square normalized diameter d_q; we explicit the scattered intensity that we denote by $v : \mathbb{R}^3 \to \mathbb{R}_+$, with respect to the expression of the intensity of the incident wave impacting the particle and of the normalized particle diameter, such that:

$$v(\mathbf{h}) \approx d_q^2 l(\mathbf{h}), \forall \mathbf{h} \in \mathbb{R}^3, \forall t \in \mathbb{N}. \tag{2.8}$$

where $l(\mathbf{h})$ is formalized in section 2.1.1 by equation (2.3). This light scattering by a particle approximated by equation (2.8) has been accounted for in the imaging of the particles model by *Cornic et al.* in [55].

As observed by *Silva et al.* in their parametric study [60], accounting for a refined Mie model allows to set up the camera system with respect to the scattering efficiencies and therefore, enhance the performance of reconstruction algorithms based on more accurate measurements. This motivates us to express a complete model for this scattering of particles. This more refined representation relies on developments pursued by Bohren and Huffman [33]. The authors state that the relationship between the incident and the scattered light is proportional and expresses this equivalence bias a scattering function. The latter is universally denoted in the literature by S_{11} and depends on the diameter of the particle d_p and on the scattering angle θ^c, expressed with regard to the c^{th} sensor surrounding the measurement region, where $c \in \{1 \dots N_c\}$, with N_c the total number of sensors around the volume. Details of the model are provided in Appendix B. The approximated scattered intensity of an imaged particle by taking into account the Mie scattering then writes:

$$v(\mathbf{h}) \approx S_{11}\left(\theta^c, d_p\right) l(\mathbf{h}). \tag{2.9}$$

As depicted by equation (2.9), the influence of the Mie scattering effect on the measurements depends on the nature of the passive tracers and on the scattering angle. Figure 2.4 illustrates the behavior of S_{11} as a function of both d_p and θ^c. Since this regime is rather complex and difficult to account for in the observation model, we make the assumption that the distribution of the particles in the scene is monodisperse; this hypothesis allows us to study the Mie effect for a fixed value of d_p. Figure 2.5 draws

the response of S_{11} as a function of θ^c. As illustrated by figure 2.5(a), one can notice dramatic changes in the amplitude of the scattered intensity whether the camera is placed in a backward or forward configuration. Figure 2.5(b) displays the effect of the particle's diameter at chosen scattering angles. The effect is reversed by the one revealed in figure 2.3; in fact, if the particle's diameter must be small in order to ensure good tracking of the flow, one can observe that scattered intensity is proportional to the size of the particle.

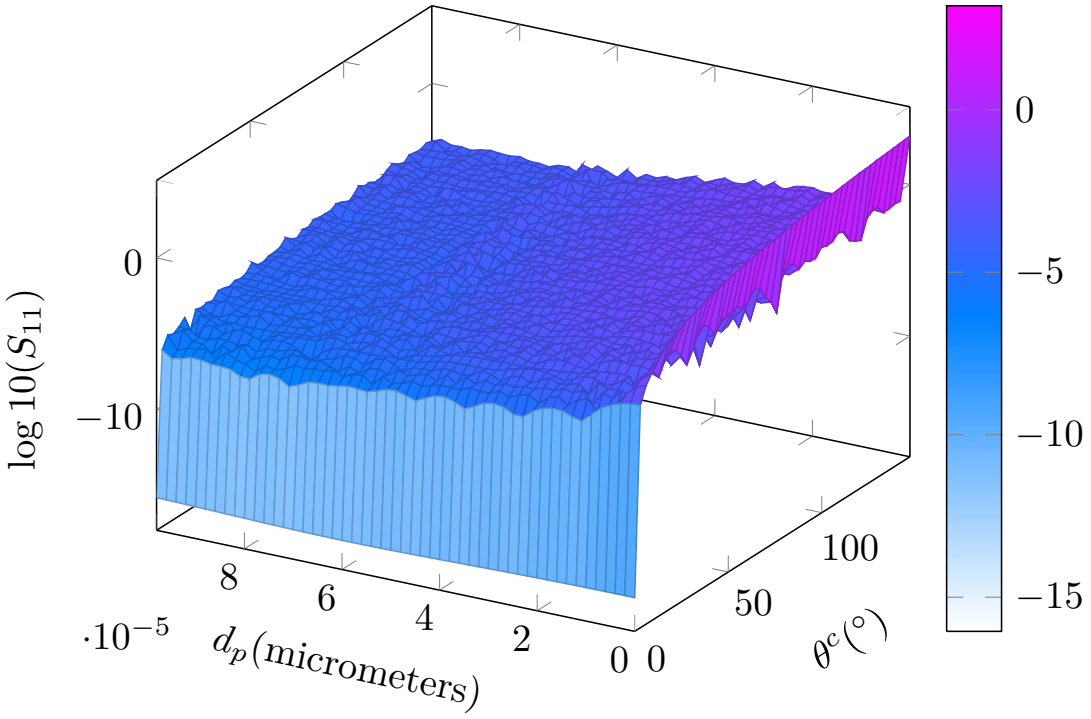

Figure 2.4: Scattered radiance profile S_{11} as a function of θ^c and d_p The plot was obtained using the toolbox MATSCAT extensively described in [159].

Regardless of the chosen approximation (whether to refer to (2.8) or (2.9)), the scattered light is a function of the particle's diameter. Experimentally, the velocity lag between the particles and the fluid is diminished as the diameter of the particles decreases; on the other hand, the visibility of the latter is ensured by particles with larger diameters. The choice of the optimal diameter for the tracers is thus a compromise on their size and therefore, a trade-off between its quick response ensured by smaller particles and a low-noise signal guaranteed by larger ones, as it arises from the analysis pursued in sections 2.2.1 and 2.2.2.

2.1.3 Sensors

The key technologies that enable tomoPIV measurements include a high-power laser source, as discussed in section 2.1.1, and high-frequency sensors. The sensors used to record the measurements of the particles in an illuminated flow need to respond to a certain number of requirements. In fact, cameras are expected to provide both high pixel count and high frame rates with sensitivity and low background noise. If until recently the Charge Coupled Device (CCD) sensors were mostly used for their ability to meet these demands,

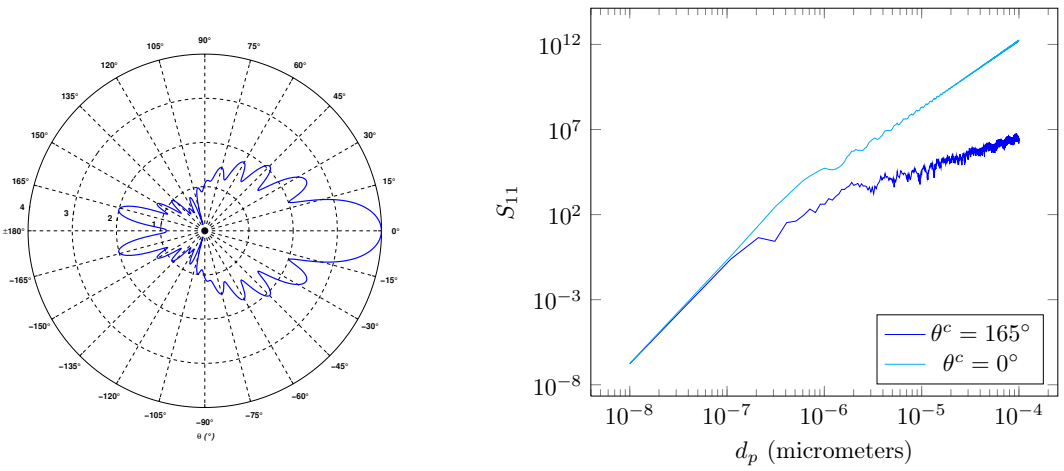

(a) (b)

Figure 2.5: Scattering function expressed in polar spherical coordinates for a small particle of diameter d_p hit by an unpolarized incident wave of wavelength $\lambda = 532nm$ in an air experiment (left) and scattering function with respect to the particle diameter d_p for fixed scattering angles (right). The plot was obtained using the toolbox MATSCAT.

the complementary metal-oxide-semiconductor (CMOS) cameras have evolved rapidly and grown to be the preferred technology for the tomoPIV systems.

CMOS cameras are typically characterized by their maximum recording rates (kHz) and their maximum resolution (MPx). A trade-off must usually occur between these two parameters, depending on the experiment (*e.g.*, TR experiments demand higher recording rates, which implies a reduction in the image resolution).

There are two classes of characteristics that are of prime importance and need to be described for subsequently defining the observation model. We distinguish between:

1. the extrinsic parameters;
2. the intrinsic parameters.

First of all, we relate to the **extrinsic** parameters, which assume a good knowledge of the sensors' position around the scene. For doing so, we introduce the following nomenclature. Let $\mathbf{h}$ be a 3D point expressed with respect to the world frame system $\mathrm{F_w}$ defined by equation (2.1). We place N_c cameras placed around a region of interest that includes $\mathbf{h}$. The sensor-related systems of coordinates used to express the position of $\mathbf{h}$ in the camera's referential frames read:

$$\mathrm{F}^{\mathrm{c}}_{\mathrm{img}} : \left(\mathbf{o}^{c}_{\mathrm{img}}, \mathbf{x}^{c}_{\mathrm{img}}, \mathbf{y}^{c}_{\mathrm{img}}\right) \tag{2.10}$$

$$\mathrm{F}^{\mathrm{c}}_{\mathrm{cam}} : \left(\mathbf{o}^{c}_{\mathrm{cam}}, \mathbf{x}^{c}_{\mathrm{cam}}, \mathbf{y}^{c}_{\mathrm{cam}}, \mathbf{z}^{c}_{\mathrm{cam}}\right), \tag{2.11}$$

where $\mathrm{F}^{\mathrm{c}}_{\mathrm{img}}$ stands for the orthogonal axes coordinates attached to the image plane of the c^{th} camera and $\mathrm{F}^{\mathrm{c}}_{\mathrm{cam}}$ the Cartesian system of coordinates attached to the c^{th} camera, $\forall c \in \{1, \ldots, N_c\}$. As illustrated by figure 2.6, the projection of $\mathbf{h}$ on the image plane writes $\mathbf{h}^c_{\mathrm{img}}$ with respect to $\mathrm{F}^{\mathrm{c}}_{\mathrm{img}}$. We denote by $\mathbf{h}^c_{\mathrm{cam}}$ the coordinates vector of $\mathbf{h}$ expressed in the $\mathrm{F}^{\mathrm{c}}_{\mathrm{cam}}$ referential. The latter transformations are performed based on the result of the calibration procedure described in section 2.1.5.

The sensors can be further described by a list of **intrinsic** parameters, which are closely related to the lens and to the camera objective. Each camera (indexed by c) is characterized by the following set of parameters:

1. the dimensions of the screen $\begin{bmatrix}\tilde{n}^c_1 & \tilde{n}^c_2\end{bmatrix}^T \in \mathbb{R}^\star_+ \times \mathbb{R}^\star_+$;
2. the number of pixels per dimension $\begin{bmatrix}n^c_1 & n^c_2\end{bmatrix}^T \in \mathbb{R}^\star_+ \times \mathbb{R}^\star_+$;
3. its magnification factor $\mathrm{Mag}^c \in \mathbb{R}^\star_+$;
4. the focal distance, $f^c \in \mathbb{R}^\star_+$ (the distance between the optical center and the camera screen);
5. the diameter of the effective lens aperture $d^c_a \in \mathbb{R}^\star_+$;
6. the f-number $f^c_\sharp \in \mathbb{R}^\star_+$, which is the ratio of the lens's focal length f^c to the diameter of the entrance pupil d^c_a.

As an informative landmark, we mention standard casted configurations in experimental settings of $N_c = 4$ cameras: each sensor has a $\begin{bmatrix}1042 & 1024\end{bmatrix}^T$ resolution on screens of size $\begin{bmatrix}20.48 & 20.48\end{bmatrix}^T$ mm for a rate of 5.4 kHz.

2.1.4 Small Particles' Imaging

The quality of tomoPIV measurements strongly relies on the design of the imaging system. On top of having to scatter sufficient light so that their imaged intensities can be distinguished from the background intensity, reliable measurements of the particles also depend on the intrinsic parameters of the sensors used to capture them. Several parameters associated with the cameras govern the quality of the imaging process: the pixel size, the focal distance, the optical magnification and the viewing direction. The same variables contribute to the formation of a certain pattern of the particles on the images, whose shape and size are of utmost importance when studying and formalizing the projection model. We will give in this section useful tools to compute the so-called particle image diameter that will subsequently be integrated in the design of the observation model.

We assume that the cameras placed around the measured region are diffraction limited, meaning that their respective images' resolution is solely limited by the instruments' theoretical limit. Let a small tracer particle be placed midway between one of the cameras and the laser source. When the plane light wave encounters the mentioned obstacle,

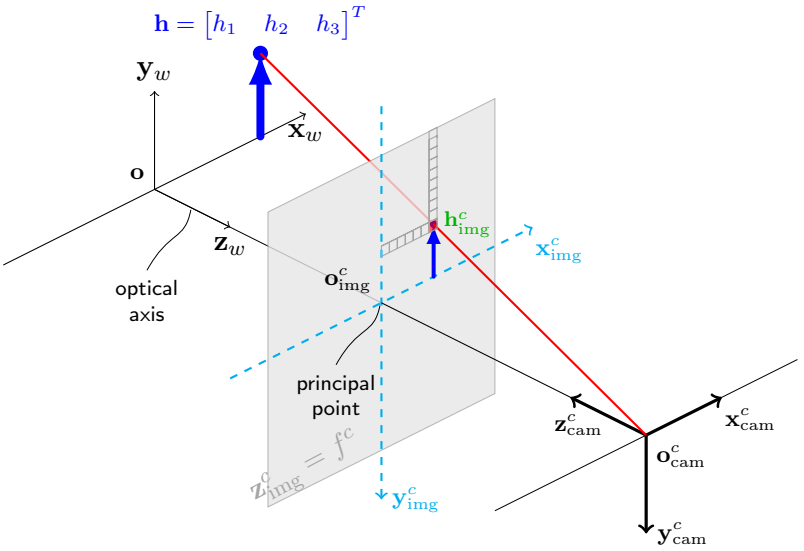

Figure 2.6: The 3 main systems of coordinates used to depict the projection of a point in space $\mathbf{h}$ into the images plane of the c^{th} camera.

diffraction will occur. In [93], the author writes that the image of a distant point source formed through perfectly aberration-free converging lens appears as a diffraction pattern, phenomenon known as the Fraunhofer diffraction. The obtained spots of light are called Airy disks and represent the Point Spread Function (PSF) of an aberration-free lens. Small aperture diameters correspond to large Airy disks and larger apertures to smaller disks, as depicted in figure 2.7. Figure 2.8 depicts the image formation of a image spot from the projection of a particle centered on a 3D point.

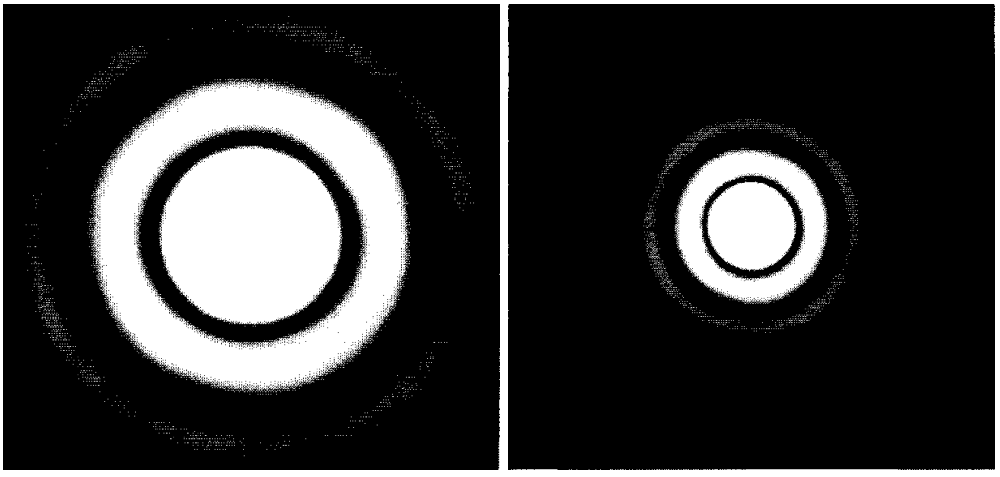

(a) (b)

Figure 2.7: Airy patterns for increasing aperture diameters (from left to right). From [93].

We are interested in expressing this physical phenomenon in signal processing terms and

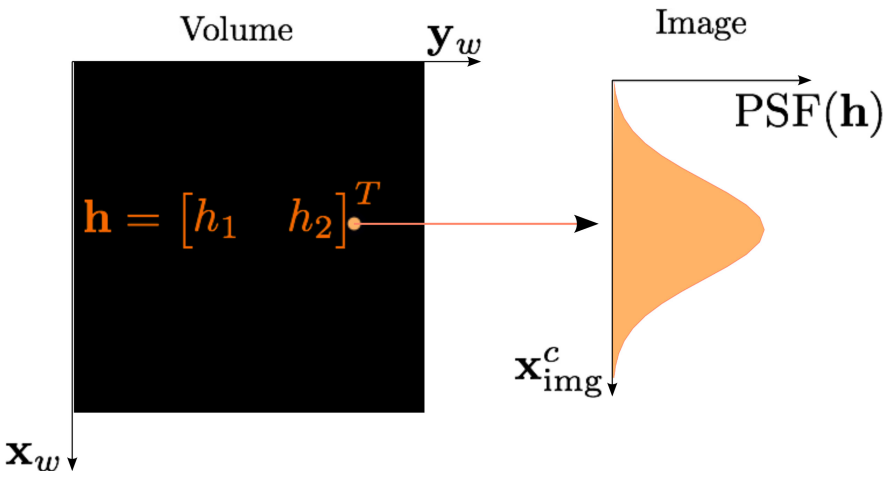

Figure 2.8: 2D rendition of the image formation on the c^{th} camera from a volumic projection of a particle centered on $\mathbf{h}$.

more precisely, in computing the diameter of an Airy disk with respect to the intrinsic parameters of a camera. For doing so, let us consider a camera, indexed by c, imaging a small particle centered on a 3D position $\mathbf{h}$, with an aperture of diameter d_a^c. The particle image diameter can be estimated by employing the so-called Fraunhofer approximation; more precisely, it can be shown that the intensity of the Airy pattern represents the Fourier transform of the aperture's transmissivity distribution [93]. The Airy function can mathematically be represented by the square of the first order Bessel function. The diameter of an Airy disk d_{diff} represents the smallest particle image that can be obtained for a given imaging configuration. Assuming that the particle imaged is in focus, the diameter of the diffraction spot is given by [88]:

$$d_{\text{diff}} = 2.44\lambda f_\sharp^c \left(1 + \text{Mag}^c\right), \tag{2.12}$$

where $f_\sharp^c$ is the f-number defined as the ratio between the focal length of the lens f^c divided by the aperture diameter d_a^c, as defined in section 2.1.3 and λ is the wavelength of the laser source.

If lens aberrations can be neglected and the PSF can be approximated by the Airy function, the following formula can be used for an estimate of the particle image diameter, as developed in [5]:

$$d_{\text{est}} = \sqrt{\left(\text{Mag}^c d_p\right)^2 + d_{\text{diff}}^2}. \tag{2.13}$$

This relation applies in the case of in-focus particles. We say that particles are in-focus when the depth of focus of the camera is equal or larger than the size of the illuminated volume along the viewing direction. The depth of focus writes, as expressed in [166]:

$$\delta_Z = 4.88 \left(f_\sharp^c\right)^2 \frac{\text{Mag}^c + 1}{\text{Mag}^c} \lambda. \tag{2.14}$$

In practice, operating within the limits of the focal depth translates by illuminating a very thin volume. Moreover, particles outside of this range are imaged on a larger area, thus the

diameter of their particle image increases. Following equation (2.14), in order to increase δ_Z , the numerical aperture $f_\sharp^c$ has to be increased, which results in a reduction of the amount of light collected by the sensor. In [156], the author shows a path to limit the out-of-focus effects for a small depth of focus without degrading the quality of the reconstruction. We review, in section 2.2, other developments in the literature coping with the physical formation of the particles and formulate an observation model which accounts for the formation of Airy pattern on the images.

2.1.5 System Calibration

The volumetric density reconstruction at each time frame is computed based on the knowledge of the interaction between a 3D position in the region of interest and a pixel on an image recorded by a camera. We recall that the three coordinates systems employed throughout the manuscript are: $\mathrm{F_w}$ defined by equation (2.1) and the sensors-related referentials $\mathrm{F^c_{img}}$ and $\mathrm{F^c_{cam}}$ defined by equations (2.12) and (2.13).

The interaction between the different coordinate systems can be represented by the functions $\mathcal{N}^c : \mathbb{R}^3 \rightarrow \mathbb{R}^3$ and $\mathcal{M}^c : \mathbb{R}^3 \rightarrow \mathbb{R}^2$. $\mathcal{N}^c(\cdot)$ stands for the homogeneous transformation that expresses the coordinates of a point $\mathbf{h}$ in the world frame with respect to each camera frame $\mathrm{F^c_{cam}}$, while $\mathcal{M}(\cdot)$ transcripts the projection of a point expressed in the frame of the c^{th} camera into the image frame $\mathrm{F^c_{img}}$, such as:

$$\mathbf{h}^c_{\text{cam}} = \mathcal{N}^c\left(\mathbf{h}\right), \tag{2.15}$$

$$\mathbf{h}^c_{\text{img}} = \mathcal{M}^c\left(\mathbf{h}^c_{\text{cam}}\right). \tag{2.16}$$

Furthermore, we formalize, based on equations (2.15) and (2.16), the projection function $\mathcal{W}^c : \mathbb{R}^3 \rightarrow \mathbb{R}^2$ defined as the composition of functions $\mathcal{N}^c(\cdot)$ and $\mathcal{M}^c(\cdot)$, as follows:

$$\mathcal{W}^c\left(\mathbf{h}^c_{\text{img}}\right) = \left(\mathcal{M}^c \circ \mathcal{N}^c\right)\left(\mathbf{h}\right), \forall \mathbf{h} \in \mathbb{R}^3, \tag{2.17}$$

where $\mathcal{W}^c$ depicts the projection of a point $\mathbf{h}$ expressed in the world frame into the camera's image plane and is crucial to building the observation model formalized in section 2.2.

The function $\mathcal{N}^c(\cdot)$ (equation (2.15)) is entirely defined by the extrinsic parameters depicted in section 2.1.3. Similarly, the function $\mathcal{M}^c(\cdot)$ (equation (2.16)) is formalized with regard to the intrinsic parameters, described here before. Implicitly, the function $\mathcal{W}^c(\cdot)$ (equation (2.17)) depends on both the extrinsic and the intrinsic parameters. Unfortunately, these parameters are unresolved; therefore, the knowledge of functions $\mathcal{N}^c(\cdot), \mathcal{M}^c(\cdot)$ and $\mathcal{W}^c(\cdot)$ requires a learning step. This procedure is the so-called the **camera calibration**, which is a necessary step in 3D computer vision applications in order to extract metric information from 2D images. A rather extensive review of common methods can be found in [192].

The calibration of the tomoPIV system usually relies on a 2D plane apparatus. In fact, the image of a calibration target is recorded with each one of the cameras at several positions in the space. The calibration target contains a number of visual tracers. Based

on their known positions, a relation can be found between them and their projections on the cameras' images. The projection is represented either by a third order polynomial in $\mathbf{x}_w$ and $\mathbf{y}_w$ [167] or by using a simple pinhole camera model (usually subsequently fitted by a bundle adjustment procedure [173]). The choice of the third order polynomial is preferred to the one of a pinhole camera model in situations where optical aberrations can be encountered (*e.g.*, geometric distortions or blurring).

Additionally, the technique has been recently improved by the adjunct of a **self-calibration** step [184]. The self-calibration technique is based on the minimization of the disparity between the images of the same particle onto the camera images and uses therefore no calibration object. The procedure consists in matching the projections of the same particle and best-fitting its 3D position by triangulation; the disparity between the image of the particle and its reprojection is then used to correct the equation of the line-of-sight passing through the respective pixel. The application of the self-calibration technique has a dramatic effect on the accuracy of the measurements since the calibration errors can be reduced from approximately $2-3$ pixels to less than 0.1 pixels.

The calibration step is primordial for the estimation of the volumetric density at each time frame. The projection function is used to further assemble the observation model; we will describe in section 2.2 various approximation techniques employed in the literature, as well as our chosen methodology.

2.1.6 Summary

We have outlined the main features related to the experimental setting of the tomoPIV system. Refined models of the scenery have been recently proposed in the literature, where factors such as the scene illumination, polydisperse seeding [51] or a simplified model of the Mie scattering [60] have been accounted for. These recent developments have motivated us to study and integrate this a priori knowledge of the scene in our observation model in order increase its physical complexity and, therefore, release the ambiguities that can be caused, among other aspects, by the oversimplified experimental representation.

2.2 Related Model

Let us formulate a mathematical abstraction of the scenario outlined in section 2.1. For doing so, we first list several simplifying assumptions meant to ease the modeling process, enumerated in section 2.2.1. Based on these hypotheses, we formalize, in section 2.2.2 the physical continuous signal and relate it to available observations. Next, we present, in section 2.2.3 the subsequent model for discretizing the 3D space and its simultaneous projection on the 2D planes.

2.2.1 General Assumptions

We have described, in section 2.1, the physical aspects of the tomoPIV system. Faithfully modeling such an intricate system increases however the non-linearity of the so-obtained system and complicates subsequent estimation.

Due to this difficulty, we must rely on a few assumptions in order to achieve a compromise on the built model between its physical pertinence and its solvability. We distinguish between physical hypothesis:

- the particles are of spherical shape;
- the velocity field is uniform over the diameter of the particle;
- the tracer particles response time is $\tau_p = 0$, which implies that the particles attain equilibrium instantly in the flow; this hypothesis has been previously developed in section 2.1.2.1;
- the particles are in a monodisperse configuration, which means that all the particles have the same diameter d_p;

and numerical conventions:

- we assume that pixels have a dimension of 1×1 (expressed in arbitrary units (arb. u.));
- we assume that voxels have a dimension of $1 \times 1 \times 1$ (expressed in arb. u.);
- we assume that the measured region is in-focus for all the sensors placed around the volume;
- the diameter of a particle d_p is much smaller than the voxel's diameter, that is: $d_p \ll \sqrt{3}$ (expressed in arb. u.).

2.2.2 Continuous frame

We will model, in this section, the principle behind the image formation for particle images introduced in section 2.1.4. Unlike the ubiquitous tomographic PIV paradigm of [74], we adopt a more well-founded particle approach closer to the physical formation of images of small particles. The latter allows for the reconstruction of particles and not blobs (as in [74, 161]) with an image formation model accounting for the PSFs of the imaging system.

2.2.2.1 Density Function and Transport Assumption

Let us first compile a series of information on the illumination model (described in section 2.1.1) of the scattering particles extensively described in section 2.1.2.2 and on their transport behavior outlined in section 2.1.2.1.

Density Function

We consider a particle, indexed by j, centered on a 3D position $\mathbf{h}^j$ at time frame t. We express the incident intensity arriving on the surface of the j^{th} particle as follows:

$$l\left(\mathbf{h}^j\right) = \tilde{i}_t \exp\left[-\frac{\left(h_1^j\right)^2}{2\sigma_f^2}\right], \tag{2.18}$$

where, as stated in section 2.1.1, $\tilde{i}_t$ stands for the intensity of the laser beam at time t.

In addition, as depicted in section 2.1.2.2, we approximate the light scattered by a particle either as proportional to the square of its normalized diameter, as reads equation (2.8), or as a result of the Mie scattering theory which expresses it as a ratio of the incident light with respect to the scattering angle and its diameter size, as reads equation (2.9). We denote by v_t^j the volumetric intensity of a particle centered on $\mathbf{h}^j$. As recalled in section 2.2.1 by hypothesis 2.2.1, we assume a monodisperse distribution of passive tracers in the flow, which makes the particle diameter d_p and, therefore, the normalized particle diameter d_q (expressed by equation (2.7) in section 2.1.2.2) invariant with regard to the studied particle. As a result, the Mie scattering function $S_{11}(\cdot)$ is solely defined with respect to the scattering angle θ^c. We define the scattering intensity function as follows:

$$scat^c = \begin{cases} d_q^2 : & \text{diameter approximation} \\ S_{11}(\theta^c) : & \text{Mie scattering approximation,} \end{cases} \tag{2.19}$$

where c is the camera index.

Finally, we obtain two approximations for the volumetric density function arriving on the surface on the c^{th}, expressed for a particle centered on a 3D point at instant t and depending on the chosen modeling for its scattering regime, which writes in its compressed form:

$$v\left(\mathbf{h}^j\right) = scat^c l\left(\mathbf{h}^j\right). \tag{2.20}$$

As previously recalled, equation (2.19) is modeled with respect to the scattering angle θ^c formed by the light source and the position of the optical center of the c^{th} sensor in the scene. Therefore, using the term **density function** is an abuse of language as the function depicted by equation (2.18) is not invariant to the sensors around the region of measurement; in fact, the latter depicts the intensity quantity arriving on the surface of the sensors around the scene.

Transport Assumption

Based on the theory expounded in section 2.1.2.1 and on the considerations made in section 2.2.1 by hypothesis 2.2.1, the seeding particles will follow the movements of the fluid and will, consequently, be governed by a displacement function. Furthermore, as reads hypothesis 2.2.1,we assume that the velocity of a particle is equated to the velocity of the fluid at the center of the particle.

We relate to the Lagrangian and Eulerian specifications of the velocity, further described in appendix A, to express the trajectory of the fluid between two instants as follows. We make the strong assumption that the Eulerian velocity is constant in the temporal lag between two Lagrangian probes. This latter hypothesis translates as follows:

$$H\left(\mathbf{h}^j, t + \triangle t\right) = H\left(\mathbf{h}^j, t\right) + u\left(\mathbf{h}^j, t\right) \triangle t, \tag{2.21}$$

where $H(\cdot)$ is the Lagrangian representation of the position at time $t + \triangle t$ of a particle located at $\mathbf{h}^j$ at time t, $u(\cdot)$ is the Eulerian specification standing for the velocity of a particle

at time t located at position $\mathbf{h}^j$ at time t and $\triangle t$ is the temporal lag between two Lagrangian probes.

2.2.2.2 Physical-Based Continuous Model

We present, in this section, the image formation model from optics described in section 2.1.4 based on quantities defined in section 2.2.2.1.

Image Formation

Recently, Champagnat et al. [49] have proposed a physical-sound approach which models realistically the physical image formation of small particles. In a nutshell, due to intrinsic properties of the imaging lenses, the projection of a small particle on an image impacts an aggregation of adjacent pixels; the latter form an Airy spot whose diameter can be estimated following the equation (2.13). The resulting image intensity on the c^{th} camera for a seeded particle located in $\mathbf{h}^j$ at instant t writes:

$$y_{j,t}^{c}\left(\mathbf{k}\right) = v\left(h^j\right)\mathcal{H}^{c}\left(\mathbf{k} - \mathcal{W}^{c}\left(\mathbf{h}^j\right)\right), \tag{2.22}$$

where $\mathcal{H}^c : \mathbb{R}^2 \to \mathbb{R}^2$ is the so-called PSF function defined on the entire image support for the c^{th} camera and $\mathbf{k} = \begin{bmatrix} k_1 & k_2 \end{bmatrix}^T \in \mathbb{R}^2$. The latter is a separable function, thus it can be written such as $\mathcal{H}^c\left(\mathbf{k}\right) = \mathcal{H}_1^c\left(k_1\right)\mathcal{H}_2^c\left(k_2\right)$, as formalized in [55]. The model proposed by the authors for $\mathcal{H}_i^c : \mathbb{R} \to \mathbb{R}, \forall i \in \{1, 2\}$ is written as the convolution between a Gaussian function and a gate function:

$$\mathcal{H}_i^c(x) = \int_{-\infty}^{+\infty} \Pi\left(t\right) g\left(x - t, \sigma_{\text{psf}}\right) \mathrm{d}t. \tag{2.23}$$

where $g(\cdot) \sim \mathcal{N}(x, \sigma^2)$ is a Gaussian function centered on $x \in \mathbb{R}$ with variance $\sigma^2 \in \mathbb{R}_+$ accounting for blur and defocalisation, and $\Pi(\cdot)$ is employed for spatial integration over the detector's surface.

The function $\mathcal{H}^c(\cdot)$ accounts for the imaged airy spot of the particle centered on $\mathbf{h}^j$ and affects weights to the intensities of the pixels belonging to the vicinity of its geometrical image $\mathcal{W}^c\left(\mathbf{h}^j\right)$. Experiments have revealed an average value of d_{est}, depicted by equation (2.13), of about $2-3$ pixels and the standard deviation σ_{psf} is chosen accordingly. Note that the expression of equation (2.23) can change with respect to the experimental configuration; moreover, σ_{psf} can vary with the depth of the scene, assuming the defocalisation is not uniform over the measured domain.

Other developments in the literature include the PSF function in the image formation model. We mention [161], where the authors include spatially-varying projection operators which account for the effects of optical distortion. Moreover, PSF calibration techniques are proposed in [162], which guarantee an image formation model in relation to the sensor configuration of the scene. Similarly, in [185], the PSF is represented by a Gaussian ellipse, which is believed to cover most of the optical distortion effects.

2.2.2.3 Approximated Continuous Model

We formalize, in this section, an approximation of the physical-sound model described in section 2.2.2.2; the latter will constitute our observation model for the inverse problems that we will solve in chapters 3 and 4, together with several seminal paper which adopted a similar model [74]. We will motivate, at the end of this segment, our promoted choice.

Image Formation

In order to mimic the physical formation of the images described in section 2.1.4 and formalized in section 2.2.2.2, we model the **intensity** of passive tracers in a fluid as a sum of blurred spheres in the space. We will henceforth make the hypothesis that there are no variations in the illumination of the scene, which implies that the intensity of the light on the surface of the particle centered on $\mathbf{h}^j$ at consecutive time frames is equated to the intensity of the laser beam, as follows:

$$l\left(\mathbf{h}^j\right) = \tilde{i}_t, \forall t \in \mathbb{N}. \tag{2.24}$$

To avoid ambiguity, we will refer from now on to the incident intensity on the surface of the particle centered on $\mathbf{h}^j$ by $\tilde{i}_t$.

As previously mentioned, the 3D **density function** of the scene at instant t can be approximated by a sum of weighted Gaussian functions which account for the evanescent energetic behavior of the Airy spots such as:

$$w_t(\mathbf{k}) = \tilde{i}_t \sum_{j=1}^{M} g^j\left(\mathbf{k} - \mathbf{h}^j\right), \forall \mathbf{k} \in \mathbb{R}^3, \tag{2.25}$$

with:

$$g^j\left(\mathbf{k}\right) = \exp\left[-\frac{\|\mathbf{k}\|^2}{2\sigma_{\text{psf}}^2}\right], \forall \sigma_{\text{psf}}^2 \in \mathbb{R}_+, \forall \mathbf{k} \in \mathbb{R}^3, \tag{2.26}$$

where σ_{psf}^2 is a scalar accounting for the variance of the Airy spots from the projection of the center position of the particles located at $\mathbf{h}^j$ with $j = 1, ..., M$, where M is the total number of seeded particles.

Note that any physically-consistent density distribution $w_t(\mathbf{k})$ must correspond to a finite-energy signal, *i.e.*, $w_t(\mathbf{k}) \in \mathcal{L}^2(\mathcal{V})$, where we assume, without further explanations, that $\mathcal{V}$ indicates the measurement region under focus. In the sequel, we will moreover assume that $w_t(\mathbf{k})$ belongs to a finite-dimensional subspace of $\mathcal{L}^2(\mathcal{V})$.

The 3D signal simultaneously projects onto the 2D planes of the cameras. Each pixel entry i from images at time t represents the integration of the 3D light intensity distribution along the cone of view Ω_i originating in the optical center of the camera and passing through the surface of the pixel, as illustrated by figure 2.10. We comprise the scattering effect in the image formation model; the latter can either register for the Mie scattering effect, or it can be expressed by a simple approximation commonly used in the litterature, as discloses equation (2.19). The formation of the i^{th} pixel on the c^{th} sensor plane at time t writes:

$$y_{i,t}^{c} = scat^{c} \int_{\Omega_i} w(\mathbf{k}) d\mathbf{k}, \forall i, t \in \mathbb{N}. \tag{2.27}$$

Transport Model

The tracer will follow the movements of the fluid and will, consequently, be governed by a displacement function. As stated by equation (2.24) in section 2.2.1, we assume that the density function is invariant along the particle's trajectory. Moreover, we have made, in section 2.2.2.1, the assumption that the Eulerian velocity of a particle is constant between two temporal frames. The transport assumption expressed by equation (2.21) therefore translates, with regard to the density constancy over the volume of interest, as follows:

$$w_{t+\triangle t}\left(\mathbf{k} + u(\mathbf{k}, t)\right) = w_t(\mathbf{k}), \forall \mathbf{k} \in \mathbb{R}^3, \tag{2.28}$$

where, for the temporal step $\triangle t = 1$, $u(\mathbf{k}, t)$ is the displacement at time frame $t + 1$ of a tracer located at position at position $\mathbf{k}$ at time t.

Promoted Choice

We will adopt, for the rest of the manuscript, the approximated model formalized by equations (2.25) and (2.27) and the transport assumption depicted by equation (2.28). First of all, our choice is historical. In fact, when we started working on the estimation of the velocity in the tomoPIV context and after surveying the literature, we found that a blob-oriented representation for the particles' distribution was standard in the community. To uphold the latter statement, let us cite seminal paper [74] and further developments of the initial application carried on in [134]. Papers treating the tomoPIV with great mathematical underpinning by Petra et al. cast a similar blob model [143,144,148]. Among other, Worth and Nickels mention a comparable model in [188].

It is not until recently that more physical-sound image formation models have started emerging in the literature. We recall [49, 162, 185]. Without entering in the details of the inverse problem formalized in chapter 3, a first benefit of the particle-based model, aside from the evident one that it respect the physical truth of the setting, is represented by the reconstruction of particles [49,185] and not 3D blobs, as in [74,134,148] and even [162]. This reinforces the sparsity of the sought signal, quality that we will discuss in detail in chapter 3. On the other hand, the artificial blob representation of a particle is favorable in the context of the inverse problem detailed in chapter 4. In fact, a more dense representation of the signal will help avoiding the peak-locking effects in the subsequent displacement estimations [9]. Moreover, as presented in the following section, we have been able to gradually adapt our model in order to take into account new developments in the literature and to advance a hybrid particle-based approach which is founded on seeking the 3D density signal in a sparse space, as in [49, 55], and the 3D velocity vectors in a dense distribution, as in [185].

2.2.3 Digitized frame

We are interested in obtaining a matrix-vector counterpart of (2.27). In order to achieve such a model, we formalize a **vo**lumetric **el**ements (voxels) representation depicted in section

2.2.3.1 which allows us to encode simultaneously for the particles' location and their intensity in the measurement region. Next, we give, in sections 2.2.3.2 and 2.2.3.3 discrete peered versions of the continuous formulation expressed in section 2.2.2.3.

2.2.3.1 Preliminary Notations

For the sake of consistency along the following sections, let us introduce certain preliminary notations that will be subsequently used and enriched throughout the manuscript. We present the mathematical description of the volume of experimentation that we denote by $\mathcal{V} \subset \mathbb{R}^3$. We assume that $\mathcal{V}$ is a regular polyhedron centered on $\mathbf{o} = \begin{bmatrix} 0 & 0 & 0 \end{bmatrix}^T$ in a canonical system of coordinates $\mathrm{F_w} : (\mathbf{o}, \mathbf{x}_w, \mathbf{y}_w, \mathbf{z}_w)$ that we call the world frame reference system, such that:

$$\mathcal{V} = [-\frac{L_1}{2}, \frac{L_1}{2}] \times [-\frac{L_2}{2}, \frac{L_2}{2}] \times [-\frac{L_3}{2}, \frac{L_3}{2}], \tag{2.29}$$

where $\times$ denotes the cartesian product and L_i is the dimension of the volume along the i^{th} coordinate of the system.

We discretize $\mathcal{V}$ as a cartesian grid made out of m cubic **vo**lumetric **el**ements (**voxels**) $\zeta^j \subset \mathbb{R}^3$ centered on $\mathbf{k}^j$, $j \in \mathcal{J} = \{1, ..., m\}$, as follows:

$$\bigcup_{j=1}^{m} \zeta^j = \mathcal{V}, \qquad \bigcap_{j=1}^{m} \zeta^j = \varnothing. \tag{2.30}$$

Moreover, as stated in section 2.2.1, we assume that the volume $\mathcal{V}$ is in focus and we describe, in appendix C a synthetic optimization procedure of the viewing configuration of the cameras with respect to the region of interest. Figure 2.10 shows a top-view illustration of the sectioned grid $\mathcal{V}$.

2.2.3.2 Blob-Based Density Function

As explained in section 2.1.4, the projection of a small particle into an image plane impacts an aggregation of adjacent pixels. To account for this image formation model, we have modeled, in section 2.2.2.3, the incident intensity of the passive tracers in a fluid as a sum of blurred spheres in the space, as writes equation (2.25). We denote the density function over $\mathcal{V}$ at time t by $x_t : \mathbb{R}^3 \to \mathbb{R}$. The digitized counterpart of equation (2.25) is built assuming the following equivalence:

$$x_t(\mathbf{k}) \approx w_t(\mathbf{k}), \forall \mathbf{k} \in \mathbb{R}^3, \tag{2.31}$$

where $w_t(\mathbf{k})$ defined by equation (2.25) and $x_t(\mathbf{k})$ is a piece-wise polynomial function. In a more explicit form, equation (2.31) can be expressed such as:

$$x_t(\mathbf{k}) = \sum_{j \in \mathcal{J}} w_t\left(\mathbf{k}^j\right) b^j(\mathbf{k}), \forall \mathbf{k} \in \mathbb{R}^3, \tag{2.32}$$

where $\{b^j(\mathbf{k})\}_{j \in \mathcal{J}}$ are piece-wise Lagrange polynomials.

2.2.3.3 Particle-Based Density Function

We have introduced, in the previous section, an approximated model of the 3D density function reckoning with the physical-sound image formation model. We concentrate, in this section, on a discretization scheme which is a compeer of equation (2.32) allowing for a distinction between the incident intensity on the surface of the particles and their 3D blob representation.

In order to represent solely the centers of the so-modeled blobs, we introduce a novel discrete space $\mathcal{R} \subset \mathbb{R}^3$. Analogically to the cuboid $\mathcal{V}$ defined by equation (2.29), $\mathcal{R}$ is a regular polyhedron centered on $\mathbf{o}$ in the F_w system of coordinates and has the same dimensions $\begin{bmatrix} L_1 & L_2 & L_3 \end{bmatrix}^T$. Therefore, the two polyhedrons coincide. We discretize $\mathcal{R}$ as a cartesian grid made out of $\tilde{m} = p^3 m$ voxels centered on $\mathbf{x}^z \in \mathbb{R}^3, \forall z \in \mathcal{Z} = \{1, ..., \tilde{m}\}$. The quantity $p \in \mathbb{N}^*$ is a discretization parameter allowing to choose the fidelity of the so-defined new discrete space $\mathcal{R}$ and thus, to choose the accuracy with which we will seek for the centers of the particles.

In the sequel, we rely on the following assumption:

Assumption 2.1. *The centers of the particles located at positions* $\mathbf{h}^j \in \mathbb{R}^3, \forall j \in \{1, \dots, M\}$, *where* M *is the number of seeded particles, can solely belong to the ensemble of grid points in* $\mathcal{R}$, *i.e.,* $\mathbf{h}^j \in \{\mathbf{x}^1, \dots, \mathbf{x}^{\tilde{m}}\}$.

We proceed to building a particle-based discrete equivalent of the continuous volumetric intensity volume of the blobs by integrating the hypothesis stated by assumption 2.1. In an analog manner as states equation (2.31), we seek for a function $\tilde{w}_t(\mathbf{k})$ approximating its continuous volumetric counterpart, such as:

$$\tilde{w}_t(\mathbf{k}) \approx w_t(\mathbf{k}), \forall \mathbf{k} \in \mathbb{R}^3. \tag{2.33}$$

Explicitly, equation (2.33) writes:

$$\tilde{w}_t(\mathbf{k}) = \tilde{i}_t \sum_{z=1}^{\tilde{m}} g\left(\mathbf{k} - \mathbf{x}^z\right) s_t\left(\mathbf{x}^z\right), \forall \mathbf{k} \in \mathbb{R}^3, \tag{2.34}$$

with $g(\cdot)$ defined by equation (2.26); the function $s_t : \mathcal{R} \to \{0, 1\}$ is computed such as:

$$s_t(\mathbf{x}) = \mathbf{1}_0\left(\left\|\mathbf{x} - \mathbf{h}^j\right\|_\infty\right), \exists j \in \{1, \dots, M\} \text{ such that } \mathbf{h}^j = \mathbf{x}, \tag{2.35}$$

where $\mathbf{1}_0(\mathbf{x})$ the indicator function.

We can express a matrix counterpart of the equation (2.34). For doing so, let $\mathbf{s}_t : (\tilde{m} \times 1)$ be the column matrix registering for the location of the particles in $\mathcal{R}$ such as $\mathbf{s}_t = \begin{bmatrix} s_t(\mathbf{x}^1) & \dots & s_t(\mathbf{x}^{\tilde{m}}) \end{bmatrix}^T$, where $s_t(\cdot)$ defined by equation (2.35). Then, equation (2.34) writes, in its matrix form:

$$\tilde{\mathbf{w}}_t = \tilde{i}_t \mathbf{G} \mathbf{s}_t, \tag{2.36}$$

with $\mathbf{G} : (m \times \tilde{m})$ collecting the coefficients of $g(\cdot)$. Figure 2.9 depicts the representations of a particle expressed in both the $\mathcal{V}$ and the $\mathcal{R}$ polyhedrons.

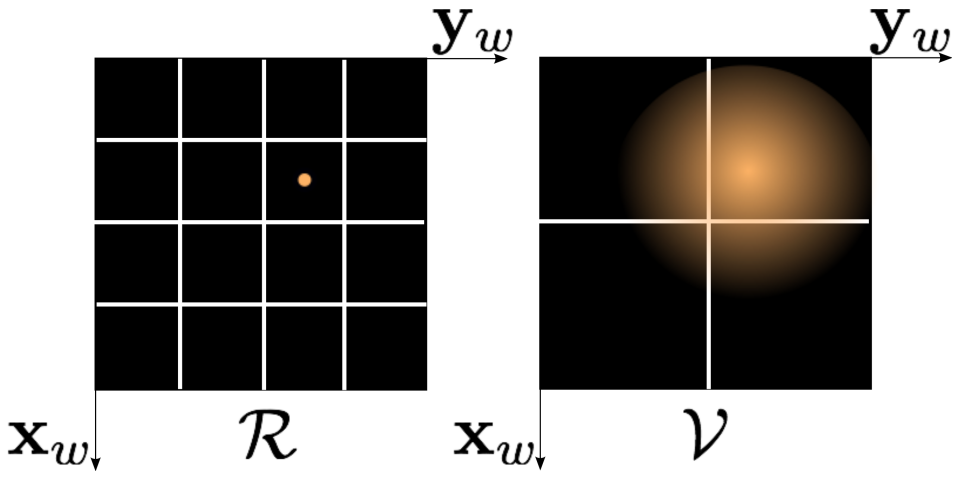

Figure 2.9: 2D rendition of the representation of the incident intensity at the surface of a particle in the $\mathcal{R}$ polyhedron (left) and of its blob-description counterpart expressed in the $\mathcal{V}$ polyhedron (right)

2.2.3.4 Image Formation

Using the equivalence expressed in equation (2.31) and plugging it into equation (2.27), we can compute the intensity of the i^{th} pixel on the c^{th} sensor plane at time t as follows:

$$y_{i,t}^c = scat^c \int_{\Omega_i^c} x_t(\mathbf{k}) \mathrm{d}\mathbf{k}. \tag{2.37}$$

In its more explicit counterpart, by inserting the definition expressed in equation (2.32), equation (2.37) writes:

$$y_{i,t}^c = scat^c \int_{\Omega_i^c} \sum_{j \in \mathcal{J}} w_t\left(\mathbf{k}^j\right) b^j(\mathbf{k}) \mathrm{d}\mathbf{k} \tag{2.38a}$$

$$= scat^c \sum_{j \in \mathcal{J}} w_t\left(\mathbf{k}^j\right) \underbrace{\int_{\Omega_i^c} b^j(\mathbf{k}) \mathrm{d}\mathbf{k}}_{d_{ij}^c}, \tag{2.38b}$$

where d_{ij}^c stands for the weight of the contribution of the density in voxel ζ^j to the energy measured within the cone of view passing through the i^{th} pixel, with $i \in \{1, \ldots, n^c\}$.The integral in the right-hand side of (2.38b) represents the volume of the intersection of the i^{th} cone of sight Ω_i^c with the j^{th} voxel ζ^j, as follows:

$$d_{ij}^c \triangleq \int_{\Omega_i^c} b^j(\mathbf{k}) \mathrm{d}\mathbf{k} = \frac{1}{\mathrm{Vol}\left(\zeta^j\right)} \int_{\Omega_i^c \cap \zeta^j} 1 \, \mathrm{d}\mathbf{k}. \tag{2.39}$$

We refer the reader to the appendix D for a discussion on the implementation of (2.39) based on a subvoxel sampling scheme. Figure 2.10 illustrates the projection formalized by

(2.37).

In its concise form, equation (2.38) writes:

$$y_{i,t}^{c} = scat^{c} \sum_{j \in \mathcal{J}} w_t\left(\mathbf{k}^{j}\right) d_{ij}^{c}. \tag{2.40}$$

Finally, expressed in matrix formulation, equation (2.40) writes:

$$\mathbf{y}_t = \mathbf{D}\mathbf{w}_t, \tag{2.41}$$

with

$$\mathbf{y}_t \triangleq \begin{bmatrix} \mathbf{y}_t^1 \\ \vdots \\ \mathbf{y}_t^{N_c} \end{bmatrix},$$

where $\mathbf{y}_t$ denotes the vector collecting the intensities of the $n = \sum_{c=1}^{N_c} n^c$ pixels at each time frame $t \in \mathbb{N}$ and $\mathbf{y}_t^c$ with $c \in \{1, \ldots, N_c\}$ collects the pixels on each sensor's image plane such as $\mathbf{y}_t^c \triangleq \begin{bmatrix} y_{1,t}^c & \cdots & y_{n^c,t}^c \end{bmatrix}^T$, with $n^c = \prod_{i \in \{1,2\}} n_i^c$. The vector $\mathbf{w}_t$ represents the incident intensity computed on the center of the voxels at instant t and writes:

$$\mathbf{w}_t \triangleq \begin{bmatrix} w_t(\mathbf{k}^1) & \cdots & w_t(\mathbf{k}^m) \end{bmatrix}^T. \tag{2.42}$$

Finally, the matrix $\mathbf{D}$ encoding the projection of the 3D discrete space into the images of the N^c cameras is the block matrix collecting the dictionaries accounting for the projection of $\mathbf{w}_t$ on each sensor, such as

$$\mathbf{D} \triangleq \begin{bmatrix} scat^1\mathbf{D}^1 \\ \vdots \\ scat^{N_c}\mathbf{D}^{N_c} \end{bmatrix}, \tag{2.43}$$

where $\mathbf{D}^c$ is build such that such that:

$$\mathbf{D}^c = \begin{bmatrix} d_{11} & \cdots & d_{1m} \\ \vdots & \ddots & \vdots \\ d_{n^c 1} & \cdots & d_{n^c m} \end{bmatrix}.$$

In order to take into account the errors in signal acquisition, we finally relax to latter model to:

$$\mathbf{y}_t = \mathbf{D}\mathbf{w}_t + \mathbf{n}_t, \tag{2.44}$$

where $\mathbf{n}_t : (n \times 1)$ is a noise vector accounting for calibration, measurement and approximation errors.

Particle-Based Image Formation

We can infer a particle-based image formation model compeer of equation (2.44) based on the model depicted by equation (2.34). Considering that matrix $\mathbf{D}$ allows for the projection of the voxel space $\mathcal{V}$ into the images' planes, the resulting vector collecting the pixel intensities

from the particle-based representation of $\mathcal{R}$ writes:

$$\mathbf{y}_t = \tilde{i}_t \mathbf{D}\mathbf{G}\mathbf{s}_t, \tag{2.45}$$

where $\tilde{\mathbf{w}}_t$ is specified by equation (2.36). We relax the model in equation (2.45) and present it concisely, as follows:

$$\mathbf{y}_t = \tilde{i}_t \mathbf{D}\mathbf{G}\mathbf{s}_t + \mathbf{n}_t. \tag{2.46}$$

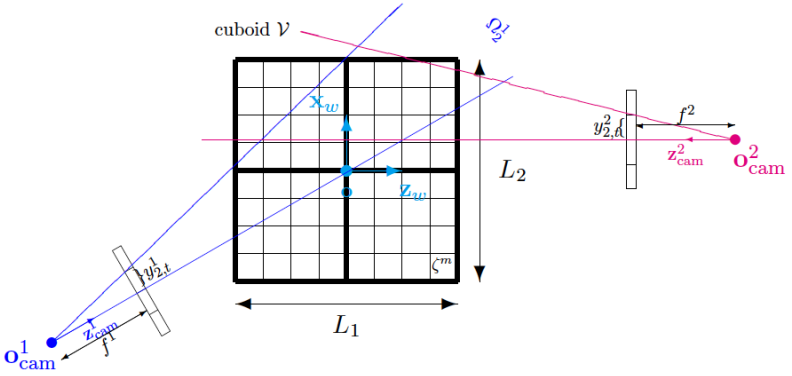

Figure 2.10: 2D Scheme of a 4-voxels cuboid in focus of two 4-pixel cameras; each voxel in $\mathcal{V}$ is divided into 4×4 subvoxels; the cone-of-sight Ω_2^1 passing through the 2^{nd} pixel of the first camera intersects subvoxels in $\mathcal{V}$, comprised within the blue lines.

Ballpark Figures of the Sampling Rates

The dimension of the observation vector $\mathbf{y}_t \in \mathbb{R}^n$ is directly linked to the intrinsic characteristics of the cameras around the scene. As specified before, its length is given by:

$$n = \sum_{c=1}^{N_c} \prod_{i=1}^{2} n_i^c,$$

where N_c is the number of cameras and the parameters $\begin{bmatrix} n_1^c & n_2^c \end{bmatrix}^T \in \mathbb{R}_+^\star \times \mathbb{R}_+^\star$ stand for the number of pixels per dimension, $\forall c \in \{1, \ldots, N_c\}$; the latter quantities have been previously defined in the sensor-related section 2.1.3.

Common values in the literature are $N_c = 4$ and $\begin{bmatrix} n_1^c & n_2^c \end{bmatrix}^T = \begin{bmatrix} 1024 & 1024 \end{bmatrix}^T$; this gives us a rough estimation of the magnitude of n of around 10^6. Despite the big amplitude of n, the tomoPIV system is generally undersampled. In fact, the choice of N_c and, implicitly, of the cameras' resolutions, is made upon material and complexity considerations. The two constraints are closely associated: as the number of cameras is limited out of cost restrictions, only a moderate number of observations are generated. It rests upon the volumetric discretization to define the final size of the problem to solve.

On this note, the resolution of the 3D space $\mathcal{V}$ is an input parameter and does not depend on a physical impediment. As recalled before, m and $\tilde{m}$ stand for the lengths of $\mathbf{w}_t$ and $\mathbf{s}_t$, respectively. Manifestly, $\tilde{m} \geq m$. The resolution m must be chosen high enough so that it resolves sufficiently the measurement space, but small enough so that the system is still solvable. Likewise, the subvoxelic fidelity expressed as a function of p must describe a subvoxelic space $\mathcal{R}$ dense enough so that the position of the center of the particle is defined with a high precision, but coarse enough to allow an accurate reconstruction from the signal processing perspective. In general, however, we have $n \ll m$ and implicitly, $n \ll \tilde{m}$.

2.2.3.5 Transport Model

We will exploit equations (2.31) and (2.32) to build a finite model approximating equation (2.28). We introduce the following definition, for $t \in \mathbb{N}$:

$$\mathbf{u}_t \triangleq \begin{bmatrix} u\left(\mathbf{k}^1, t\right) & \cdots & u\left(\mathbf{k}^m, t\right) \end{bmatrix}^T, \tag{2.47}$$

where $\mathbf{u}_t$ is the vector collecting the velocity field of the fluid at the centers $k^j, \forall j \in \mathcal{J}$ of each voxel, at each time frame t. Consequently, we define the incident intensity distribution of the particles displaced at time t by vector $\mathbf{u}_t$ such as:

$$\mathbf{w}_{t+1}(\mathbf{u}_t) \triangleq \left[w_{t+1}\left(\mathbf{k}^j + \mathbf{u}_{t,j}\right) \right]_{j \in \mathcal{J}}^T. \tag{2.48}$$

The vector $\mathbf{w}_{t+1}$ represents the incident intensity at instant $t+1$ computed on the center of the voxels of the discrete grid $\mathcal{V}$:

$$\mathbf{w}_{t+1} \triangleq \begin{bmatrix} w_{t+1}\left(\mathbf{k}^1\right) & \cdots & w_{t+1}\left(\mathbf{k}^m\right) \end{bmatrix}^T.$$

Then, by exploiting the equivalence stated by equation (2.28) and plugging it together with newly-defined vectors $\mathbf{w}_t$ and $\mathbf{w}_{t+1}(\mathbf{u}_t)$, we can conclude that:

$$\mathbf{w}_t = \mathbf{w}_{t+1}\left(\mathbf{u}_t\right). \tag{2.49}$$

Exploiting equation (2.49) by using simple algebra, it can be seen that:

$$\mathbf{w}_t = I\left(\mathbf{u}_t\right) \mathbf{w}_{t+1}, \tag{2.50}$$

where $I\left(\mathbf{u}_t\right)$ is a matrix which explicitly depends on the considered interpolation.

Equation (2.50) expresses the density conservation assumption over the discretized grid between two time frame. In the sequel, in order to account for small changes in the illumination of the scene and interpolation errors, we will slightly relax the latter model as follows:

$$\mathbf{w}_t = I\left(\mathbf{u}_t\right) \mathbf{w}_{t+1} + \mathbf{n}_{e_t}, \tag{2.51}$$

where $\mathbf{n}_{e_t} : (m \times 1)$ is a vector accounting for errors due to the brightness variation between two time frames and approximation.

Particle-Based Transport Assumption

The transport equation relating the particle-based volumetric densities functions, depicted by equation (2.36), between two instants can be expressed, in an analog manner as outlined by equation (2.50), by using the interpolation operator $I(\mathbf{u}_t)$ with regard to the displacement field between two frames and writes:

$$\tilde{\mathbf{w}}_t\left(\mathbf{u}_t\right) = I\left(\mathbf{u}_t\right)\tilde{\mathbf{w}}_{t+1}. \tag{2.52}$$

We account for the errors due to the brightness variation between two time frames and the sub-voxel precision of the location of the particles by relaxing the model presented here above such as:

$$\tilde{\mathbf{w}}_t = I\left(\mathbf{u}_t\right)\tilde{\mathbf{w}}_{t+1} + \tilde{\mathbf{n}}_{e_t}. \tag{2.53}$$

2.2.4 Summary

We have given a mathematical transcription of the physical properties of the tomoPIV system described in section 2.1. We have listed, in section 2.2.1, a few simplifying assumptions upon which we based our model. Section 2.2.2 grouped the continuous depiction of the image formation models available in the literature and presented with a proposed approximated counterpart of the physically pertinent model, followed by the subsequent 3D transport equation. Finally, in section 2.2.2 we have submitted a discretization scheme for the elected representation of the studied system. As a run-down on the current section, we retain that:

1. the state-of-the-art physically pertinent image formation model at this date is given by equation (2.22) and allows for the detection of particles;
2. we formalize and employ henceforward in the manuscript the image formation model depicted by equation (2.27) and its subsequent transport equation assumption given by equation (2.28);
3. we present, in section 2.2.3, two discretization schemes allowing us to juggle between a particle-based representation - suitable for the reconstruction of the 3D signal - and a blob-based model - appropriate in the case of velocity fields detection out of dense volumetric images.

Chapter 3. Volume Reconstruction

We have introduced, in chapter 2, two models relating the unknown volumetric data to the collected image measurements. We reproduce here below the two models, which change whether the unknown coefficients of the 3D density distribution in the cuboid are represented as Gaussian blobs centered on particles or particles. The blob-based representation transcribes, at each time frame t in a temporal sequence, as follows:

$$\mathbf{y}_t = \mathbf{D}\mathbf{w}_t, \tag{3.1}$$

where the column vector $\mathbf{w}_t \in \mathbb{R}^m$ collects the intensities of the Gaussian blobs in the volume whereas the vector $\mathbf{y}_t \in \mathbb{R}^n$ collects the pixel intensities of all $N_c \in \mathbb{N}$ cameras. The dictionary $\mathbf{D} \in \mathbb{R}^{n \times m}$ encodes the projection operator between the 3D and the 2D spaces. The second model writes:

$$\mathbf{y}_t = \mathbf{B}\mathbf{s}_t, \tag{3.2}$$

where $\mathbf{B} = \tilde{i}_t\mathbf{D}\mathbf{G}$, as suggested by equation (2.36); the function $\tilde{i}_t(\cdot)$ depicts the incident laser light on the surface of the particles at each time frame t, $\mathbf{s}_t \in \mathbb{R}^{\tilde{m}}$ is a binary vector accounting for the presence of a particle at a sub-voxel position and the dictionary $\mathbf{G} \in \mathbb{R}^{m \times \tilde{m}}$ encodes the interaction between a particle centered on a sub-voxel and its blob representation in the voxel space $\mathcal{V}$. As a reminder, $\tilde{m} = p^3 m$, where $p \in \mathbb{N}$ depicts the sub-voxelic precision of the particle representation in equation (3.2).

Both paradigms have their respective interest, as emphasized in the previous chapter. We stress here that the procedures applied to one model can be easily extended to the other one. For this reason and in order to ease the theoretical description throughout the current chapter, we will single-handedly refer to the model depicted by equation (3.1), unless explicitly mentioned otherwise. Furthermore, the temporal index has been dropped for the sake of simplicity. The simplified version of equation (3.1) writes:

$$\mathbf{y} = \mathbf{D}\mathbf{w}. \tag{3.3}$$

The retrieval of $\mathbf{w}$, and thus, of the volumetric intensity reconstruction out of the available information in $\mathbf{y}$ requires an inversion - term used here as an abuse of language - of the operator $\mathbf{D}$. The problem we are trying to solve is therefore an *inversion problem* with respect to a *fully discrete model*, and, more particularly, a *3D image reconstruction from projections problem*.

Figure 3.1 illustrates the work paradigm typically employed in the tomoPIV community when dealing with fully discrete models of the so-defined experimental fluid mechanics phenomenon. The methodology has been extensively described in [48] and in its companion paper [46] in the context of the Positron Emission Tomography. We follow the same standard as depicted below.

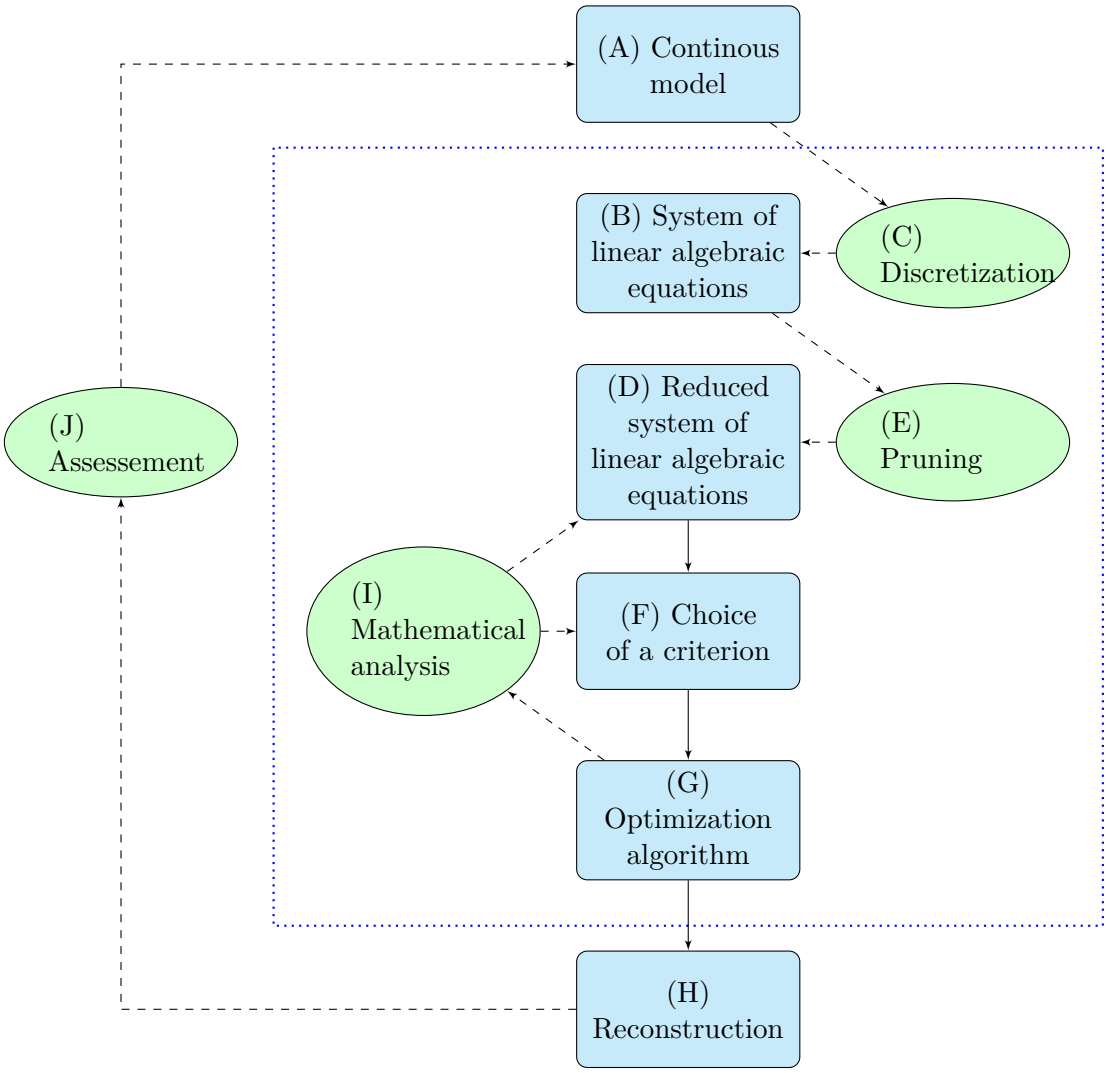

Figure 3.1: Generic fully discrete model adapted for the tomoPIV scenario. Block A, Block B, Block C have been extensively described in chapter 2. The current chapter focuses on the subsequent steps leading to an estimation of original real-world signal. The dashed blue box emphasizes the mathematical effort underlying the classical methodology for 3D image reconstruction out of projections. Adapted from [48].

We have begun our analysis in chapter 2, where we first formulated the original continuous volume reconstruction problem - which corresponds to Block A in figure 3.1 - and formalized the discrete problem - Block B, Block C - resulting in system (3.3). We

pursue our investigation by studying the properties of the digitized model accounting for the tomoPIV system's physical layout. Intrinsic characteristics of the scene as well as hallmarks arising from the employed methodologies in chapter 2 impact on the derived model. Succinctly, the system is very large and often underdetermined with $n \ll m$; the projection matrix $\mathbf{D} \in \mathbb{R}^{n \times m}$ is very sparse and in general not full rank. Analysis of the physical signal implies non-negativity and parsimony of the volumetric intensity distribution. Details and discussions on such features are given in section 3.1.

Classical solution in the tomoPIV literature, depicted in section 3.3, search for a solution of (3.3) by the methods of projections into convex sets. These procedure do not, however, account for noisy settings, nor for physical constraints on the signal. As it turns out, noise resulting from measurement inaccuracies and discretization coarseness may corrupt the data. Furthermore, due to a limited number of available observations, such systems may have infinitely many solutions. To cope with this conundrum, a criterion - step illustred in figure 3.1 by Block F - issued from the optimization theory and most often relying on physical priors must be established in order to single out the best solution out of all those satisfying (3.3). The study of such solution concepts is the main focus of this chapter. We will first discuss appropriate choices for the objective function ensuring the reconstruction pertinence with respect to the constraints imposed by the arrogated model in and extensively depicted in section 3.4. Then, in section 3.5 and 3.6, we put to the forth that procedures with the same computational/storage requisites as the classical algebraic methods can be derived in the general framework of *proximal methods*. The underlying idea behind these concepts is portrayed in figure 3.1 by Block G. Block I suggests the mathematical effort invested in solving the inverse linear problem.

We note that we can otherwise exploit the sparsity structure of the matrix $\mathbf{D}$, which is due to a limited number of basis functions on the line of sight of each camera pixel. This sparse structure impacts the observation vector $\mathbf{y}$, often resulting in numerous zero measurements. Based on the latter, it is convenient to determine a set of reduced dimensionality (approximately) equivalent to problem (3.3). The resulting stylized problem is obtained after a so-called pruning procedure. The last-mentioned steps are illustrated in figure 3.1 by Block D, Block E. The different approaches in the literature will be presented and discussed in section 3.9.

The goal of the latter steps is to output an estimation of the solution to the initial problem - see in figure 3.1, Block H - is retrieved. We assess the performance of the presented paradigms in a realistic synthetic setting in section 3.10 - this step is portrayed in figure 3.1, Block J, that suggests the interpretations of quantitative comparison between the estimated solution and the ground truth.

The main contributions of this chapter can be read in Sections 3.5 and 3.6. More specifically, we will show, in Section 3.5, that the tomoPIV problem can be recast within a general optimization framework and that powerful convex-optimization tools, that is methods belonging to the general framework of proximal methods [136], can be used to solve the resulting problem. Then, we will introduce to the tomoPIV community a new methodology belonging to the general framework of the ADMM paradigms [34] and we will show its appropriateness within the context of our application.

3.1 System Features

The discrete system (3.3) depicting a tomoPIV layout is underdetermined. In fact, this underdetermination is closely related to the **discretization** fidelity of the digitized model. The latter impacts on aspects related to the complexity of the model and to its solvability from the mathematical point of view. The level of undersampling of a tomoPIV system is a result of the trade-off on the choice of the volumetric space discretization: a larger number of voxels ensures a higher precision on the particles' centers, but, simultaneously, generates a higher number of columns in the interaction dictionary, that increases the **ill-posedness** of the problem. For instance, in practice we often choose the metric sizes of the vertices of the squared, respectively cubic pixel and voxel as approximately equal. Furthermore, we suppose, in this example, that $\mathcal{V}$ is cubic and the images are square. Then, posing that the number of voxels per dimension equals the number of pixels by dimension, we can simply express the ratio between the number of rows and the number of columns of $\mathbf{D}$ as $\frac{N_c}{n_d}$, where N_c is the number of cameras and n_d is the number of pixels per dimension, where $n_d \gg N_c$.

Due to ill-conditioning, the system may have an infinite number of solutions. In practice, we usually exploit some *a priori* information on the original signal in order to single out a solution. On this note, let us distinguish between the model represented by equation (3.3), where $\mathbf{w}$ is a variable, the original discretized 3D signal $\tilde{\mathbf{w}}$ having generated the observations such that $\mathbf{y} = \mathbf{D}\tilde{\mathbf{w}}$ and the estimated solution that we will denote by $\mathbf{w}^\star$. Following the description of the experimental set-up made in the previous chapter, we have concluded that the tomoPIV signal $\tilde{\mathbf{w}}$ is non-negative and sparse.

The original 3D signal that we aim to reconstruct represents intensities and it is therefore a non-negative signal. In fact, our signal processing transcription of this phenomenon respects this non-negativity property. The laser intensity function, introduced in section 2.1.1, $\tilde{i}_t : \mathbb{R}^3 \to \mathbb{R}_+$ defined in each 3D point in $\mathcal{V}$ is a non-negative signal. Furthermore, the physically-sound shading intensity function $l : \mathbb{R}^3 \to \mathbb{R}_+$ is defined in a positive domain, as writes equation (2.3). We can therefore deduct that the continuous approximation of the volumetric density function at each time frame $v_t : \mathbb{R}^3 \to \mathbb{R}_+$, explicited by equation (2.20) where we drop the position index, also corresponds to a non-negative signal. As the discretization schemes do not induce non-negativity in the so-obtained digitized volumetric function, we will assume henceforward that $\tilde{\mathbf{w}}$ is a non-negative vector.

By the nature of the experimental setting, there is more unresolved space in the measuring volume $\mathcal{V}$ than seeded particles. The vector $\tilde{\mathbf{w}}$ thus contains more zero-components (corresponding to the empty space in the flow) than non-zero coefficients (corresponding to the intensities of the scatterers). An example depicted in [156] gives a hint on the size of the unresolved space with respect to particle volumetric concentration. In fact, let us denote by C_p the particle concentration; the latter varies whether the experiments are conducted in water ($C_p \in [0.5, 3]\ \frac{\#\text{particles}}{\text{mm}^3}$) or in air ($C_p \in [10, 20]\ \frac{\#\text{particles}}{\text{mm}^3}$).

3.2 Notations

We define the indicator function $\mathbb{I}_{\mathcal{X}}(\mathbf{x})$ of a set $\mathcal{X}$ as

$$\mathbb{I}_{\mathcal{X}}(\mathbf{x}) = \begin{cases} 0 & \text{if } \mathbf{x} \in \mathcal{X} \\ +\infty & \text{otherwise.} \end{cases} \tag{3.4}$$

The projection operator of a point $\mathbf{v}$ on a convex set $\mathcal{X}$ is defined as:

$$\Pi_{\mathcal{X}}(\mathbf{v}) = \arg\min_{\mathbf{x}\in\mathcal{X}} \|\mathbf{x} - \mathbf{v}\|_2.$$

The logarithm or the exponential of a vector $\mathbf{v} \in \mathbb{R}^n$ has to be understood component-wise: if $\mathbf{v} \in \mathbb{R}^n$, $\log(\mathbf{v}) = [\log v_i]_{1\leq i\leq n} \in \mathbb{R}^n$ (resp. $e^{\mathbf{v}} = [e^{v_i}]_{1\leq i\leq n} \in \mathbb{R}^n$). In the sequel, we assume that log denotes the Napierian logarithm, *i.e.*, $\log e = 1$. Let $\mathbf{d}_{\bullet,j}$ denote the j^{th} column of a matrix. In an analogue manner, let the column vector $\mathbf{d}_{j,\bullet}$ denote its j^{th} row.

3.3 Standard Procedures for tomoPIV Volume Reconstruction

Since the advent of tomoPIV, several volume reconstruction procedures have been studied in the literature. The most popular methodologies in the current state of the art are undeniably the the so-called *"Row-Action Methods"* (the reader may refer to [45] for an extensive review).

The main idea underlying row-action methods consists in searching for a solution of (3.3) (with possibly non-negativity constraints) by iteratively projecting a current estimate onto some convex subsets defining the set of feasible solutions. For a thorough depiction of their architecture, the reader should refer to [48]. We limit here our analysis to items destined to elucidate the main idea behind their formalism. In a nutshell, a row-action method: *(i)* does not alter the original matrix; *(ii)* does not perform operations on the matrix as a whole; *(iii)* depends, at the current iteration, solely on the value of the previous estimate. The latter points are crucial for the tomoPIV application. In fact, the interest of the tomoPIV community has been mainly focused on procedures exhibiting low computational and storage requirements. The row-action methods are indeed well adapted to our application since: *(i)* their complexity (per iteration) remains linear in the size of the problem; *(ii)* the matrix $\mathbf{D}$ need not be stored explicitly. We briefly describe the most popular algorithms belonging to this family hereafter.

Algebraic Reconstruction Technique (ART)

Let us first notice that any solution of (3.3) lies at the intersection of the n hyperplanes defined by the rows of $\mathbf{D}$. More specifically, let $\mathbf{d}_{i,\bullet}$ be the i^{th} row of $\mathbf{D}$ and $\mathcal{H}_i$ the corresponding hyperplane, *i.e.*,

$$\mathcal{H}_i = \{\mathbf{h} \in \mathbb{R}^m | \mathbf{d}_{i,\bullet}^T \mathbf{h} = y_i\}. \tag{3.5}$$

Then, $\mathbf{w}$ is a solution of (3.3) if and only if $\mathbf{w} \in \cap_{i=1}^{n} \mathcal{H}_i$.

The philosophy behind the algebraic methods consists in looking for a solution of (3.3) by sequentially projecting the current estimate onto the hyperplanes $\mathcal{H}_i$'s. The typical step of the algebraic family follows the following iteration update:

$$\mathbf{w}^{(k+1)} = \mathbf{w}^{(k)}_{\mathcal{H}_i}, \tag{3.6}$$

where

$$\mathbf{w}_{\mathcal{H}_i} = \mathbf{w} + \gamma \frac{y_i - \mathbf{d}_{i,\bullet}\mathbf{w}}{\|\mathbf{d}_{i,\bullet}\|_2^2} \mathbf{d}_{i,\bullet}^T, \tag{3.7}$$

with γ denotes the (relaxed [1]) projection of $\mathbf{w}$ onto $\mathcal{H}_i$. We note that, although we did not explicitly include it in our notations, the relaxation parameter γ in (3.7) can vary at each iteration. The simplest algebraic reconstruction technique, the "Kaczmarz" method [104] (sometimes simply referred to as ART) corresponds to a fixed $\gamma \in (0, 2)$ and to a cyclic control $i = k \mod n$. Note that its "randomized" counterpart selects the rows i randomly with probability proportional to $\|\mathbf{d}_{i,\bullet}\|_2^2$ [97].

The Kaczmarz method iteratively projects the current estimate $\mathbf{w}^{(k)}$ onto *one* given hyperplane $\mathcal{H}_i$. Other methodologies, coined SIRT, aim at exploiting the projections on *all* the hyperplanes $\mathcal{H}_i$ at each iteration, *i.e.*,

$$\mathbf{w}^{(k+1)} = \sum_{i=1}^{n} p_i \, \mathbf{w}^{(k)}_{\mathcal{H}_i}, \tag{3.8}$$

where $p_i > 0$ is some weighting factor. The well-known "Cimmino" [53] or "SART" [8] correspond to particular choice of parameters γ and p_i's. More generally, SIRT can be written under the general form:

$$\mathbf{w}^{(k+1)} = \mathbf{w}^{(k)} + \alpha^{(k)} \mathbf{W}\mathbf{D}^T\mathbf{\Gamma}(\mathbf{y} - \mathbf{D}\mathbf{w}^{(k)}), \tag{3.9}$$

where $\alpha^{(k)} > 0$ and $\mathbf{W}$, $\mathbf{\Gamma}$ are some positive-definite matrices. Formulation (3.8) corresponds to the case where $\mathbf{W}$ and $\mathbf{\Gamma}$ are diagonal matrices.

Finally, let us mention that variants of Kaczmarz and SIRT have also been proposed to search for a *non-negative* solution of (3.3), [182, Chapter 9]. The corresponding algorithms, referred to "Kaczmarz+" and "SIRT+" in the sequel, respectively take the form:

$$\mathbf{w}^{(k+1)} = \Pi^m_{\mathbb{R}_+} \left(\mathbf{w}^{(k)}_{\mathcal{H}_i} \right), \quad i = k \mod n, \tag{3.10}$$

$$\mathbf{w}^{(k+1)} = \Pi^m_{\mathbb{R}_+} \left(\mathbf{w}^{(k)} + \alpha^{(k)} \mathbf{W}\mathbf{D}^T\mathbf{\Gamma}(\mathbf{y} - \mathbf{D}\mathbf{w}^{(k)}) \right), \tag{3.11}$$

where $\Pi_{\mathbb{R}_+}(\cdot)$ denotes the projection operator onto the positive orthant and $\mathbf{\Gamma}$ and $\mathbf{W}$ are diagonal matrices.

1. The standard Euclidean projection corresponds to the case $\gamma = 1$.

The algebraic methods enjoy desirable convergence properties. If (3.3) admits one single solution, Kaczmarz and SIRT converge to this solution; if more than one solution exists, the convergence point depends on the initial value $\mathbf{w}^{(0)}$. If (3.3) does not admit any solution, SIRT converges to a point $\mathbf{w}^{(\infty)}$ minimizing the weighted least-square $(\mathbf{y} - \mathbf{D}\mathbf{w}^{(k)})^T\mathbf{\Gamma}(\mathbf{y} - \mathbf{D}\mathbf{w}^{(k)})$ from any initial guess, result shown independently in [103] and [47]; on the other hand, the Kaczmarz iteration has been shown to converge, but not necessarily to a solution minimizing the weighted least-square seen above [96]. The same type of conclusion holds for Kaczmarz+ and SIRT+: if (3.3) admits at least one non-negative solution, both procedures converge to such a point. In the opposite case, SIRT+ converges to a minimizer of $\min_{\mathbf{w}\geq 0}(\mathbf{y}-\mathbf{D}\mathbf{w}^{(k)})^T\mathbf{\Gamma}(\mathbf{y}-\mathbf{D}\mathbf{w}^{(k)})$ whereas the sequence $\{\mathbf{w}^{(k)}\}$ generated by Kaczmarz+ cannot be expected to converge. The rate of convergence of the Kaczmarz method are difficult to compute analytically; faster convergence has been empirically observed by using the rows of $\mathbf{D}$ randomly [97]. The convergence rate of the initial iterations of SIRTs depend on the choice of the relaxation parameter; in fact, while initially the iteration vector approaches a regularized solution, continuing the recursions often leads to iteration vectors corrupted by noise (phenomenon coined "semi-convergence" and studied for SIRT algorithms in [73]).

Within the tomoPIV context, the solution of the problem (3.3) has been sought with a Kaczmarz algorithm in [143, 147]. In [151], the author submits a constrained version of Kaczmarz's algorithm and proves its convergence, even in the perturbed case, to a least squares solution of the reconstruction problem, under somewhat weak hypothesis. SIRT methods have been considered to solve our inverse problem in [140] and [139], that is Cimmino and SART, respectively. We stress that in [140], the authors submit an extended version of Cimmino's algorithm which converges to the least squares solution in the general perturbed case.

Multiplicative Algebraic Reconstruction Technique (MART)

The multiplicative algebraic techniques are built on the same spirit as ART: they look for a solution of (3.3) by iteratively projecting the current estimate onto some hyperplane(s) $\mathcal{H}_i$. A specificity of MARTs is that they carry out projections with respect to the KL distance [112]. We note that the use of the KL distance as projection metric implicitly imposes that the constraint $\mathbf{w} \geq 0$ is in force. Hence, the procedures described hereafter look for a *nonnegative* solution of (3.3).

The simplest procedure belonging to the multiplicative family obeys the following recursion [95]:

$$w_j^{(k+1)} = w_j^{(k)} \left(\frac{y_i}{\mathbf{d}_{i,\bullet}^T \mathbf{w}^{(k)}} \right)^{\gamma d_{ij}}, \tag{3.12}$$

with $\gamma \leq \min\{\mathbf{d}_{\bullet,j}\}$, for $\forall j$ chosen such that the observation entries are strictly positive, $\forall j$ chosen such that the observation matrix has only non-negative entries. The procedure is simply referred to as MART in the literature.

MART only exploits one row of $\mathbf{D}$ at each iteration. Another procedure, taking benefit

from all the rows of $\mathbf{D}$ at each iteration, has also been proposed [40]:

$$w_j^{(k+1)} = w_j^{(k)} \prod_{i=1}^{n} \left(\frac{y_i}{\mathbf{d}_{i,\bullet}^T \mathbf{w}^{(k)}} \right)^{\gamma d_{ij}}, \tag{3.13}$$

with γ, i, j chosen as above. This procedure is usually referred to as SMART.

The nature of $\mathbf{w}^{(\infty)}$ depends on whether (3.3) admits a nonnegative solution or not. In the former case, $\mathbf{w}^{(\infty)}$ depends on the initial value $\mathbf{w}^{(0)}$. More specifically, it has been shown in [40] that (S)MART converges to the unique solution of the following problem:

$$\min_{\mathbf{w} \geq 0} \mathrm{KL}(\mathbf{w}, \mathbf{w}^{(0)}) \quad \text{subject to } \mathbf{y} = \mathbf{D}\mathbf{w}. \tag{3.14}$$

where $\mathrm{KL}(\mathbf{u}, \mathbf{v}) \triangleq \sum_i u_i \log(u_i/v_i) + v_i - u_i$ denotes the KL distance. Interestingly, if $\mathbf{w}^{(0)}$ is constant and $\mathbf{y} = \mathbf{D}\mathbf{w}$ has non-negative solutions, it has been shown in [115] that MART converges to the solution that maximizes the Shannon entropy, that is:

$$\min_{\mathbf{w} \geq 0} \sum_i w_i \log w_i \quad \text{subject to } \mathbf{y} = \mathbf{D}\mathbf{w}. \tag{3.15}$$

If (3.3) does not admit a nonnegative solution, SMART converges to the unique minimizer of $\mathrm{KL}(\mathbf{y}, \mathbf{D}\mathbf{x})$, see [40]. Regarding MART, the nature of $\mathbf{w}^{(\infty)}$ is unknown in this case as noted by Herman in [94]. In [72], the author demonstrates linear convergence rates for MART. Moreover, *Petra et al.* empirically show sublinear convergence, see [143, Section 6].

The tomoPIV volume reconstruction problem with (S)MARTs has been considered in the literature in a considerable number of articles. Starting with the seminal paper [74], the algorithm has been later adopted in [15, 29, 61, 143, 161, 171] and used as an enhancement to the subsequent velocity estimation in [134]. A very recent contribution in *row-actions* methods adapted for the tomoPIV application propose constraining the upper bound on the feasible points [142]. This operation is enabled by designing an algorithm which aims at minimizing the generalized distance of the *Fermi-Dirac* entropy.

3.4 Inverse Problem

As previously stated, due to a limited number of available observations, the tomoPIV system generically depicted by equation (3.3) may have infinitely many solutions. To tackle this shortcoming, the preferred modus operandi in volume reconstruction from limited data is to resort to a procedure exploiting known information on the original signal in order to find, among the numerous solutions, the vector $\tilde{\mathbf{w}}$ which has generated the measurements $\mathbf{y}$. For doing so, we capitalize on the noted features of $\tilde{\mathbf{w}}$, evoked here-above, that is its **non-negativity** and its **sparsity**. While making allowance for the non-negativity can simply be accomplished by explicitly constraining the sough solution, enforcing its sparsity is less trivial. In fact, the latter constraint requires the resolution of an optimization problem minimizing a function which encourages the sparsity on the sought solution. In the optimization approach, we usually opt for an objective function $l_r : \mathbb{R}^m \to \mathbb{R}_+$ which

accomplishes this task. In accordance to the previous statements, the resulting optimization problem writes:

$$(P^0) : \mathbf{w}^\star = \arg\min_{\mathbf{w}} l_r(\mathbf{w}) \text{ such that } \begin{cases} \mathbf{D}\mathbf{w} = \mathbf{y}; \\ \mathbf{w} \geq 0, \end{cases} \tag{3.16}$$

where the 0 superscript describes the inverse problem in the consistent case, when we suppose that the system is not perturbed by noise. The first constraint ensures that the signal is in adequacy with the recorded measurement, while the latter guarantees the positivity of the estimated solution.

In practice, the system is often error-prone. In fact, several factors such as the discretization of the continuous phenomenon or some measurements inaccuracies may alter the collected data $\mathbf{y}$. In order to take into account this noise on the observations, we allow for a small gap between the latter and the model. The resulting optimization problem writes:

$$(P^\varepsilon) : \mathbf{w}^\star = \arg\min_{\mathbf{w}} l_r(\mathbf{w}) \text{ such that } \begin{cases} l_d(\mathbf{D}\mathbf{w}, \mathbf{y}) \leq \varepsilon; \\ \mathbf{w} \geq 0, \end{cases} \tag{3.17}$$

with $\varepsilon \in \mathbb{R}_+$. $l_d : \mathbb{R}^n \times \mathbb{R}^n \to \mathbb{R}_+$ is a "distance"-like function.

The problem (P^ε) yields several equivalent formulations in the context of convex optimization. For instance, we can express (P^ε) as unconstrained optimization problem which searches for the signal as a compromise between the approximation quality quantified by $l_d(\cdot, \cdot)$ and the metric defined by $l_r(\cdot)$:

$$\begin{aligned} (R) : \ \mathbf{w}^\star &= \arg\min_{\mathbf{w}} l_d(\mathbf{D}\mathbf{w}, \mathbf{y}) + r l_r(\mathbf{w}) \\ \text{such that } \mathbf{w} &\geq 0, \end{aligned} \tag{3.18}$$

with $r \in \mathbb{R}_+^\star$.

Another alternative to (3.17) is achieved by seeking the vector checking the properties of $l_r(\cdot)$ which minimizes the approximation error:

$$(A) : \mathbf{w}^\star = \arg\min_{\mathbf{w}} l_d(\mathbf{D}\mathbf{w}, \mathbf{y}) \text{ such that } \begin{cases} l_r(\mathbf{w}) \leq a; \\ \mathbf{w} \geq 0, \end{cases} \tag{3.19}$$

with $a \in \mathbb{R}_+^\star$.

Let us note that, on top of their interest from an algorithmic point of view, the different formulations stated in (3.17), (3.18), (3.19) also show some interests from a practical point of view. On the one hand, ε and a have clear physical meanings since they respectively correspond to a measure of the noise level affecting the data, and the level of sparsity of the sought signal (*i.e.*, a measure of the density of seeded particles in the fluid). On the other hand, r has usually no particular physical meaning. Tuning the value of this parameter may thus require some cumbersome "trial-and-error" procedure. If $l_r(\cdot)$ and $l_d(\cdot, \cdot)$ are convex,

problems (3.17) and (3.18) are equivalent for some value of ε and r. More specifically, a solution of (P^{ε}), $\forall\varepsilon$ such that the problem is feasible, is either $\mathbf{w} = \mathbf{0}_m$ or a minimizer of (R), for some $r > 0$. However, for a given value of ε (resp. a), finding the value of r leading to an equivalence between (3.17)(resp. (3.19)) and (3.18) is usually not a trivial task.

Functions $l_r(\cdot)$ and $l_d(\cdot,\cdot)$ are carefully built with respect to theoretical appropriateness and performance suitability. The choices and their respective implications of $l_r(\cdot)$ and $l_d(\cdot,\cdot)$ will be discussed in sections 3.4.1 and 3.4.2.

3.4.1 Choices of the Cost Function on the Signal

Of paramount importance in solving (P^{ε}) and its variations is the choice of $l_r(\cdot)$ such that it respects and reinforces intrinsic properties of the signal. In fact, since the positivity constraint can be explicitly included in our optimization problem, $l_r(\cdot)$ should ideally be a function enforcing the sparsity of the solution. In this section, we first review some choices of $l_r(\cdot)$ classically adopted by the signal processing/tomoPIV community. Then, we review some functions enforcing the sparsity.

Standard Approach

The most straightforward example of a commonly used paradigm in the signal processing community involves searching for the solution of system (3.3) under a constant function

$$l_r(\mathbf{w}) = 1. \tag{3.20}$$

The subsequent problem minimizing the function defined by equation (3.20) finds the solution as the intersection point of all hyperplanes $\{\mathbf{w}|\,\langle\mathbf{d}_i,\mathbf{w}\rangle = y_i\}, \forall i \in \{1,\ldots,n\}$, when there is no noise corruption of the data or within the neighborhood of the so-defined hyperplanes, in the perturbed scenario. A further restriction involves looking for solutions satisfying $w_j \geq 0, \forall j \in \mathcal{J}$, imposing thus the non-negative constraint on the estimate. Generally, the problem built with respect to a constant functional has an infinity of solutions. In the sequel, we will concentrate on more apt functions in order to select a single solution out of all those satisfying the geometric constraints.

An omnipresent function in the signal processing community is the squared ℓ_2-norm; intuitively, the latter represents the physical length of a vector $\mathbf{w}$ in $\mathbb{R}^m$. This choice is interesting and extensively used due to its strong convexity that outputs an unique minimizer. The subsequent optimization problem minimizes the function:

$$l_r(\mathbf{w}) = \frac{1}{2}\|\mathbf{w}\|_2^2, \text{ with } \|\mathbf{w}\|_2 \triangleq \sqrt{\left(\sum_j w_j^2\right)}. \tag{3.21}$$

The most commonly employed regularization implicitly adopted by the tomoPIV community is the entropy-based optimization criterion, first addressed within the studied application in [74], that is:

$$l_r(\mathbf{w}) = -ent(\mathbf{w}), \text{ with } ent(\mathbf{w}) \triangleq \sum_j w_j \log w_j, \tag{3.22}$$

where $ent(\cdot)$ is also known as the *Shannon entropy* function which maps the non-negative orthant $\mathbb{R}_+^m$ into $\mathbb{R}$. The main idea behind this formalization is to interpret the signal $\mathbf{w}$ as a probability distribution that allows to subsequently assign it to an entropy measure in order to indicate its randomness or uncertainty. Adding the non-negativity constraint on the sought solution is necessary to ensure the definition of the $\log(\cdot)$ function on $\mathbb{R}_+^\star$. We define $0 \log 0 = 0$ and continuously extend $l_r(\mathbf{w})$, which is strictly convex on $\mathbb{R}_+^m$.

The upper-depicted choices can however be problematic within the tomoPIV context. In fact, neither one of the standard choices enforces the sparsity of the sought solution, thus better alternatives are preferred.

Functions Enforcing Sparsity

Recently, the volumetric estimation problem has been expressed in a sparse representation (SR) context in order to enforce the prior that in the visualized volume there is more empty space than seeded particles [17, 55, 147]. Thus, the problem (3.3) can be studied from the general point of view of SR context, which is a modern research field that deals with the study of the *exact* reconstruction of a signal $\tilde{\mathbf{w}}$ acquired by an incomplete linear measurement (3.3), provided the latter is sparse, *i.e.*, it has a small number of non-zero coefficients. A straightforward manner of quantifying the sparsity of a signal is by counting the number of its non-zero elements; the cardinality of the support of $\mathbf{w}$ is obtained by computing its ℓ_0-"norm" [2], as writes:

$$l_r(\mathbf{w}) = \|\mathbf{w}\|_0 , \text{ with } \|\mathbf{w}\|_0 \triangleq \sum_j |w_j|^0. \tag{3.23}$$

While a problem minimizing equation (3.23) strongly enforces the sparsity on the sought solution, the so-defined function $l_r(\mathbf{w})$ is discontinuous and non-differentiable in 0; we must thus resort to combinatorial programs in order to minimize it, that rely on an exhaustive search of all combinations of columns possible, which is not reckonable for high dimensions.

In order facilitate the resulting optimization problem, one can consider the ℓ_p-norm instead:

$$l_r(\mathbf{w}) = \|\mathbf{w}\|_p , \text{ with } \|\mathbf{w}\|_p \triangleq \left(\sum_j |w_j|^p \right)^{\frac{1}{p}} , \tag{3.24}$$

where the interesting choice of p resides in the ensemble $(0, 1)$. The smaller we choose p, the more we enforce the sparsity structure of the signal. Moreover, $l_r(\mathbf{w})$ is continuous, but non-differentiable in 0. The subsequent program minimizing $l_r(\mathbf{w})$ is not convex and it may display local minima.

The evoked difficulties have been bypassed with the introduction of a relaxed prior based

2. where the double quotes mark notation is used to give a broader sense on the classical norms, as first conveyed by *Donoho* in [62]. We keep in mind that the ℓ_0-"norm" is often referred to as a *pseudo-norm* since it fails to validate the homogeneity property of norms, while ℓ_p-"norm", with $p \in (0, 1)$ is referred to as a *quasi-norm* as it solely verifies the *quasi*-triangular inequality condition. In the sequel, we will make an abuse of language and include the latter measurements in the all-embracing *norm* category.

on the ℓ_1-norm, that is:

$$l_r(\mathbf{w}) = \|\mathbf{w}\|_1 , \text{ with } \|\mathbf{w}\|_1 \triangleq \sum_j |w_j|. \tag{3.25}$$

Non-negativity constraints can be implicitly enforced by considering the indicator function of the positive orthant as a regularization function, *i.e.*,

$$l_r(\mathbf{w}) = \mathbb{I}_{\mathbb{R}^m_+}(\mathbf{w}). \tag{3.26}$$

Finally, taking (3.25) and (3.26) into account, it is easy to see that both non-negativity *and* sparsity can be enforced with the following choice for l_r:

$$l_r(\mathbf{w}) = \|\mathbf{w}\|_1 + \mathbb{I}_{\mathbb{R}^m_+}(\mathbf{w}) = \mathbf{1}^T\mathbf{w} + \mathbb{I}_{\mathbb{R}^m_+}(\mathbf{w}). \tag{3.27}$$

The motivation behind the choice of solving (3.25)-(3.27) instead of (3.23) or (3.24) relies on the study of their respective convexity. In fact, both $\|\mathbf{w}\|_0$ and $\|\mathbf{w}\|_p, \forall p \in (0,1)$ are non-convex; conversely, for $p \geq 1$, the corresponding norms are convex. In contrast, for $p = 1$, in the same operating regimes, the sparsity of the correspondent estimated signal will be inferior to that of the solution output by minimizing $\|\mathbf{w}\|_0$ or $\|\mathbf{w}\|_p, \forall p \in (0,1)$. See section 3.8 for a discussion on conditions guaranteeing that the problems built with respect to function (3.23) and (3.25) share the same unique solution.

Figure 3.2 provides a visual depiction of the ℓ_p-balls for the aforementioned p values - figures 3.2(a-c), respectively - and of the $-ent(\cdot)$ball - figure 3.2(d). We consider a 1-dimensional signal $\mathbf{y}$ and the projection dictionary $\mathbf{D} \in \mathbb{R}^{n \times m}$ with $n = 1, m = 2$. We have $\mathbf{y} = \mathbf{D}\tilde{\mathbf{w}}$ with $\tilde{\mathbf{w}} = \begin{bmatrix} \tilde{w}_1 & 0 \end{bmatrix}^T$. For each considered norm, we draw the level lines (cyan, green) to which we superimpose the line defined by $\mathbf{y} = \mathbf{D}\mathbf{w}$ (purple). As rendered in the image, for $p < 1$, the level lines are non-convex, whereas for $p \geq 1$ and for $-ent(\cdot)$, the latter are convex (which enables the use of efficient algorithms to solve the subsequent optimization programs). The solutions of problems minimizing the ℓ_p-norm and maximizing the entropy are located at the intersection of the line $\mathbf{y} = \mathbf{D}\mathbf{w}$ with the lowest level line (drawn here in green) and it is depicted by $\mathbf{w}^\star$. For $p \leq 1$, the latter will be sparse ($w_1^\star \neq 0, w_2^\star = 0$), but for $p > 1$ and $-ent(\cdot)$, $\mathbf{w}^\star$ will have more non-zero atoms than the original sought signal ($w_j^\star \neq 0, \forall j \in \{0,1\}$).

3.4.2 Choices on the Function Penalizing the Prediction-Observation Discrepancy

The received observations are noisy due to the discretization and physical phenomena which have been overlooked in our modelization, such as:

Measurement inaccuracies : First of all, as previously described in section 2.1.1, any intensity levels recorded on the images that is outside of our region of interest depicted by $\mathcal{V}$ (see equation (2.29)) will contribute to a decrease of the SNR of the density volumetric function. Next, the measurements may be corrupted by calibration-induced errors (see section 2.1.5);

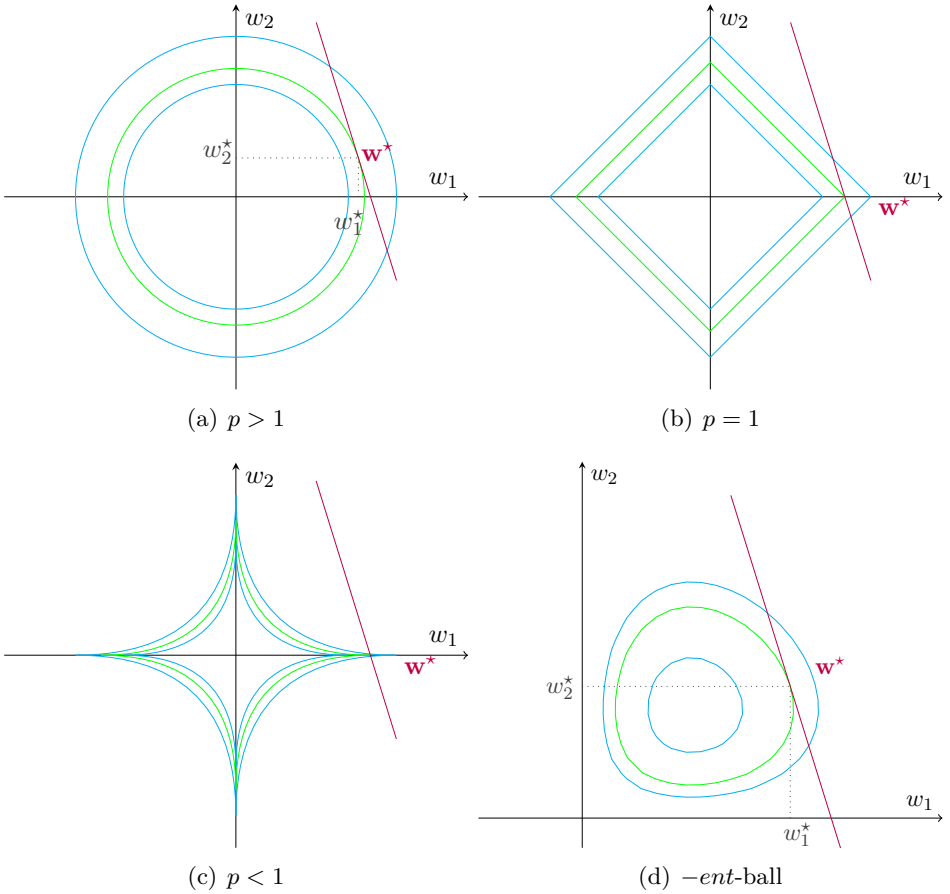

(a) $p > 1$ (b) $p = 1$

(c) $p < 1$ (d) $-ent$-ball

Figure 3.2: (a)-(c): ℓ_p-balls of radius $\|\mathbf{w}\|_p$, with $\mathbf{w} = \begin{bmatrix} w_1 & w_2 \end{bmatrix}^T$ centered at the origin; (d): $-ent(\mathbf{w})$-ball. The purple line is dictated by the model $\mathbf{y} = \mathbf{D}\mathbf{w}$. The solutions of subsequent problems are given by $\mathbf{w}^\star$, located at the intersection of the observations equation with the lowest level curve, emphasized here in green.

Simplifying assumptions : As specified throughout the section 2.1, and summed-up in section 2.2.1, we have built our continuous paradigm based upon several simplifications of intricate physical phenomena;

An oversimplified discretization scheme : The discretization scheme formalized in section 2.2.3 resulting in the digital counterpart of the continuous model and expressed by the equations (3.1) and (3.2), induces a further approximation in the model. In fact, as explained in section 2.2.3.4, not only do we have to impose a certain coarseness in the 3D discretization scheme, but the integration of the volumetric intensity along the line-of-sight of the cameras' pixels imposes the choice of approximating basis function.

The noise induced by the latter phenomena is difficult to accurately take into consideration into our model. Therefore, we consider, in this section, two choices for the loss functions penalizing the discrepancy between the the observations and the model.

Euclidean Distance

The ubiquitous Euclidean distance writes:

$$l_d(\mathbf{Dw}, \mathbf{y}) = \frac{1}{2} \|\mathbf{Dw} - \mathbf{y}\|_2^2 , \tag{3.28}$$

with the particularity that $l_d(\cdot, \cdot)$, known as the half-squared Euclidean norm of the prediction-observation discrepancy, has the symmetry property in $\mathbf{Dw}$ and $\mathbf{y}$, otherwise not present in other generalized distances. Minimizing $l_d(\mathbf{Dw}, \mathbf{y})$ over all $\mathbf{w} \in \mathbb{R}^m$ for some fixed $\mathbf{y}$ leads us to the usual metric projection. The resultant regularization approach is the least-squares fit. Additionally, we can constraint the solution to be positive or upper and lower bounded.

Kullback-Leibler Distance

The Kullback-Leibler (KL) distance writes:

$$l_d(\mathbf{Dw}, \mathbf{y}) = \sum_{j=1}^{n} \left((\mathbf{d}_j \mathbf{w}) \log \frac{(\mathbf{d}_{j,\bullet} \mathbf{w})}{y_j} + y_j - (\mathbf{d}_{j,\bullet} \mathbf{w}) \right) , \tag{3.29}$$

which is the *Kullback-Leibler cross-entropy* function from statistics. Adding the non-negativity constraint on the sought solution is necessary to ensure the definition of the $\log(\cdot)$ function on $\mathbb{R}_+^\star$.

3.5 Beyond (M)ART with Proximal Methods

Row-action methods have been at the core of the tomoPIV application since its inception, extensively used for their: *(i)* fast initial convergence towards a satisfying solution *(ii)* row-oriented architecture enabling parallelism for modern grid computations. The standard schemes of ART and MART come however with some limitations: *(i)* the solution is most often a function of the initialization point $\mathbf{w}^{(0)}$ *(ii)* the study of the convergence in a perturbed setting is still an open question *(iii)* the methods do not exploit the sparse structure of the sought solution. Our goal is to go towards methods for smooth optimization robust for noisy settings and allowing to incorporate different priors on the signal via regularization.

Our section is organized as follows. In section 3.5.1 we discuss gradient projection methods and variants for smooth optimization. In section 3.5.2 we focus on the application of such schemes to our application and we make some interesting connections between the former and standard algebraic schemes.

3.5.1 The Gradient Project Method (GPM) and Variants

The GPM is a well-known procedure, looking for a solution of

$$\min_{\mathbf{w} \in \mathcal{W}} f(\mathbf{w}), \tag{3.30}$$

where $\mathcal{W} \subset \mathbb{R}^m$ is a convex set and $f : \mathbb{R}^m \to \mathbb{R}$ is a continuously differentiable convex function. GPM is defined by the following recursion:

$$\mathbf{w}^{(k+1)} = \Pi_{\mathcal{W}} \left(\mathbf{w}^{(k)} - \alpha^{(k)} \nabla f(\mathbf{w}^{(k)}) \right), \tag{3.31}$$

where $\alpha^{(k)} > 0$ is some step factor, $\nabla f(\mathbf{w}^{(k)})$ denotes the gradient of $f(\mathbf{w})$ evaluated at $\mathbf{w}^{(k)}$ and $\Pi_{\mathcal{W}}(\mathbf{v})$ is the Euclidean (orthogonal) projection of $\mathbf{v}$ onto $\mathcal{W}$ (see section 3.2).

Several variants and extensions of GPM have been proposed in the literature. We present two of them hereafter: the "nonlinear gradient projected method" [23] and the "proximal gradient method" [136].

The Nonlinear GPM

The nonlinear GPM is motivated by the fact that the standard GPM step (3.31) can also be expressed as

$$\mathbf{w}^{(k+1)} = \arg\min_{\mathbf{w} \in \mathcal{W}} \left\{ \nabla f(\mathbf{w}^{(k)})^T \mathbf{w} + \frac{1}{2\alpha^{(k)}} \|\mathbf{w} - \mathbf{w}^{(k)}\|_2^2 \right\}.$$

The argument in the right-hand side can be understood as a linear approximation of $f(\mathbf{w})$ around $\mathbf{w}^{(k)}$, penalized by a "proximity term" $\frac{1}{2\alpha^{(k)}} \|\mathbf{w} - \mathbf{w}^{(k)}\|_2^2$. Based on this observation, Beck and Teboulle proposed a "nonlinear GPM" in [23], relying on different proximity terms. More specifically, the recursion of the nonlinear GPM reads

$$\mathbf{w}^{(k+1)} = \arg\min_{\mathbf{w} \in \mathcal{W}} \left\{ \nabla f(\mathbf{w}^{(k)})^T \mathbf{w} + \frac{1}{\alpha^{(k)}} \mathrm{D}(\mathbf{w}, \mathbf{w}^{(k)}) \right\}, \tag{3.32}$$

where $\mathrm{D}(\mathbf{u}, \mathbf{v}) : \mathbb{R}^m \times \mathbb{R}^m \to \mathbb{R}_+$ is a Bregman distance [36]. The use of a different proximity distance can lead to easier update steps, with possibly closed-form solutions.

The Proximal Gradient Method (PGM)

Another extension of GPM is the so-called PGM [136]. This type of methodology focuses on optimization problems of the form:

$$\min_{\mathbf{w}} f(\mathbf{w}) + g(\mathbf{w}), \tag{3.33}$$

where $f : \mathbb{R}^m \to \mathbb{R}$ and $g : \mathbb{R}^m \to \mathbb{R}$ are closed, proper, convex and f is differentiable. The recursion defined by the proximal gradient algorithm reads as

$$\mathbf{w}^{(k+1)} = \mathrm{prox}_g(\mathbf{w}^{(k)} - \alpha^{(k)} \nabla f(\mathbf{w}^{(k)})), \tag{3.34}$$

where $\mathrm{prox}_g(\cdot)$ is the proximal operator of g, see Appendix E. The proximal operator can be evaluated very efficiently in a number of situations, depending on the nature of $g(\mathbf{w})$.

The PGMs have recently sparked a surge of interest, mainly because these procedures enable to efficiently handle non-smooth optimization problems. In particular, we can easily constraint the solution to be **sparse** and/or **non-negative** by making appropriate choices of non-differentiable functions. To this effect, we provide the closed-form expressions of prox_g for the choices $g(\mathbf{w}) = \|\mathbf{w}\|_1$, $g(\mathbf{w}) = \mathbb{I}_{\mathbb{R}_+^m}(\mathbf{w})$ and $g(\mathbf{w}) = \mathbf{1}^T\mathbf{w} + \mathbb{I}_{\mathbb{R}_+^m}(\mathbf{w})$ in Appendix E. It can also be noticed that the proximal gradient algorithm encompasses the (standard) GPM as a particular case. More specifically, (3.34) reduces to (3.31) as soon as $g(\mathbf{w}) = \mathbb{I}_{\mathcal{W}}(\mathbf{w})$.

In this next section, we will apply this type of methodologies to problem of the form (3.18) and (3.19).

On Some Convergence Tactics

The standard GPM, nonlinear GPM and PGM enjoy the same type of convergence properties. They all converge to a minimizer of the considered problem provided that the step factors $\alpha^{(k)}$ are properly chosen. We refer the reader to [23, 27, 136] for a discussion on this topic. The three procedures also exhibit a speed of convergence scaling as [3] $\mathcal{O}(k^{-1})$ provided that f obeys some mild regularity conditions (more precisely, f should have a Lipschitz-continuous gradient) [177].

In a series of works (see, for a compiled review [177] and reference therein), Nesterov showed that this rate of convergence can be improved up to $\mathcal{O}(k^{-2})$ by combining the standard updates (3.31), (3.32) or (3.34), with proper interpolation steps. The latter steps being of negligeable complexity, the resulting procedures keep the same computational burden per iteration while improving significatively the number of iterations required to reach a given accuracy. As an example, we provide below the acceleration scheme of the PGM employed in [24], which corresponds to *Nesterov's* 'first method' [132]:

$$\begin{aligned} \mathbf{z}^{(k+1)} &= \mathbf{w}^{(k)} + \omega^{(k)}(\mathbf{w}^{(k)} - \mathbf{w}^{(k-1)}) \\ \mathbf{w}^{(k+1)} &= \text{prox}_g(\mathbf{z}^{(k+1)} - \alpha^{(k)}\nabla f(\mathbf{z}^{(k+1)})) \end{aligned} \tag{3.35}$$

with $\omega^{(k)} \in [0, 1)$. Clearly, the accelerated update (3.35) is similar to (3.34), with a simple interpolation step (*i.e.*, the evaluation of $\mathbf{z}^{(k+1)}$) carried out before applying the proximal operator. We note that interpolation only involves additions and scalar multiplications, leading to a negligible computational overhead.

It was shown in [132] that the resulting gradient method with convergence rate $\mathcal{O}(k^{-2})$ is an "optimal" first order method for smooth problems. Strictly speaking, these methodologies can also be applied to non-convex problems. In this case, however, the general convergence properties mentioned above do not necessarily hold.

A similar tactic combined with the classic PGM has been developed by *Birgin et al.* in [30]. The algorithm, coined "Spectral Projected Gradient", accelerates the descent rates

3. More precisely, the sequences $\{\mathbf{w}^{(k)}\}$ generated by these procedures are such that $\big(f(\mathbf{w}^{(k)}) - \min_{\mathbf{w}} f(\mathbf{w})\big) \leq C_f k^{-1}$, where C_f is some constant depending on the regularity of f.

by a spectral gradient choice of steplength, method proposed by *Barzalai et Borwein* in [21].

3.5.2 PGM Applied to Tomo-PIV Problem (3.18)

In this section, we focus on the application of PGMs on problem (3.18). We emphasize some connections existing between this framework and some standard algorithms. From these observations, we point out that their speed of convergence can be improved by using Nesterov's acceleration schemes (see section 3.5.1).

Letting $f(\mathbf{w}) = l_d(\mathbf{y}, \mathbf{D}\mathbf{w})$ and $g(\mathbf{w}) = rl_r(\mathbf{w})$, PGM recursion (3.34) particularized to problem (3.18) takes the form:

$$\mathbf{w}^{(k+1)} = \text{prox}_{rl_r}\left(\mathbf{w}^{(k)} - \alpha^{(k)}\nabla l_d(\mathbf{y}, \mathbf{D}\mathbf{w}^{(k)})\right) \tag{3.36}$$

with $\nabla l_d(\mathbf{y}, \mathbf{D}\mathbf{w}) = -\mathbf{D}^T(\mathbf{y} - \mathbf{D}\mathbf{w})$ for $l_d(\mathbf{y}, \mathbf{D}\mathbf{w}) = \frac{1}{2}\|\mathbf{y} - \mathbf{D}\mathbf{w}\|_2^2$ and the operator $\text{prox}_{rl_r}(\cdot)$ depends on the definition of $l_r(\mathbf{w})$. We remind the reader that the closed-form expressions of $\text{prox}_{rl_r}(\cdot)$ for $l_r(\mathbf{w})$ defined in (3.25)-(3.27) are provided in Appendix E.

Several standard tomoPIV algorithms can be regarded as particular instances of PGM for some choice of $l_d(\mathbf{y}, \mathbf{D}\mathbf{w})$ and $l_r(\mathbf{w})$. Let us first consider the case where $l_d(\mathbf{y}, \mathbf{D}\mathbf{w}) = \frac{1}{2}\|\mathbf{y} - \mathbf{D}\mathbf{w}\|_2^2$ and $l_r(\mathbf{w}) = 1$. This choice corresponds to searching for a solution of $\min_{\mathbf{w}} \|\mathbf{y} - \mathbf{D}\mathbf{w}\|_2^2$ without imposing any constraint of $\mathbf{w}$. In this case, the PGM recursion reduces to

$$\mathbf{w}^{(k+1)} = \mathbf{w}^{(k)} + \alpha^{(k)}\mathbf{D}^T(\mathbf{y} - \mathbf{D}\mathbf{w}^{(k)}). \tag{3.37}$$

Recursion (3.37) corresponds to a gradient step for minimizing $f(\mathbf{w}) = \frac{1}{2}\|\mathbf{y} - \mathbf{D}\mathbf{w}\|^2$ and is equivalent to SIRT with $\mathbf{W} = \mathbf{I}$ and $\mathbf{\Gamma} = \mathbf{I}$. In the same way, setting $l(\mathbf{y}, \mathbf{D}\mathbf{w}) = \frac{1}{2}\|\mathbf{y} - \mathbf{D}\mathbf{w}\|_2^2$ and $r(\mathbf{w}) = \mathbb{I}_{\mathbb{R}_+}(\mathbf{w})$, that is imposing positivity constraints on $\mathbf{w}$, we obtain

$$\mathbf{w}^{(k+1)} = \Pi_{\mathbb{R}_+^n}\left(\mathbf{w}^{(k)} + \alpha^{(k)}\mathbf{D}^T(\mathbf{y} - \mathbf{D}\mathbf{w}^{(k)})\right), \tag{3.38}$$

which is equivalent to SIRT+ for $\mathbf{W} = \mathbf{I}$ and $\mathbf{\Gamma} = \mathbf{I}$. Equivalence between SIRT/SIRT+ and PGM is also valid for $\mathbf{W} \neq \mathbf{I}$ and $\mathbf{\Gamma} \neq \mathbf{I}$ under some conditions; we do however not elaborate on this subject hereafter to keep the discussion as simple as possible.

Let us make two remarks. First, we see from (3.36) that SIRT/SIRT+ can be extended to account for the sparsity of the sought signal, without increasing the overall complexity of the procedure. Indeed, as shown in Appendix E, $\text{prox}_{rl_r}(\cdot)$ takes the form of a simple thresholding operator irrespective of the choice of $l_r(\mathbf{w})$ in (3.25), (3.26) or (3.27) (see (E.2), (E.3) and (E.4) respectively). The complexity of (3.36) is therefore dominated by the evaluation of the gradient $\nabla l_d(\mathbf{y}, \mathbf{D}\mathbf{w})$ and scales as $\mathcal{O}(mn)$. Hence, exploiting the sparsity of the sought signal does come at no extra cost.

Second, since SIRT and SIRT+ can be understood as PGM algorithms, they can be accelerated by using Nesterov's scheme, see section 3.5.1. More generally, the standard PGM recursion (3.36) can be accelerated as in (3.35) by using a interpolation step. We thus

obtain

$$\mathbf{z}^{(k+1)} = \mathbf{w}^{(k)} + \omega^{(k)}(\mathbf{w}^{(k)} - \mathbf{w}^{(k-1)}) \tag{3.39}$$

$$\mathbf{w}^{(k+1)} = \text{prox}_{rl_r}\left(\mathbf{z}^{(k+1)} - \alpha^{(k)}\nabla l_d(\mathbf{y}, \mathbf{D}\mathbf{z}^{(k+1)})\right) \tag{3.40}$$

with $\omega^{(k)} \in [0, 1)$. The acceleration depends on a proper choice of $\omega^{(k)}$. In our simulation, we set $\omega^{(k)} = \frac{k}{k+3}$ as suggested in [136, Section 4.3].

In [139], a SIRT method subject to sparsity constraints combined with stepsize selection of *Barzalai-Borwein* [21] was proposed and tested for a tomoPIV-"like" setting.

3.5.3 Nonlinear GPM Applied to Tomo-PIV Problem (3.19)

In this section we focus on problem (3.19). We consider an approach based on nonlinear GPMs. We thus consider the simpler problem: $\min_{\mathbf{w}\in\mathbb{R}^m_+} l_d(\mathbf{y}, \mathbf{D}\mathbf{w})$, that is the sparsity constraint "$\|\mathbf{w}\|_1 \leq a$" is not taken into account. Setting $f(\mathbf{w}) = l_d(\mathbf{y}, \mathbf{D}\mathbf{w})$, $\mathcal{W} = \mathbb{R}^m_+$ and considering the KL distance as a proximity operator in (3.32), the nonlinear GPM then reads:

$$\mathbf{w}^{(k+1)} = \arg\min_{\mathbf{w}\in\mathbb{R}^m_+}\{(\nabla l_d(\mathbf{y}, \mathbf{D}\mathbf{w}^{(k)}))^T\mathbf{w} + \frac{1}{\alpha^{(k)}}\text{KL}(\mathbf{w}, \mathbf{w}^{(k)})\}.$$

Using standard optimality conditions, the solution of this problem can also be expressed as

$$\mathbf{w}^{(k+1)} = \text{diag}(e^{-\alpha^{(k)}\nabla l(\mathbf{y}, \mathbf{D}\mathbf{w}^{(k)})})\,\mathbf{w}^{(k)}, \tag{3.41}$$

where $\text{diag}(\mathbf{v}) \in \mathbb{R}^{m\times m}$ is a square diagonal matrix with diagonal elements $\mathbf{v} \in \mathbb{R}^m$.

Update (3.41) can be seen as a general multiplicative rule where each element of the previous estimate $\mathbf{w}^{(k)}$ is multiplied by a factor depending on the gradient of the cost function $\nabla l_d(\mathbf{y}, \mathbf{D}\mathbf{w}^{(k)})$. Interestingly, if one considers the particular case $l_d(\mathbf{y}, \mathbf{D}\mathbf{w}) = \text{KL}(\mathbf{y}, \mathbf{D}\mathbf{w})$, (3.41) reduces to the SMART recursion defined in (3.13). SMART can therefore be understood as a particular instance of nonlinear GPM algorithm.

We make the remark that we can optionally consider problem (3.18) and apply a nonlinear GPM to access to its solution. For instance, by adding the sparsity constraints $l_r = \|\mathbf{w}\|_1$, the update rule simply writes:

$$\mathbf{w}^{(k+1)} = \text{diag}(e^{-\alpha^{(k)}(1+r)\nabla l(\mathbf{y}, \mathbf{D}\mathbf{w}^{(k)})})\,\mathbf{w}^{(k)}. \tag{3.42}$$

Finally, solving (3.18) with $l_r = \|\mathbf{w}\|_0$ reduces to solving iteration (3.41), combined with "hard thresholding", see equation (E.5) in Appendix E.

To conclude this section, let us emphasize that, because they belong to the families of nonlinear PGMs or PGMs, all the algorithms proposed above can also be accelerated by using Nesterov's methodology described at the end of section 3.5.1. We mention that, following this approach, an accelerated version of SMART has been proposed in [142].

3.6 Tomo-PIV Reconstruction based on the Alternating Direction Method of Multipliers

This section addresses the Alternating Direction Method of Multipliers (ADMM) theory, a modern signal processing tool to tackle convex optimization which relies on coordinated subproblems to solve the larger encompassing problem [34]. In particular, we depict, in section 3.6.1, that general ADMM framework. In section 3.6.2, we focus on a variant of the ADMM iterates to address the problem (3.17) and show its pertinence within for the tomoPIV problem.

3.6.1 Alternating Direction Method of Multipliers (ADMM)

The ADMM focuses on the following type of optimization problem:

$$\begin{aligned} &\min_{\mathbf{w}} f(\mathbf{w}) + g(\mathbf{z}) \\ &\text{subject to } \mathbf{A}\mathbf{w} + \mathbf{z} = 0 \end{aligned} \tag{3.43}$$

where $f : \mathbb{R}^m \to \mathbb{R}$, $g : \mathbb{R}^n \to \mathbb{R}$ are closed, proper and convex functions. The difference from the general equality constrained problem (3.17) is that variable $\mathbf{w}$ has been split into two part, here $\mathbf{w}$ and $\mathbf{z}$ with the objective function separable across the splitting. We note that the conditions on $f(\cdot)$ and $g(\cdot)$ are pretty mild; in particular, $f(\cdot)$ and $g(\cdot)$ are not required to be differentiable and can take on infinite values. For example, considering $f(\cdot)$ to be the indicator function of some convex set $\mathcal{W}$, that is $f(\mathbf{w}) = \mathbb{I}_{\mathcal{W}}(\mathbf{w})$, is a valid choice in the optimization framework presented hereafter.

ADMM is an iterative procedure searching for a minimizer of (3.43) via the following recursion:

$$\begin{aligned} \mathbf{w}^{(k+1)} &= \arg\min_{\mathbf{w}} f(\mathbf{w}) + \tfrac{\rho}{2}\|\mathbf{A}\mathbf{w} + \mathbf{z}^{(k)} + \mathbf{u}^{(k)}\|_2^2 \\ \mathbf{z}^{(k+1)} &= \arg\min_{\mathbf{z}} g(\mathbf{z}) + \tfrac{\rho}{2}\|\mathbf{A}\mathbf{w}^{(k+1)} + \mathbf{z} + \mathbf{u}^{(k)}\|_2^2 \\ \mathbf{u}^{(k+1)} &= \mathbf{u}^{(k)} + \mathbf{A}\mathbf{w}^{(k+1)} + \mathbf{z}^{(k+1)}, \end{aligned} \tag{3.44}$$

where $\rho > 0$ is a penalty parameter associated to the distance-like squared ℓ_2-norm and $\mathbf{u} \in \mathbb{R}^n$ is the dual variable of the *augmented Lagrangian* for problem (3.43). We refer the reader to the very good tutorial on ADMM [34] for an explanation of the rationale behind this type of methodology.

ADMM has recently sparked a surge of interest in the signal-processing community for several reasons. First, the conditions on $f(\cdot)$ and $g(\cdot)$ in (3.43) (*i.e.*, closed, proper and convex) are mild and (3.43) therefore encompasses a large number of optimization problems as particular cases. Second, the ADMM recursion (3.44) convergences to a solution of (3.43) under very general conditions, see [34, section 3.2]. Third, although ADMM is known to be slow to converge to a solution with high accuracy, it has been shown empirically that ADMM converges to modest accuracy in a few tens of iterations. Finally, the optimization problems involved in the updates of $\mathbf{w}^{(k+1)}$ and $\mathbf{z}^{(k+1)}$ in (3.43) admit very fast implementation or even closed-form solution in many setups; moreover ADMM is still ensured to converge if inexact minimizations are carried out in the $\mathbf{w}$ and $\mathbf{z}$ updates, see [68]. These two last features make

ADMM very appealing in large-scale problems where modest accuracy is often sufficient but computational load is of utmost importance.

3.6.2 Application to Tomo-PIV Problem (3.17)

In this section, we apply ADMM to the tomoPIV reconstruction problem. We focus on (3.17) with $l_d(\mathbf{y}, \mathbf{D}\mathbf{w}) = \|\mathbf{y} - \mathbf{D}\mathbf{w}\|_2$ and $l_r(\mathbf{w})$ defined as in (3.25), (3.26) or (3.27). Our derivations are inspired from the "C-SALSA" algorithm proposed in [7].

First, notice that (3.17) can equivalently be rewritten as

$$\min_{\mathbf{w},\mathbf{z}_1,\mathbf{z}_2} l_r(\mathbf{z}_1) + \mathbb{I}_{\mathcal{B}(\mathbf{y},\epsilon)}(\mathbf{z}_2) \quad \text{subject to} \begin{cases} \mathbf{z}_1 = \mathbf{w} \\ \mathbf{z}_2 = \mathbf{D}\mathbf{w} \end{cases}, \tag{3.45}$$

where $\mathcal{B}(\mathbf{y}, \epsilon) = \{\mathbf{v} \in \mathbb{R}^n \,|\, \|\mathbf{y} - \mathbf{v}\|_2 \leq \epsilon\}$ is the ℓ_2 ball of radius ϵ centered on $\mathbf{y}$. Letting $\mathbf{z} = [\mathbf{z}_1^T \mathbf{z}_2^T]^T \in \mathbb{R}^{n+m}$, one can then easily re-expressed (3.45) in the standard ADMM form (3.43) by considering the following substitutions:

$$\begin{aligned} f(\mathbf{w}) &= 1, \\ g(\mathbf{z}) &= l_r(\mathbf{z}_1) + \mathbb{I}_{\mathcal{B}_{(\mathbf{y},\epsilon)}}(\mathbf{z}_2), \\ \mathbf{A} &= -\begin{pmatrix} \mathbf{I}_n \\ \mathbf{D} \end{pmatrix}. \end{aligned} \tag{3.46}$$

Particularizing the ADMM update rules (3.44) to this particular setup, we obtain

$$\begin{aligned} \mathbf{w}^{(k+1)} &= \arg\min_{\mathbf{w}} \|\mathbf{w} - \mathbf{z}_1^{(k)} - \mathbf{u}_1^{(k)}\|_2^2 + \|\mathbf{D}\mathbf{w} - \mathbf{z}_2^{(k)} - \mathbf{u}_2^{(k)}\|_2^2 \\ \begin{cases} \mathbf{z}_1^{(k+1)} &= \mathrm{prox}_{\rho^{-1} l_r}(\mathbf{w}^{(k+1)} - \mathbf{u}_1^{(k)}) \\ \mathbf{z}_2^{(k+1)} &= \Pi_{\mathcal{B}(\mathbf{y},\epsilon)}(\mathbf{D}\mathbf{w}^{(k+1)} - \mathbf{u}_2^{(k)}) \end{cases} \\ \begin{cases} \mathbf{u}_1^{(k+1)} &= \mathbf{u}_1^{(k)} - \mathbf{w}^{(k+1)} + \mathbf{z}_1^{(k+1)} \\ \mathbf{u}_2^{(k+1)} &= \mathbf{u}_2^{(k)} - \mathbf{D}\mathbf{w}^{(k+1)} + \mathbf{z}_2^{(k+1)}. \end{cases} \end{aligned}$$

Let us briefly comment on the different steps of this recursion. The $\mathbf{w}$-update is equivalent to solving a least-square problem, whose closed-form solution is given by

$$(\mathbf{I}_n + \mathbf{D}^T\mathbf{D})^{-1}(\mathbf{z}_1^{(k)} + \mathbf{u}_1^{(k)} + \mathbf{D}^T(\mathbf{z}_2^{(k)} + \mathbf{u}_2^{(k)})). \tag{3.47}$$

We note that the inverse of $\mathbf{I}_n + \mathbf{D}^T\mathbf{D} \in \mathbb{R}^{m \times m}$ can also be expressed as

$$(\mathbf{I}_n + \mathbf{D}^T\mathbf{D})^{-1} = \mathbf{I}_n - \mathbf{D}(\mathbf{I}_n + \mathbf{D}\mathbf{D}^T)^{-1}\mathbf{D}^T, \tag{3.48}$$

which only requires the inversion of an $n \times n$ matrix. Moreover, the matrix to invert does not vary from iteration to iteration; one can therefore take benefit from a Cholesky factorization of $(\mathbf{I}_n + \mathbf{D}\mathbf{D}^T)^{-1}$ to evaluate (3.47) with a complexity scaling as $\mathcal{O}(nm + n^2)$, see [136, Section 6.1.1]. We note that this approach requires the storage of the (dense) $n \times n$ matrix of the Choleski decomposition. If such a storage resource is not available, the minimization appearing in the $\mathbf{w}$-update can also be approximated by a few steps of a conjugate-gradient method. This resulting procedure only requires the storage of

vectors of size n and has a complexity scaling as $\mathcal{O}(nm)$. This approach is valid because, as mentioned previously, ADMM with inexact minimization steps is ensured to converge [68].

The $\mathbf{z}$-update requires to apply some simple proximal and projection operators. The update of $\mathbf{z}_1$ rely on the proximal operators of (3.25), (3.26) or (3.27) (depending on the definition of $l_r(\mathbf{w})$). The implementation of these operators, defined in (E.2), (E.3) and (E.4), resorts to very simple element-wise thresholding operations. Their complexity thus scales as $\mathcal{O}(m)$.

The update of $\mathbf{z}_2$ requires the projection of $\mathbf{D}\mathbf{w}^{(k+1)} - \mathbf{u}_2^{(k)}$ onto the ℓ_2 ball $\mathcal{B}(\mathbf{y}, \epsilon)$. This projection operator has a simple closed-form expression, see [7, section 3]:

$$\Pi_{\mathcal{B}(\mathbf{y},\epsilon)}(\mathbf{v}) = \mathbf{y} + \begin{cases} \epsilon \frac{\mathbf{v}-\mathbf{y}}{\|\mathbf{v}-\mathbf{y}\|_2} & \text{if } \|\mathbf{v}-\mathbf{y}\|_2 > \epsilon \\ \mathbf{v}-\mathbf{y} & \text{if } \|\mathbf{v}-\mathbf{y}\|_2 \leq \epsilon \end{cases} \tag{3.49}$$

This operation can thus be performed with a complexity scaling as $\mathcal{O}(m)$.

Finally, the updates of $\mathbf{u}_1$ and $\mathbf{u}_2$ only involve simple vector additions. As a consequence, the overall complexity of the ADMM recursion is dominated by the $\mathbf{w}$-update and scales therefore as $\mathcal{O}(nm + n^2)$ (or $\mathcal{O}(nm)$ if a conjugate-gradient method is considered).

3.7 Other Computational Methods for Sparse Linear Solutions

In retrospect, we have addressed, in Section 3.3, the tomoPIV problem from the general viewpoint of standard (multiplicative) algebraic methods. In Section 3.5, we have migrated towards an optimization framework and shown how standard methods can be recast with proximal gradient methodology and constrained such that they enforce physical *a priori* (*i.e.*, non-negativity, sparsity) on the signal. Alongside these developments, we have introduced in the tomoPIV community the ADMM methods for smooth (sparsity constrained) optimization. We have mainly focused on the latter two categories to address problem (3.17) (and variants) with $l_r(\cdot)$ a function enforcing the sparsity of the signal. Due to their attractive computational/storage properties, convergence rates and "trendiness"; there are nevertheless myriads of other (precursor) algorithms to solve this problem.

The goal of this section is to survey some of the existing methods for the sake of completeness. Well encompassing reviews of algorithms seeking a sparse solution to a linear inverse problem can be found in [81, 176, 191]. To give a foretaste of the remainder of the section, **Greedy Pursuit** methods iteratively build up the sparse vector $\mathbf{w}$ by making a succession of locally-optimal decisions, **Convex Relaxation** methods, which encompass most of the methods depicted in the previous chapters, approximate a problem founded on the ℓ_0 norm by its corespondent expressed by ℓ_1 norm, **Nonconvex Optimization** methodologies relax the nonconvex ℓ_0 problem with another related nonconvex functional (typically a ℓ_p-norm, with $p < 1$, or smoothed counterparts of the ℓ_p-norms), and **Bayesian Algorithms** express the sparse representation problem as the solution of a Bayesian inference problem and apply statistical tools to solve it (see [98] for a review of

the state of the art techniques and novel contributions). We will insist, in the sequel, on the former three categories. Note that this classification does not entail disjoint sets of algorithms.

Greedy Pursuit

The pursuit algorithms, also known as greedy procedures, aim at solving problems of type P^0 with $l_r(\mathbf{w}) = \|\mathbf{w}\|_0$ (and variants - see section 3.4) by *(i)* updating the support vector of the sparse decomposition by selecting or deselecting elements of the support vector of the sought signal; *(ii)* making their decision with respect to local metrics, *i.e.*, leading to the highest decrease of their respective objective function. In a nutshell, one can distinguish between several approaches based on the update of the support vector: the *forward*, the *backward* and the *forward-backward* paradigms.

The first category updates the SR support by adding new atoms to the sparse basis. If classical Orthogonal Least Squares (OLS) [52], Matching Pursuit (MP) [120] and Orthogonal MP (OMP) [137] schemes select one atom per iteration, an enhancement has been brought to the latter procedures which enables the selections of more than one atom at once, see Stagewise Orthogonal MP (StOMP) [66]. Contrary to this method, the *backward* family (see [57]), submits an iterative procedure which starts from a support containing all the atoms and successively deselects the less pertinent ones. Its poor performance in the context of an under-determined dictionary makes it unsuitable within our application. The latter class, *i.e.*, the *forward-backward* family allows the selection and the deselection of new atoms. The implementation of these steps in an alternating rhythm allows the correction of possible errors: once we have selected (respectively, deselected) a false (respectively, correct) atom, it will still be possible to deselect (respectively, select) it. We mention the Subspace Pursuit (SP) [59], Compressed Sensing Matching Pursuit (CoSaMP) [131] and Single Best Replacement (SBR) [168] algorithms among the most notable.

With regard to their heuristic architecture, the guarantees of greedy algorithms to obtain a global optimum for a dictionary $\mathbf{D}$ are rather restrictive [175]. These procedures are however interesting for their simplicity and low complexity for relatively high performances in term of various quantifying metrics (energy recovery, detection rate, ...).

The performance of several greedy algorithms with respect to the algebraic state-of-the-art procedure have already been analyzed with regard to our application in [17, 55]. Moreover, proximal algorithms combined with hard-thresholding depicted in Section 3.5 joins the Iterative Hard Thresholding (IHT) procedure introduced in [32]. Numerical simulations for tomoPIV have showed that the sparsity maximization approach outperforms classical algebraic schemes with respect to accuracy in **certain operating regimes of interest**, that is for low-to-moderate seeding densities [18]. This empirical study joins the statements of the Compressed Sensing (CS) literature. In fact, as *Tropp et Wright* state in [176], the frontier between the performance of greedy versus more sophisticated optimization schemes is blurry.

Convex Relaxation

Another family of such algorithms approximates the ℓ_0-norm by the ℓ_1-norm in order to transform the initial problem, non-convex into a convex one, such that classical optimization schemes. Among other, proximal gradient method (and variants) constrained by a ℓ_1-norm (depicted in Section 3.5) can be cast to solve the convex relaxation problem. Let us briefly depict two of them.

A classical solution and one of the first considered to solve the ℓ_1 constrained problem is the "Interior Point Method". We refer the reader to tutorials that review the literature up to that point on the variations of the discussed paradigm [83, 152, 190] and to the early inception papers [109, 111, 122, 129]. In [154], the author applies a primal-dual interior-point scheme where the subproblems are formulated as linear least squares that can be solved simultaneously (see [35]) with iterative procedures. This methodology is somewhat reminiscent of the dual decomposition of the ADMM methodology. Implementations are available in SparseLab toolbox [64]. This first approach does not account for the non-negativity of the signal. To cope with this shortcoming, so-called barrier-log approaches have been developed. A generic formulation of the said procedure can be read in [191, Algorithm 1]. A barrier-log implementation of the primal-dual interior-point algorithm is available in the ℓ_1-magic package [42]. The algorithm requires $\mathcal{O}(\sqrt{m})$ iterations and each iteration can be executed in $\mathcal{O}(n^3)$ operations. In general, interior point methods are not competitive with upper-coming gradient methods.

Homotopy, also known as active set or pivoting have been proposed in [67, 70, 119, 135, 178]. This class of method exploit the fact that the objective function $l_d(\mathbf{Dw}, \mathbf{y}) + r l_r(\mathbf{w})$ undergoes an homotopy from the ℓ_2-ball to the ℓ_1-ball as r decreases. We define

$$\mathcal{X}_{path} \triangleq \{\mathbf{w}_r^\star | r \in [0, \infty)\}, \tag{3.50}$$

the solution path that follows the changes in r: when $r \to \infty$, $\mathbf{w}_r^\star = \mathbf{0}_m$; when $r \to 0$, $\mathbf{w}_r^\star$ converges to the solution of P^0 with $l_r(\mathbf{w}) = \|\mathbf{w}\|_1$. It was shown ([67, 70, 135]) that the solution path $\mathcal{X}_{path}$ is piece-wise constant as a function of r. The algorithmic scheme operates such that it identifies "breakpoints" leading to changes in the support set of $\mathbf{w}_r^\star$, *i.e.*, the nearest value of r at which the derivative of the piece-wise linear function changes. Thus, the homotopy method starts out at $\mathbf{w}_r^\star = 0$, and successively builds a sparse solution by adding or removing elements from its active set. Clearly, in a sparse setting, this approach is much more favorable than in a dense one, since, as long as the solution has few nonzeros, homotopy will reach the solution in a few steps. An implementation developed for the Least Absolute Shrinkage and Selection Operator (LASSO) problem is available in the SparseLab toolbox [64]. The latter requires, for a k-sparse vector, $2k$ matrix-vector multiplications to identify the k non-zeros in $\mathbf{w}_r^\star$ together with $\mathcal{O}(nk^2)$ for other algebraic operations. The cost is comparable with OMP. For sparse-enough solutions, the active set method is efficient.

The convex relaxation problem has been considered in a tomographic scenario in [19, 142, 145], displaying convincing results in terms of accuracy of approximation versus sparsity.

Nonconvex Optimization

Procedures addressing the nonconvex roblem P^0 with $l_r(\mathbf{w}) = \|\mathbf{w}\|_0$ require an often untractable combinatorial search. It is possible to replace the original ℓ_0-norm with its convex counterpart, that is, for example, the ℓ_1-norm, which renders equivalent solutions, under well defined conditions, see section 3.8. However, the ℓ_1-norm penalizes more heavily the larger coefficients than the smaller ones [44]. A "weighted" counterpart of the ℓ_0 minimization problem has been advanced in [44] to cope with this imbalance. This ploy is meant to mimic minimizing the ℓ_p-norm on the signal, where $p < 1$. We seek to solve the following problem:

$$\min_{\mathbf{w}} \|\mathbf{P}\mathbf{w}\|_1 \text{ such that } \mathbf{D}\mathbf{w} = \mathbf{y}, \tag{3.51}$$

where $\mathbf{P}$ is the diagonal matrix with weights $p_j \in \mathbb{R}_+^\star, \forall j \in \{1, \ldots, m\}$ on the diagonal. The algorithm proposed in [44] casts the so-formalized problem as a linear program, where the weights are computed, for each iteration l, as follows:

$$p_j^{l+1} = \frac{1}{|w_j^{(l)}| + \varepsilon_w}, \forall j \in \{1, \ldots, m\}, \tag{3.52}$$

where ε_w should be slightly smaller than the expected non-zero magnitude of $w_j^{(0)}$.

We mention that we have paired the above technique with the proximal gradient methods previously described and extensively tested it in our assessment campaign. The results have not been satisfactory enough to make it to the manuscript, as no real gain came out ahead of the ℓ_1 constrained algorithms. We believe this unsoundness may be caused by the high dependency of the computation of the weights on the tuning parameter ε_w (refer to equation (3.52)). As it turns out, in the context of our application, this procedure is not robust to the choice of ε_w.

3.8 Guarantees Related to the ℓ_0- and ℓ_1-norms

Since the solution of (P^0) with $l_r(\mathbf{w}) = \|\mathbf{w}\|_1$ is sparse and thanks to the the convexity of the minimized ℓ_1-norm, it turns out that the optimization problem minimizing (3.25) is much easier to solve than the problem minimizing (3.23) and it represents an interesting counterpart for problems minimizing the ℓ_p-norm, $\forall p > 1$, which minimize a convex norm, but result in denser estimations.

Recent studies focused on the theoretical study of conditions ensuring that problems (P^0) with $l_r(\mathbf{w}) = \|\mathbf{w}\|_p$, with $p \in [0, 1]$ have the same unique solution. Such theoretical recovery guarantees revolve around thresholds on critical parameters of problems, which relate the sparsity of the solution to the number of measurements and their properties. We will review, in this section, recent results from CS and their respective applications within the tomoPIV context.

First of all, let us distinguish between the two case studies approached in the related literature:

1. worst-case analysis: the deterministic study of conditions under which the unique

solution of (P^0) is recovered [71,89]; this is also known as the strong recovery scenario ;

2. average-case analysis: the study of conditions for unique recovery which hold, on average, with high probability; also known as the weak recovery case [65,66].

Analysis in CS recently shifted from 1. to 2. Following the same pattern, recovery analysis in tomoPIV followed the same track, trending from *strong recovery analysis* [144,148] to the study of *weak recovery conditions* [141,146]. We summarize in this section these results.

Conditions for the recovery of a sparse signal depend both on its sparsity and on the design of the dictionary. The signal retrieval performance can be decomposed in 3 sub-problems: *(i)* $\mathbf{w}^\star$ must be the unique minimum of (3.23); *(ii)* $\mathbf{w}^\star$ must be the unique minimum of (3.25), for $p = 1$; *(iii)* the equivalence of problems minimizing the ℓ_0- and ℓ_1-norms for $\mathbf{D}$ must hold. Conditions on $\mathbf{D}$ within the CS literature involve a high spark of the matrix, a small mutual coherence and a small Restricted Isometry Property (RIP) constant, as it will be detailed next.

Definition 3.1 ([63, Definition 1]). *Given an arbitrary matrix* $\mathbf{D} \in \mathbb{R}^{n\times m}$, $spark(\mathbf{D})$ *is the smallest possible number of linearly depended columns of* $\mathbf{D}$.

A $k-$sparse vector is defined such that $\|\mathbf{w}\|_0 = k$. As stated in [63, Theorem 8], any $k-$sparse solution of $\mathbf{Dw} = \mathbf{y}$ with $\|\mathbf{w}\|_0 < \frac{spark(\mathbf{D})}{2}$ is the unique solution of (P_0). Unfortunately, $spark(\mathbf{D})$ is Non-deterministic Polynomial-time hard (NP-hard) to compute.

The next result is based on a measure quantifying the similarities between the columns of a matrix.

Theorem 3.1 ([63, Theorem 7]). *Given an arbitrary matrix* $\mathbf{D} \in \mathbb{R}^{n\times m}$, *its mutual coherence writes:* $\mu(\mathbf{D}) = \max_{j\neq l} \frac{|\langle \mathbf{d}_{\bullet,l}, \mathbf{d}_{\bullet,j}\rangle|}{\|\mathbf{d}_{\bullet,l}\|\|\mathbf{d}_{\bullet,j}\|}$. *If*

$$\|\mathbf{w}\|_0 < \frac{1}{2}\left(1 + \frac{1}{\mu(\mathbf{D})}\right),$$

then $\mathbf{w}^\star$ *is the unique solution of* (P^0) *with* $l_r(\mathbf{w}) = \|\mathbf{w}\|_p$.

If $\mathbf{D}$ is an orthogonal dictionary (*i.e.*, $\|\mathbf{d}_{\bullet,j}\|_2 = 1, \forall j \in \mathcal{J}$, $\langle \mathbf{d}_{\bullet,j}, \mathbf{d}_{\bullet,l}\rangle = 0$ if $j \neq l$ and $n = m$), then $\mu(\mathbf{D}) = 0$. For $n < m$, we necessarily have $\mu(\mathbf{D}) > 0$. If two columns of the dictionary are alike, provided $\|\mathbf{d}_{\bullet,j}\|_2 = 1, \forall j \in \mathcal{J}$, we obtain $\mu(\mathbf{D}) = 1$. Such an occurrence induces confusion in the construction of a sparse representation of the measurement vector $\mathbf{y}$. In [38, Theorem 2], the non-negativity of the matrix entries is taken into account to study the bounds on the mutual coherence of $\mathbf{D}$.

The most popular condition for enabling stable recovery to date has been introduced by *Candés* in [43].

Definition 3.2 ([43, Definition 1.1]). *A matrix* $\mathbf{D}$ *has the Restricted Isometry Property* $RIP_{\iota,k}$ *if, for any* $k-$*sparse vector the relation*

$$(1-\iota)\|\mathbf{w}\|_2^2 \leq \|\mathbf{Dw}\|_2^2 \leq (1+\iota)\|\mathbf{w}\|_2^2, \forall \mathbf{w}, \tag{3.53}$$

holds, for some $\iota \in [0, 1)$.

Equation (3.53) implies that a matrix $\mathbf{D}$ cannot satisfy $RIP_{\iota,k}$ is $k > spark(\mathbf{D})$.

In [41], $RIP_{\iota,k}$ with $\iota < \sqrt{2} - 1$, then all $k-$sparse solutions $\mathbf{w}^\star$ of $\mathbf{Dw} = \mathbf{y}$ are unique and solve (P^0) with $l_r(\mathbf{w}) = \|\mathbf{w}\|_p$. See [41, Theorem 1.2] for the noisy counterpart of (3.1). It has been proved in [50] that bounds on binary matrices are even more restrictive. The latter proposition encourages us to compute matrix elements d_{ij} following (D.5) by using the largest number of subvoxels, within computational limits.

In [144], the latter properties of $\mathbf{D}$ have been analytically computed for a classic scenario of the tomoPIV application. Recovery bounds on $spark(\mathbf{D})$, on $\mu(\mathbf{D})$ and on $RIP_{\iota,k}$ are extremely pessimistic. A weaker form of equivalence has been studied by *Petra et al* (see [144, Section 5]), by exploiting the fact that the reduced feasible (to be formalized in a following section) might result in an overdetermined linear system whose underlying solution is obviously unique. The authors obtain a critical sparsity parameter k, which, for a binary matrix $\mathbf{D}$, writes:

$$k(N) \approx 4N^{0.342+0.011 \log N}, \tag{3.54}$$

where N is a size parameters, assuming the voxel space (respectively, the images) are cubic (respectively square) with $N^d, d \in \{2, 3\}$. Moreover, they prove that the expected performance equals the low particle densities used as a rule-of-thumb by engineers in tomoPIV.

3.9 Pruning

As seen throughout the chapter 3, the depicted algorithmic schemes have a complexity depending on the dimensions of the system $\mathbf{y} = \mathbf{Dw}$. Unfortunately, a common tomoPIV system casts around 10^6 measurements for at least 4 times more voxels, see section 2.2.3.4. An efficient technique to reduce these dimensions is to resort to a **pruning** procedure. As previously seen, the original 3D signal accounts for a limited number of scattering passive tracers with regard to the physical dimensions of the experimental volume. Therefore, we only need to reconstruct the non-zeros coefficients of the unknown vector. To do so, one can exploit the sparsity of $\mathbf{y}$ and $\mathbf{D}$ in order to determine *a priori* which coefficients in the sought vector are non-zeros. As a reminder, the sparsity of $\mathbf{D}$ is due to the nature of the discretization scheme; the latter has only a few non-zero coefficients as a result of a small number of basis function present to the cone-of-view corresponding to each pixel in the camera's image. This pattern engenders numerous zero-measurements y_i, $\forall i \in \{1, \ldots, n\}$. The problem has been already tackled in the literature. We overview below the main pruning techniques.

The standard procedure is common to all the state-of-the-art pruning. Let $\mathcal{G}$ define the feasible set of the solution to problem (3.3), that is:

$$\mathcal{G} \triangleq \{\mathbf{w} | \mathbf{Dw} = \mathbf{y}, w_j \geq 0\}. \tag{3.55}$$

We denote by $\mathcal{J} = \{1, \ldots, m\}$ the set containing the indexes of the voxels in $\mathcal{V}$. Analogically, we define by $\mathcal{I} = \{1, \ldots, n\}$ the set containing the indexes of the pixels. The

here-reviewed pruning procedures aim at partitioning the sets $\mathcal{I}$ and $\mathcal{J}$ into complementary subsets in the goal of discerning the lines and the columns that could be containing information. Let us introduce the nomenclature utilized in the sequel. For given sets $\mathcal{I}, \mathcal{J}$, matrix $\mathbf{D}_{\mathcal{I}\mathcal{J}}$ denotes the submatrix $\mathbf{D}$ with rows and columns indexed by $\mathcal{I}$ and $\mathcal{J}$, respectively. Analogically, $\mathbf{y}_{\mathcal{I}}$ denotes the subvector indexed by elements in $\mathcal{I}$. $\mathcal{I}^C$ stands for the complement of $\mathcal{I}$. Formally, we define the following partitions:

$$\mathcal{Y}^C \triangleq \{i \in \mathcal{I} | c_1\} \text{ and } \mathcal{Y} \triangleq \mathcal{I} \setminus \mathcal{Y}^C; \tag{3.56}$$

$$\mathcal{D}^C \triangleq \{j \in \mathcal{J} | c_2\} \text{ and } \mathcal{D} \triangleq \mathcal{J} \setminus \mathcal{D}^C, \tag{3.57}$$

where the constraints c_1, c_2 are crucial to the pruning procedure and characteristic of each one of the following methods.

The reduced feasible set finally writes:

$$\mathcal{G}_{red} \triangleq \{\mathbf{w}_{\mathcal{D}} | \mathbf{D}_{\mathcal{Y}\mathcal{D}}\mathbf{w}_{\mathcal{D}} = \mathbf{y}_{\mathcal{Y}}, w_j \geq 0\}. \tag{3.58}$$

Feasible Reduced Set (FRS)

The following developments have been introduced in [143] and enriched in [144]. *Petra et al.* exploit the sparsity of measurement vector $\mathbf{y}$ and that of the dictionary $\mathbf{D}$ in order to build up the reduced feasible set $\mathcal{G}_{red}$. In fact, they remove the equations with zero right-hand side by the setting the constraints c_1 and c_2 as follows:

$$c_1 : y_i = 0; \tag{3.59}$$

$$c_2 : \exists i \in \mathcal{Y}^C \text{ such that } d_{ij} > 0. \tag{3.60}$$

We reproduce here-below a very important remark:

Proposition 3.1. *[see [143, Prop. 1]] Let $\mathbf{D} \in \mathbb{R}^{n \times m}, \mathbf{y} \in \mathbb{R}^n$ have all non-negative entries and $\mathcal{G}, \mathcal{G}_{red}$ defined as in (3.55) and (3.58) respectively, where we plug in the constraints defined by equations defined by (3.59) and (3.60). Then*

$$\mathcal{G} = \{\mathbf{w} \in \mathbb{R}^m | \mathbf{w}_{\mathcal{D}^C} = 0 \text{ and } \mathbf{w}_{\mathcal{D}} \in \mathcal{G}_{red}\}. \tag{3.61}$$

The FRS approach implies that a particular measurement vector $\mathbf{y}$ induces the partitions $\mathcal{D}, \mathcal{D}^C, \mathcal{Y}, \mathcal{Y}^C$ and the correspondent, possibly overdetermined dictionary $\mathbf{D}_{\mathcal{Y}\mathcal{D}}$. Then, proposition 3.1 entails that the original feasible set is equivalent to the reduced set, provided the vector $\mathbf{w}_{\mathcal{D}}$ is padded by zeros, for all $j \in \mathcal{D}^C$.

Remark

For the following procedures, the constraint c_1 remains unchanged, thus the sets $\mathcal{Y}, \mathcal{Y}^C$.

Multiplicative Line of Sight (MLOS)

In [15], the authors arrive at a similar reduced set by redefining c_2 as follows:

$$c_2 : \prod_{c=1}^{N_c} \hat{y}^c \left(\mathcal{W}^c \left(\mathbf{k}^j \right) \right) = 0, \tag{3.62}$$

where $\mathcal{W}^c : \mathbb{R}^3 \rightarrow \mathbb{R}^2, \forall c \in \{1, \ldots, N_c\}$ is the projection function defined in section 2.1.5 by equation (2.17), $\mathbf{k}^j$ is the center of a voxel $\zeta^j \in \mathcal{V}, \forall j \in \mathcal{J}$ and $\hat{y}^c : \mathbb{R}^2 \rightarrow \mathbb{R}$ is a interpolation operator defined as follows:

$$\hat{y}^c(\mathbf{x}) = \sum_{i=1}^{n_1^c n_2^c} y_i^c p_i \left(\mathbf{x} \right), \forall \mathbf{x} \in \mathbb{R}^2, \tag{3.63}$$

where $p_i : \mathbb{R}^2 \rightarrow \mathbb{R}$ is an interpolation polynomial.

Additionally, Atkinson et Soria [15] propose an initialization scheme for the solution of the so-simplified system $\mathbf{D}_{\mathcal{Y}\mathcal{D}}\mathbf{w}_{\mathcal{D}} = \mathbf{y}_{\mathcal{Y}}$, that writes:

$$w_{\text{init},j} = \left[\prod_{c=1}^{N_c} \hat{y}^c \left(\mathcal{W}^c \left(\mathbf{k}^j \right) \right) \right]^{\frac{1}{N_c}}, \forall j \in \mathcal{D}. \tag{3.64}$$

Multiplicative First Guess (MFG)

In [188], the authors compute a novel reduced set based on the redefinition of the constraint c_2 as follows:

$$c_2 : \prod_{c=1}^{N_c} \left(\mathbf{d}_{\bullet,j}^c \right)^T \mathbf{y}^c = 0. \tag{3.65}$$

The proposed initialization scheme for the solution of the so-simplified system $\mathbf{D}_{\mathcal{Y}\mathcal{D}}\mathbf{w}_{\mathcal{D}} = \mathbf{y}_{\mathcal{Y}}$ is obtained by plugging the constraint (3.65) in equation (3.57) and writes:

$$w_{\text{init},j} = \left[\prod_{c=1}^{N_c} \left(\mathbf{d}_{\bullet,j}^c \right)^T \mathbf{y}^c \right]^{\frac{1}{N_c}}, \forall j \in \mathcal{D}. \tag{3.66}$$

The MLOS Local Maxima (LocM) Approach

More recently, *Cornic et al.* proposed a novel pruning scheme specific to the particle-based projection scheme formalized in [55] and in its companion paper [49]. In fact, they formalize a so-called MLOS function closely related to the MLOS pruning technique described here-above. The latter writes:

$$\text{MLOS}(\mathbf{k}) = \left[\prod_{c=1}^{N_c} \hat{y}^c \left(\mathcal{W}^c \left(\mathbf{k} \right) \right) \right]^{\frac{1}{N_c}}, \tag{3.67}$$

$\forall \mathbf{k} \in \mathbb{R}^3$. We recall that $\mathcal{W}^c(\cdot)$ is the projection function (see (2.17)) and $\hat{y}^c : \mathbb{R}^2 \to \mathbb{R}$ is a interpolation operator defined by equation (3.63).

Under the strong hypothesis that particles in $\mathcal{V}$ do not interact with each other, the authors show that the function MLOS($\mathbf{k}$) yields local maxima if $\mathbf{k}$ belongs to the vicinity of a particle. Based on the latter hypothesis, the authors redefine the feasible reduced set by setting the constraint c_2 by estimating the local maxima of the MLOS($\cdot$) function with morphological operators. Said otherwise, the set $\mathcal{D}$ is defined by the local maxima of the MLOS function. We mention that, in practice, the authors search for local maxima of a **thresholded** MLOS function.

Summary

We have presented, in the current section, procedures to reduce the dimension of the original system stated by (3.3). Among the cited paradigms, only the FRS approach guarantees a reduced feasible set equivalent to the initial problem (see the proof in [143]). As for the remaining procedures, there are not any theoretical guarantees that the corresponding reduced feasible sets contain all the columns in the $\mathbf{D}$ dictionary that have generated the original signal. We will assess the performance of these procedure in a comparative synthetic study in the experimental report and empirically show which one of the latter respects the original feasible set.

3.10 Assessement

This section aims of depicting our assessment campaign in order to validate the depicted procedures throughout the current chapter. First of all, we describe the settings of the visualizing system. Then, we define some functions quantifying the reconstruction quality. Finally, competitive results in sections 3.10.4 and 3.10.5 illustrate our previous claims. All our experiments are reproducible.

3.10.1 Synthetic Setting

Let us remind here that we have designed two models to depict the 3D-2D projection within a tomoPIV setting. The first one, *i.e.*, $\mathbf{y} = \mathbf{D}\mathbf{w}$, mimics the occurrence when the vector $\mathbf{w} \in \mathbb{R}^m$ collects the intensities of the Gaussian blobs present in the cuboid. The second model writes $\mathbf{y} = \mathbf{B}\mathbf{s}$, with $\mathbf{B} = \tilde{i}\mathbf{D}\mathbf{G}$, where the function $\tilde{i}(\cdot)$ depicts the incident laser light on the surface of the particles at each time frame and $\mathbf{s} \in \mathbb{R}^{\tilde{m}}$ is a binary vector accounting for the presence of a particle at a sub-voxel position in the refined cuboid. Naturally, the dictionary $\mathbf{G} \in \mathbb{R}^{n \times \tilde{m}}$, where $\tilde{m} = p^3 m$, encodes the interaction between a particle centered on a sub-voxel and its blob representation in the voxel space $\mathcal{V}$. Let $\widetilde{\mathbf{w}}$, respectively $\widetilde{\mathbf{s}}$ be the actual blob, respectively particle distributions, *i.e.*, the ground-truth. Let $\mathbf{y}$ be the actual observation vector. We can then estimate the blob densities, that we denote by $\mathbf{w}^\star$ or seek for the intensity distribution of the particles, that we denote by $\mathbf{s}^\star$. In the latter case, the blob distribution is obtained by $\mathbf{w}^\star = \tilde{i}\mathbf{G}\mathbf{s}^\star$. Let us note that, in the following experiments, the intensity scattered by the particles' centers is $\tilde{i} = 1$ and the Gaussian blobs have a variance $\sigma^2_{psf} = 0.8$. In the sequel, all of our results are averaged on

50 different experiments.

We consider an ill-posed problem inspired by the real-world application [74]. For doing so, we designate a cuboid partitioned into a cartesian grid of $61 \times 61 \times 31$ voxels, with voxel unit set at 1 arbitrary units (arb. u.). The origin of the scene frame is chosen in the center of the cuboid. We place 4 cameras around the scene of interest such that the volume's shape is visible on each sensor (see Appendix C); each camera has a CCD sensor of size 3×3 arb. u., for a 61×61 resolution and a 3.1098 arb. u. focal distance. The latter considerations give $\mathbf{D} \in \mathbb{R}^{14884 \times 70699}$ (which gives a ratio between the number of observations and the number of unknowns of $\frac{n}{m} = 0.2105$, which is close to the case depicted in [142], where the ratio was 0.25) and $\mathbf{B} \in \mathbb{R}^{14884 \times 565592}$, for $p = 2$ in the latter case (which generates the ratio $\frac{n}{\tilde{m}} = 0.0263$, close to the case study depicted in [55], where the ratio was of 0.0141).

The seeding density of the volume varies from 0.02365 to 0.4222 ppp, which corresponds to a maximal sparsity of $\|\widetilde{\mathbf{w}}\|_0 = 42417$ and of maximal $\|\widetilde{\mathbf{s}}\|_0 = 1571$, for the structured version of the model.

The test scenarios generated distinguish then by: *(i)* how we generate the volumetric distribution of the particles; *(ii)* how we decode; *(iii)* the noise level on the observation. That being said, we create three test cases, as follows:

Test Case 1 : The particles have been generated randomly at ideal positions in $\mathcal{R}$, *i.e.*, at the center of the subvoxels $\mathbf{x}^j, \forall j \in \mathcal{Z}$ (see section 2.2.3.3); we refer to **Test Case 1(a)** for $p = 1$ and to **Test Case 1(b)** for $p = 2$.

Test Case 2 : The particles have been generated randomly in $\mathcal{V}$. This means that the center of the particles are not longer (necessarily) located at the center of a (sub-)voxel, as considered by model $\mathbf{y} = \mathbf{Bs}$; as a consequence, there is **modeling** noise on our data. We refer to **Test Case 2(a)** for $p = 1$ and to **Test Case 2(b)** for $p = 2$.

Test Case 3 : The particles have been generated randomly in $\mathcal{V}$ and a Gaussian noise of variance 0.01 has been added to the observation vector $\mathbf{y}$; as a consequence, our system is corrupted by modeling and measuring noise. We refer to **Test Case 3(a)** for $p = 1$ and to **Test Case 3(b)** for $p = 2$.

All the tests presented in this article have been performed using a Matlab implementation of the algorithms. We have adapted our programs for grid computations and ran extensive tests on the **IGRIDA** computing grid nested at INRIA Rennes-Bretagne Atlantique.

3.10.2 Description of Evaluation Criteria

The quality of the pruning procedure and of the volume reconstruction is assessed by several means with respect to, usually, quantities describing the seeding concentrations in the volume.

On the Abscissa

One way of estimating the ppp inherent to the visualizing system has been described in [133]. Let $\breve{\mathbf{y}}^c$ be the filtered vector which is the output of a hard thresholding computation on the measurements collected by the camera image plane indexed by c, $\mathbf{y}^c$ such as:

$$\breve{\mathbf{y}}^c \doteq \left[\breve{y}_i^c\right]_{i\in\{1,\dots,n^c\}}^T = \left[y_i^c \mathbf{1}\{|y_i^c| > thr\}\right]_{i\in\{1,\dots,n^c\}}^T,$$

where $thr \in \mathbb{R}_+^\star$ is chosen with respect to the (guessed) actual seeding concentration. The ppp for the c^{th} camera is then estimated as:

$$\text{ppp}^c = \frac{\|\breve{\mathbf{y}}^c\|_0}{n^c}, \tag{3.68}$$

where $\|\breve{\mathbf{y}}^c\|_0$ counts the number of non-zero elements in $\breve{\mathbf{y}}^c$. In a synthetic setting, we can alternatively compute the ppp value as the ratio between the sparsity of the blob vector and the number of pixels in one image, provided all the sensors have the same intrinsic features.

From the signal processing viewpoint, we quantify the reconstruction accuracy with respect to the sparsity of the signal, *i.e.*, $\|\widetilde{\mathbf{w}}\|_0$ or $\|\widetilde{\mathbf{s}}\|_0$.

On the Ordinate

The quality of the reconstruction is classically assessed in the tomoPIV by means of the so-called *quality factor*. As it turns out, the latter operator simply computes the normalized correlation factor as writes:

$$Q = \frac{\widetilde{\mathbf{w}}^T}{\|\widetilde{\mathbf{w}}\|_2} \frac{\mathbf{w}^\star}{\|\mathbf{w}^\star\|_2} \tag{3.69}$$

Alternatively, we quantify the estimation quality in terms of the mean squared error, namely:

$$MSE = \frac{\|\widetilde{\mathbf{w}} - \mathbf{w}^\star\|_2^2}{\|\widetilde{\mathbf{w}}\|_0}. \tag{3.70}$$

Pattern Recognition Tools

We propose to introduce some known measures in pattern recognition and information retrieval. In fact, a "detection" is a True Positive (TP) if it coincides with the center of a true particle; a correct rejection of such a particle is a True Negative (TN). A detection is a False Positive (FP), *i.e.*, a ghost particle, if it does not coincide with the position of a true particle. A particle is considered as a False Negative (FN) if it is not detected. Furthermore, the True Positive Rate (TPR) quantifies the "sensitivity" of a system and writes:

$$\text{TPR} = \frac{\sharp\text{TP}}{\sharp\text{TP} + \sharp\text{FN}}, \tag{3.71}$$

where $\sharp$ stands for "number of".

The "miss rate" is assessed by the False Positive Rate (FPR) measure, that is:

$$\text{FPR} = \frac{\sharp\text{FP}}{\sharp\text{FP} + \sharp\text{TN}}. \tag{3.72}$$

The "precision" is assessed by the Positive Predictive Value (PPV) measure as writes:

$$\mathrm{PPV} = \frac{\sharp\mathrm{TP}}{\sharp\mathrm{TP} + \sharp\mathrm{FP}}. \tag{3.73}$$

In signal detection theory, a Receiver Operating Characteristic (ROC) curve, is a graphical plot which illustrates the performance of a binary classifier system as its discrimination threshold is varied. It is created by plotting the fraction of true positives out of the total actual positives (quantified by the TPR) versus the fraction of false positives out of the total actual negatives (measured by the FPR), at various threshold settings.

3.10.3 Nomenclature

Let us recap here the algorithms depicted throughout the current chapter and associate them with simple nomenclature.

The standard algebraic methods have been described in section 3.3. We will call ART the procedure that iterates following (3.6). The SIRT procedures are represented by Cimmino and SART (described under their general form by equation (3.8)). Their positivity constrained counterparts (see equation (3.10)) are coined ART+, Cimmino+ and SART+.

In the same section, we describe the multiplicative algebraic techniques which follow the same algorithmic scheme with the difference that they carry out projections with respect to the KL. We call MART the standard procedure, see equation (3.12), and SMART its simultaneous counterpart, see equation (3.13).

We present, in section 3.5, gradient projected methods (and variants) and show connections to the standard methods discussed here-above. In particular, in section 3.5.2, we focus on proximal variants of the algebraic methods. The proximal variant of SIRT is coined ISTA, see equation (3.37), in this manuscript to align our nomenclature with the current signal processing literature. Its positivity constrained counterpart is denoted by ISTA+ and described by equation (3.38). We can extend ISTA to account for the sparsity of the signal (see (3.36)); the proximal operator enabling this regularization are given, in Appedix E, for ISTAℓ_1 by (E.2), for ISTAℓ_1+ by (E.4), for ISTAℓ_0 by (E.5) (otherwise known in the signal processing community as the Iterative Hard-Thresholding technique) and for ISTAℓ_0+ by (E.6).

The ISTA algorithms can be accelerated by using Nesterov's scheme, see section 3.5.1. More generally, the standard PGM recursion (3.36) can be accelerated as in (3.35) by using a interpolation step. Then, the accelerated variants write: FISTA, FISTA+, FISTAℓ_1, FISTAℓ_1+, FISTAℓ_0, FISTAℓ_0+.

In section 3.5.3, the SMART iteration is expressed as a Nonlinear GPM iteration, see (3.41). Combined with thresholding, see Appendix E, we obtain SMARTℓ_0, SMARTℓ_1. We can accelerate the SMART scheme by Nesterov's methodology, resulting in the FSMART iteration. Equation (3.42) expresses its ℓ_1 regularized variant, coined FSMARTℓ_1, whereas FSMART combined with hard-thresholding gives us FSMARTℓ_0.

Finally, section 3.6 introduces us to the ADMM theory. We focus, in section 3.6.2, on applying the latter scheme to the the problem (3.17), otherwise known in the signal processing community as the Basis Pursuit Denoising (without non-negativity constraints). Depending on the definition of the regularizing function $l_r(\cdot)$, we denote the algorithmic schemes respectively by bpADMM+, bpADMMℓ_1, bpADMMℓ_1+, bpADMMℓ_0, bpADMMℓ_0+.

3.10.4 Pruning Assessement

Among the pruning procedures depicted in section 3.9, we can distinguish between two categories. On one hand, there are the binary classifiers which discriminate based upon a null threshold, *i.e.*, the FRS and the LocM techniques. On the other hand, the remaining techniques, *i.e.*, MLOS and MFG, usually build their respective reduced sets with a varying discriminating threshold. The values of the latter are however chosen empirically in the literature. The ROC curve depicted in Figure 3.3 traces the TPR with respect to the FPR computed at a varying thresholds for the MLOS and MFG procedures. We have computed, for comparison, the TPR against the FPR for the remaining procedures, namely the FRS and the LocM techniques. The curves depicted by Figure 3.3 repeat this process for values of ppp of 0.02365, 0.18973 and 0.4222.

The purpose of a good pruning technique is to eliminate as many as possible (ideally, all) columns that do not contribute to the image formation while retaining as many as possible (ideally, all) columns which have participated into building the observations. Only the FRS guarantees that no such "good column" will be excluded out of the reduced set. Figure 3.3 empirically proves this claim; indeed, regardless of the scenario, the FRS techniques always output a TPR equal to 1, while the FPR decreases with regard to the ppp value. Nevertheless, its FPR value is always inferior to those of the remaining techniques, when the latter have reached, for a given threshold, a TPR equal to 1. This implies that the FRS technique is the preferred choice in order to guarantee the lowest FPR rate for a reduced feasible set equivalent to the original one.

Figure 3.4 reveals, for varying ppp values, the PPV and TPR measures. For non-binary techniques (*i.e.*, MLOS and MFG), the measurements have been computed for the threshold minimizing the distance to the point $(\text{TPR} = 1, \text{FPR} = 0)$. The PPV curve, closer to 0 than to 1, gives a hint on the number of false detections. We remark the outstanding precision of the FRS technique for low to moderate values of ppp. The TPR curve is very close to 1, for the FRS and the LocM techniques (we disregard here the performance of the LocM technique for blob reconstruction because the procedure was not designed to perform well in the latter case). This translates into a very high hit rate.

Finally, Figures 3.5 and 3.6 give a visual flavor of the initial volume distributions estimated with the pruning techniques, computed for a ppp $= 0.1$ in a scenario corresponding to **Test Case 1(b)**. In fact, we have shown, in section 3.9, that initial intensity values are suggested by the authors for the elements belonging to the feasible reduced set. We refer to equation (3.64) for the MLOS procedure and to equation (3.66) for the MFG technique. Similarly, the initializing scheme given by (3.64) is employed for the LocM technique, but on a (generally) more restrained set than that corresponding to MLOS. We act in a

similar manner for the FRS technique and suggest to initialize its corresponding feasible reduced set by the values suggested by the MLOS scheme, that is by equation (3.64). The so-obtained volumetric distributions are depicted by Figure 3.6. Figures 3.6(a-d) depict the blob reconstruction, *i.e.*, we reconstruct directly $\mathbf{w}^\star$. We notice in particular that, while the FRS, MFG and MLOS output similar results, the LocM tends to prune less spurious particles; this result is in coherence with the procedure's architecture, which is meant to detect the peaks of the volumetric distribution and not blobs of aggregated particles. Figures 3.6(e-f) illustrate the blob formation through $\mathbf{w}^\star = \widetilde{i}\mathbf{G}\mathbf{s}^\star$; this implies that we seek to estimate the particle distribution corresponding to $\mathbf{s}^\star$. We notice especially that the FRS approach is notably adapted to this context, whose visual depiction is very similar to that of the original signal, see Figure 3.5.

Based on our analysis and bolstered by the visual depiction of Figure 3.6, we will focus in the sequel of our study on the pruning of our system with the FRS technique. Moreover, as the latter seems to be very effective when we seek to reconstruct the intensity of the particles (*i.e.*, we decode following the model $\mathbf{y} = \widetilde{i}\mathbf{D}\mathbf{G}\mathbf{s}$), see Figure 3.6(e), we will focus our attention on the reconstruction of the particles rather than the blob distribution.

We have addressed, in our pruning assessment section, mainly the **Test Case 1**. Note that we have conducted experiments for the other two test cases. Since the results inherent to **Test Case 2-3** are similar to those shown above (which lead us to the same conclusions), we have not shown them here to avoid redundancy.

3.10.5 Volume Reconstruction Assessement

We proceed to an extensive assessment campaign, for all test cases depicted above and for all the algorithms described throughout the chapter. We remind the reader that the nomenclature used to refer these algorithms in provided in section 3.10.3.

Let us first observe the behavior of our system in an ideal case. For doing so, we compute the *Oracle* curve against the seeding concentration of the volume. In a nutshell, the *Oracle* curve assumes that the vector support of the original tomoPIV signal is known and computes the least-square solution on the elements corresponding to this support. Figure (3.7) shows the performance of such a procedure, in the sense of the quality factor and of the mean-squared error, for the ideal **Test Case 1(a)**. In this case, we known there exist a solution to our system (3.1) and the latter technique obviously finds it, for each value of the ppp metric ranging from 0.02365 to 0.4222. We mention that, within this range, we always obtain an overdetermined dictionary, *i.e.*, the number of its columns (corresponding to the support of $\widetilde{\mathbf{w}}$) is always smaller than the number of observations. Running the algorithms depicted throughout the current chapter on the same ideal scenario will give us an idea of how our methods behave when dealing with an underdetermined dictionary, as we will see in the sequel.

First, let us analyse the features of our pruned system for the same range of ppp. We seek for the estimated volumetric distribution in the feasible reduced set defined by equations (3.59) and (3.60). This corresponds to the FRS technique, that we have chosen for its better performance compared to other state-of-the-art techniques (refer to previous

section for details). Figure 3.8 is destined to give an intuition on the reduced corresponding dictionaries, for all test cases. Notice how the problem is overly overdetermined for **Test Case 1-3(a)** for values of $\|\tilde{\mathbf{w}}\|_0$ going up until ≈ 7000 and for **Test Case 1-3(b)** for values of $\|\tilde{\mathbf{w}}\|_0$ reaching up to ≈ 3000.

We point out the the images have been generated using the scenarios described by the tests cases introduced in Section 3.10.1. As we mentioned before, regardless of the approach employed to generate the images, we always seek to reconstruct the particles' intensity distribution, meaning that we decode following the model $\mathbf{y} = \tilde{i}\mathbf{D}\mathbf{G}\tilde{\mathbf{s}}$. As a general rule, **Test Case ·(a)** implies that we seek the particles in a less refined space (for $p = 1$), whereas **Test Case ·(b)** entails that we seek for the particle distribution at a sub-voxelic accuracy (with $p = 2$). Concerning the image generation, **Test Case 1(·)** generates the images using the model $\mathbf{y} = \tilde{i}\mathbf{D}\mathbf{G}\tilde{\mathbf{s}}$, meaning that the particles are ideally placed in the center of the voxels (when $p = 1$, leading to **Test Case 1(a)**) or sub-voxels (when $p = 2$, leading to **Test Case 1(b)**). **Test Case 2(·)** generates the observations following the model $\mathbf{y} = \mathbf{D}\tilde{\mathbf{w}}$, implying that we will have **modeling noise** on our system when decoding with model $\mathbf{y} = \mathbf{B}\mathbf{s}$. **Test Case 3(·)** produces the observation following $\mathbf{y} = \mathbf{D}\tilde{\mathbf{w}} + \mathbf{n}$, where $\mathbf{n}$ is a Gaussian noise of variance 0.01 corrupting the images (due to calibration, approximation errors, measurements). We mention in advance that all of the following methods have been stopped after 120 iterations, for all test cases.

Let us now focus on **Test Case 1(a)** and give comparative results by classes of algorithms. Figure 3.9 reveals performance report for the algebraic algorithms (*i.e.*, ART, SART, Cimmino and their positivity-constrained variants). First of all, we observe that the positivity-constrained methods perform overly better than their unregulated counterparts in terms of quality of reconstruction and MSE. Secondly, we notice an undeniable superiority of ART against its compeers. Also, we notice a correlation between the moment when the dictionary becomes underdetermined (see Figure 3.8 (top row, left)) and the moment when the performance of all the algorithms start to degrade, at around ppp $= 0.1$. Let us point out that, in this ideal scenario where a solution to (3.2) exists, the latter methods converge to this solution. If the Cimmino and SART do not have the same end-point after the same number of iterations as ART, it is because the former have a slower convergence speed. We have not compared the converge behavior of the algebraic methods together, but Figure 3.19 (left) does give an order of contrast between ART and other methods belonging to different algorithm class. Finally, Figure 3.13 (top row) shows the computational burden of each algebraic algorithm against each other. Cimmino/Cimmino+ methods perform considerably faster; this is due to their Matlab implementation, see [91]. We will, from now on, retain ART for our future experiments, due to its better overall performance.

Figure 3.10 depicts the behavior of MART, SMART, SMARTℓ_0 and SMARTℓ_1 against their accelerated variants, that is FSMART, FSMARTℓ_0 and FSMARTℓ_1. First, we notice that the MART, SMART, SMARTℓ_0 and SMARTℓ_1 superimpose. As it turns out, MART and SMART solve the same problem, so they converge to the same end-point after 120 iterations. SMARTℓ_l solves $\mathbf{w}^\star = \arg\min_{\mathbf{w}} \mathrm{KL}(\mathbf{D}\mathbf{w}, \mathbf{y}) + r\,\|\mathbf{w}\|_l$, with $l \in \{0, 1\}$ and r a tuning parameter chosen with respect to each ppp value. Here, r ranges between 0.7 and 0.01: the higher the seeding concentration, the less we threshold. SMARTℓ_0 applies a hard-thresholding at each iteration on the coefficients computed by SMART; since SMART

and SMARTℓ_0 attain the same solution, it results that the latter does not eliminate coefficients belonging to the feasible set of the solution. SMARTℓ_1 solves a ℓ_1-constrained KL minimization problem, but it does converge to a similar solution as its unconstrained variants (with small differences at very low seeding values). Concerning the accelerated versions of SMART, we notice that the FSMART, FSMARTℓ_0 and FSMARTℓ_1 have a similar behavior. FSMART solves the same problem as SMART; the fact that it yields better reconstruction accuracy is due to the Nesterov's first method, which considerably enhances the convergence speed towards the solution. Figure 3.19(a), which depicts (among others) SMARTs and FSMARTs convergence rates, backs up our theoretical claims. Moreover, notice how the behavior of (S)MARTs is affected by the underdetermination of the decoding dictionary (around ppp $= 0.8$, see Figure 3.8 (top row, left), while FSMARTs' performance starts to decay for higher seeding values. As for the constrained variants of FSMART, we recall that the former solve the same problems as the constrained SMARTs, *i.e.*, $\mathbf{w}^\star = \arg\min_{\mathbf{w}} \mathrm{KL}(\mathbf{Dw}, \mathbf{y}) + r\,\|\mathbf{w}\|_l$, combined with the acceleration scheme, with r is chosen as here-above. We notice slight enhancement of FSMART combined with hard-thresholding (*i.e.*, FSMARTℓ_0). This implies that, at low seeding concentration, FSMARTℓ_0 successfully zeroes out spurious coefficients. FSMARTℓ_1 follows the path of its unconstrained variant, except for low-densities, where it seems to slightly degrade the accuracy of the reconstruction compared to FSMART; this is simply due to a poor choice of the r parameter, which is rather difficult to tune because it does not hold a clear physical underpinning. Computationally, all (F)SMARTs perform similarly, with the exception of MART, which attains prohibitive time, as expected, see Figure 3.13 (middle). As a sum-up, we retain that *(i)* Nesterov's first problem combined with the KL minimization problem yields significantly better reconstruction quality due to faster rates of convergence for the same computational burden; *(ii)* the ℓ_0 constrained (F)SMARTs reveal their interest in a low-seeding context; *(iii)* MART attains the same solution as its simultaneous compeers, but within a dramatically higher computational time; we can henceforth eliminate it for future experiments.

Figure 3.11 depicts the demeanor of proximal variants of the algebraic methods - (F)ISTA and counterparts - and that of the ADMM techniques. We recall that (F)ISTA algorithms solve problem (3.18) with r chosen varying between 0.7 and 0.01, inversely proportional to the sparsity of the signal, and functions $l_d(\mathbf{y}, \mathbf{Dw}) = \frac{1}{2}\|\mathbf{y} - \mathbf{Dw}\|_2^2$ and $l_r(\mathbf{w}) = 1$ (for ISTA/FISTA) or a function enforcing the sparsity for (ISTAℓ_l/FISTAℓ_l, with $l \in \{0, 1\}$). We can optionally encourage the latter schemes to constrain the positivity on the sought signal (*i.e.*, ISTA+(ℓ_l)/FISTA+(ℓ_l)). Let us also recall that FISTAs are an accelerated variant of ISTAs. Looking back at Figure 3.11, we first notice that ISTA+, ISTAℓ_1 and ISTAℓ_1+ are superimposed. This implies that, for this algorithmic scheme, constraining the original problem with positivity or sparsity does record a noticeable gain in performance. A similar behaviour can be observed for FISTA+, FISTAℓ_1 and FISTAℓ_1+. Notice that the threesome is generally superimposed, with slight differences observable for high densities on the Q curve and for low densities on the MSE curve, where FISTA+ outperforms its ℓ_1 constrained compeers. We recall that FISTAs are accelerated variants of ISTAs, which explains the performance enhancement in the same number of iterations. The ℓ_0 constrained variants of ISTAs have a rather heretical behavior; first of all, the corresponding problems are not convex and yield more restrictive guarantees of convergence toward a unique solution. Equivalently, accelerating ISTAℓ_0(+) with Nesterov's first scheme

does not uphold guarantees towards convergence. In practice, we average our results over 50 experiments. One or several bad recoveries can thus easily alter the averaged metric in a point, generating thus a wavering overall behavior for ISTAℓ_0, ISTAℓ_0+ and FISTAℓ_0, FISTAℓ_0+ (where the two latter are superimposed). The ADMMs solve the problem $\mathbf{w}^\star = \arg\min_{\mathbf{w}} l_r(\mathbf{w})$ such that $l_d(\mathbf{Dw}, \mathbf{y}) \leq \varepsilon$ with $l_d(\cdot)$ and $l_r(\cdot)$ defined as for ISTAs/FISTAs and $\varepsilon = \sigma_e^2 \|\widetilde{\mathbf{w}}\|_0$, where σ_e^2 is the variance of the noise reigning the data. Notice, on Figure 3.11, how bpADMM+, bpADMMℓ_1 and bpADMMℓ_1+ (which are superimposed) attain close-to-perfection performance. Although they solve a problem equivalent to that solved by the (F)ISTAs (in the convex case), notice on Figure 3.19 (left) that the ADMMs convergence rates are considerably faster than those of FISTAs (which are, theoretically faster than those of ISTAs). As for the $\ell_0(+)$ constrained ADMM, notice how the performance is competitive for moderate seeding values and only starts to degrade around ppp ≈ 1.2 for bpADMMℓ_0 and around ppp ≈ 1.65 for bpADMMℓ_0+. The latter observation also shows the gain of constraining the positivity on the signal for ADMMs, where bpADMMℓ_0+ convergences considerably faster than bpADMMℓ_0, see Figure 3.19 (left). As a recap, we retain that the performance of ISTAs are dramatically enhanced by the accelerating scheme leading to a more accurate reconstruction for a same number of observations (see procedures FISTAs on Figure 3.11). The ADMMs schemes for convex problems act almost flawlessly in this ideal scenario as they converge faster than proximal gradient methods. Computationally, we refer to Figure 3.13 which classifies between the ISTA/FISTA and the ADMM schemes. As we can see, the former are up to 6 times faster than the latter. This is in part due to the fact the our implementation uses a **LU** decomposition to solve a set of linear equations. Additionally, this step necessitates the storage of an $n \times n$ matrix. We point out that ADMMs complexity could be decreased by using a conjugate-gradient step instead.

Figure 3.12 recaps our previous comments. For the sake of conciseness, we have excluded from the said-figure solely the algorithms that do not hold much interest. For example, Cimmino and SART perform slightly worse than ART and the ISTAs is always out-performed by FISTAs. Going back to Figure 3.12, we notice that the ℓ_0 constrained algorithms generally behave poorly for moderate to high seeding densities. The SMARTs are outperformed by methods for convex optimization, *i.e.*, FISTAs, FSMARTs, and ADMMs. The order we mentioned them in is not chosen randomly, but to rank their performance from worse to best. We can see that the bpADMM class for convex optimization (*i.e.*, bpADMM+, bpADMMℓ_1 and bpADMMℓ_1+) preserves its competitive performance even for high seeding densities, whereas the runners-up, *i.e.*, the FSMART and FISTA, "break" at high-to-moderate ppp, that is around 0.15. For these last classes of methods, unsurprisingly, the convergence speed acts similarity, making the ADMMs for convex optimization the faster-decay convergence rate algorithm within unperturbed settings.

In the sequel of our study, we will henceforth focus on the algorithms which have performed best in the previous scenario and will restrain the values of the ppp to 0.12, which is closer to real-world applications. Figure 3.14 reiterates the former study with the difference that the particles are sought in a more refined volumetric space (refer to the description of **Test Case 1(b)** for details). We notice in particular how the ADMM methods for convex optimization predominantly outperform the FSMARTs class. As in the first case scenario, the ℓ_0 constrained algorithms act rather poorly for moderate-to-high

seeding density. Standard state-of-the-art algorithms ART+ and SMART are surpassed by their proximal variants, *i.e.*, FISTA+ and FSMART, respectively. Figure 3.12 (right) shows the convergence rates of the chosen algorithms. As it turns out, the ADMMs for convex optimization decay faster than their concurrent, *i.e.*, the FSMARTs.

We mention that, for the sequel of our study, we have excluded the ART, as it performs similarly to (F)ISTA, but at a very elevated computational price. Similar remarks as those made for **Test Case 1(a-b)** stand for figures depicting the behavior of the algorithms in remaining test cases. As a reminder, **Test Case 2(a-b)** adds noise to the particles' positions. In fact, in contrast to **Test Case 1(a-b)**, where the particles have been ideally placed at the center of the (sub-)voxels, in **Test Case 2(a-b)** we generate the particles' positions randomly in the cuboid. This generates **modeling** noise in our system. This perturbation reflects strongly in **Test Case 2(a)** - see Figure 3.15. In fact, none of the algorithms reach a perfect quality reconstruction, in contrast to Figure 3.12, where bpADMM+, for example, maintained a very small gap to $Q = 1$, even for high seeding densities. Here, FSMARTs tend to slightly outperform the bpADMMs for convex optimization. Figure 3.20 (left) shows the convergence rate for the chosen algorithms, for $\mathrm{ppp} = 0.0758$. Apart from the behavior of algorithms for convex optimization which act in accordance to the theory (and to the previous scenario) and sustain the performance in terms of MSE seen on Figure 3.15, we observe peculiar demeanor of ℓ_0 constrained algorithms, which are either stagnate or increasing the MSE between the iterates and the ground truth. This conduct reflects on their performance in Figure 3.15. We notice an effect of semi-convergence for bpADMMℓ_1; in contrast, bpADMMℓ_1+'s convergence decays normally. This implies that constraining the positivity on bpADMMℓ_1 improves to a certain degree the reconstruction. This modeling noise reflects less in **Test Case 2(b)** - see Figure 3.16. This is explained by the fact the placing **randomly** the particles in a much more **refined** grid decreases the standard deviation of the latter with respect to the voxel centers and thus diminishes the overal **modeling** noise. Thus, the performance of the algorithms in **Test Case 2(b)** is closely related to that of the algorithms in **Test Case 1(b)**. We notice thought that bpADMM for convex optimization tends to degrade in comparison to its behavior in the ideal **Test Case 1(b)**. This lets us to believe that the latter is less robust to noisy schemes than the FSMARTs. We can refer to Figure 3.20(right) in order to observe their respective convergence rates. We notice that even if bpADMM for convex optimization and FSMARTs attain the same solution, the former seems to decay faster. Thus, we can stop the computations after only 40 iterations.

Test Case 3(a-b) appends, in addition to the volumetric noise, some perturbing artefacts on the observations (refer to the description of **Test Case 3(a-b)** for details). The latter case scenarios are meant to give a flavor of the behavior of the algorithms in a real-world setting. We remark that the observation noise does not alter in particular the behavior of the algorithms in comparison to **Test Case 2(a-b)**. That being said, observations made about **Test Case 2(a-b)** can be transferred when dealing with **Test Case 3(a-b)**: differing performance of the ℓ_0 constrained algorithms, overall very good performance of bpADMM for convex optimization and FSMARTs, which routinely outperform state-of-the-art SMARTs and FISTAs, the **modeling** noise - more important **Test Case 3(a)** - alters more severely the performance of algorithms in contrast to that in **Test Case 3(b)**, which barely affects them. Same observations stand for the convergence study, see Figure 3.21. In this

study, it turns out that the **modeling** noise may alter more seriously the accuracy of the estimations than noise corrupting the 2D images (coming from measuring, approximations errors, calibration). This latter remark strongly suggests that a refined volumetric grid is suitable for the tomoPIV setting. However, we keep in mind that the noise variance on the observation chosen for out setting might be slightly lower than that on the noise affecting real 2D observations from a tomoPIV setting.

3.11 Summary

In this chapter, we have gone beyond standard procedures used in tomoPIV by recasting the tomoPIV problem within a general optimization framework. In particular, we have shown that physical constraints can be properly handled by defining an adequate optimization problem. Then, we have made some interesting connections between standard methods and the proximal methods by showing that the former are particular cases of the latter. Finally, we have introduced to the tomoPIV community the ADMM methods that outperform in most cases state-of-the-art procedures.

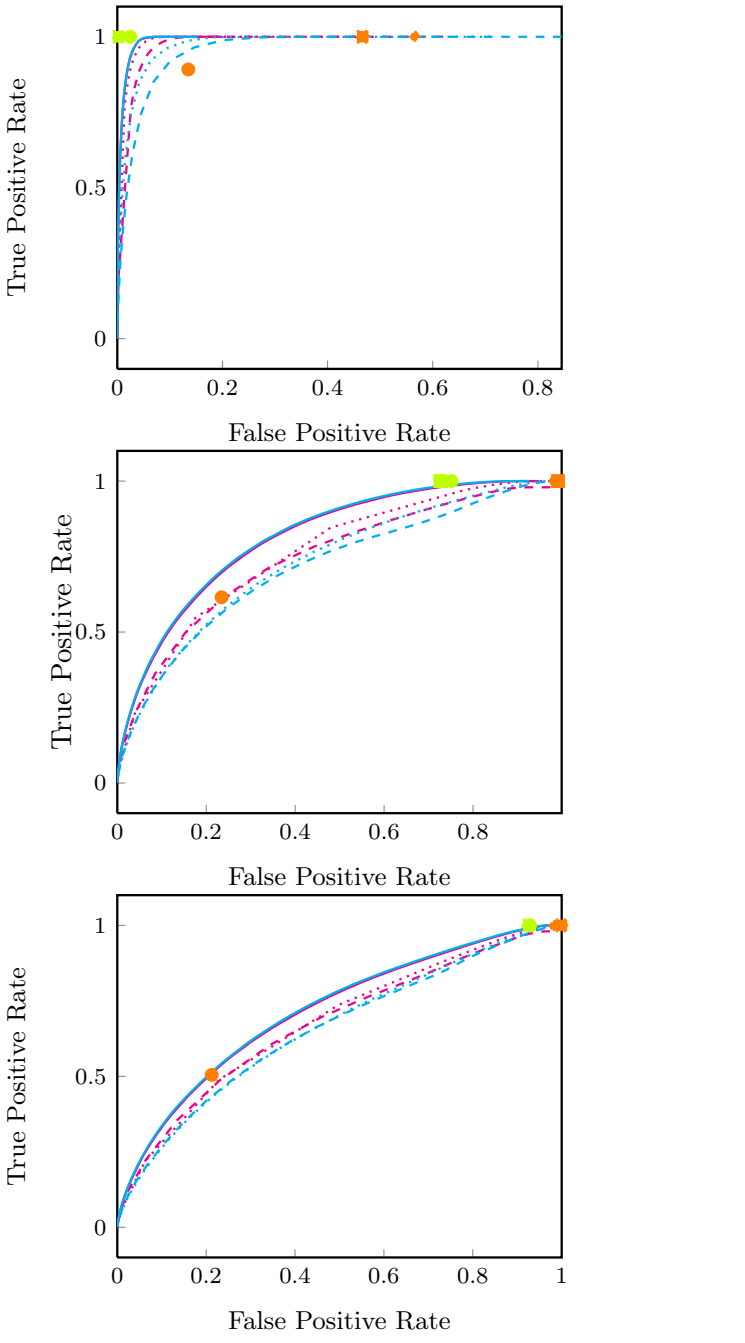

Figure 3.3: Roc curve for the pruning procedures for **Test Case 1(a-b)**. When the name of the procedure is prefixed by "blobs", we estimate the initial blob distribution $\mathbf{w}^\star$; alternatively, when the name of the procedure is prefixed by "PSF", we estimate $\mathbf{s}^\star$ and compute $\mathbf{w}^\star = \tilde{i}\mathbf{G}\mathbf{s}^\star$. From up downwards, the ppp value is 0.02365, 0.18973 and 0.4222.

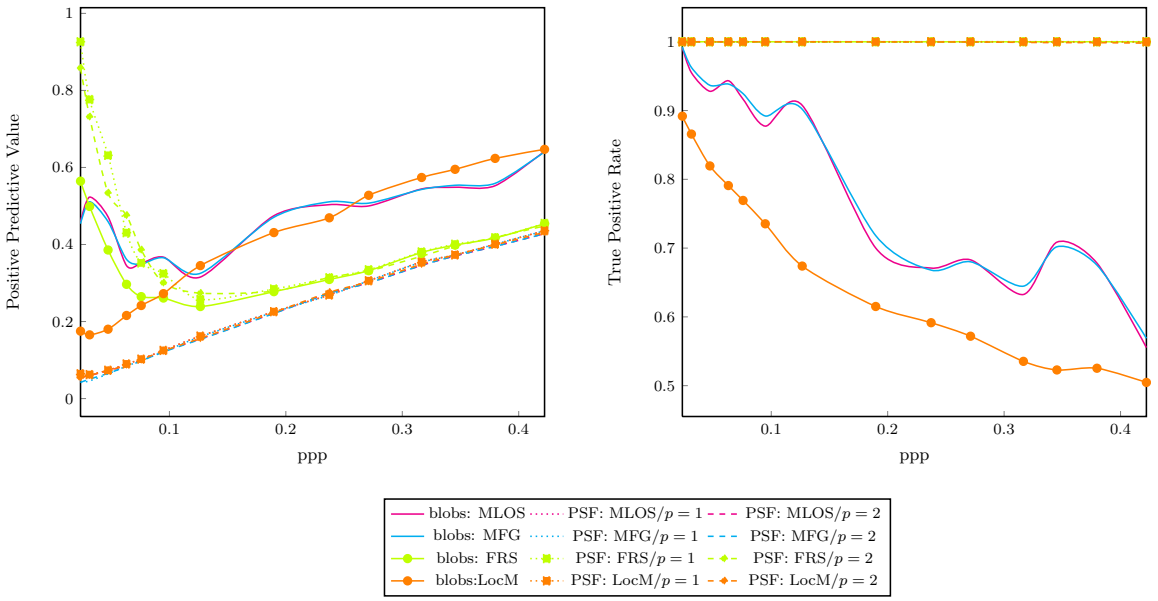

Figure 3.4: PPV/TPR curves for the pruning procedures for **Test Case 1(a-b)**. The same nomenclature conventions as for those used in Figure 3.3 stand. Here, the ppp values evolve from 0.02365 to 0.4222.

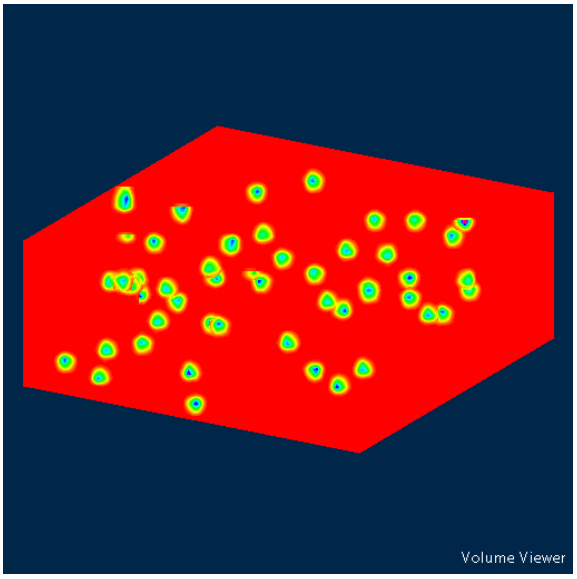

Figure 3.5: Original ideal distribution; the particles have been generated at ideal positions in $\mathcal{R}$, *i.e.*, at the center of the subvoxels $\mathbf{x}^j, \forall j \in \mathcal{Z}$.

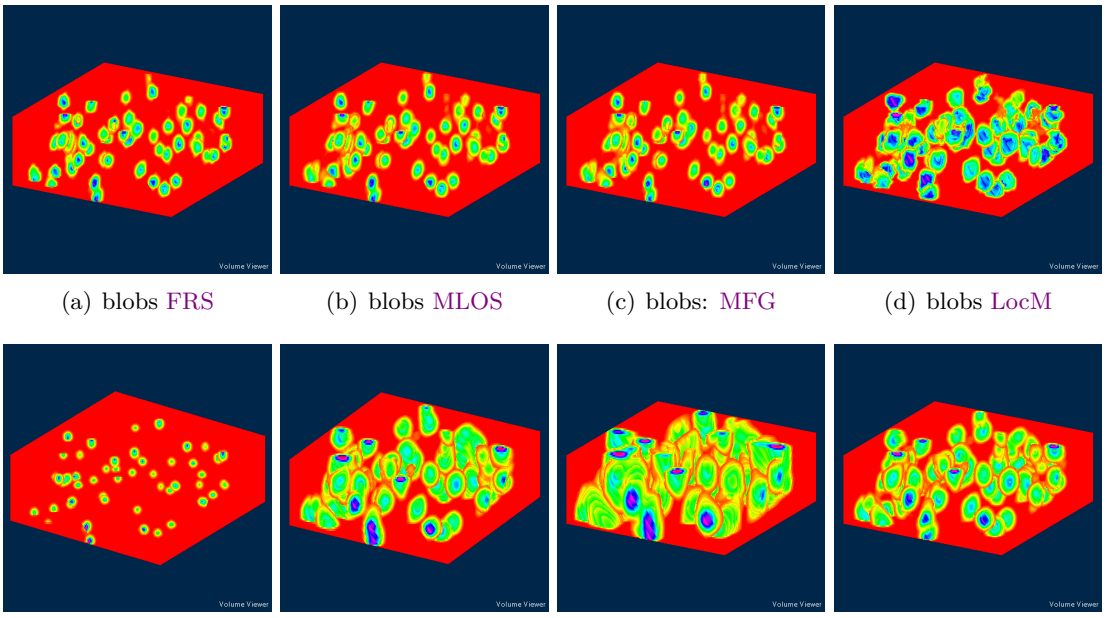

(a) blobs FRS (b) blobs MLOS (c) blobs: MFG (d) blobs LocM

(e) PSF FRS, $p = 2$ (f) PSF MLOS, $p = 2$ (g) PSF MFG, $p = 2$ (h) PSF LocM, $p = 2$

Figure 3.6: Estimated ideal distribution. The pruned volumetric densities (a)-(d) have been estimated following the model stated by equation (3.1), while the pruned volumetric densities (e)-(h) have been decoded following the model in equation (3.2), with the $\mathcal{R}$-space discretization parameter $p = 2$.

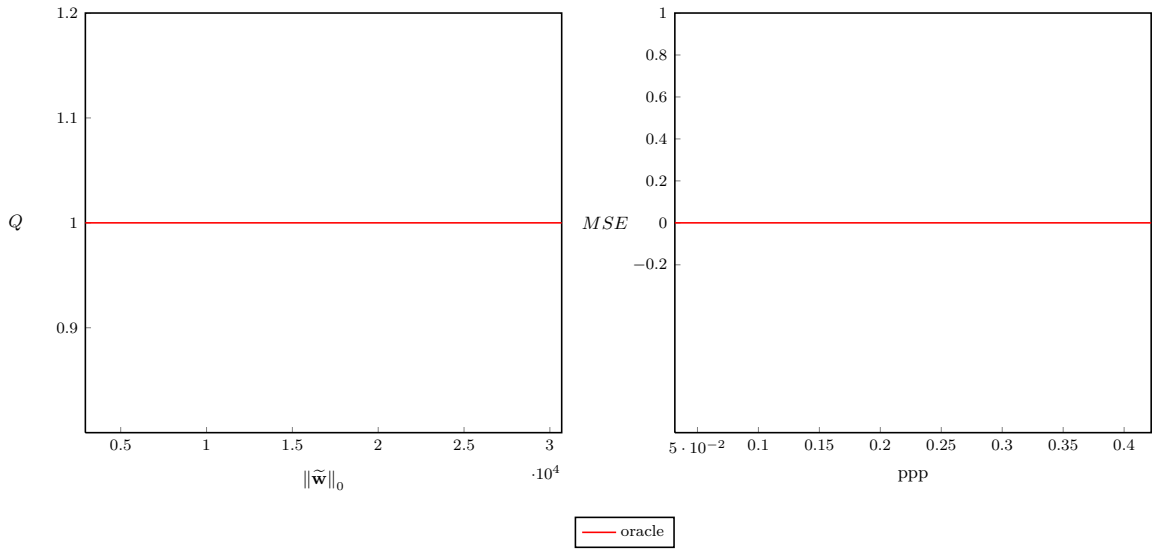

Figure 3.7: Oracle curve for **Test Case 1(a)**. Left: Quality factor with respect to the sparsity of the signal. Right: Mean squared error with respect to the ppp number.

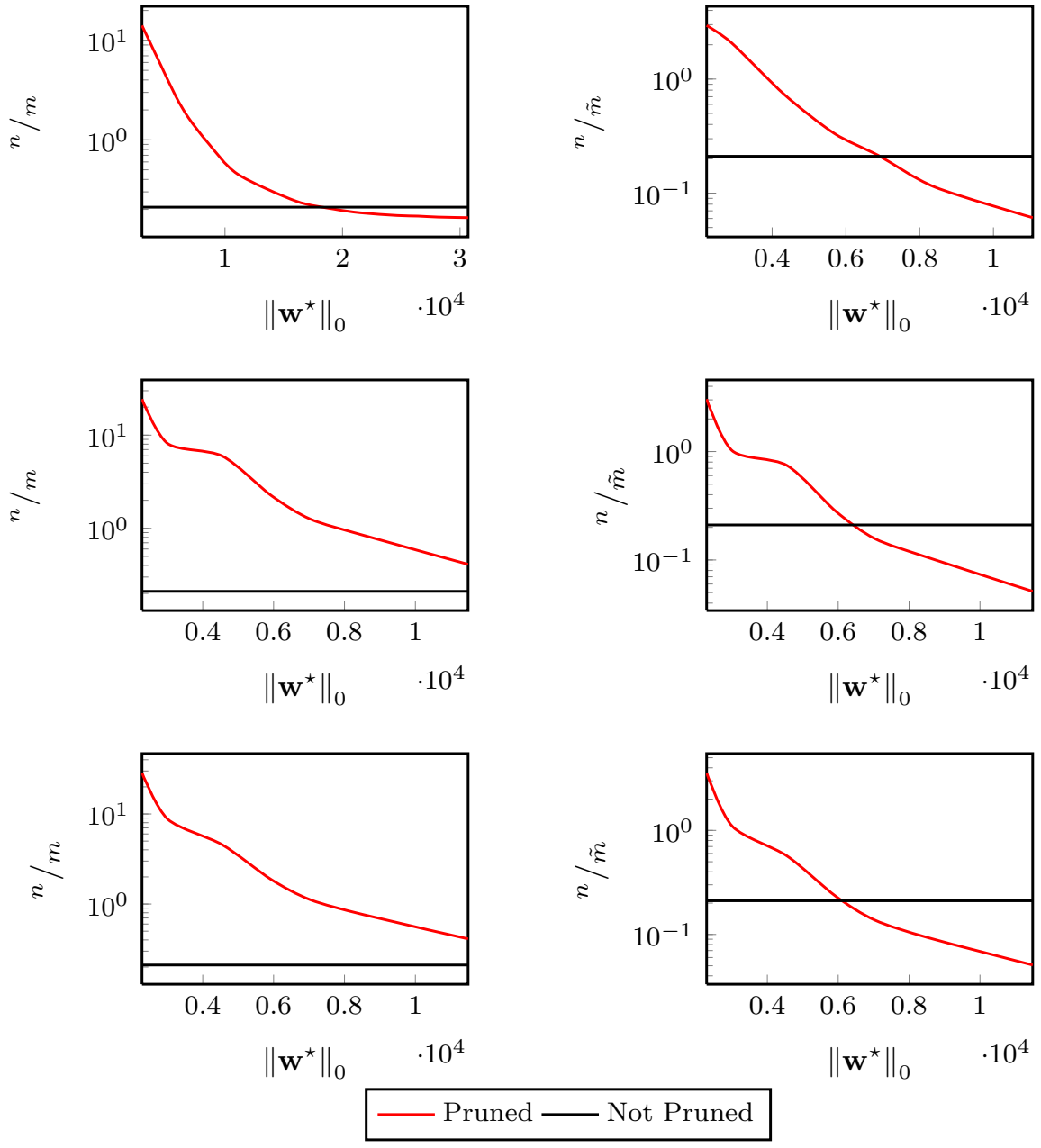

Figure 3.8: The ratio between the number of observations and the unknowns output by FRS pruning for all test cases against the ppp values, from up downward **Test Case 1-3**(·), from left to right **Test Case** ·**(a-b)**.

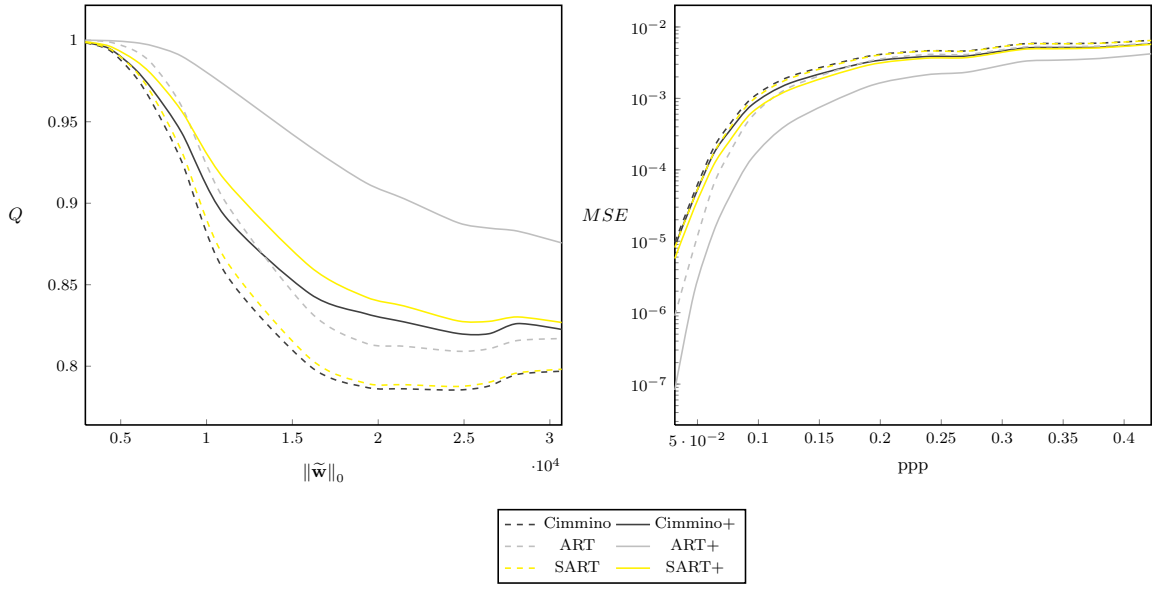

Figure 3.9: ARTs assessement for **Test Case 1(a)**. Left: Quality factor with respect to the sparsity of the signal. Right: Mean squared error with respect to the ppp number.

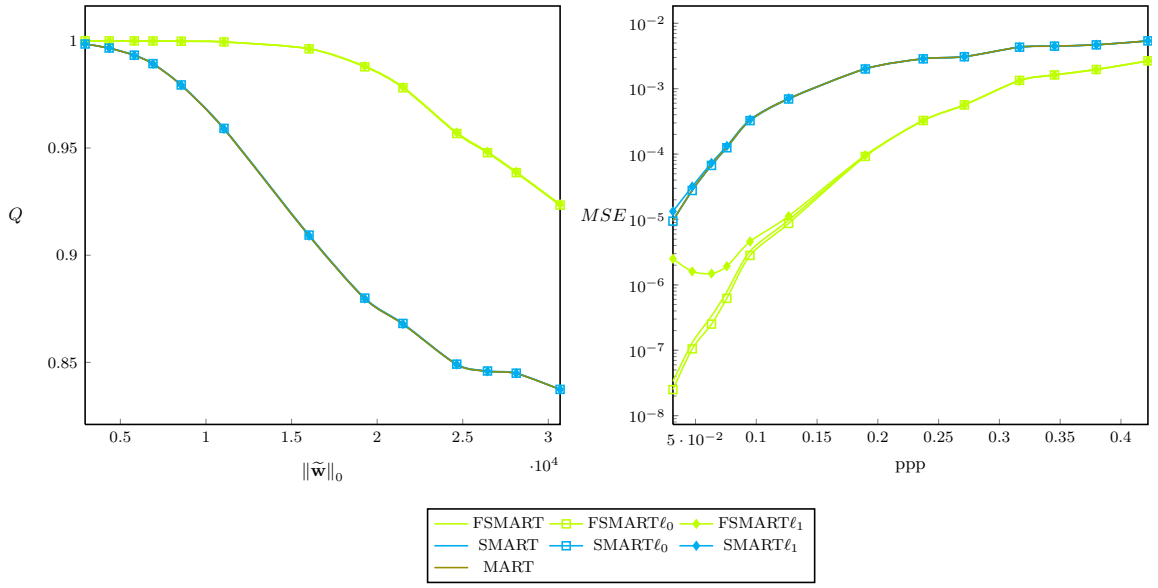

Figure 3.10: SMARTs assessement for **Test Case 1(a)**. Left: Quality factor with respect to the sparsity of the signal. Right: Mean squared error with respect to the ppp number.

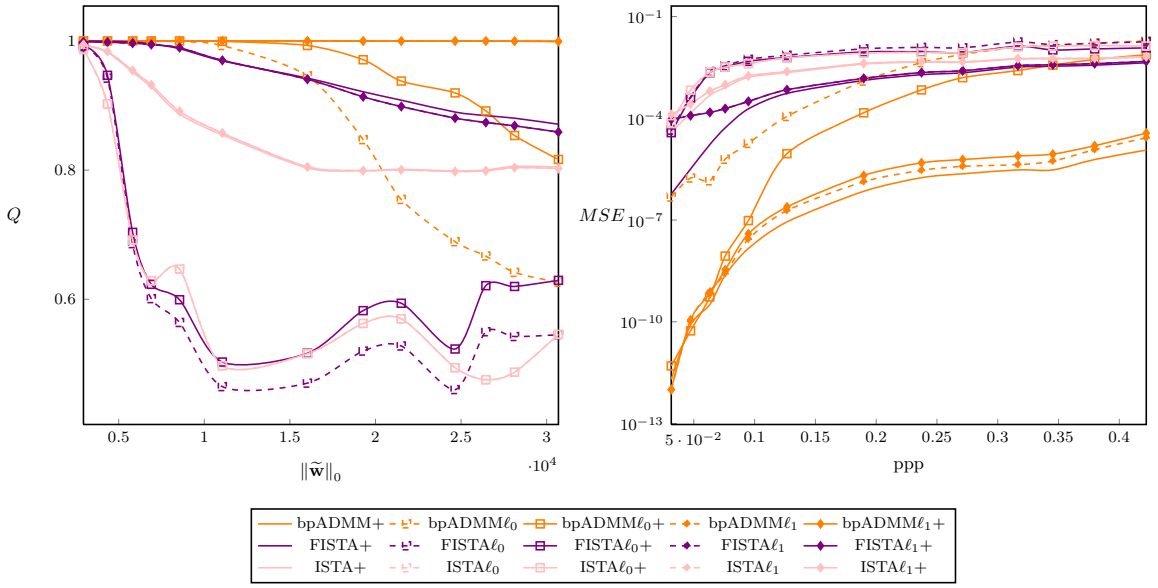

Figure 3.11: Accelerated techniques assessement for **Test Case 1(a)**. Left: Quality factor with respect to the sparsity of the signal. Right: Mean squared error with respect to the ppp number.

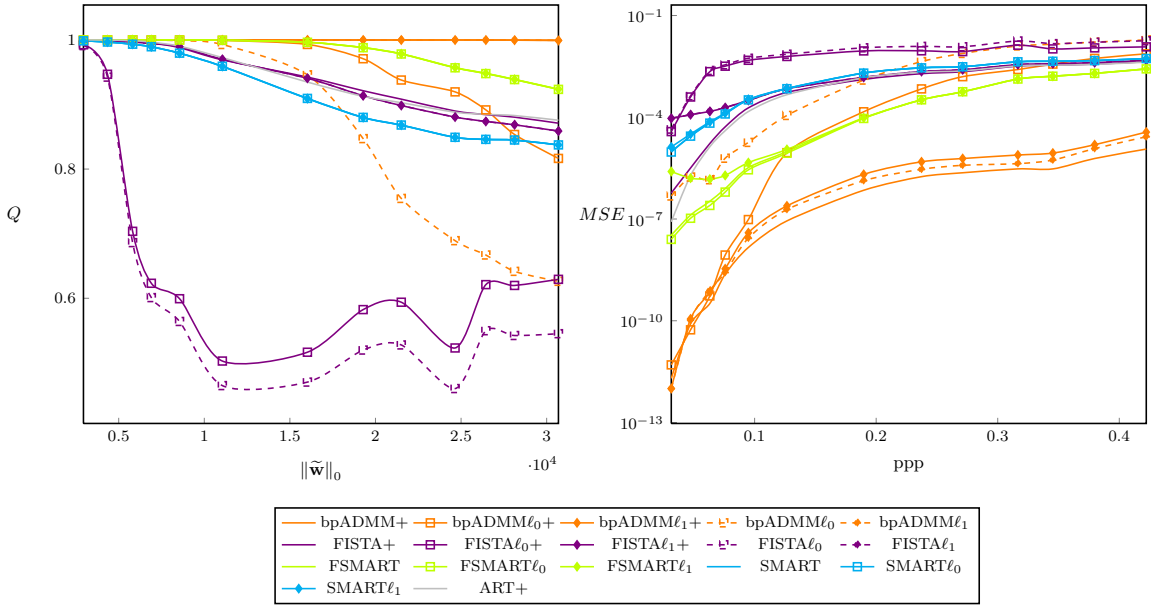

Figure 3.12: Assessement for **Test Case 1(a)**

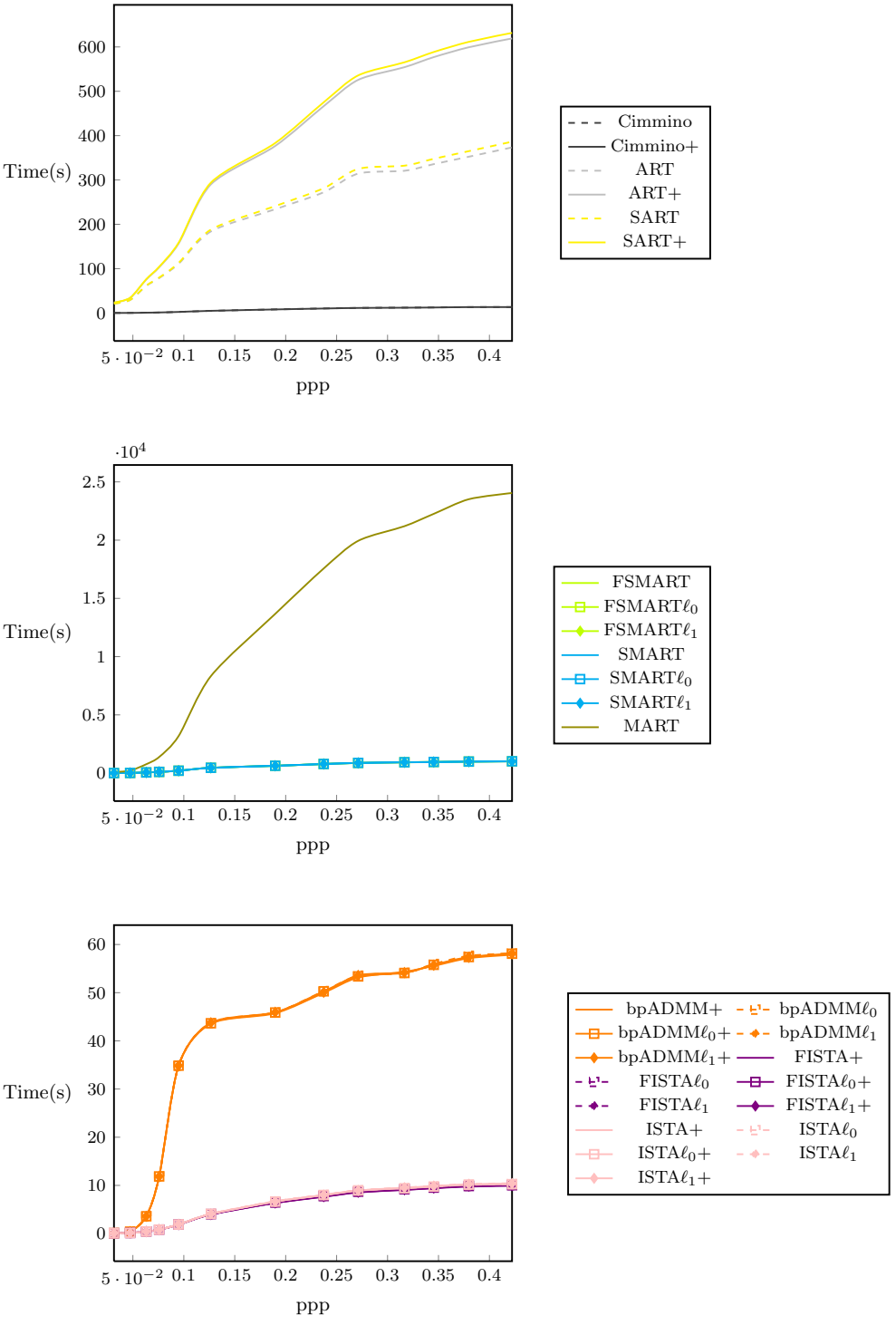

Figure 3.13: Computational time for all algorithms for **Test Case 1(a)**.

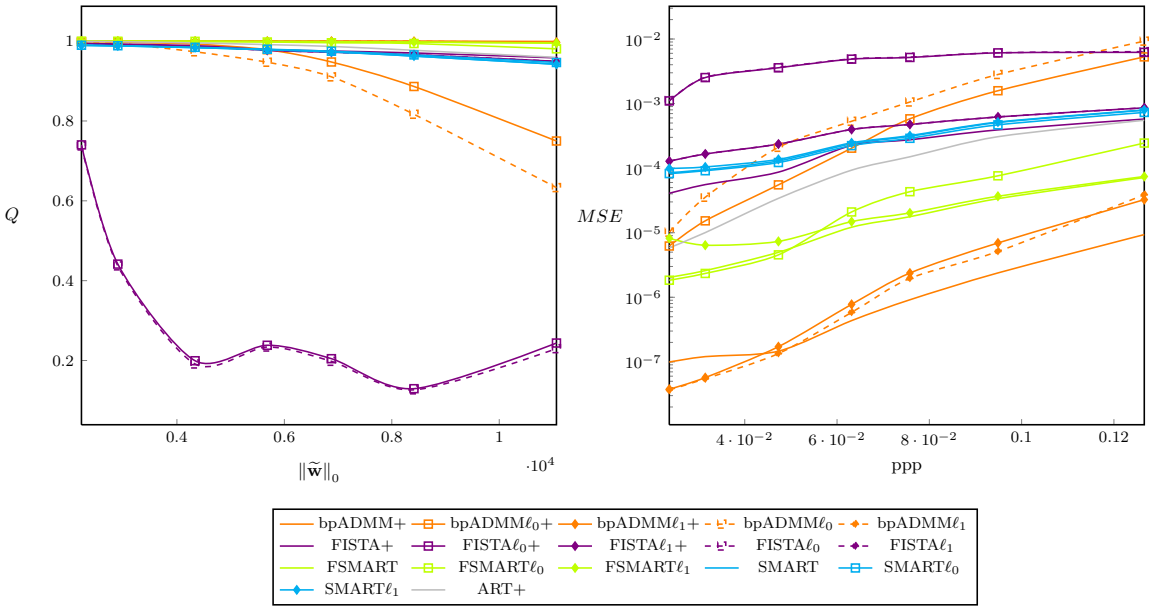

Figure 3.14: Assessement for **Test Case 1(b)**

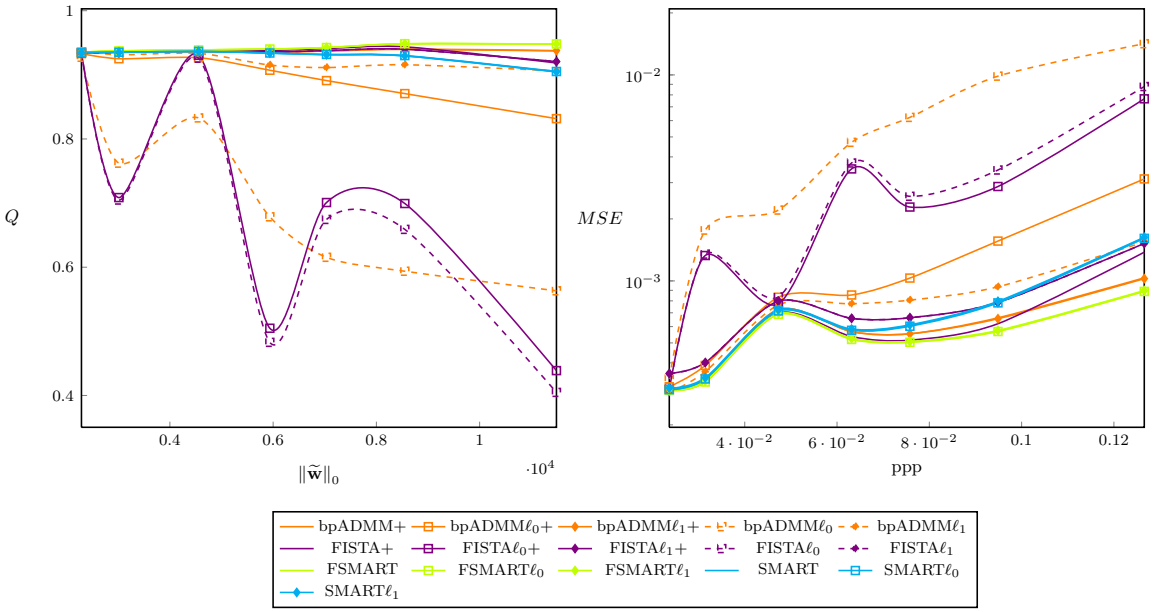

Figure 3.15: Assessement for **Test Case 2(a)**

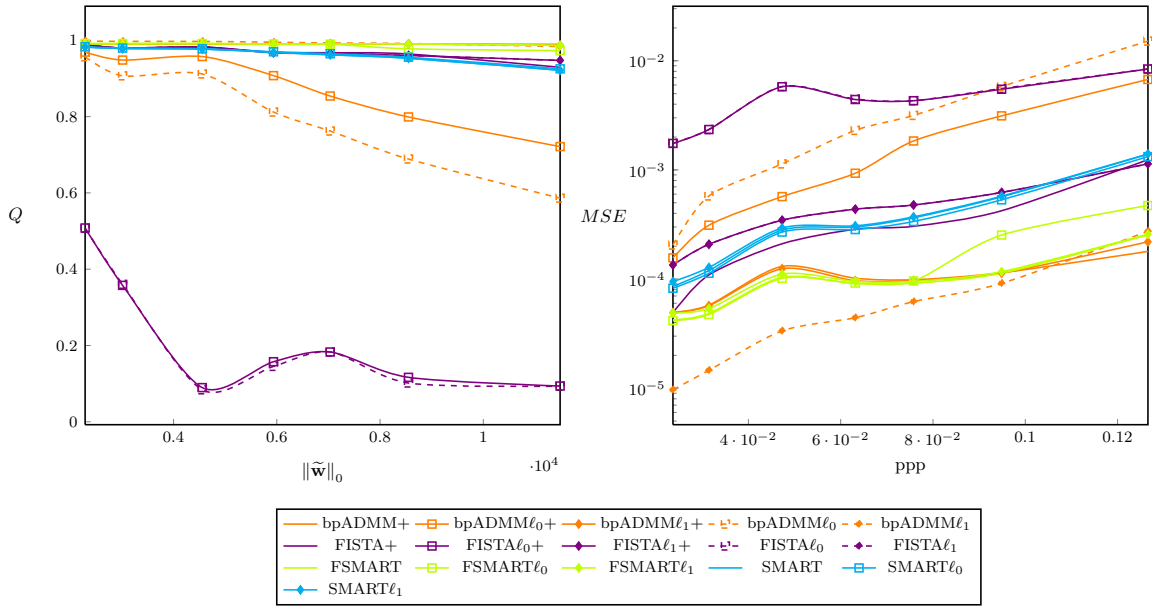

Figure 3.16: Assessement for **Test Case 2(b)**

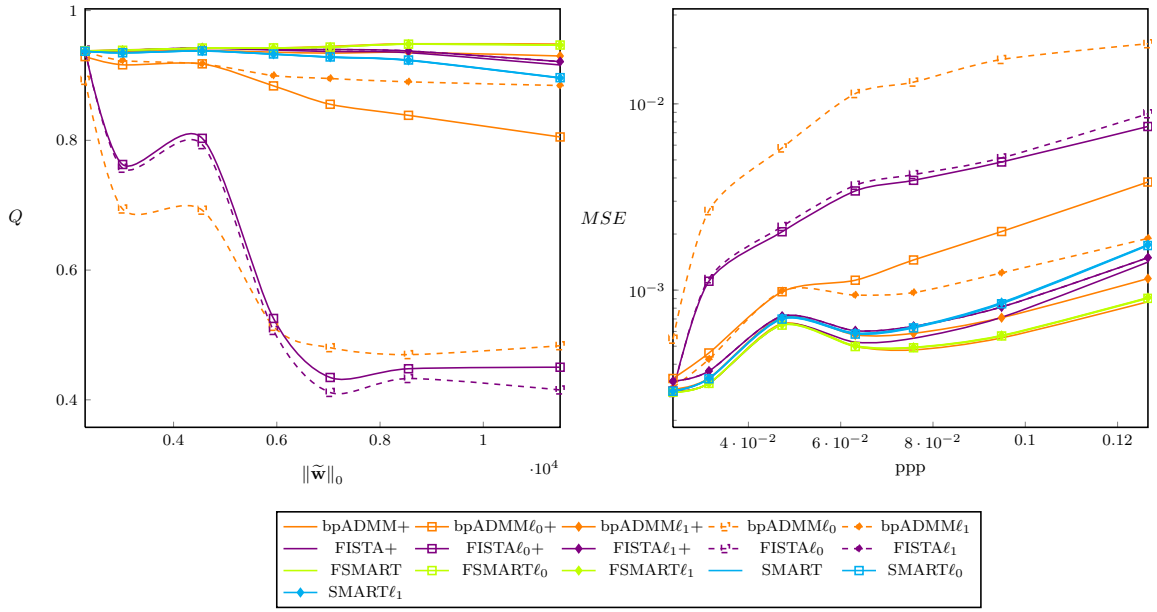

Figure 3.17: Assessement for **Test Case 3(a)**.

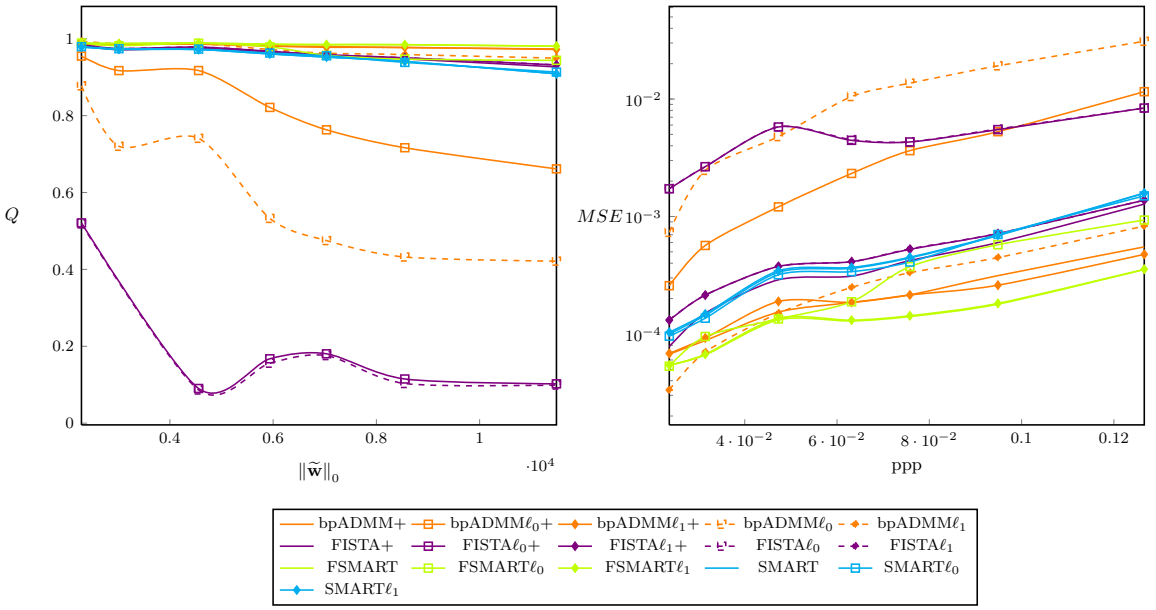

Figure 3.18: Assessement for **Test Case 3(b)**.

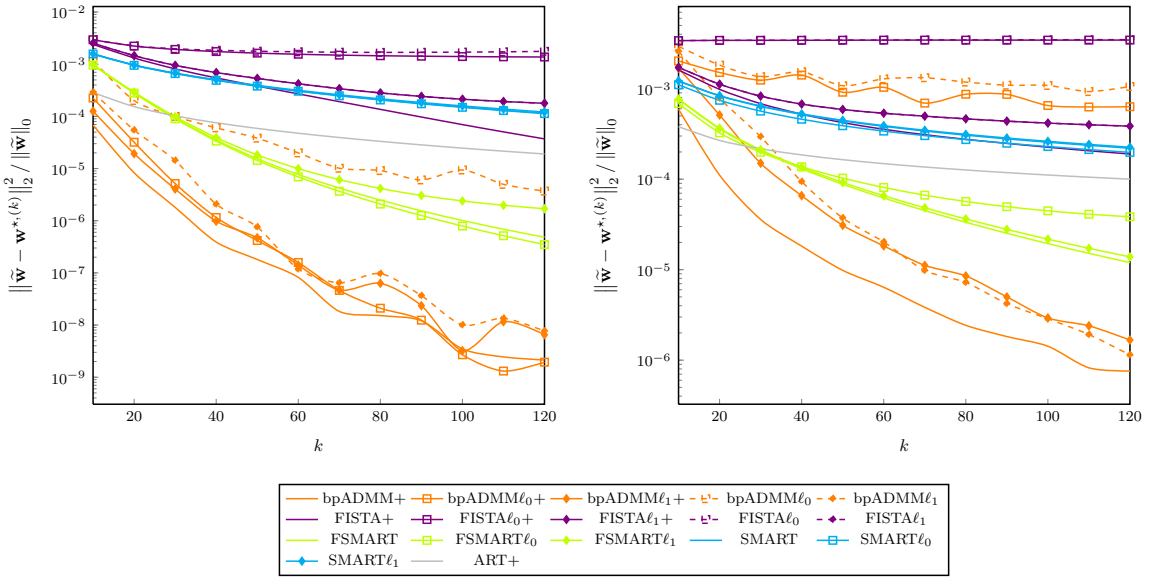

Figure 3.19: Convergence for **Test Case 1** for $ppp = 0.0758$. Left : **Test Case 1(a)**; right: **Test Case 1(b)**.

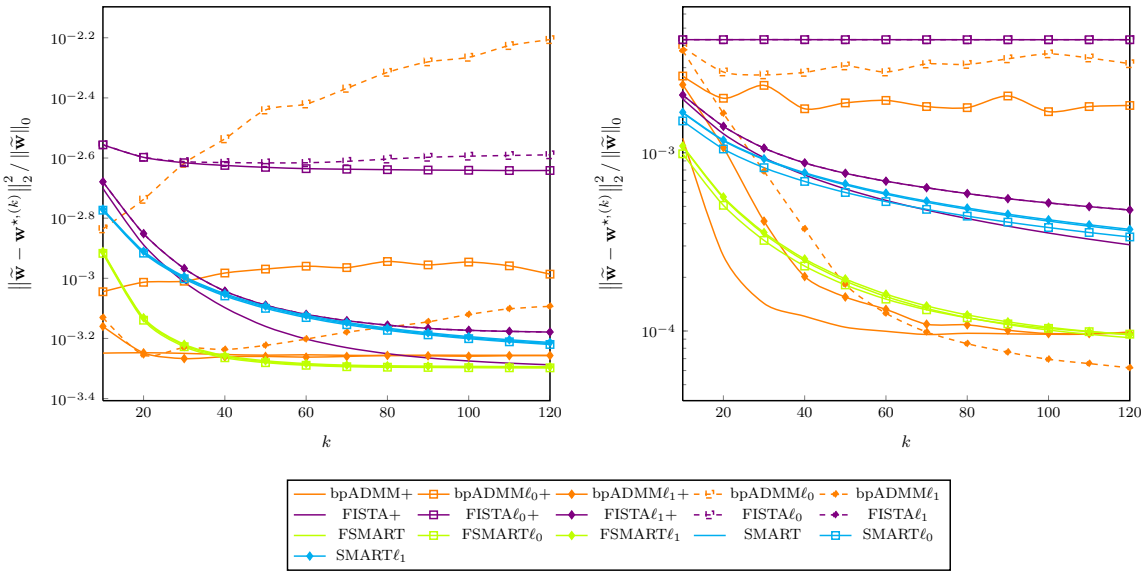

Figure 3.20: Convergence for **Test Case 2** for $ppp = 0.0758$. Left : **Test Case 2(a)**; right: **Test Case 2(b)**.

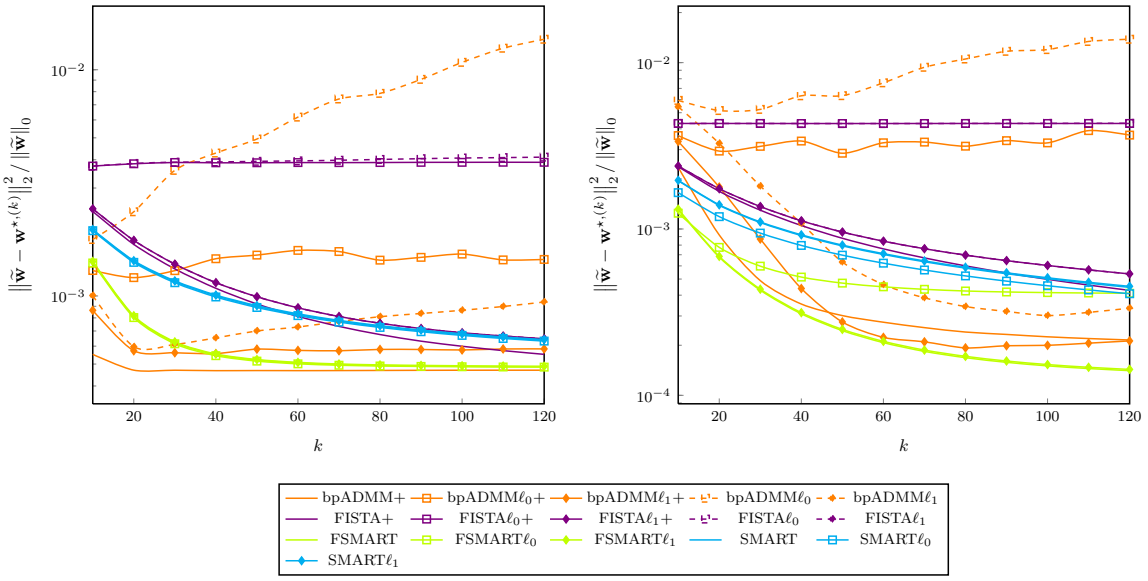

Figure 3.21: Convergence for **Test Case 3** for $ppp = 0.0758$. Left : **Test Case 3(a)**; right: **Test Case 3(b)**.

Chapter 4. Velocity Estimation

We have presented, in the first chapter, techniques for enabling vision-based observations and analysis of fluid dynamics. Moreover, we have motivated our choice for focusing on the tomoPIV system in our effort to estimate the 3D velocity of the turbulent fluids. If classical *optical flow* computes the 2D motion directly out of the planar measurements, more recent *scene flow* usually relies on the previously estimated 3D volumetric intensity distributions. The procedures depicted in chapter 3 are thus of paramount importance for the current study. The next step, exposed throughout the current chapter, is to exploit the volumetric images in order to retrieve the velocity of the turbulent fluids.

A classical estimation scheme in tomoPIV consists in reconstructing two successive 3D intensity distributions of seeded particles and then sequentially applying a post-processing procedure for the retrieval of the 3D velocity field [74]. Recently, a novel procedure has been advanced which estimates the fluid motion out of consecutive volumetric frames by taking into account their linked structure [134]. Motivated by the advancement in the computer vision field and the tomoPIV community, we propose alternative procedures to both of the already established paradigms. With the aim of going towards a joint procedure, we focus on formulating the optimization problems by taking in regard the physical anatomy of the scene. For doing so, we introduce a formulation which accounts for the nexus between structure and motion. The current chapter is organized as follows. We present, in section 4.1, image-related features leading to the formulation of an *a priori* information for the model design. We review the optical flow literature in Section 4.2, with focus on terms related to the photometric constraints and on terms modeling constraints on the velocity field. Section 4.3 presents our contributions which are twofold: *(i)* transitioning from a classic 2D setting to a 3D setting *(ii)* estimating jointly the 3D volumetric distribution of the particles **and** the velocity fields that propels them. Finally, Section 4.4 presents results to defend our proposed approach.

4.1 Features

The **optical flow** recovers the *apparent 2D displacement* of a 3D scene depicted by a sequence of images, usually retrieved by a camera. Historically, the retrieval of physical motion out of a sequence of images is performed by analyzing the optical flow [101, 116]. Optical flow surveys can be read in [22, 82, 128] and references therein. The relation between the latter and the physical motion is however not straightforward. In fact, common visual

sensors project the 3D scene onto a 2D plane. This inevitably results in loss of information, some of which might be of paramount importance for the interpretation of the physical motion. Moreover, other conundrums might enhance the ambiguities (*e.g.*, occlusions - when an object passes behind another one).

A way of compensating loss of data is trough simultaneous imaging from multiple viewing angles. This is achieved by arranging multiple cameras around the scene of interest and capturing video of the activity with respect to a (usually) known calibration of the visual system. The correspondent motion quantity, coined **scenic flow** [181], estimates the *3D displacement* of points in a volumetric region of interest out of sequences of images **and** and calibration.

The estimation of both scenic and optical flow rely on the same features depicted by the image system. We present, in sequel, an unified framework for the 2D/3D setups. In order to do that, we consider a cartesian grid $\mathcal{V} \subset \mathbb{R}^a$ with $a \in [2, 3]$, centered on positions $\mathbf{k}^j \in \mathbb{R}^a$, where $j \in \{1, \ldots, m\}$ and $m \in \mathbb{N}^\star$ is the number of resolved points. The grid follows the constraints made in section 2.2.3, *i.e.*, equations (2.29) and (2.30). Our observable image quantity at a position $\mathbf{k}^j$ writes $w_t(\mathbf{k}^j)$. The quantity $u(\mathbf{k}^j, t) \in \mathbb{R}^a$ is the velocity field of the fluid at the position $\mathbf{k}^j$ at time t. The vector $\mathbf{w}_t$ collects the intensities at the center of the grid positions, at time t, as writes $\mathbf{w}_t \triangleq \begin{bmatrix} w_t(\mathbf{k}^1) & \ldots & w_t(\mathbf{k}^m) \end{bmatrix}^T$. Analogically, the matrix $\mathbf{u}_t$ collects the **instantaneous velocity** in $\mathcal{V}$ such as $\mathbf{u}_t \triangleq \begin{bmatrix} u^T(\mathbf{k}^1, t) & \ldots & u^T(\mathbf{k}^m, t) \end{bmatrix} \in \mathbb{R}^{ma}$.

Brightness Constancy

As previously stated in chapter 2, we rely on the assumption of *brightness consistency* scattered by a point in $\mathcal{V}$ along its trajectory. A linear differential formulation of this assumption is known as the Optical Flow Constraint (OFC) and writes:

$$\frac{\mathrm{d}\mathbf{w}_t}{\mathrm{d}x} = \frac{\partial \mathbf{w}_t}{\partial t} + \left[u(\mathbf{k}^j, t)^T \nabla_{\mathbf{k}} w_t(\mathbf{k}^j) \right]_{j \in \{1,\ldots,m\}} = \mathbf{0}_m, \tag{4.1}$$

We note that the equation (4.1) is linear with respect to $\mathbf{u}_t$, which considerably facilitates the subsequent computation build on the OFC.

We recall that $I(\mathbf{u}_t)\,\mathbf{w}_{t+1} = \left[w_{t+1}(\mathbf{k}^j + u(\mathbf{k}^j, t)) \right]_{j \in \{1,\ldots,m\}}$ stands for the displaced image between time t and $t+1$, as it has been initially introduced in Chapter 2. The operator $I(\mathbf{u}_t) \in \mathbb{R}^{m \times m}$ corresponds to the warping process; the latter depends explicitly on the motion field $\mathbf{u}_t$ and on the chosen polynomial image interpolation. Let us note that $I(\mathbf{0}_{ma})\,\mathbf{w}_{t+1} = \mathbf{w}_{t+1}$.

A non-linear formulation of OFC leads to the cancellation of the Displacement Frame Difference (DFD). Following the upper-defined nomenclature, we have the transport equation:

$$I(\mathbf{u}_t)\,\mathbf{w}_{t+1} - \mathbf{w}_t = \mathbf{0}_m, \tag{4.2}$$

We refer the reader to chapter 2 for an extensive reading of computations and assumptions leading towards equation (4.2) for tomoPIV scene flow context. Throughout this chapter,

we make an abuse of notation and consider, for the temporal step $\delta t = 1$, that the matrix $\mathbf{u}_t$ collects the **displacement** vectors at time frame t of a tracers located grid positions for the DFD formulation (4.2), while $\mathbf{u}_t$ keeps its original interpretation for the OFC formulation (4.1).

We notice that by linearizing equation (4.2) around $\mathbf{u}_t = \mathbf{0}_{ma}$, we obtain an approximation of the OFC, where the temporal derivative $\frac{\partial \mathbf{w}_t}{\partial t}$ has been replaced by a finite difference, that is:

$$\mathbf{w}_{t+1} - \mathbf{w}_t + \left[u(\mathbf{k}^j, t)^T \nabla(I^T_{j,\bullet}(\mathbf{0}_{ma}))\mathbf{w}_t\right]_{j\in\{1,\dots,m\}} = \mathbf{0}_m, \tag{4.3}$$

where $I_{j,\bullet}(\mathbf{u}_t) : \mathbb{R}^{ma} \to \mathbb{R}^m$ stands for the j^{th} line of the warping matrix $I(\cdot)$ and $\nabla(I^T_{j,\bullet}(\mathbf{0}_{ma})) \in \mathbb{R}^{a\times m}$ is the Jacobian matrix of $I_{j,\bullet}$.

4.2 Classical Motion Estimation Methods

The main idea underlying classical motion estimation methods is to search for a solution of problems (4.1) or (4.2) in terms of motion quantity, assuming the image domain $\mathbf{w}_t$ is completely known $\forall t$. Equation (4.1) defines a local constraint on the (apparent) image motion, *i.e.*, the normal velocity vector perpendicular to the constraint line (refer to figure 4.1 for a visual representation). Writing, for a point $\mathbf{k}^j \in \mathcal{V}$, $u(\mathbf{k}^j, t) = u_\perp(\mathbf{k}^j, t) + u_\parallel(\mathbf{k}^j, t)$, where $u_\perp(\mathbf{k}^j, t) \in \mathbb{R}^a$ and $u_\parallel(\mathbf{k}^j, t) \in \mathbb{R}^a$ are the components perpendicular and tangential to the brightness isosurface, respectively, we obtain that:

$$u_\perp(\mathbf{k}^j, t) = -\frac{\partial w_t(\mathbf{k}^j)}{\partial t} \frac{\nabla(I^T_{j,\bullet}(\mathbf{0}_{ma}))\mathbf{w}_t}{\left\|\nabla(I^T_{j,\bullet}(\mathbf{0}_{ma}))\mathbf{w}_t\right\|_2^2} \tag{4.4}$$

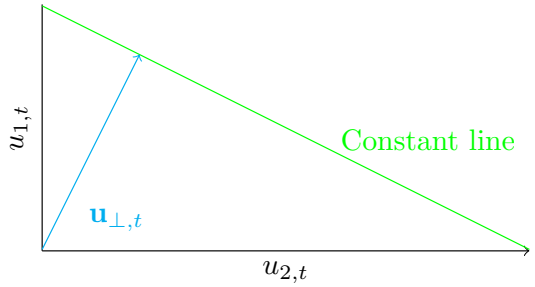

Figure 4.1: The optical flow constraint defines a line in the velocity space.

This constraint only allows us to compute the normal component. Therefore, the optical/scene flow constraint is inherently ill-posed. This occurrence is known as the *aperture problem*; a 2D visual rendition of the phenomenon can be observed on figure 4.2. In order to close the subsequent gradient-based estimation problem, it is necessary to resort to regularization schemes applied to the estimated motion in order to compensate the lack of information from images and transform the initial problem into a well-posed one.

The common approach to solve a motion estimation problem is to minimize a global

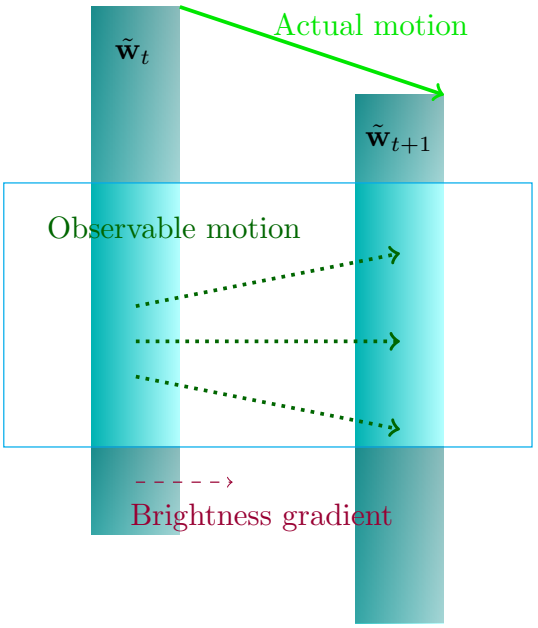

Figure 4.2: An illustration of the aperture problem. The observation window does not capture the vertical component of the displacement between two frames of a rectangular object.

functional exploiting some a priori information we may have on the signal. Such a functional usually contains two main terms: *(i) the data term*, which englobes a photometric constraint with respect to the scene motion; *(ii) the regularization term*, which stands for regularization enforcing regularity constraints on the motion field. Most estimation schemes rely on the so-described paradigm. Therefore, we can distinguish between the schemes endorsing this method depending on the construction of the functional. We present here below a general formulation of the motion estimation problem, that is:

$$\min_{\mathbf{u}_t} f_d\left(\mathbf{u}_t\right) \text{ subject to } f_r(\mathbf{u}_t) \leq \varepsilon, \tag{4.5}$$

where, as evoked earlier, the term $f_r(\cdot)$ is designed to ensure some property on the solution, while the term $f_d(\cdot)$ usually guarantees the respect of the brightness constraint. This constrained minimization problem can alternatively be written as an augmented Lagrangian formulation, that is:

$$\min_{\mathbf{u}_t} f_d\left(\mathbf{u}_t\right) + \lambda f_r(\mathbf{u}_t). \tag{4.6}$$

The literature is abundant in choices of these terms, which can be adapted depending on the nature of the images, on the application and its subsequent specificities [128]. A brief classification can be read in the remainder of this section.

Choices of $f_r(\cdot)$

The choice of the so-called *regularization* term is of utmost importance as it implicitly defines the solution we are looking for. For example, the most common paradigm is to consider the original motion as rigid. This prior enables the design of local parametric

formulation on the motion fields, leading to the following regularization term :

$$u(\mathbf{k}, t) = P(\mathbf{k})\,\boldsymbol{\Theta}, \tag{4.7}$$

where $P(\mathbf{k}) \in \mathbb{R}^{a \times s_p}$ is the matrix depending on the chosen parametrization and $\boldsymbol{\Theta} \in \mathbb{R}^{s_p}$ is the parameter vector. The subsequent regularization term naturally writes:

$$f_r(\mathbf{u}_t, \boldsymbol{\Theta}) = \sum_j \left\| u(\mathbf{k}^j, t) - P\left(\mathbf{k}^j\right) \boldsymbol{\Theta} \right\|_2^2, \tag{4.8}$$

An affine, quadratic, linear or constant parametrization can be chosen. In the latter case, we constrain the velocity fields to be constant over $\mathcal{V}$ by choosing $P(\mathbf{k}^j) = \mathbf{I}_a$, where $\mathbf{I}_a \in \mathbb{R}^{a \times a}$ is the eye matrix. Moreover, if we refer to problem (4.5) constrained by $f_r(\mathbf{u}_t, \boldsymbol{\Theta})$ (where $f_r(\cdot)$ is defined by (4.8) with $\varepsilon = 0$), we notice that the former is equivalent to addressing problem (4.6) with the velocity prior defined as follows:

$$f_r(\mathbf{u}_t, \boldsymbol{\Theta}) = \sum_j \mathbb{I}_{\{\boldsymbol{\Theta}\}}(u(\mathbf{k}^j, t)) \tag{4.9}$$

where we recall that the indicator function has been defined in Chapter 4.

When dealing with observation outliers (*e.g.*, some discontinuities in the image domain) the use of the ℓ_2-norm may lead towards erroneous estimations in the vicinity of the boundaries. In this case, a *robust cost function* may be considered in order to penalize model discrepancies, see [31,86,102]. Whatever the cost function, the retrieval of the optical flow, coined *image registration* in the computer vision community, then resumes to finding the set of points which best aligns model and data. Within this framework, we cite seminal paper [28] and ongoing ensuing research [20,84]. In practice, the so-defined prior leads to a re-formalized brightness constancy assumption accounting for the parameter model, as we will see in the next paragraph.

In the context of systems for fluid visualization, the recorded images capture the non-rigid motion of the seeded particles (see chapter 2). Thus, classical regularization schemes as stated based on (4.8) are not well-suited for turbulent fluid estimation. In fact, as suggested by the high non-linearity of the Navier-Stokes equation (see (1.1), chapter 1), turbulence is described mathematically by chaotic fluctuations of flow variables of the velocity field as well as a high sensitivity to initial and boundary conditions over a wide range of 3D scales and amplitudes. In order to best mimic the behavior of the flow, one can rely on its physical kinematics properties to account for its salient features, *i.e.*, numerous vortical structures characterizing the turbulent regime of the fluid. We refer the reader to [92] for a regularization inspired by *Kolmogorov*'s work on turbulent flow self-similarity and recent results in the study of turbulent flows. Although modeling the strong spatio-temporal dependency of the flow motion is ideal, the resolution of a such global functional implies high computational means.

A first attempt at fluid-dedicated motion estimators was give in [58], where a parametric formulation of the velocity vector with a small number of vortex and source particles was phrased. In [16], the authors opted for a piece-wise linear formulation.

In practice, we resort to locally smoothing priors which mimic qualitative regularity properties of the fluid motion, *i.e.*, coherent blobs of vorticity and divergence. In fact, the volume-preserving constrain on the flow *divergence* operator $\mathrm{div}(u(\mathbf{k},t)) = \nabla \cdot u(\mathbf{k},t) = 0$ is derived from the mass conservation principle with incomprehensibility hypothesis. The *curl* operator $\mathrm{curl}(u(\mathbf{k},t)) = \nabla \times u(\mathbf{k},t)$ describes the vortical structures in the turbulent flows. Methods preserving these quantities have been introduced in a motion estimation context in [169] and further enriched in [56]. The corresponding regularization term which penalizes strong curl and divergence gradients writes:

$$f_r(\mathbf{u}_t) = \sum_j \left\| \nabla_{\mathbf{k}} \,\mathrm{curl}(u(\mathbf{k}^j,t)) \right\|_2^2 + \beta \left\| \nabla_{\mathbf{k}} \,\mathrm{div}(u(\mathbf{k}^j,t)) \right\|_2^2, \tag{4.10}$$

with $\beta > 0$ some tuning parameter.

Finally, the most common smoothing prior choice for f_r is:

$$f_r(\mathbf{u}_t) = \sum_j \left\| \nabla u(\mathbf{k}^j,t) \right\|_2^2. \tag{4.11}$$

The upper-defined functional, introduced by *Horn et Schunck* [101] penalizes strong gradients of the velocity vector. The subsequent minimization problem can be approximated using calculus of variations and the solution can be sought using an iterative descent method.

Let us note that in practice, the data term aims at coping with the aperture problem and/or inserting some *a priori* information on the application.

We keep in mind that most of the literature referring to such global optimization schemes, including the references cited here-above, has been placed in the context of optical flow estimation, *i.e.*, in the 2D domain. The chosen discretization scheme implies that, for a square image of L^2 pixels, the sought velocity fields has $2L^2$ components. As an example, for a typical 1024×1024 pixels image, the number of unknowns rises to 2097152, for a two-frame sequence. If the regularization term copes at some extent to this under-determination, in the tridimensional case the latter is even more drastic, along with the dimensions of the problem. This represents part of the explanation why such priors have not yet been tackled in the tomoPIV context. Even so, global regularization terms for motion retrieval of turbulent fluids is of utmost interest for the detection and metrology of the coherent tridimensional structures that come into play in flows. Applying such tools within this context is however to be treated with great caution due to the subsequent computational effort. The challenge is to design a low-complexity *Navier-Stokes*-inspired global regularization term and opens up interesting perspectives for future research.

Choices of $f_d(\cdot)$

Formalizing the choice of the so-called *data term* allows the complete depiction of the optimization problem (4.5) in terms of the transported image quantity. The data prior is usually derived from brightness constancy assumption (there are nevertheless myriads of other model in the literature). For instance, if we refer to the DFD term defined by equation

(4.2), we have that:

$$f_d\left(\mathbf{u}_t\right) = \left\|\mathbf{w}_t - I(\mathbf{u}_t)\mathbf{w}_{t+1}\right\|_2^2. \tag{4.12}$$

In an analogue manner, a counterpart to (4.11) linear in $\mathbf{u}_t$ can be obtained from equation (4.3). As stated in the previous paragraph, the choice of the squared ℓ_2-norm can be replaced by more sophisticated robust cost function in order to avoid discontinuities in the image domain. We will briefly review in the sequel such methods.

The most intuitive local technique models the brightness consistency under a similarity function, as follows:

$$f_d\left(\mathbf{u}_t\right) = C\left(\mathbf{w}_t, I(\mathbf{u}_t)\mathbf{w}_{t+1}\right), \tag{4.13}$$

with $C(\cdot)$ is defined with respect to, *e.g.*, the DFD expressed by equation (4.2) or the correlation function between the elements of the consecutive considered neighborhoods, that is:

$$C\left(\mathbf{w}_t, I(\mathbf{u}_t)\mathbf{w}_{t+1}\right) = -\mathbf{w}_{t+1}I^T(\mathbf{u}_t)\mathbf{w}_t, \tag{4.14}$$

or, alternatively, its counterpart centered on the mean value of the respective windows and normalized by their variance. The *digital image correlation* technique has been broadly adopted due to their implementation in the Fourier domain, which is however theoretically defined uniquely for periodical signals. Enhancement to the regular correlation schemes have been proposed in the literature, both in 2D [25] and 3D [133] context in order to adapt locally the shape and the orientation of the window.

Fluid dedicated *data terms* have been proposed in the literature. In [56], the data term derived from the continuity equation writes:

$$f_d\left(\mathbf{u}_t\right) = \left\|I(\mathbf{u}_t)\mathbf{w}_{t+1} - \mathbf{w}_t e^{-\operatorname{div}(\mathbf{u}_t)}\right\|_2^2.$$

In practice, the optimization problem depicted by equation (4.5) can be solved **locally** around each grid position, enabling thus parallelism. This worthwhile scheme results in a dramatic complexity alleviation which facilitates the problem of tridimensional motion estimation. In fact, as mentioned before, we would ideally resort to a Navier-Stokes global prior to model the flow displacement. As it turns out, such an optimization problem engenders prohibitive computational time, even in a bidimensional framework. The trade-off is to have recourse to a local technique formalized in the 3D space. Thus, a multiviewing framework compensates the loss of data that cannot be retrieved by solely relying on the brightness constancy assumption.

An Algorithmic Example

Let us give an illustration of the minimization of problem (4.6), for particular choices of the function $f_d(\cdot)$ and $f_r(\cdot)$, respectively. In particular, let $f_r(\mathbf{u}_t, \boldsymbol{\Theta}) = \sum_j \mathbb{I}_{\{\boldsymbol{\Theta}\}}(u(\mathbf{k}^j, t))$. Constraining the velocity field to be constant over the volume leads us to the following functional:

$$\min_{\mathbf{u}_t} f_d(\boldsymbol{\Theta}, \mathbf{u}_t) + \lambda \sum_j \mathbb{I}_{\{\boldsymbol{\Theta}\}}(u(\mathbf{k}^j, t)). \tag{4.15}$$

When the data term constrains the DFD, *i.e.*, $f_d(\mathbf{u}_t) = \|\mathbf{w}_t - I(\mathbf{u}_t)\mathbf{w}_{t+1}\|_2^2$, problem (4.16) becomes:

$$f_d(\boldsymbol{\Theta}) = \|\mathbf{w}_t - I(\mathbf{u}_{\boldsymbol{\Theta}})\mathbf{w}_{t+1}\|_2^2, \tag{4.16}$$

where $\mathbf{u}_{\boldsymbol{\Theta}}$ concatenates m times the vector $\boldsymbol{\Theta}$.

This leads to the ubiquitous LK estimator [116]. Within the tomoPIV context, the LK problem has already been tackled in [110, 114, 183]. In practice, we appeal to an iterative gradient-based descent procedure in order to access to the solution of the (4.15). Thus, starting from an initial velocity guess $\boldsymbol{\Theta}^{(0)}$, the iterates write:

$$\boldsymbol{\Theta}^{(l+1)} = \boldsymbol{\Theta}^{(l)} - \alpha^{(l)}\mathbf{S}^{(l)}\nabla_{\boldsymbol{\Theta}} f_d(\boldsymbol{\Theta}), \tag{4.17}$$

where $\alpha^{(l)}$ the step-size parameter can optionally be optimized at each iteration (*e.g.*, by the *Armijo rule*). The positive definite matrix $\mathbf{S}^{(l)}$ allows profiling the descent direction; a simple choice would be the identity matrix, which leads however to slow convergence. Analogically to the step-size, the descent direction can be estimated at each iteration (*e.g.*, as the Hessian matrix of the objective function with respect to the current estimate). For solid theoretical background, see [27].

4.3 Joint Local Method

Several algorithms have been proposed in the field of computer vision, and, later, adapted for the tomoPIV application, to associate the information from multiple views in order to output a single 3D representation of the scene. Although conceptually interesting, these procedures suffer from some possible drawbacks, when applied to a 3D problem:

1. the reconstruction of the 3D density function is performed independently of the temporal sequence. In reality, the instantaneous volumetric distributions can be modeled like a 3D entity deformed by a displacement (*i.e.*, the fluid flow). Therefore, any information on the displacement field could be taken into account in the reconstruction of the density function;

2. The estimation of the displacement field is computed between pairs of reconstructed 3D intensity distributions at consecutive time frames. In practice, the quality of these reconstructed volumetric distributions can be affected by the low number of observations and measurement imprecisions. The noise affecting these estimations is not taken into account in the current literature. The velocity estimation algorithms can therefore be improved by accounting for the imprecisions governing the reconstruction of 3D density distributions and of the displacement field between them.

In the previous section, we have assumed that the volumetric images $\mathbf{w}_t, \forall t$ are known. In a 3D framework, however, the latter quantities are accessed by "inversing" the linear system (3.3), which models the projection of a discrete 3D space into the planar images (as a reminder, the subsequent estimation problem is addressed by (3.16) and counterparts). The **ideal** formulation of the joint problem expressing the nexus between instantaneous

volumetric reconstruction and velocity retrieval accounts thus for possible perturbations on the initial estimated 3D images $\mathbf{w}_t^\star$ and aims at optimizing the actual volumetric quantity with respect to the velocity fields that propels it, that is:

$$\begin{aligned} &\min_{\mathbf{w}_t, \mathbf{w}_{t+1}, \mathbf{u}_t} l_d(\mathbf{y}_t, \mathbf{D}\mathbf{w}_t) + l_d(\mathbf{y}_{t+1}, \mathbf{D}\mathbf{w}_{t+1}) + f_d(\mathbf{w}_t, \mathbf{w}_{t+1}, \mathbf{u}_t) \\ &\text{such that } l_r(\mathbf{w}_t) \leq a, l_r(\mathbf{w}_{t+1}) \leq a, f_r(\mathbf{u}_t) \leq \varepsilon, \end{aligned} \tag{4.18}$$

with a and ε some tuning parameter; priors $l_d(\cdot), l_r(\cdot)$ and $f_d(\cdot), f_r(\cdot)$ have been extensively described in section 3.4 and 4.2, respectively. This general formulation of the joint volume velocity reconstruction has not been, to our knowledge, yet tackled in the literature. Nevertheless, solving (4.18) is to be approached with caution. In practice, we aim at solving the problem **locally** around each particle. However, the volume reconstruction problem is hard to break into local sub-problem, which complicates the general formulation of (4.18). For complexity reasons, we resort to similar **local** joint volume velocity estimation functionals.

Our initial research is motivated by [74], where the authors introduced the tomoPIV measurement technique. Their work set the grounds for the estimation of 3D motion fields of lightly seeded particles in a turbulent fluid from the images captured by a finite number of cameras disposed around the illuminated volume. The challenge is to accurately reconstruct the 3D intensity distribution of a sufficiently large number of seeded particles and their respective velocity fields. The idea is thus to go towards a joint estimation of volume and velocity framework. In the tomoPIV context, *Novara et al.* have recently proposed an enhancement to the classical scheme through an iterative procedure whose aim is to initialize the algebraic procedure by a first guess accounting for both successive views of the scene [134]. We give here below a **personal** interpretation of their problem within a general optimization context, as opposed to the original paper, where a more heuristic scheme has been phrased. Their unconstrained joint optimization problem writes:

$$\min_{\mathbf{w}_t, \mathbf{w}_{t+1}, \mathbf{u}_t \in \mathcal{U}_t} l_d(\mathbf{y}_t, \mathbf{D}\mathbf{w}_t) + l_d(\mathbf{y}_{t+1}\mathbf{D}\mathbf{w}_{t+1}) + f_d(\mathbf{w}_t, \mathbf{w}_{t+1}, \mathbf{u}_t) \tag{4.19}$$

where the velocity vector $\mathbf{u}_t$ is sought in the discrete state spaces along the temporal frame collected by the set $\mathcal{U}_t$. More explicitly, *Novara et al.* choose the data term $f_d(\cdot)$ as a correlation function (see equation (4.14)) and penalize the discrepancy between the 3D volumetric signal and the projection model by a KL distance (see equation (3.29)). The authors access to the minimum of (4.19) by solving the 3 optimization problems nested in the upper-defined functional, as follows:

$$\mathbf{w}_t^{(l+1)} = \arg\min_{\mathbf{w}_t} l_d(\mathbf{y}_t, \mathbf{D}\mathbf{w}_t), \tag{4.20}$$

$$\mathbf{w}_{t+1}^{(l+1)} = \arg\min_{\mathbf{w}_{t+1}} l_d(\mathbf{y}_t, \mathbf{D}\mathbf{w}_{t+1}), \tag{4.21}$$

$$\mathbf{u}_t^{(l+1)} = \arg\min_{\mathbf{u}_t \in \mathcal{U}_t} f_d\left(\mathbf{w}_t^{(l+1)}, \mathbf{w}_{t+1}^{(l+1)}, \mathbf{u}_t\right). \tag{4.22}$$

where problems (4.20) and (4.21) are solved by SMART initialized with $\frac{1}{2}\left(\mathbf{w}_t^{(l)} + I(\mathbf{u}_t^{(l)})\mathbf{w}_{t+1}\right)$ and $\frac{1}{2}\left(\mathbf{w}_{t+1}^{(l)} + I(-\mathbf{u}_t^{(l)})\mathbf{w}_t\right)$, respectively. This initialization aims at reducing the intensity of ghost particles; moreover, as the function $l_d(\cdot)$ is convex, setting a righteous initialization point considerably speeds up the convergence to the solution of the volume reconstruction problem. The so-called Motion enhancement technique (MTE) yields better performance than classically employed 3D digital correlations with respect to the geometric topology of the sought particles.

Joint Volume Velocity Estimation (JVVE)

In the same spirit as the refined estimation paradigm in (4.19), we aim in this work at proposing a novel continuous global formulation of the nexus between instantaneous volumetric reconstruction and velocity retrieval. More specifically, we consider the following optimization problem:

$$\begin{aligned} \min_{\mathbf{w}_t, \mathbf{w}_{t+1}, \mathbf{u}_t} f_d(\mathbf{w}_t, \mathbf{w}_{t+1}, \mathbf{u}_t) + \lambda \left[\|\mathbf{w}_t - \mathbf{w}_t^\star\|_2^2 + \|\mathbf{w}_{t+1} - \mathbf{w}_{t+1}^\star\|_2^2 \right] \\ \text{such that } f_r(\mathbf{u}_t) = 0, \end{aligned} \tag{4.23}$$

where λ_t is a tuning parameter modeling the trade-off between the data term $f_d(\cdot)$ and the priors on the volumetric image given by the second term. The data term $f_d(\cdot)$ enforces the brightness constancy assumption and is chosen here as the squared ℓ_2-norm of the DFD, function previously defined by (4.12). The second term of the functional penalizes the discrepancies discrepancies between $\mathbf{w}_t$ and the volume estimated during the volume reconstruction step $\mathbf{w}_t^\star$, $\forall t$ in the temporal sequence, where $\mathbf{w}_t^\star$ solves the optimization problem:

$$\min_{\mathbf{w}_t} l_d(\mathbf{y}_t, \mathbf{D}\mathbf{w}_t) \text{ such that } l_r(\mathbf{w}_t) \leq \tau. \tag{4.24}$$

Finally, we make the choice of a local **constant** parametric formulation for the velocity field, that is $f_r(\mathbf{u}_t, \boldsymbol{\Theta}) = \sum_j \mathbb{I}_{\{\boldsymbol{\Theta}\}}(u(\mathbf{k}^j, t))$(refer to equation (4.8) for further depiction). Let us then express our problem for these particular choices of functions, over a small neighborhood around a grid position $\mathbf{k} \in \mathcal{V}$ of size m_s. Let $\mathbf{w}_t(\mathbf{k}), \mathbf{w}_t^\star(\mathbf{k})$ collect the intensities of the volumetric densities $\mathbf{w}_t, \mathbf{w}_t^\star$ on the considered neighborhood. The vector $\mathbf{u}_{\boldsymbol{\Theta}}$ concatenates m_s times the elements of $\boldsymbol{\Theta}$. By plugging the latter considerations in (4.23), we obtain the following local joint volume-velocity functional:

$$\begin{aligned} f_j\left(\mathbf{w}_t(\mathbf{k}), \mathbf{w}_{t+1}(\mathbf{k}), \boldsymbol{\Theta}\right) = \|\mathbf{w}_t(\mathbf{k}) - I(\mathbf{u}_{\boldsymbol{\Theta}})\mathbf{w}_{t+1}(\mathbf{k})\|_2^2 + \\ \lambda \left[\|\mathbf{w}_t(\mathbf{k}) - \mathbf{w}_t^\star(\mathbf{k})\|_2^2 + \|\mathbf{w}_{t+1}(\mathbf{k}) - \mathbf{w}_{t+1}^\star(\mathbf{k})\|_2^2 \right], \end{aligned} \tag{4.25}$$

where λ can be understood a the ratio between the noise variances of the brightness constancy and that of the volumetric density discrepancy. We stress that, for $\mathbf{w}_t = \mathbf{w}_t^\star$, the expression in (4.25) is equivalent to (4.16). Thus, the problem reduces to solving the iterations $\boldsymbol{\Theta}^{(l+1)}$ by computing the expression in (4.17), where l denotes the iteration number.

Similar to the iterative LK descent scheme, we will resort to a gradient descent technique to look for the minimum of problem (4.25). Therefore, to solve for both the density distributions and displacement fields at the same time, we inject the sought vectors in an iterative descent procedure in the aim of coherently optimizing the 3D intensity consecutive topologies and their related flow field with regard to their joint structure. The sequence of minimizations writes, starting from initial guesses $\mathbf{w}_t^{(0)}(\mathbf{k}), \mathbf{w}_{t+1}^{(0)}(\mathbf{k}), \boldsymbol{\Theta}^{(0)}$:

$$\begin{bmatrix} \mathbf{w}_t^{(l+1)}(\mathbf{k}) \\ \mathbf{w}_{t+1}^{(l+1)}(\mathbf{k}) \\ \boldsymbol{\Theta}^{(l+1)} \end{bmatrix} = \begin{bmatrix} \mathbf{w}_t^{(l)}(\mathbf{k}) \\ \mathbf{w}_{t+1}^{(l)}(\mathbf{k}) \\ \boldsymbol{\Theta}^{(l)} \end{bmatrix} - \alpha^{(l)} \mathbf{S}^{(l)} \nabla_{\mathbf{w}_t, \mathbf{w}_{t+1}, \boldsymbol{\Theta}} f_j \left(\mathbf{w}_t(\mathbf{k}), \mathbf{w}_{t+1}(\mathbf{k}), \boldsymbol{\Theta} \right) \tag{4.26}$$

We note that partial derivative of $f_j \left(\mathbf{w}_t(\mathbf{k}), \mathbf{w}_{t+1}(\mathbf{k}), \boldsymbol{\Theta} \right)$ with respect to $\boldsymbol{\Theta}(\mathbf{k})$ is equivalent to that of the problem (4.17) since only the correspondent term in (4.25) depends on $\boldsymbol{\Theta}$. The partial derivatives of $f_j \left(\mathbf{w}_t(\mathbf{k}), \mathbf{w}_{t+1}(\mathbf{k}), \boldsymbol{\Theta}^{(l)} \right)$ can be efficiently evaluated via the following formula:

$$\nabla_{\mathbf{w}_t} f_j \left(\mathbf{w}_t(\mathbf{k}), \mathbf{w}_{t+1}(\mathbf{k}), \boldsymbol{\Theta} \right) = 2\lambda \left[\left(\mathbf{w}_t(\mathbf{k}) - \mathbf{w}_t^{\star}(\mathbf{k}) \right) + \left(\mathbf{w}_t(\mathbf{k}) - I(\mathbf{u}_{\boldsymbol{\Theta}(\mathbf{k})}) \mathbf{w}_t(\mathbf{k}) \right) \right] \tag{4.27}$$

$$\begin{aligned} \nabla_{\mathbf{w}_{t+1}} f_j \left(\mathbf{w}_t(\mathbf{k}), \mathbf{w}_{t+1}(\mathbf{k}), \boldsymbol{\Theta} \right) &= 2\lambda \left[\left(\mathbf{w}_{t+1}(\mathbf{k}) - \mathbf{w}_{t+1}^{\star}(\mathbf{k}) \right) \right] \\ &\quad + 2\lambda \left[\left(-I^T(\mathbf{u}_{\boldsymbol{\Theta}}) \mathbf{w}_t(\mathbf{k}) + I^T(\mathbf{u}_{\boldsymbol{\Theta}}) I(\mathbf{u}_{\boldsymbol{\Theta}}) \mathbf{w}_{t+1}(\mathbf{k}) \right) \right] \end{aligned} \tag{4.28}$$

4.4 Assessement

We have proposed in this chapter an alternative to state-of-the-art methods for velocity estimation in a tomoPIV setting. The purpose of this section is to characterize our methods with emphasis on its response in different synthetic scenarios, compared to more classical methodologies employed in tomoPIV. This section is organized as follows. First of all, we bring some additional information on the synthetic setting described in Section 3.10.1. We then proceed to describing the metrics used to quantify our results and associate some intuitive nomenclature to employed methods. Finally, Section 4.4.4 provides our assessment outcome.

4.4.1 Synthetic Setting

The volumetric density estimation of the particles is a crucial step towards the accurate reconstruction of the velocity fields. The output of the former has a knock-on effect on the subsequent/joint velocity estimation. For this reason, we will briefly recall here the test settings we have considered in Section 3.10 for the volume retrieval. Then, we will give details on our displacement test.

Recall on Image Models

We have established in the previous chapter that we decoded the tomoPIV signal following the model $\mathbf{y} = \mathbf{B}\mathbf{s}$, with $\mathbf{B} = \tilde{i}\mathbf{D}\mathbf{G}$. As it turns out, the corresponding estimated signal, *i.e.*, $\mathbf{s}^{\star}$ is the **sparse** intensity distribution of the particles in the 3D scene. We take advantage of our **structured-sparsity** model to recompute the **denser** blob distribution,

that is $\mathbf{w}^\star = \mathbf{G}\mathbf{s}^\star$, which is more advantageous for the subsequent velocity estimation than the sparse distribution. Notice that this computation acts as a smoothing of the image sequences. We indicate that the volumetric densities $\mathbf{w}_t^\star, \forall t$ are estimated with bpADMM+, refer to the previous chapter for details.

We remind the reader that we have distinguished between three test cases for the image generation, refer to Section 3.10.1 for details. In a nutshell, **Test Case 1(·)** considers an ideal scenario where the images are computed following $\mathbf{y} = \mathbf{B}\tilde{\mathbf{s}}$; **Test Case 2(·)** considers a perturbed setting where $\mathbf{y} = \mathbf{D}\tilde{\mathbf{w}}$, meaning that we add some model noise on the particle positions; **Test Case 3(·)** estimated the volumetric densities out of perturbed images, that is $\mathbf{y} = \mathbf{D}\tilde{\mathbf{w}} + \mathbf{n}_t$. In **Test Case ·(a)**, we compute these estimations in a rough grid, whereas in **Test Case ·(b)**, we consider a refined grid. Based on the conclusions brought out by the assessment report in Chapter 3, working in the latter case increases the accuracy of the estimated volumetric intensities, as the modeling vector decreases as the refinement of the grid increases. We will thus estimate the velocity field in **Test Case ·(b)** and we will keep this notation for coherence purposes.

We will work in the same synthetic scenario as the one depicted in Section 3.10.1. We call to mind that we have estimated the volumetric intensities on a cuboid partitioned into a cartesian grid of $61 \times 61 \times 19$ voxels, with voxel unit set at 1 arb. u. In order to avoid border discontinuities, we reconstruct the velocity fields out of the initially estimated densities on a smaller grid of of $47 \times 47 \times 7$ voxels, with voxel unit set at 1 arb. u.. Moreover, as all of the tested methods can be divided in local problem, we thus estimated local velocity fields on windows of size $m_s = m_w \times m_w \times m_w$.

Precision on the Transport Model

We compute the sequence of volumetric densities with respect to the velocity field following:

$$I\left(\tilde{\mathbf{u}}_t\right)\tilde{\mathbf{w}}_{t+1} - \tilde{\mathbf{w}}_t = \mathbf{0}_m, \tag{4.29}$$

where $\tilde{\mathbf{u}}_t = \left[\tilde{u}^T\left(\mathbf{k}^1, t\right) \quad \dots \quad \tilde{u}^T\left(\mathbf{k}^m, t\right)\right]$ is the actual fluid velocity, $\tilde{\mathbf{w}}_t, \tilde{\mathbf{w}}_{t+1}$ are the ground truth volumetric intensities and $I(\cdot)$ is the warping operator. The velocity field $\tilde{\mathbf{u}}_t$ is computed as a shear displacement. The displacement at each grid point writes:

$$\tilde{u}\left(\mathbf{k}^j, t\right) = \begin{bmatrix} a_u k_3^j & 0 & 0 \end{bmatrix}^T, \tag{4.30}$$

where $a_u = 0.05$ arb. u.

4.4.2 Description of Evaluation Criteria

The quality of the velocity estimation can be addressed with respect to the average norm of the error between estimated and ground truth displacement in each point, that is:

$$MSE = \frac{\left\|\tilde{u}\left(\mathbf{k}^j, t\right) - \boldsymbol{\Theta}^\star\right\|_2^2}{a}, \tag{4.31}$$

where $\boldsymbol{\Theta}^\star$ is the j^{th} estimated velocity field and a the dimension of the space. We specify that for our experiment we have chosen $a = 3$.

The Angular Displacement Error (ASE) computes the angular deviation between estimated and ground truth displacement and writes:

$$ASE = \arccos\left(\frac{\tilde{u}^T\left(\mathbf{k}^j, t\right)}{\left\|\tilde{u}\left(\mathbf{k}^j, t\right)\right\|_2}\frac{\boldsymbol{\Theta}^\star}{\left\|\boldsymbol{\Theta}^\star\right\|_2}\right). \tag{4.32}$$

4.4.3 Nomenclature

We will compare our method with two other techniques, extensively employed in the literature. The latter address the problem (4.6) with $f_r(\mathbf{u}_t, \boldsymbol{\Theta}) = \sum_j \mathbb{I}_{\{\boldsymbol{\Theta}\}}(u(\mathbf{k}^j, t))$, same as our method. For $f_d(\boldsymbol{\Theta}) = \|\mathbf{w}_t - I(\mathbf{u}_{\boldsymbol{\Theta}})\mathbf{w}_{t+1}\|_2^2$, we will refer to the Iterative LK method. When the velocity is sought on a discrete state space, we will call it LK-Discrete. For $f_d\left(\mathbf{u}_{\boldsymbol{\Theta}}\right) = C\left(\mathbf{w}_t, I(\mathbf{u}_{\boldsymbol{\Theta}})\mathbf{w}_{t+1}\right)$, see equation (4.13), where we seek the displacement vector on a discrete state space, we will refer to 3D-Cross Correlations. Our method has been coined JVVE.

4.4.4 Velocity Reconstruction Assessement

We are interested in how our method responds to different tomoPIV settings, compared to state-of-the-art procedures. To alleviate the complexity of the calculations, we have computed our quantifying metrics on a slice of the cuboid corresponding to $k_3^j = 0$, $\forall j \in \{1, \ldots, m\}$. Let us first observe the magnitude of the ground truth displacement on Figure 4.3; the magnitude of the fields is of sub-voxelic order and varies rather slowly. The latter represents a shear layer displacement field and follows the formula (4.30), where the linear displacement gradient $a_u = 0.05$ is chosen small. According to [78], such a choice tends to encourage the coherent displacement of ghost particles and thus, to aggravate the corresponding velocity estimation.

Let us now consider a scenario characterized by a very high seeding density, *i.e.*, ppp $= 0.34$. As mentioned before, the volumetric densities are estimated with bpADMM+ in a setting depicted by **Test Case 1(b)**. We obtain a volumetric reconstruction quality factor of $Q = 0.8954$ for $\mathbf{w}_t^\star$ and of $Q = 0.9156$ for $\mathbf{w}_{t+1}^\star$. Figure 4.5 offers an illustration of $\widetilde{\mathbf{w}}_t$ versus $\mathbf{w}_t^\star$ for consecutive frames. We notice in particular the low quality of the reconstruction, translated here by missed detections and ghost particles. Starting from these volumetric estimations, the velocity fields are computed locally on $5 \times 5 \times 5$ windows. Figure 4.4 portrays such a scenario, for **Test Case 1(b)**; more specifically, it illustrates the magnitude of the reconstructed velocity fields for our chosen methods. While the profile of the ground truth velocity field is respected, we notice some debris which suggest that the methods have failed to accurately reconstruct the motion in a few isolated areas. Our method copes to a higher degree than the Iterative LK procedure with spurious reconstructions; we acknowledge the fact that it outputs a lower number of heretical estimations than its compeer, managing thus to correct some underdeterminations on the reconstructed volumetric space. We address however the fact that due to its architecture, in the context on a low-resolved space, JVVE zeroes out the subsequent velocity estimation. The discrete methods output similar results. More precisely, both the LK-Discrete and the

3D-Cross Correlations techniques roughly respect the velocity profile illustrated by Figure 4.4. The former fail nevertheless to reconstruct finer scales of the displacement fields, contrary to the their continuous counterparts and despite seeking for the velocity values on a generous discrete grid $\mathcal{U}_t \in \mathbb{R}^3, \text{Card}(\mathcal{U}_t) = 13456$ centered around the ground truth value. Figures 4.6 and 4.7 portray respectively the MSE and ASE in each space position. The latter are easy to read in companionship to Figure 4.4 and support our previous claims. The MSE chart is in adequacy with the magnitude chart: whenever the velocity is biased, the MSE increases. As observed in the magnitude profiling, the performance of the continuous methods are somewhat mirrored in that of their discrete compeers, which output less resolved estimations. As for the ASE figure, we notice higher angular deviations from the ground truth when the latter approaches zero; the associated reconstruction have however a very low magnitude. We retain from this test case that *(i)* the space needs to be sufficiently resolved in order to enable an accurate velocity reconstruction *(ii)* the volumetric reconstruction needs to yield a high quality factor, which otherwise impacts negatively the subsequent motion estimation.

The conclusion to the latter case study is nevertheless antagonistic; as we have seen in Chapter 3, the quality factor of the reconstruction diminishes inversely proportional to the seeding density. There is a need for a trade-off. We evolve thus towards **Test Case 1(b)**, where we choose a lower, more tractable seeding density, *i.e.*, ppp $= 0.2$. bpADMM+ outputs reconstructions of quality factors of $Q : 0.9533$ for $\mathbf{w}_t^\star$ and of $Q = 0.9713$ for $\mathbf{w}_{t+1}^\star$. The original volumetric densities and the correspondent reconstructions are visible on Figure 4.9, where we can see that the latter are more faithful to their original rendition than in the previous test case. Figure 4.8 shows slightly less accurate reconstructed magnitude of the velocity signal than the ones output in the previous case study. While the magnitude of the velocity output by JVVE transitions (almost) smoothly from left to right, some detritus are still visible on the magnitude charts retrieved with the Iterative LK method and the discrete techniques. The discrete methods seem to output more debris in the case of a less-resolved volumetric space, contrary to the previous study case, where the ppp number was considerably higher. The same observations translate to Figures 4.10 and 4.11 illustrating respectively, the MSE and the ASE in each grid point, which show that our method copes with some indeterminations there where its compeers have failed.

Finally, we simulate a scenario closer to the real-world application, for ppp $= 0.2$. To recall, in *i.e.*, **Test Case 3(b)** model noise is added on the particle position and the 2D observations are perturbed with a Gaussian noise of variance 0.01. Here, bpADMM+ retrieves the volume with a quality factor of $Q = 0.8411$ for $\mathbf{w}_t^\star$ and of $Q = 0.8555$ for $\mathbf{w}_{t+1}^\star$. Figure 4.13 renders these reconstructions (bottom row) with respect to their original counterparts (top row); more specifically, the low quality factors are explained by the ghost particles and the missed detections, phenomena clearly noticeable on the said charts. Figure 4.12 illustrates the magnitude of the subsequent velocity reconstructions. Overall, the performance is slightly deteriorated compared to the ideal previous scenario. Moreover, figures 4.14 and 4.14 lead to the same conclusion. Whatever the scenario, JVVE deals better than its unregularized companion with some underdeterminations related to poorly reconstructed volumes.

In practice, the problem is more complex and there are myriads experimental factors to

account for. Our assessment study gives us an intuition of the benefits of minimization an appropriately formalized regularized functional in a tomoPIV scenario. In fact, we have seen in the current report that constraining the data term may help adjusting some of the errors on the previously estimated 3D intensities. We believe that further constraining the velocity field may considerably enhance the accuracy of the motion estimation.

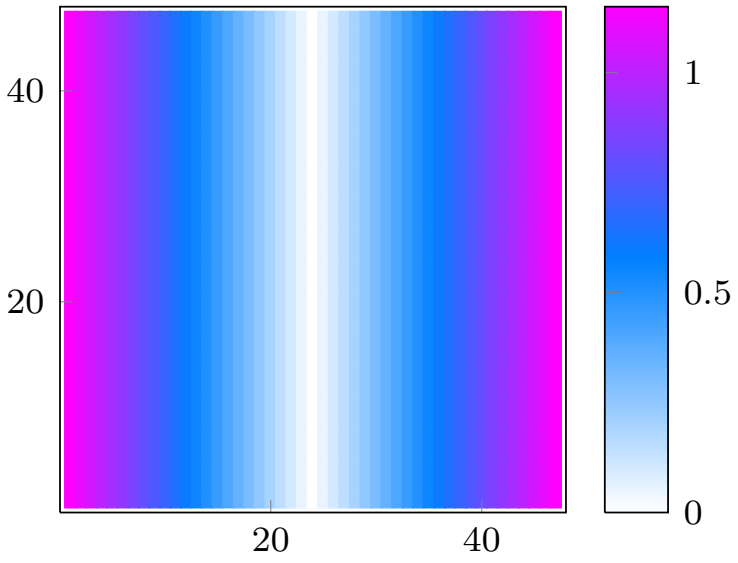

Figure 4.3: Magnitude of the ground truth velocity.

4.5 Summary

In an analogue way as for the volume reconstruction problem, we have shown in the current chapter that the tomoPIV velocity problem can be recast within a general optimization framework. More specifically, we have evolved towards a joint volume-velocity reconstruction problem by properly formalizing the nexus between these unknown quantities. Results have shown that our so defined method copes better than its unregularized counterpart with some imprecisions on the initially estimated volumetric distribution, making it more suitable for real-world application.

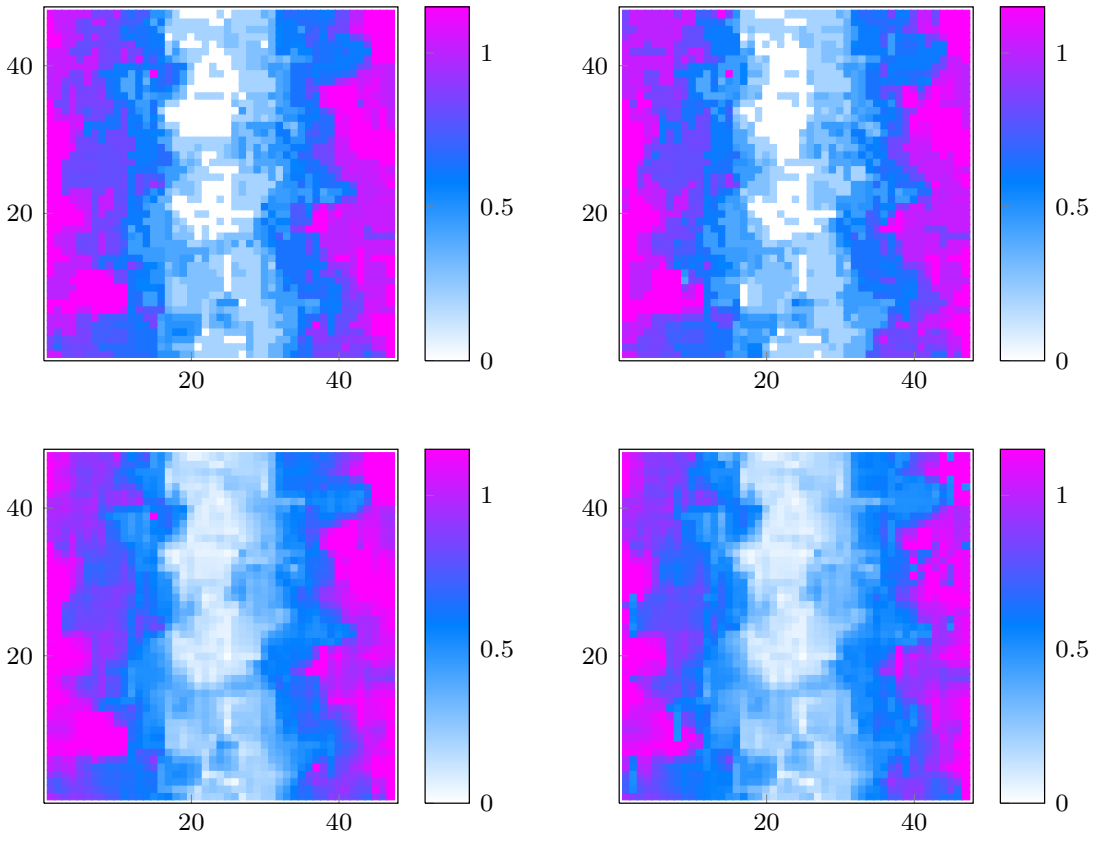

Figure 4.4: Magnitude of the reconstructed velocity fields, for ppp = 0.34 in **Test Case 1(b)**. Top row, from left to right: LK-Discrete and 3D-Cross Correlations. Bottom row, from left to right: Iterative LK and JVVE.

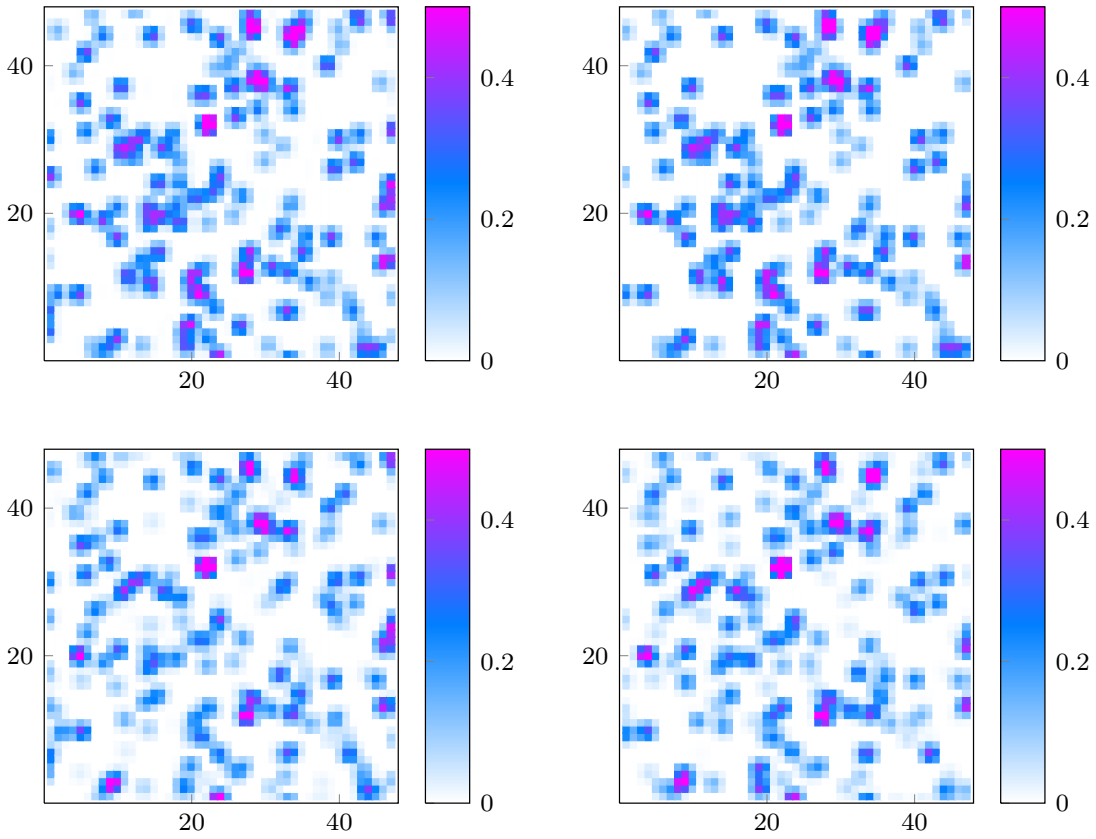

Figure 4.5: Ground truth (top row) and estimated volumetric densities (bottom row) at consecutive time frames (from left to right) for ppp = 0.34 in **Test Case 1(b)**.

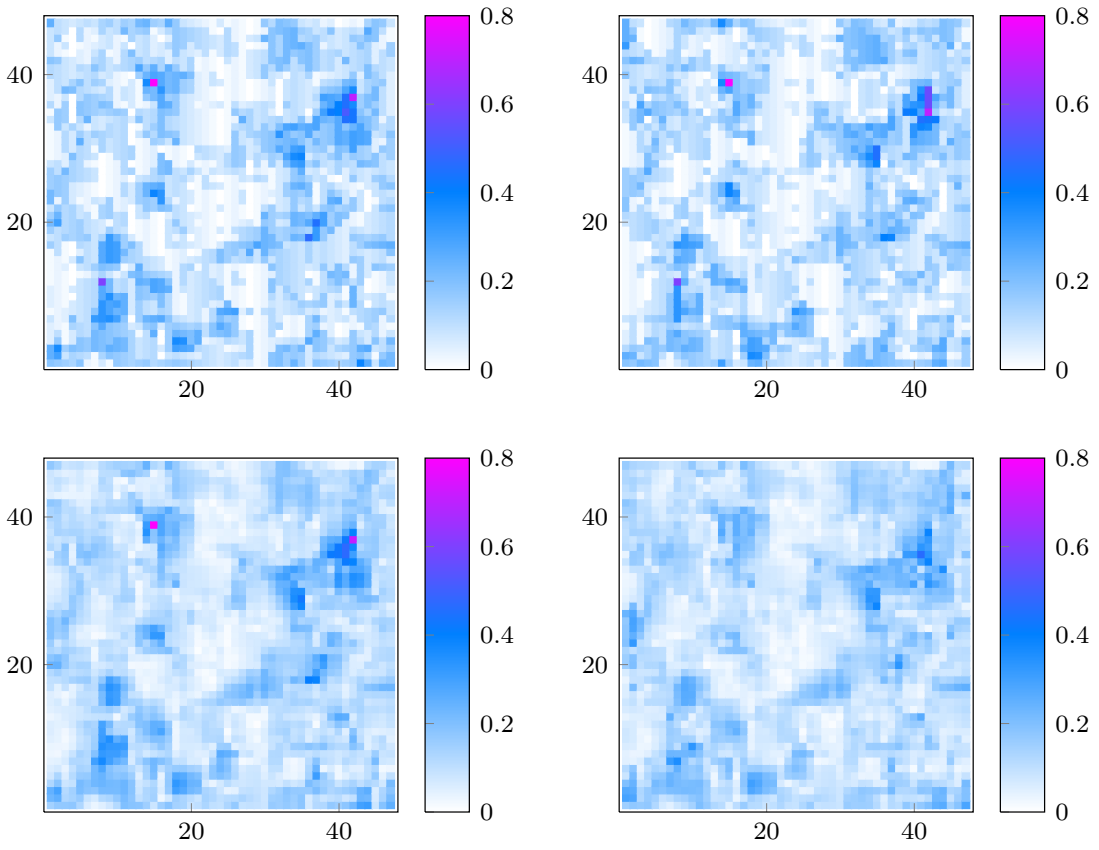

Figure 4.6: MSE for ppp $= 0.34$ in **Test Case 1(b)**. Top row, from left to right: LK-Discrete and 3D-Cross Correlations. Bottom row, from left to right: Iterative LK and JVVE.

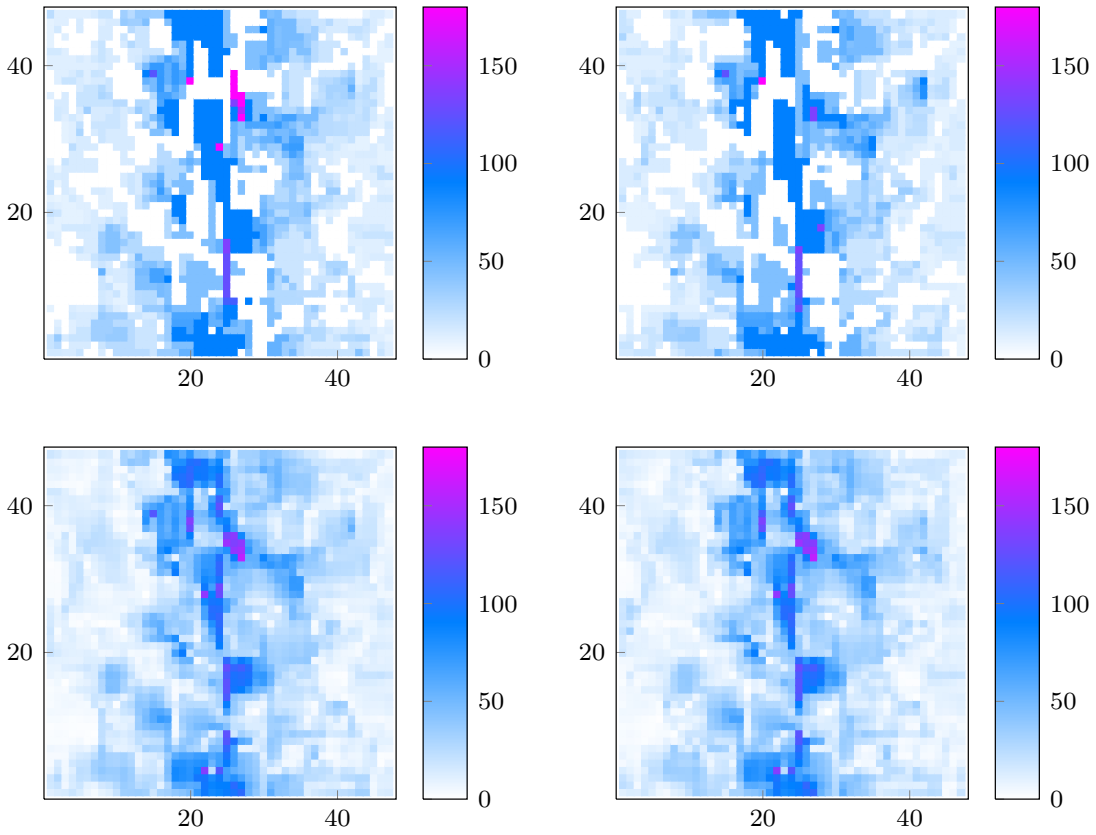

Figure 4.7: *ASE* for ppp = 0.34 in **Test Case 1(b)**. Top row, from left to right: LK-Discrete and 3D-Cross Correlations. Bottom row, from left to right: Iterative LK and JVVE.

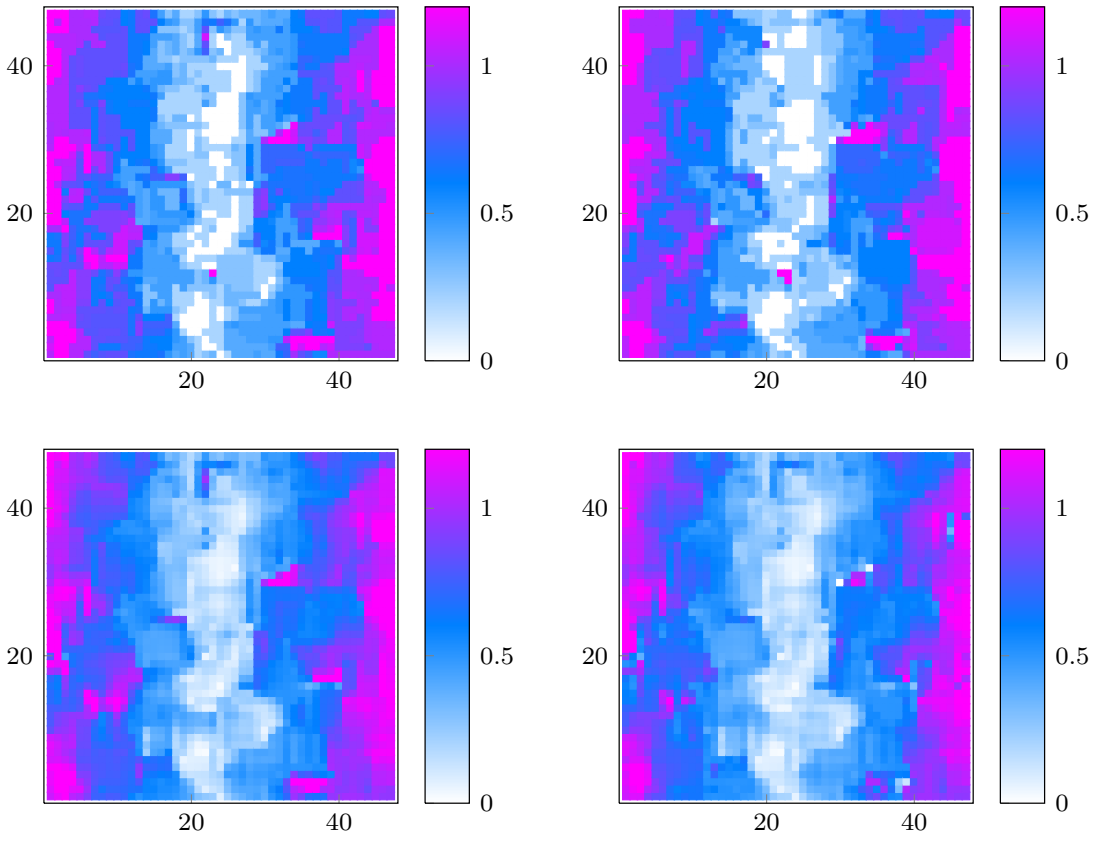

Figure 4.8: Magnitude of the reconstructed velocity fields, for ppp = 0.2 in **Test Case 1(b)**. Top row, from left to right: LK-Discrete and 3D-Cross Correlations. Bottom row, from left to right: Iterative LK and JVVE.

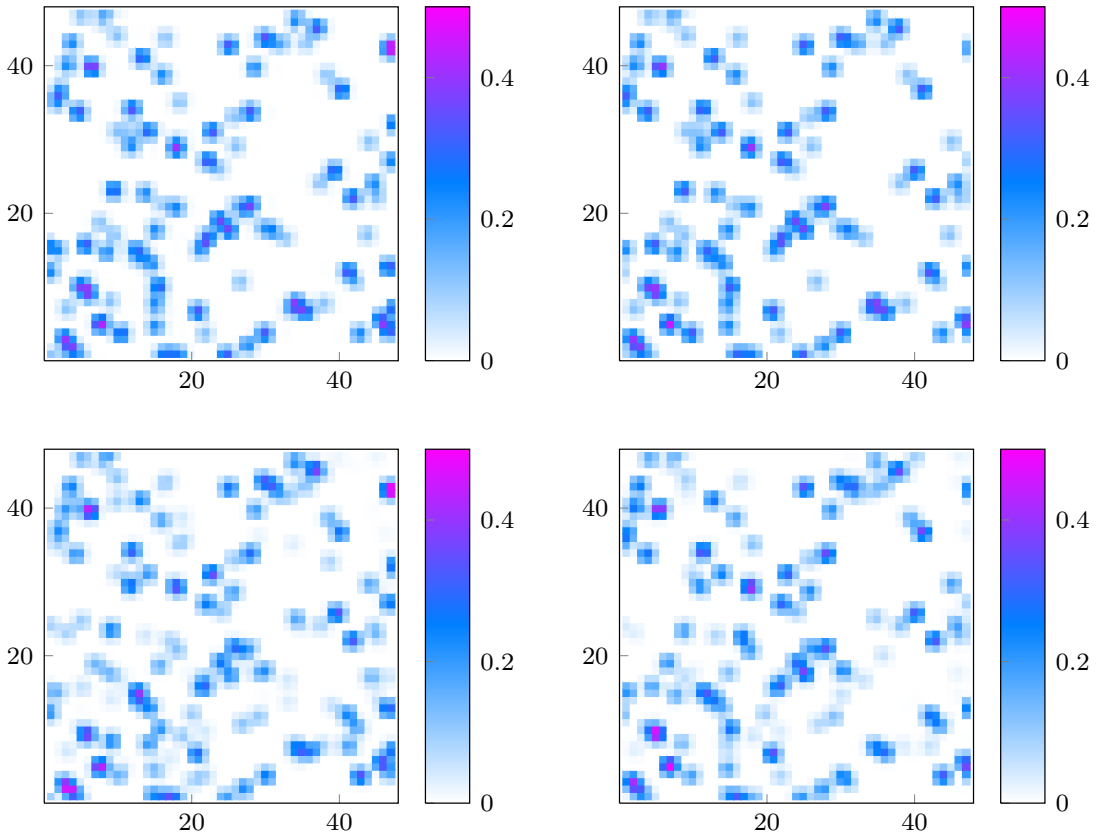

Figure 4.9: Ground truth (top row) and estimated volumetric densities (bottom row) at consecutive time frames (from left to right) for ppp = 0.2 in **Test Case 1(b)**.

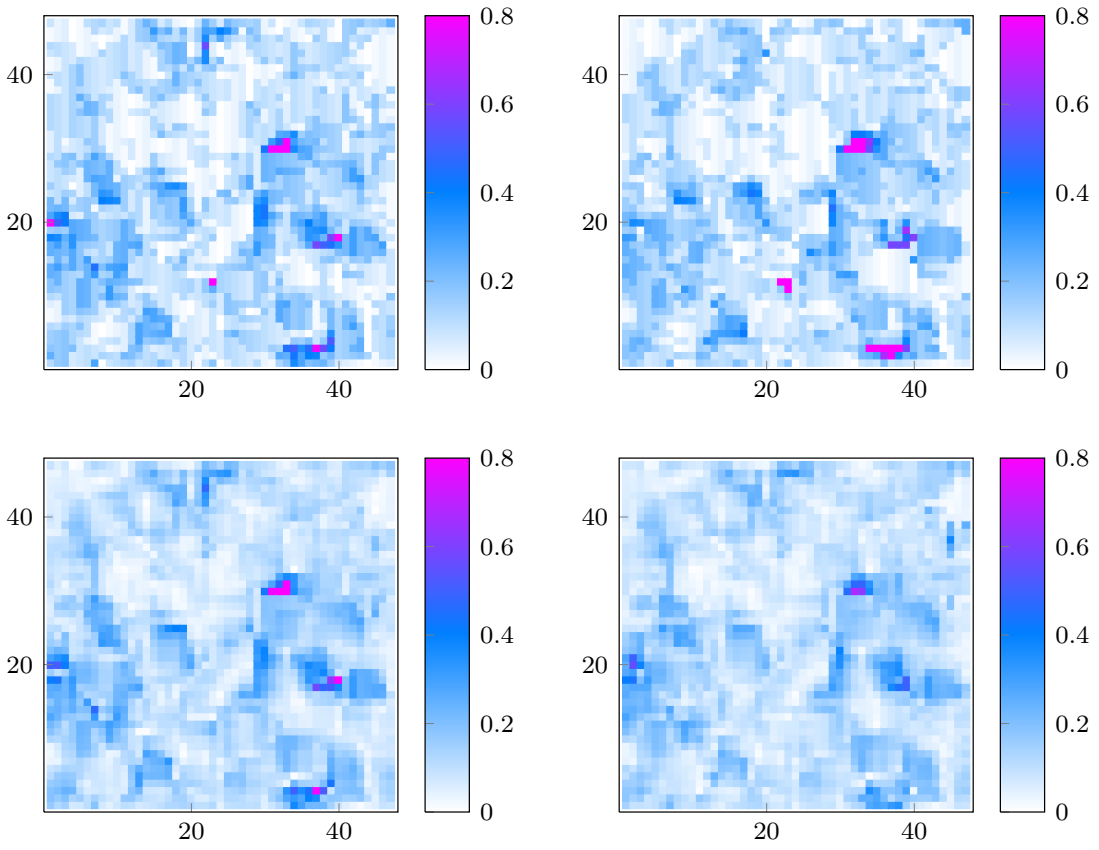

Figure 4.10: MSE for ppp = 0.2 in **Test Case 1(b)**. Top row, from left to right: LK-Discrete and 3D-Cross Correlations. Bottom row, from left to right: Iterative LK and JVVE.

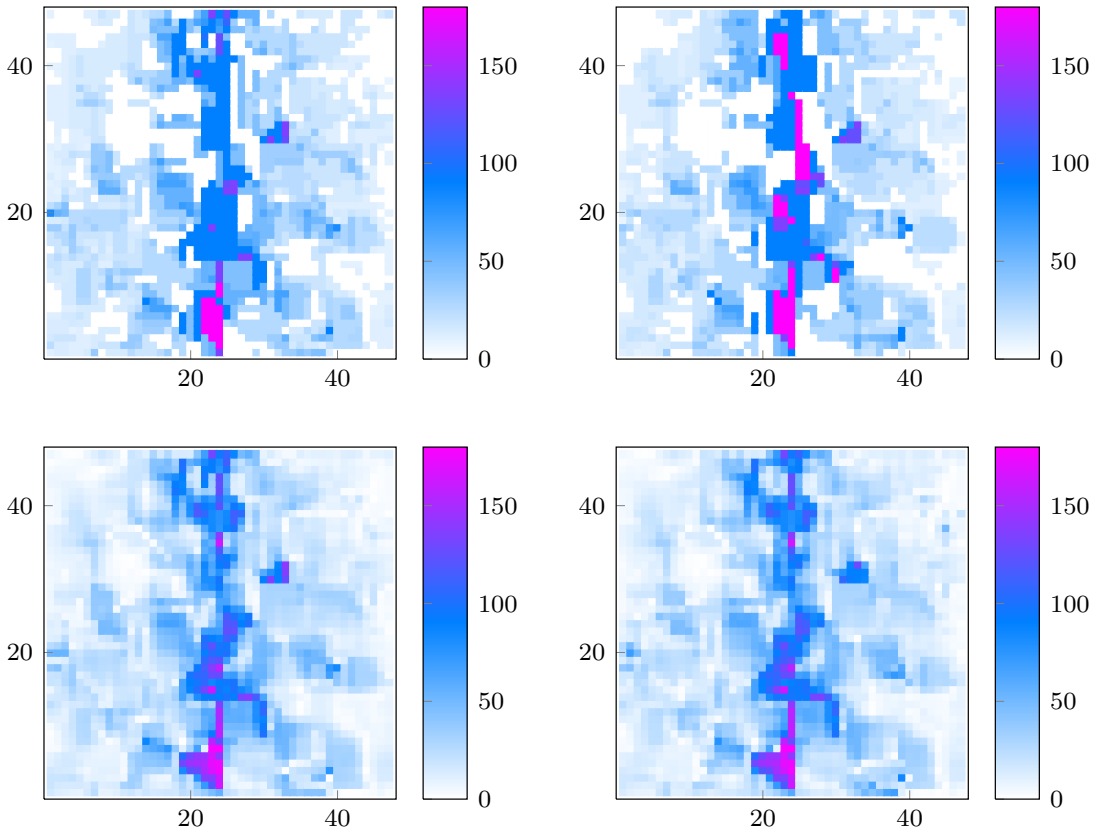

Figure 4.11: *ASE* for ppp = 0.2 in **Test Case 1(b)**. Top row, from left to right: LK-Discrete and 3D-Cross Correlations. Bottom row, from left to right: Iterative LK and JVVE.

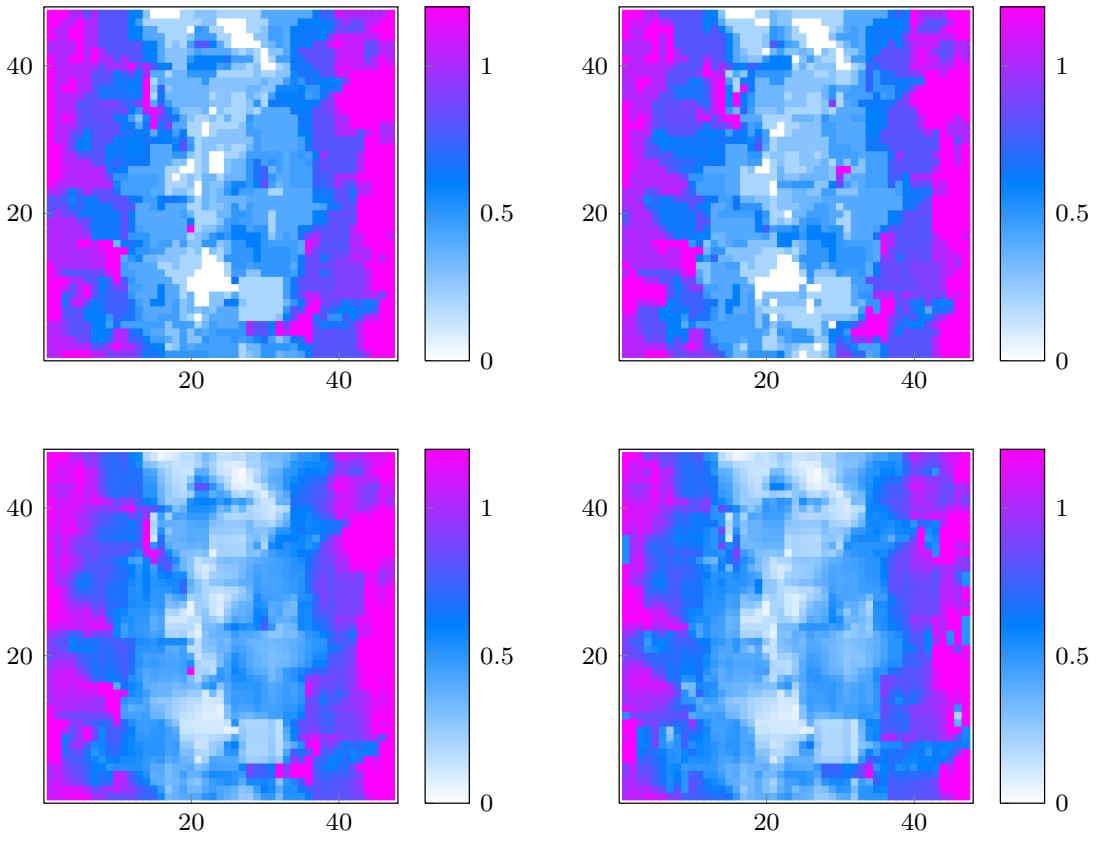

Figure 4.12: Magnitude of the reconstructed velocity fields, for ppp = 0.2 in **Test Case 3(b)**. Top row, from left to right: LK-Discrete and 3D-Cross Correlations. Bottom row, from left to right: Iterative LK and JVVE.

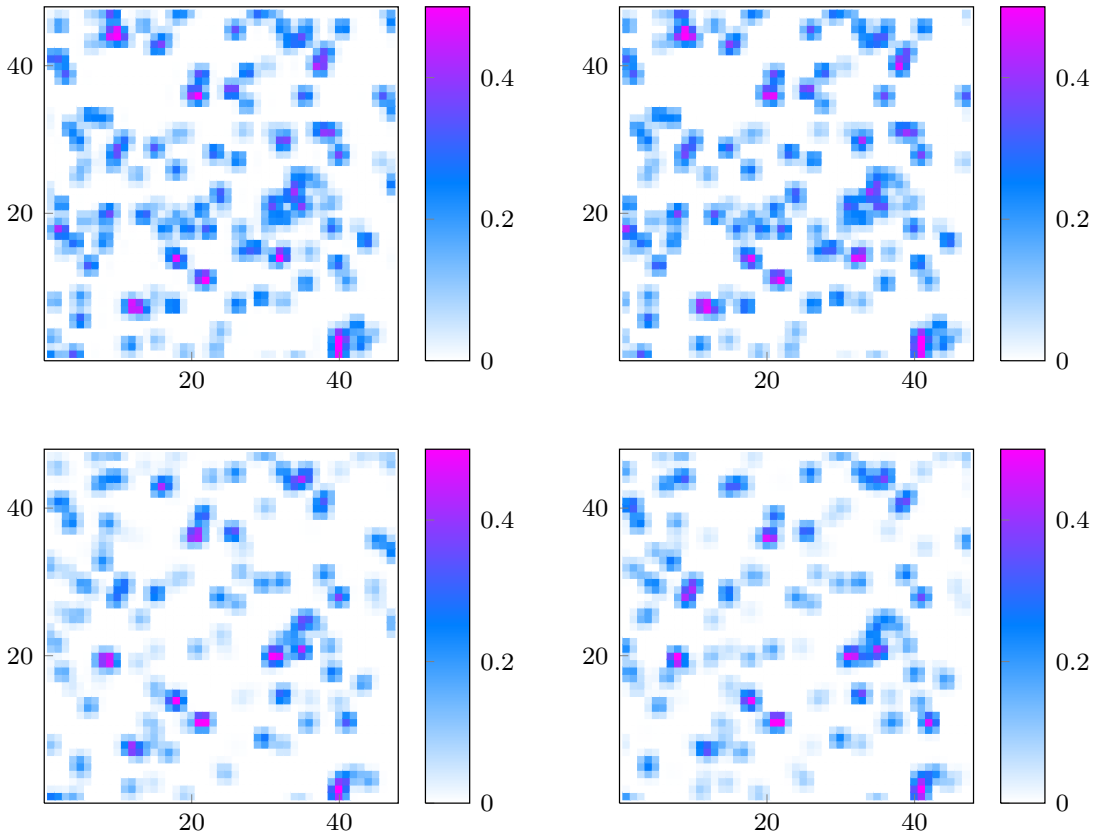

Figure 4.13: Ground truth (top row) and estimated volumetric densities (bottom row) at consecutive time frames (from left to right) for ppp = 0.2 in **Test Case 3(b)**.

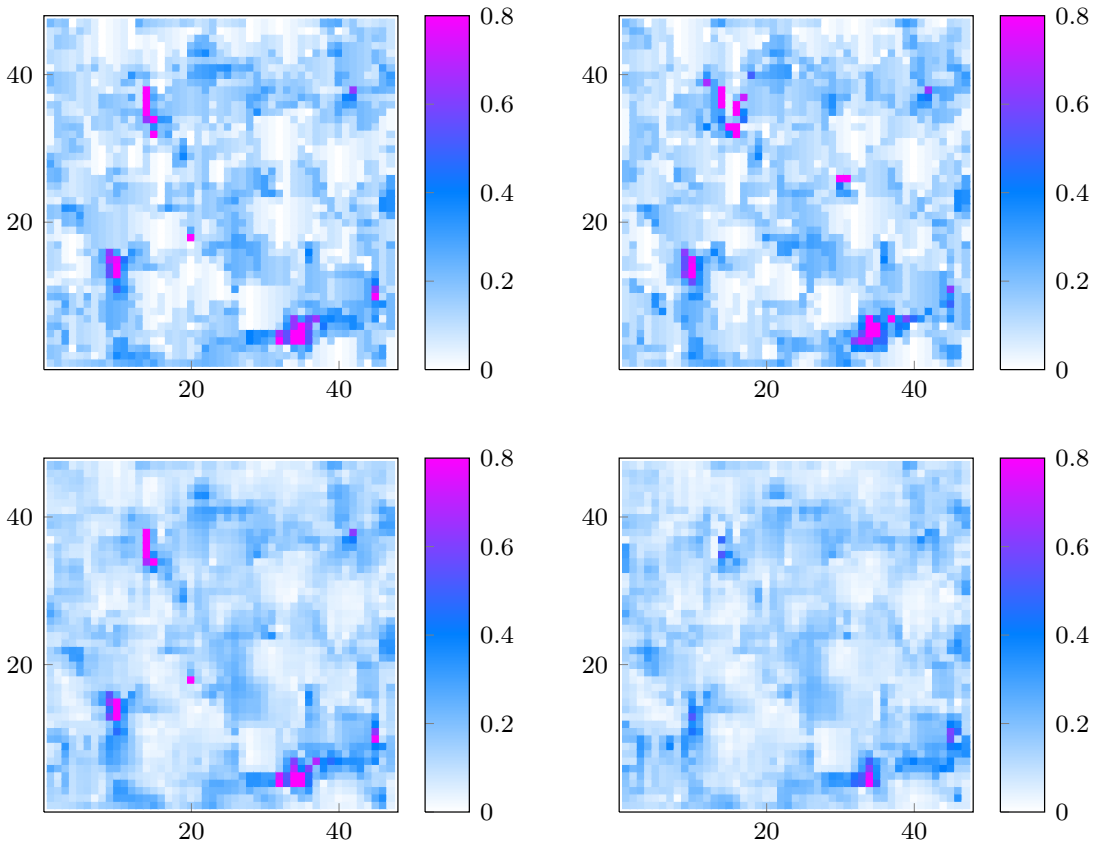

Figure 4.14: MSE for ppp $= 0.2$ in **Test Case 3(b)**. Top row, from left to right: LK-Discrete and 3D-Cross Correlations. Bottom row, from left to right: Iterative LK and JVVE.

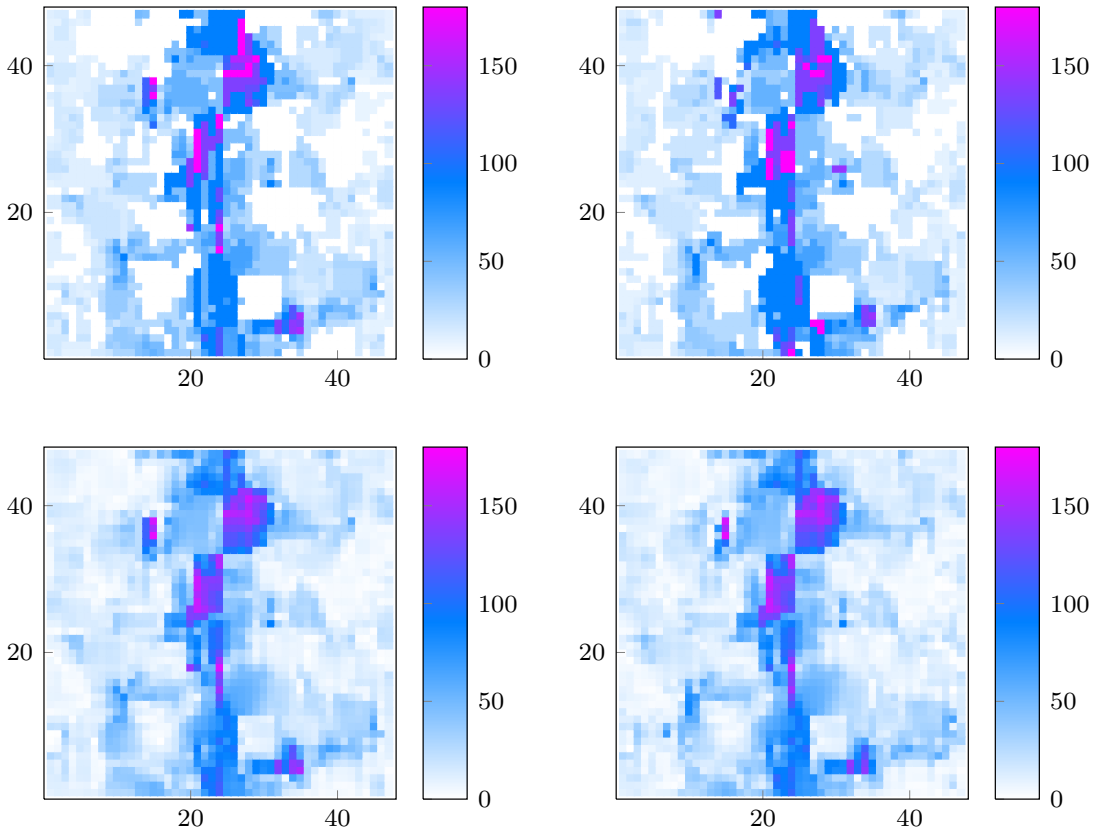

Figure 4.15: *ASE* for ppp = 0.2 in **Test Case 3(b)**. Top row, from left to right: LK-Discrete and 3D-Cross Correlations. Bottom row, from left to right: Iterative LK and JVVE.

Chapter 5. Conclusion and Perspectives

The challenge of the modern understanding of the 3D turbulent flows involves the need for *(i).* a reliable sensing technology *(ii).* the design of low-complexity estimation tools *(iii).* physically-sound priors. Classical approaches in computational fluid mechanics - such as Direct Numerical Simulation (DNS) of Large Eddy Simulation (LES) - to access to a quantitative information of the turbulence are confined to a limited range of physical scales that cannot fully describe the high non-linearities of the turbulent flow. To cope with this impediment, novel techniques relying on processing image sequences have been advanced (*e.g.*, [56]). Their methodology relies on conjugating approaches issued from the computer vision community with physical knowledge on fluid dynamics with the intent of designing an accurate motion estimator. Most of these procedures are formalized within a bidimensional framework, *i.e.*, they reconstruct a 2D motion field out of two consecutive 2D images, making them unsuitable for several fluid regimes with high 3D structures. Estimating the fluid motion within a 3D framework seems more pertinent. In seminal work [74], the velocity fields are retrieved from previously estimated volumetric densities. More recent contributions have opened the way towards a joint estimation approach [134]. These latter-day convincing results lead to predict that estimating the volumetric distribution with regard to the motion field that links them is the appropriate modus operandi towards rigorous retrieval of turbulent fluid flow.

In this thesis we have proposed a novel joint solution to address the task of 3D fluid motion estimation out of multiple sequences of synchronized 2D images. The theoretically frame has been presented with connections to the computer vision and signal processing fields, as well as to the tomoPIV community. Our work can be divided into three main tasks: *(i).* the design of a physically sound model with respect to the nature of the visualized scene *(ii).* the devise of volume reconstruction algorithmic schemes with low complexity that take into account known priors on the physical signal and output a satisfying estimation within a few iterations *(iii).* the formalization of a velocity reconstruction scheme that accounts for noisy settings and for the linked structure between two instantaneous volume reconstructions.

We have presented in chapter 2 the image formation and transport models with physical underpinning. In particular, we have advanced an alternative to the image formation models employed for the tomoPIV application. In fact, classical models within the community account for the Point Spread Function (PSF) inherent to the projection of a point into

a planar image by modeling the physical seeders as *particle blobs*, *i.e.*, voxel aggregates of several voxels width centered of the particle center, see [74]. However, their model is such that is does not allow the reconstruction of particle positions solely. More recently, *Champagnat et al.* have issued a physically sound projector that allows to recover the particle vision [49]. Their sparse reconstruction does not guarantee a good subpixel accuracy in the subsequent displacement estimation. Our hybrid contribution in terms of the projection model allows us to recover a sparse volumetric distribution and to estimate the velocity on its smoothed counterpart.

The row-action methods for volume reconstruction have gained a lot of interest in the tomoPIV community, despite suffering of a certain number of caveats. We have addressed this problem in chapter 3. More specifically, we have shown that the tomoPIV problem can be recast within a general optimization framework and that powerful convex-optimization tools can be used to solve the resulting problem. Firstly, we have put to forth that both physical constraints (sparsity/nonnegativity) and noisy observations can be properly handled by defining an adequate optimization problem. Then, we have emphasized that procedures with the same computational/storage features as the algebraic methods can be derived by exploiting the general framework of proximal methods [136]. In particular, we have shown that some standard algebraic methods can be seen as particular cases of proximal algorithms applied to a cost function not enforcing sparsity.

For the tomoPIV application, the velocity fields are usually computed out of consecutive 3D intensity volumetric distributions previously computed [74]. It is not until recently that the optimization framework has been formalized jointly in terms of volume and velocity [134]. In chapter 4, we have formulated an innovative penalty criterion as an intensity conservation function with respect to both the fluid trajectory and the static volumetric intensity distributions, which allows us to coherently optimize the 3D intensity consecutive topologies and their related flow field with regard to their shared structure .

The performance of our methods has been assessed by means of 3D simulations. A comparative study with state of the art paradigms acknowledged, for a random average case scenario of the tomographic application, its enhancement towards more accurate estimations for both the volume and the velocity reconstructions. Besides its relevance regarding tomoPIV, our methods are also suitable for any other complex scenes (medical imaging, crowd tracking, ...).

Discussions and Perspectives

The conclusions on our methodologies forecast several enhancements to *(i).* current procedures designed with regard to the tomoPIV application *(ii).* already established signal processing paradigms applicable to different set-ups.

Towards a Refined Model

The projection model depicted in chapter 3 are based upon several simplifying assumptions, depicted in section 2.2.1. More precisely, we have approximated the realistic image formation model which accounts for the PSF. The idea would be to rephrase our

volume reconstruction model by benefiting from recent developments, such as accounting optical distortion effects [185] or integrating the parameters of the PSF in the calibration procedure.

Another refinement in the projection model is relative to the light scattering of the seeded particles. In fact, we have made the simplifying assumption that all the particles have the same diameter. In experimental scene, we are often confronted with a polydisperse seeding. Integrating a partial modeling of Mie scattering and of the particle diameter should be very effective for real-world experiments.

Sparse Pruning

We have led, in chapter 3, an all-encompassing comparison of the state of the art pruning procedures designed for the tomoPIV application which implicitly incorporate sparsity priors. A recent contribution [55] shows that tracer particles are quasi-systematically in the direct vicinity of local maxima of reconstructions obtained with a more classical approach [15]. This recent procedure relies on a heuristic scheme and is prone to degrade the feasible set of the solutions to the volumetric estimation problem. Our input would be to use signal processing tools to estimate the local maxima of the volumetric initial reconstruction by explicitly incorporating sparsity priors. On long term, we would theoretically investigate under which constraints the correspondent reduced feasible set is equivalent to its original counterpart.

Proximal Methods for Noisy Settings

Synthetic assessment of the volume reconstruction problem leads to think that proximal gradient algorithms penalized by a "proximity term" $\alpha^{(k)}\mathrm{D}(\bullet, \bullet^{(k)})$, where $\mathrm{D}(\cdot, \cdot)$ is a Bregman distance, are more robust within a noisy setting. More precisely, we have considered the case when the proximity term is defined by the KL divergence. Our interest is to tackle the volume reconstruction problem with an entropic ADMM, *i.e.*, by penalizing its correspondent proximity term by means of the KL divergence. Moreover, our enthusiasm for this class of algorithms is enhanced by its variants which can address the discrepancy-distance constrained model, see equation (3.6). This enables us to tune the associated regularizing parameter based on some physical intuition of the noise governing the observations, contrary to the proximal gradient methods (and variants) which solve problems (3.18) and (3.19) (with affiliated regularizing parameters less obvious to calibrate based on physical apprehension).

On long term, we would be interested in studying the convergence properties of such a algorithm, question which is still open in the signal processing community.

Low-complexity Velocity Estimators with Physical Priors

The state-of-the-art review in chapter 4 has revealed some fluid dedicated estimator, addressed until not solely in a 2D framework. On short term, it would be interesting to integrate to our joint functional operators mimicking regularity properties of the fluid motion, *i.e.*, coherent blobs of vorticity and divergence.

Such priors remain locally smoothing regularization terms and do not account for the global behavior of the chaotic fluctuations of turbulent flows. A recent contribution in the bidimensional context [92] suggested such a powerful scheme by accounting for the temporal relationship between the velocity fields (namely the Navier-Stokes equations). Since in a 3D context such estimation problems are far out of reach for current computational ressources, approximations of large-scale dynamical systems can be investigated to obtain a reduced-order counterpart of the original model.

Experimental Assessment

The robustness of our methods with respect to different characterizations of a real scene (i.e., change in illumination, large displacement fields) is to be verified by intensive experiments on real data. Furthermore, such parameters can be accounted for in future work and open the way for the design of a problem formulation closer to the physical anatomy of the scene.

Appendix A. Lagrangian and Eulerian Specification of the Flow Field

In the study of fluid motion there are two main approaches to describing the velocity profile through time and space. The first, known as the Lagrangian viewpoint, involves watching the trajectory of each individual fluid parcel as it travels from an initial location throughout the measurement domain. Plotting the position of such an individual parcel through time gives the pathline of the parcel. The alternative is the Eulerian description. The Eulerian specification of the flow field is a way of studying its properties as functions of time as the flow passes through fixed spatial locations.

In the sequel we will express, without further depiction, both the Lagrangian and Eulerian specifications of the flow field in the frame reference defined by $\mathrm{F_w} : (\mathbf{o}, \mathbf{x}_w, \mathbf{y}_w, \mathbf{z}_w)$.

Description

In the Lagrangian specification, we mentioned the fact that the fluid motion may be viewed as the motion of small identifiable fluid parcels. Accordingly, we can consider the positions $H(\cdot)$ of these fluid parcels as a function of the time. If we label the fluid elements with their Cartesian coordinates $\mathbf{h}^j = \begin{bmatrix} h_1^j & h_2^j & h_3^j \end{bmatrix}^T \in \mathbb{R}^3, \forall j \in \mathbb{N}$ expressed with respect to $\mathrm{F_w}$ at an initial time $t = 0$, the positions $H(\cdot)$ thus become functions of $\mathbf{h}^j$ and t. Therefore, in the Lagrangian depiction giving the position of the parcel labeled by $\mathbf{h}^j$ at time t, the flow is described as follows:

$$H(\mathbf{h}^j, t). \tag{A.1}$$

As a convention, we will write in the sequel the position of the parcel labeled by $\mathbf{h}^j$ at time t as H_t^j. Figure A.1(a) shows two different fluid particles and their particle paths for a short period of time.

In the Eulerian specification of the flow field, the flow quantities are depicted as functions of time as the flow passes through fixed spatial locations. Figure A.1(b) is a simple representation of this scenario. Specifically, the flow is described by a function

$$u(\mathbf{h}, t), \tag{A.2}$$

giving the flow velocity at position $\mathbf{h} \in \mathbb{R}^3$ at time t.

The two specifications are related as follows:

$$u(H(\mathbf{h}, t), t) = \frac{\partial H}{\partial t}(\mathbf{h}, t), \tag{A.3}$$

because both sides describe the velocity of the parcel labeled a at time t.

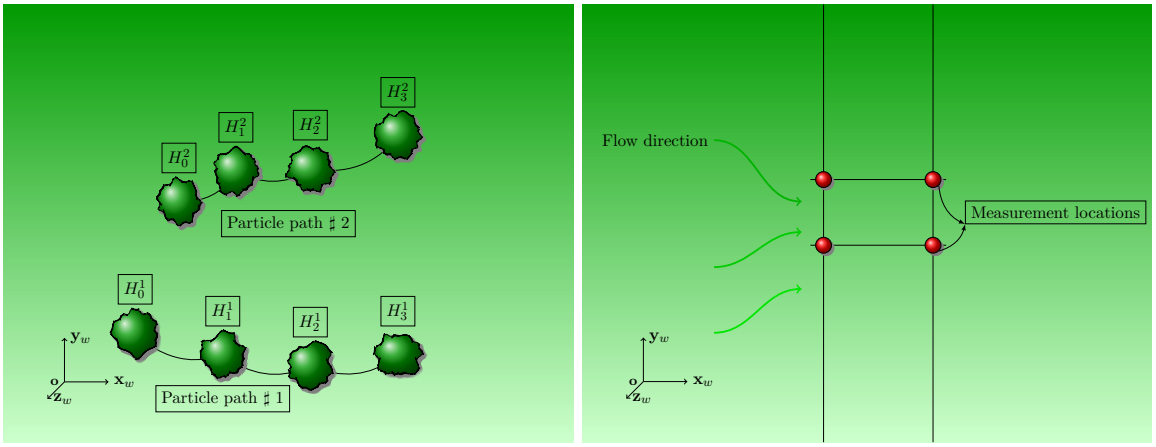

(a) Fluid particles and trajectories in Lagrangian view of fluid motion. The notation H_t^j represents particle $\sharp j$ at time t.

(b) Eulerian view of fluid motion.

Figure A.1: Eulerian and Lagrangian specifications of the fluid flow

Appendix B. Mie Scattering Coefficients

Our goal is to express an angle-dependent scattering model, where the scattering angle is defined as the angle between the light source direction and the detector direction in the scattering plane of the particle. The current appendix compiles essential definitions and developments destined to the comprehension of the light scattering theory by small particles and provides tools for accounting for local illumination for isotropic homogeneous spheres in the illumination model in the context of the tomoPIV application.

The light scattering behavior of a homogeneous and isotropic sphere is a subject highly documented and can be described either by geometrical optics [179] or using field wave theory [33]. We relate to the latter approach and reproduce results from the literature which assume a plane wave and solve it with respect to the boundary conditions between the medium and the surface of the particle.

Preliminaries

The nomenclature adopted in this appendix adheres to that given by figure B.1, which depicts the coordinates systems used to express the wave and the scattering planes. The incident wave is defined in the $(\mathbf{m}, \mathbf{x}_i, \mathbf{y}_i, \mathbf{z}_i)$ system originating in the center of the particle positioned in $\mathbf{m} \in \mathcal{V}$ and it propagates in the $\mathbf{z}_i$ direction.The orthonormal basis vectors $(\mathbf{e}_x, \mathbf{e}_y, \mathbf{e}_z)$ are in the directions of the positive $\mathbf{x}_i, \mathbf{y}_i$ and $\mathbf{z}_i$ axes. $(\mathbf{e}_r, \mathbf{e}_\theta, \mathbf{e}_\phi)$ are the orthonormal basis vectors associated with the spherical polar coordinate system (r, θ, ϕ), where θ is the scattering angle. The scattering plane is defined by the wave vector of the incident plane wave that we denote by $\mathbf{q}_i$ and the scattering vector $\mathbf{q}_s$ (defined with respect to the particle's center and the optical center of the sensor); it is convenient to resolve both the incident and the scattered light into components parallel $(\mathbf{e}_{\parallel \cdot})$ and perpendicular to the scattering plane $(\mathbf{e}_{\perp \cdot})$, with $\cdot \in \{i, s\}$, where i holds for incident and s for scattered. The polarization of the wave in the $\mathbf{e}_{\perp s}$ direction is associated with the $S_1(\theta, d_p)$ scattering function and the parallel polarization in the $\mathbf{e}_{\parallel s}$ direction is associated with the $S_2(\theta, d_p)$ scattering function, where d_p is the diameter of the particles, supposed much smaller than the wavelength of the medium.

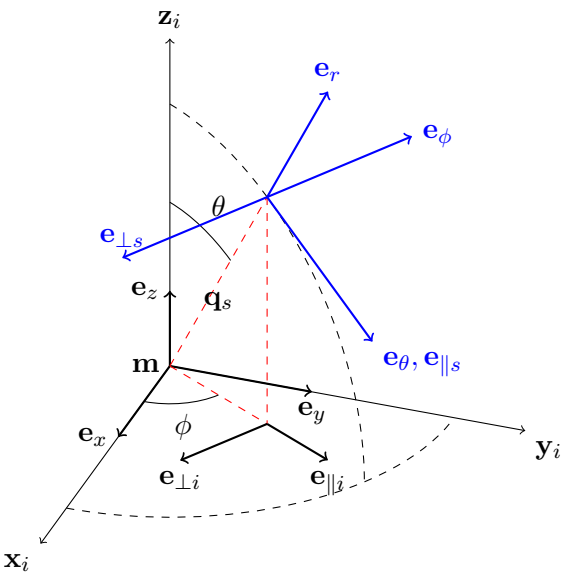

Figure B.1: Definition of the incident coordinates system and of the scattering plane.

Mie Scattering

This section is destined to give shallow theoretical insight for the computation of a set of Mie coefficients a_n, b_n, responsible for describing the efficiencies of extinction and scattering and two angular scattering function $S_1(\theta, d_p), S_2(\theta, d_p)$, responsible for the approximation of the propagation of the incident wave E_i with respect to the scattered wave E_s.

The projection of the electric vector field of the incident wave onto the two polarization directions (*i.e.*, perpendicular and parallel to the scattering plane), expressed with regard to the scattering functions $S_1(\theta, d_p), S_2(\theta, d_p)$ writes:

$$E_s = \begin{bmatrix} E_{s\theta} \\ E_{s\phi} \end{bmatrix} = \frac{\exp(-j\mathbf{q}_i^T \mathbf{q}_s)}{\mathbf{q}_i^T \mathbf{q}_s} \begin{bmatrix} S_1(\theta, d_p) & 0 \\ 0 & S_2(\theta, d_p) \end{bmatrix} \begin{bmatrix} -\sin\theta & \cos\theta \\ \cos\theta & \sin\theta \end{bmatrix} E_i \tag{B.1}$$

Assuming the near field effects are negligible with respect to the far field scattering, the resulting components of the scattered electric field then follow the form of a simple spherical wave. In the effort of giving a straightforward mathematical solution to the poorly intuitive problem of how a sphere of given size and optical properties absorbs and scatters light, Bohren and Huffman show that both the incident and the scattered field may be expanded in a infinite series of vector spherical harmonic ([33], eq. 4.45). Moreover, assuming that the scattered field is uniformly convergent such that the infinite series can be truncated at n_c terms, a small approximation error is guaranteed for n_c sufficiently big. The expressions of the scattering functions then write:

$$\begin{cases} S_1(\theta, d_p) = \sum_{n=1}^{n_c} \frac{2n+1}{n(n+1)} (a_n \pi_n + b_n \tau_n) \\ S_2(\theta, d_p) = \sum_{n=1}^{n_c} \frac{2n+1}{n(n+1)} (a_n \tau_n + b_n \pi_n), \end{cases} \tag{B.2}$$

where τ_n and π_n are angle-dependent functions computed following the recurrence formulas:

$$\begin{cases} \pi_n = \frac{2n+1}{n(n+1)} \cos\theta \pi_{n-1} - \frac{n}{n-1}\pi_{n-2}, \\ \tau_n = n\cos\theta\pi_n - (n+1)\pi_{n-1}, \end{cases} \tag{B.3}$$

stating with:

$$\pi_0 = 0; \pi_1 = 1.$$

and a_n and b_n are scattering coefficients obtained from the boundary conditions. In order to explicit the latter, we define the relative refractive index m and the size parameter x_p such as:

$$m = \frac{N_p}{N_m}, x_p = \frac{2\pi N_m d_p}{\lambda}, \tag{B.4}$$

where N_m and is the refractive index the medium. We further introduce the following functions used in the Mie theory:

$$\psi_n(\varpi) = \varpi j_n(\varpi) \tag{B.5}$$

$$\xi_n i(\varpi) = \varpi h_n^{(1)}(\varpi), \tag{B.6}$$

which are linear combinations of the spherical Bessel function j_n and of the spherical Bessel function of third kind $h_n^{(1)}$ (also known as the Hankel function). For completeness, the relationship between Bessel and spherical Bessel functions J_v, Y_v, with $v = n + \frac{1}{2}$ is given:

$$j_n(\varpi) = \sqrt[2]{\frac{\pi}{2\varpi}} J_v(\varpi) \tag{B.7}$$

$$y_n(\varpi) = \sqrt[2]{\frac{\pi}{2\varpi}} Y_v(\varpi), \tag{B.8}$$

and the Hankel function writes:

$$h_n^{(1)}(\varpi) = j_n(\varpi) + j y_n(\varpi). \tag{B.9}$$

Provided the permeability of the particle and the surrounding medium are equal, the scattering coefficients write:

$$\begin{cases} a_n = \frac{m\psi_n(mx_p)\psi_n^{'}(x_p) - \psi_n(x_p)\psi_n^{'}(mx_p)}{m\psi_n(mx_p)\xi_n^{'}(x_p) - \xi_n(x_p)\psi_n^{'}(mx_p)}, \\ b_n = \frac{\psi_n(mx_p)\psi_n^{'}(x_p) - m\psi_n(x_p)\psi_n^{'}(mx_p)}{\psi_n(mx_p)\xi_n^{'}(x_p) - m\xi_n(x_p)\psi_n^{'}(mx_p)}. \end{cases} \tag{B.10}$$

We express the fields into components parallel ($E_{\parallel \cdot}$) and perpendicular ($E_{\perp \cdot}$) to the scattering plane:

$$\begin{cases} E_{\parallel \cdot} = \cos\phi E_{x \cdot} + \sin\phi E_{y \cdot}, \\ E_{\perp \cdot} = \sin\phi E_{x \cdot} - \cos\phi E_{y \cdot}, \end{cases} \tag{B.11}$$

where $E_{x \cdot}$ and $E_{x \cdot}$ are the component of the incident wave along the $\mathbf{X}_i$ and $\mathbf{Y}_i$ axis, respectively. We can now express the relation between incident and scattered light such

that:

$$\begin{bmatrix} E_{\parallel s} \\ E_{\perp s} \end{bmatrix} = \frac{\exp[j\mathbf{q}_i(\mathbf{q}_s - z)]}{-j\mathbf{q}_i\mathbf{q}_s}) \begin{bmatrix} S_2(\theta, d_p) & 0 \\ 0 & S_1(\theta, d_p) \end{bmatrix} \begin{bmatrix} E_{\parallel i} \\ E_{\perp i} \end{bmatrix} \tag{B.12}$$

In order to represent the polarization state of a light ray traveling through space, we relate to the Stokes parameter $I.$ which is a measurement of the irradiance of the light:

$$I. =< E_{\parallel .} E^*_{\parallel .} + E_{\perp .} E^*_{\perp .} >, \tag{B.13}$$

$* \in \{ext, sca, abs\}$, where the latter notations hold for the extinction, the scattering and the absorption of the incident beam, according to three regimes of an electromagnetic wave hitting a particle in a non-absorbing medium. For an incident beam hitting a small particle in a non-absorbing medium, assuming the light is non-polarized, I_s writes:

$$I_s = S_{11}(\theta, d_p) I_i, \tag{B.14}$$

where

$$S_{11}(\theta, d_p) = \frac{1}{2}(|S_2(\theta, d_p)|^2 + |S_1(\theta, d_p)|^2). \tag{B.15}$$

Appendix C. Synthetic Configuration of the Imaging System

In our effort to closely depict the tomoPIV system, we synthesize the projection of the 3D space into the images. Note that $\mathcal{M}^c(\cdot)$ is entirely defined by the set of parameters $(f^c, d_1^c, d_2^c, n_1^c, n_2^c)$ characterizing the c^{th} camera, whereas $\mathcal{N}^c(\cdot)$ is defined with respect to the homogeneous matrix expressing the world coordinates with respect to the camera's coordinates.

Let $\mathcal{P}^c \subset \mathbb{R}^2$ be the image screen of the c^{th} camera. Then, $\mathcal{P}^c$ has its origin $\mathbf{o}^c = \begin{bmatrix} 0 & 0 \end{bmatrix}^T$ in the middle of the screen of the c^{th} camera's canonical reference system of coordinates such that:

$$\mathcal{P}^c = [-\frac{d_1^c}{2}, \frac{d_1^c}{2}] \times [-\frac{d_2^c}{2}, \frac{d_2^c}{2}], \tag{C.1}$$

where $\times$ denotes the cartesian product and $d_i^c \in \mathbb{R}$ is the dimension of the image plane along the i^{th} coordinate of the image system.

Let $\mathcal{H} = \{\mathbf{h}^1, \ldots, \mathbf{h}^8\} \in \mathbb{R}^3$ be the ensemble of the vertices of the cuboid $\mathcal{V}$. We suppose that the parameters of the cameras are completely known, which allows us to express the projections of the vertices into each one of the camera's planes following the model of a pinhole camera, such that:

$$\begin{cases} \mathbf{h}^{c,v} = \mathcal{N}^c(\mathbf{h}^v), \\ \mathbf{h}_{\text{img}}^{c,v} = \mathcal{M}^c(\mathbf{h}^{c,v}), \forall v \in \{1, \ldots, 8\}, \forall c \in \{1, \ldots, N_c\}, \end{cases} \tag{C.2}$$

where the ensemble $\mathcal{H}_{\text{img}}^c = \{\mathbf{h}_{\text{img}}^{c,1}, \ldots, \mathbf{h}_{\text{img}}^{c,8}\}$ collecting the projections of the vertices into the image plane is expressed in camera pixel coordinates and $\mathcal{H}^c = \{\mathbf{h}^{c,1}, \ldots, \mathbf{h}^{c,8}\}$ is expressed with respect to the camera coordinates system. Moreover, let $h_3^{c,v}$ designate the coordinates of the elements $\mathcal{H}_{\text{img}}^c$ along the $\mathbf{z}_{\text{cam}}^c$ axis.

We are interested in strategically placing the optical center $\mathbf{o}_{\text{cam}}^c$ of each camera such that all the vertices project within the boundaries of the their respective image planes. Firstly, we choose an initial position of the camera optical center expressed in world frame reference system. Then, we resort to an iterative dichotomous procedure which gradually advances

or withdraws $\mathbf{o}_{\text{cam}}^{c}$ with respect to the vertices' projections within the predefined limits $[m^c, M^c], m^c, M^c \in \mathbb{R}_+^3, M^c > m^c$ which write:

$$\begin{cases} m^c = 0; \\ M^c = L \left\| \begin{bmatrix} L_1 & L_2 & L_3 \end{bmatrix}^T \right\|, \forall L \in \mathbb{N}^\star; \\ \mathbf{d}^c = \frac{\mathbf{o} - \mathbf{o}_{\text{cam}}^c}{\|\mathbf{o}_{\text{cam}}^c\|}. \end{cases} \tag{C.3}$$

Algorithm 1 illustrates this optimization procedure.

for $c \leftarrow 1$ **to** N_c **do**
  0. Initialization $\mathbf{o}_{\text{cam}}^{c} = M^c, \forall c \in \{1, \ldots, N_c\}$;
  $\epsilon^c = 0, \epsilon^0 = 10 \exp -5$;
  Compute $\mathcal{H}_{\text{img},(0)}^{c}, h_{3,(0)}^{c,v}$ at the 0^{th} iteration;
  1. Choose L such that:

$$\begin{cases} \mathcal{H}_{\text{img},(0)}^{c} \subset \mathcal{P}^c; \\ h_{3,(0)}^{c,v} \geq f^c, \forall v \in \{1, \ldots, 8\}. \end{cases}$$

  2. repeat
    $l \leftarrow l + 1$;
    $a^c = \frac{m^c + M^c}{2}$;
    $\mathbf{o}_{\text{cam}}^{c} = a^c d^c$;
    Compute $\mathcal{H}_{\text{img},(l)}^{c}, h_{3,(l)}^{c,v}$ at the l^{th} iteration;
    if

$$\begin{cases} \mathcal{H}_{img,(l)}^{c} \subset \mathcal{P}^c; \\ h_{3,(l)}^{c,v} \geq f^c, \forall v \in \{1, \ldots, 8\}. \end{cases}$$

     then
      $m^c = a^c$;
    else
      $M^c = a^c$;
    end
    $\epsilon^c = M^c - m^c$;
  until $\epsilon^c > \epsilon^0$;
end

Algorithm 1: Optimization of the Imaging System

Figure C.1 illustrates the result of algorithm 1 for a 4-cameras configuration placed around a small volume of $\begin{bmatrix} L_1 & L_2 & L_3 \end{bmatrix}^T = \begin{bmatrix} 11 & 11 & 11 \end{bmatrix}^T$ images by cameras of $\begin{bmatrix} d_1^c & d_2^c \end{bmatrix}^T = \begin{bmatrix} 21 & 21 \end{bmatrix}^T$, for $c \in \{1, \cdots, 4\}$.

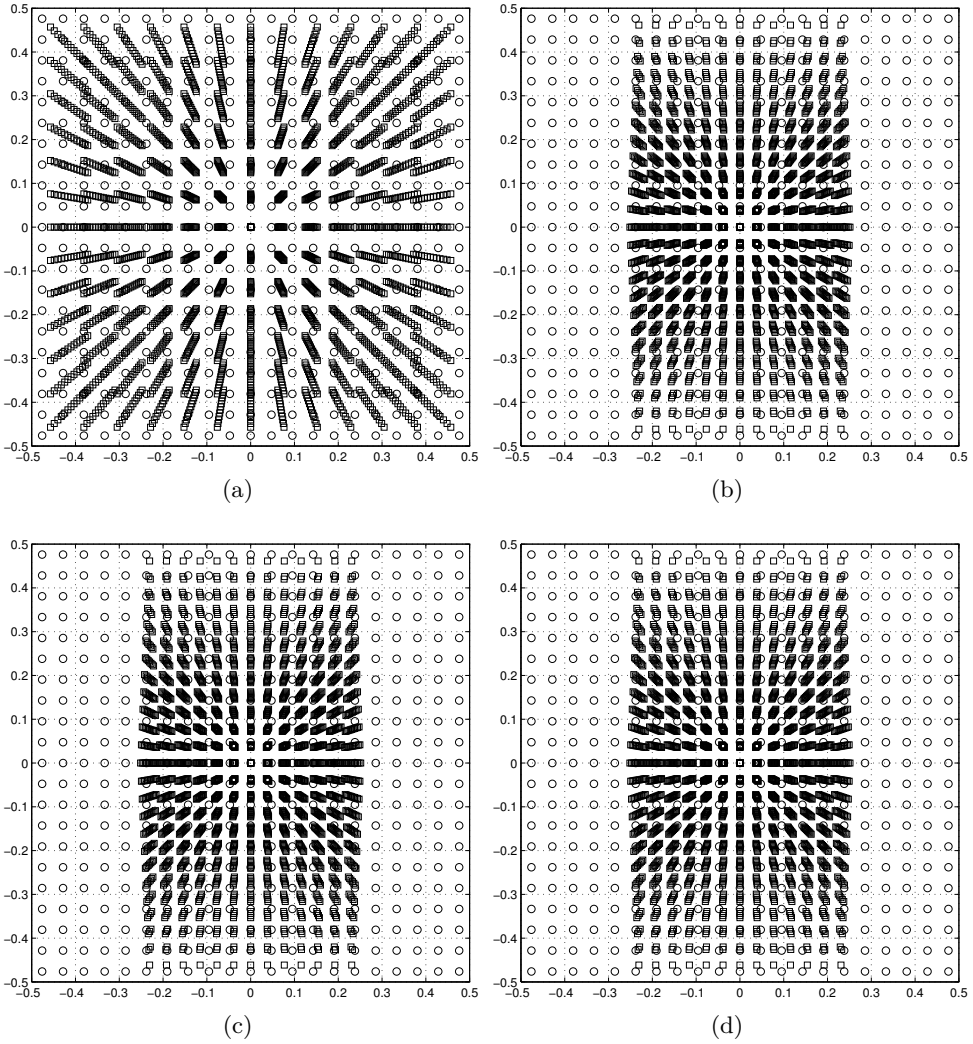

Figure C.1: Synthetic system calibration for a 4-cameras configuration with $\vec{d}_{\mathcal{O}^c} \in \{\begin{bmatrix}0 & 0 & 1\end{bmatrix}^T, \begin{bmatrix}0.7071 & 0 & 0.7071\end{bmatrix}^T, \begin{bmatrix}0 & 0.7071 & 0.7071\end{bmatrix}^T, \begin{bmatrix}-0.7071 & 0 & 0.7071\end{bmatrix}^T\}$. The circles represent the pixel coordinates and the squares depict the projection in the cameras' planes of the voxel centers.

Appendix D. Implementation of (2.39)

We assume hereafter that the $b_j(\mathbf{k})$'s, expressed in (2.39), are defined as rectangular-pulse functions, that is:

$$b_j(\mathbf{k}) \triangleq \begin{cases} 1/\mathrm{Vol}(\zeta_j), & \text{if } \mathbf{k} \in \zeta_j, \\ 0, & \text{otherwise,} \end{cases} \tag{D.1}$$

where $\mathrm{Vol}(\zeta_j) \triangleq \int_{\zeta_j} 1 \, \mathrm{d}\mathbf{k}$ denotes the volume of the voxel.

The practical implementation of (2.37) requires the numerical evaluation of (D.1) . We adopt a "subvoxel" approach inspired by [170]. The latter considers the subdivision of a voxel ζ_j in a set of cubic subvoxels $\chi_{l,j} \subset \zeta_j$ with $l = 1, \ldots, n_{sv}$ such that

$$\bigcup_{l=1}^{n_{sv}} \chi_{l,j} = \zeta_j, \qquad \bigcap_{l=1}^{n_{sv}} \chi_{l,j} = \varnothing. \tag{D.2}$$

Using this definition, (2.39) can be rewritten as

$$d_{ij}^c = \frac{1}{\mathrm{Vol}(\zeta_j)} \sum_{l=1}^{n_{sv}} \int_{\Omega_i^c \cap \chi_{l,j}} 1 \mathrm{d}\mathbf{k}. \tag{D.3}$$

We then use the following approximation

$$\int_{\Omega_i^c \cap \chi_{l,j}} 1 \mathrm{d}\mathbf{k} \simeq \frac{\mathrm{Vol}(\zeta_j)}{n_{sv}}, \tag{D.4}$$

if the line of sight joining the center of $\chi_{l,j}$ to the optical center $\mathbf{o}_{\mathrm{cam}}^c$ crosses the ith pixel and set $\int_{\Omega_i^c \cap \chi_{l,j}} 1 \mathrm{d}\mathbf{k} = 0$ otherwise. Note that this approximation is equivalent to assuming that subvoxel $\chi_{l,j}$ is either is totally included or excluded from cone of sight Ω_i^c. Letting n_{ij}^c be the number of subvoxels satisfying (D.4), we finally obtain:

$$d_{ij}^c = \frac{n_{ij}^c}{n_{sv}}. \tag{D.5}$$

Appendix E. The Proximal Operator

In this section we elaborate on the proximal operator, which appears as building block in proximal gradient and ADMM methods. Formally, the proximal operator of a convex proper function $f(\mathbf{x}) : \mathbb{R}^m \to \mathbb{R} \cup \{+\infty\}$ is defined as follows:

$$\text{prox}_f(\mathbf{v}) = \arg\min_{\mathbf{x}} f(\mathbf{x}) + \frac{1}{2}\|\mathbf{x} - \mathbf{v}\|_2^2. \tag{E.1}$$

We note that the proximal operator is always well-defined since $f(\mathbf{x}) + \frac{1}{2}\|\mathbf{x} - \mathbf{v}\|_2$ is strictly convex and proper, and therefore there exists one unique point minimizing this function. Interestingly, $\text{prox}_f(\mathbf{v})$ can be seen as a generalization of the orthogonal projection operator onto a convex set. Indeed, letting $f(\mathbf{x}) = \mathbb{I}_{\mathcal{X}}(\mathbf{x})$ be the indicator function of a convex set $\mathcal{X}$, the proximal operator of $f(\mathbf{x})$ reduces to

$$\begin{aligned}\text{prox}_f(\mathbf{v}) &= \arg\min_{\mathbf{x}\in\mathcal{X}} \|\mathbf{x} - \mathbf{v}\|_2^2, \\ &= \Pi_{\mathcal{X}}(\mathbf{v}),\end{aligned}$$

that is, $\text{prox}_f(\mathbf{v})$ is equivalent to the orthogonal projection of $\mathbf{v}$ onto $\mathcal{X}$.

Proximal operators admit a closed-form solution for many choices of $f(\mathbf{x})$. Hereafter, we provide the expressions of the proximal operators corresponding to some of the functions $f(\mathbf{x})$ encountered in the main body of the paper. These expressions are derived from standard convex optimality conditions. We refer the reader to [136, Section 6] for detailed derivations.

If $f(\mathbf{x}) = \lambda\|\mathbf{x}\|_1$, $\lambda > 0$, the proximal operator takes the form:

$$\left(\text{prox}_{\lambda\|\mathbf{x}\|_1}(\mathbf{v})\right)_i = \begin{cases} v_i - \lambda & v_i \geq \lambda \\ 0 & |v_i| \leq \lambda \\ v_i + \lambda & v_i \leq -\lambda \end{cases}. \tag{E.2}$$

This operator is often referred to as "soft thresholding" because it zeroes all the components of $\mathbf{v}$ whose amplitude is below λ and slightly decreases the amplitude of the other coefficients.

When $f(\mathbf{x}) = \mathbb{I}_{\mathbb{R}_+^m}(\mathbf{x})$, $\text{prox}_{\mathbb{I}_{\mathbb{R}_+^m}}(\mathbf{v})$ is equivalent to the orthogonal projection of $\mathbf{v}$ onto the

positive orthant, that is

$$\left(\text{prox}_{\mathbb{I}_{\mathbb{R}^m_+}}(\mathbf{v})\right)_i = \left(\Pi_{\mathbb{R}^m_+}(\mathbf{v})\right)_i = \begin{cases} v_i & \text{if } v_i \geq 0 \\ 0 & \text{otherwise.} \end{cases} \tag{E.3}$$

The proximal operator corresponding to $\lambda\|\mathbf{x}\|_1 + \mathbb{I}_{\mathbb{R}^m_+}(\mathbf{x})$ reads as

$$\left(\text{prox}_{\lambda\|\mathbf{x}\|_1+\mathbb{I}_{\mathbb{R}^m_+}}(\mathbf{v})\right)_i = \begin{cases} v_i - \lambda & v_i \geq \lambda \\ 0 & \text{otherwise.} \end{cases} \tag{E.4}$$

Finally, let us mention that the proximal operator can also be well-defined (*i.e.*, the solution of (E.1) exists and is unique) for some functions $f(\mathbf{x})$ which are non-convex. For example, $f(\mathbf{x}) = \lambda\|\mathbf{x}\|_0$ leads to

$$\left(\text{prox}_{\lambda\|\mathbf{x}\|_0}(\mathbf{v})\right)_i = \begin{cases} v_i & |v_i| \geq \sqrt{\lambda} \\ 0 & \text{otherwise.} \end{cases} \tag{E.5}$$

This operator is often referred to as "hard thresholding" since it zeroes all the components of $\mathbf{v}$ below a given threshold and leaves unchanged the other ones. The proximal operator corresponding to $\lambda\|\mathbf{x}\|_0 + \mathbb{I}_{\mathbb{R}^m_+}(\mathbf{x})$ reads

$$\left(\text{prox}_{\lambda\|\mathbf{x}\|_0+\mathbb{I}_{\mathbb{R}^m_+}}(\mathbf{v})\right)_i = \begin{cases} v_i & v_i \geq \sqrt{\lambda} \\ 0 & \text{otherwise.} \end{cases} \tag{E.6}$$

Bibliography

[1] E.H. Adelson and J.Y.A. Wang. Single lens stereo with a plenoptic camera. *IEEE Trans. Pattern Anal. Mach. Intell.*, 1992.

[2] R.J. Adrian. Twenty years of particle image velocimetry. *Exp. Fluids*, 39(27), 2005.

[3] R.J. Adrian. Bibliography of Particle Velocimetry Using Imaging Methods: 1917-1995. In *DLR, Göttingen Anniversary Edition*, 2009.

[4] R.J. Adrian and J. Westerweel. *Particle Image Velocimery.* Cambridge Aerospace Series, 2010.

[5] R.J. Adrian and C.-S. Yao. Pulsed laser technique application to liquid and gaseous flows and the scattering power of seed materials. *Applied Optics*, 1985.

[6] H.-E. Albrecht, M. Borys, N. Damaschke, and C. Tropea. *Laser Doppler and Phase Doppler Measurement Techniques.* Springer, 2002.

[7] M.V. Alfonso, J.M. Bioucas-Dias, and M.A. Figueiredo. An Augmented Lagrangian Approach to the Constrained Optimization Formulation of Imaging Inverse Problems. *IEEE Trans Image Process*, 20(3), 2011.

[8] A.H. Andersen and A.C. Kak. Simultaneous Algebraic Reconstruction Technique (SART): a superior implementation of the ART algorithm. *Ultasonic Imaging*, 6, 1984.

[9] K.P. Angele and B. Muhammad-Klingmann. A simple model for the effect of peak-locking on the accuracy of boundary layer turbulence statistics in digital PIV. *Exp. Fluids*, 38(3), 2005.

[10] C.C. Antonio Cenedese, F. Furia, L. Marchetti, M. Moroni, and L. Shindler. 3D particle reconstruction using light field imaging. In *SALTFM*, 2012.

[11] E. Arnaud, É. Mémin, R. Sosa, and G. Artana. A Fluid Motion Estimator for Schlieren Image Velocimetry. In *ECCV*, 2006.

[12] M.P. Arroyo and C.A. Greated. Stereoscopic particles image velocimetry. *Meas. Sci. Technol.*, 2(12), 1991.

[13] M.P. Arroyo and K.D. Hinsch. Recent Developments of PIV towards 3D Measurements. In *Particle Image Velocimery : New Developments and Recent Applications*. Springer, 2008.

[14] C. H. Atkinson. Reconstruction techniques for tomographic PIV (tomo-PIV) of turbulent boundary layer. In *SALTFM*, 2008.

[15] C. H. Atkinson and J. Soria. An efficient simultaneous reconstruction technique for tomographic particle image velocimetry. *Exp. Fluids*, 47(4-5), 2009.

[16] D. Auroux and J. Fehrenbach. Identification of velocity fields for geophysical fluids from a sequence of images. *Exp. Fluids*, 21(3), 2011.

[17] I. Barbu, C. Herzet, and E. Mémin. Sparse models and pursuit algorithms for PIV tomography. In *Forum on recent developments in Volume Reconstruction techniques applied to 3D fluid and solid mechanics*, Poitiers, France, November 2011.

[18] I. Barbu, C. Herzet, and E. Mémin. Sparse models and pursuit algorithms for PIV tomography. In *FVR*, 2011.

[19] I. Barbu, C. Herzet, and É. Mémin. Joint Estimation of Volume and Velocity in TomoPIV. In *PIV*, 2013.

[20] A. Bartoli and U. Castellani. 3D Shape Registration. In *3D Imaging, Analysis and Applications*. Springer, 2012.

[21] J. Barzilai and J.M. Borwein. Two point step size gradient methods. *IMA J. Numer. Anal.*, 8, 1988.

[22] S.S. Beauchemin and J.L. Barron. The Computation of Optical Flow. *ACM Comput. Surv.*, 27(3), 1995.

[23] A. Beck and M. Teboulle. Mirror descent and nonlinear projected subgradient methods for convex optimization. *Oper. Res. Lett.*, 31(3), 2003.

[24] A. Beck and M. Teboulle. A Fast Iterative Shrinkage-Thresholding Algorithm for Linear Inverse Problems. *SIAM J. Imaging Sci.*, 31(3), 2009.

[25] F. Becker, B. Wieneke, S. Petra, A. Schröder, and C. Schnörr. Variational Adaptive Correlation Method for Flow Estimation. *IEEE Image Process.*, 21(6), 2012.

[26] J. Belden, T.T. Truscott, M.C. Axiak, and A.H. Techet. Three-dimensional synthetic aperture particle image velocimetry. *Meas. Sci. Technol.*, 21(12), 2010.

[27] D.P. Bertsekas. *Nonlinear Programming*. Athena Scientific, 1999.

[28] P.J. Besl and N.D. McKay. A Method for Registration of 3-D Shapes. *IEEE Trans. Pattern Anal. Mach. Intell.*, 14(2), 1992.

[29] A.V. Bilsky, V.A. Lozhkin, D.M. Markovich, and M.P. Tokarev. Low computation cost reconstruction technique for Tomo-PIV. In *FVR*, 2011.

[30] E.G. Birgin, J.M. Martinez, and M. Raydan. Nonmonotone spectral projected gradient methods on convex sets. *SIAM J Optimiz.*, 10(4), 2000.

[31] M.J. Black. The robust estimation of multiple motions: Parametric and piecewise-smooth flow elds. *Comput. Vis. Image Und.*, 63(1), 1996.

[32] T. Blumensath and Davies. M.E. Iterative hard thresholding for compressed sensing. *Appl. Comput. Harmon. Anal.*, 27(3), 2009.

[33] C.F. Bohren and D.R. Huffman. *Absorption and Scattering of Light by Small Particles.* A Wiley-Interscience Publication, 1983.

[34] S.P. Boyd, N. Parikh, E. Chu, B. Peleato, and J. Eckstein. Distributed Optimization and Statistical Learning via the Alternating Direction Method of Multipliers. *Found. Trends Mach. Learning*, 3(1), 2011.

[35] S.P. Boyd and L. Vandenberghe. *Convex Optimization.* Cambridge University Press, 2004.

[36] L. Bregman. The relaxation method of finding the common point of convex sets and its application to the solution of problems in convex programming. *USSR Comp. Math. Math.+*, 7(3), 1966.

[37] C. Brucker. 3-D scanning PIV applied to an air flow in a motored engine using digital high-speed video. *Meas. Sci. Technol.*, 8(12), 1997.

[38] A.M. Bruckstein, M. Elad, and M. Zibulevsky. On the Uniqueness of Nonnegative Sparse Solutions to Underdetermined Systems of Equations. *IEEE Transf. Inf. Theory*, 54(11), 2008.

[39] S. Burgman, C. Brücker, and W. Schröder. Scanning PIV measurements of a laminar separation bubble. *Exp. Fluids*, 41(2), 2006.

[40] C.L. Byrne. Iterative Image Reconstruction Algorithms Based on Cross-Entropy Minimization. *IEEE Trans. Image Process.*, 2(1), 1993.

[41] E.J. Candès. The Restricted Isometry Property and Its Implications for Compressed Sensing. *Comptes Rendus Mathématiques*, 346(9-10), 2008.

[42] E.J. Candès and J. Romberg. ℓ_1-magic recovery of sparse signals via convex programming. Technical report, California Inst. Technol., 2005.

[43] E.J. Candès and T. Tao. Decoding by Linear Programming. *IEEE Transf. Inf. Theory*, 51(12), 2005.

[44] E.J. Candès, M.B. Wakin, and S.P. Boyd. Enhancing Sparsity by Reweighted ℓ_1 Minimization. *J. Fourrier Anal. Appl.*, 14(5), 2008.

[45] Y. Censor. Row-Action Methods for Huge and Sparse Systems and Their Applications. *SIAM Rev.*, 23(4), 1981.

[46] Y. Censor. Finite Series-Expansion Reconstruction Methods. *Proc. IEEE*, 71(3), 1983.

[47] Y. Censor and T. Elfving. Block-iterative algorithms with diagonally scaled oblique projections for the linear feasibility problem. *SIAM J. Matrix Anal. Appl.*, 24, 2002.

[48] Y. A. Censor and S. A. Zenios. *Parallel Optimization: Theory, Algorithms and Applications*. Oxford University Press, 1997.

[49] F. Champagnat, P. Cornic, A. Cheminet, B. Leclaire, and G. Besnerais. Tomographic PIV: particles vs blobs. In *PIV*, 2013.

[50] V. Chandar. A Negative Result Concerning Explicit Matrices With The Restricted Isometry Property, 2008.

[51] A. Cheminet, B. Leclaire, F. Champagnat, P. Cornic, and G. Besnerais. On factors affecting the quality of tomographic reconstruction. In *PIV*, 2013.

[52] S. Chen, C.F.N. Cowan, and P.M. Grant. Orthogonal Least Squares Learning Algorithm for Radial Basis Function Networks. *IEEE Trans. Neural Netw.*, 2(2), 1991.

[53] G. Cimmino. Calcolo approsimato per le soluzioni dei sistemi di equazioni lineari. *La Ric. Sci.*, 14(2), 1938.

[54] S. Coëtmellec, C. Buraga-Lefebvre, D. Lebrun, and C. Özkul. Application of in-line digital holography to multiple plane velocimetry. *Meas. Sci. Technol.*, 12(9), 2001.

[55] P. Cornic, F. Champagnat, A. Cheminet, B. Leclaire, and G. Besnerais. Computationally efficient sparse algorithms for tomographic PIV Reconstruction. In *PIV*, 2013.

[56] T. Corpetti, É. Mémin, and P. Perez. Dense estimation of fluid flows. *Pattern Anal. Mach. Intel.*, 2002.

[57] C. Couvreur and Y. Bresler. On the Optimality of the Backward Greedy Algorithm for the Subset Selection Problem. *SIAM J. Matrix Anal. Appl.*, 21, 2000.

[58] A. Cuzol and É. Mémin. Vortex and source particles for fluid motion estimation. *Lect. Notes Comput. Sc.*, 3459, 2005.

[59] W. Dai and O. Milenkovic. Subspace Pursuit for Compressive Sensing: Closing the Gap Between Performance and Complexity. *CoRR*, 2008.

[60] C.M. de Silva, R. Baidya, M. Khashehchi, and I. Marusic. Assessment of tomographic PIV in wall-bounded turbulence using direct numerical simulation data. *Exp. Fluids*, 52(2), 2012.

[61] S. Discetti and T. Astarita. Acceleration of tomo-PIV by multigrid reconstruction schemes. In *SALTFM*, 2010.

[62] D. L. Donoho. Sparse Components of Images and Optimal Atomic Decompositions. Technical report, Constr. Approx., 2001.

[63] D. L. Donoho and M. Elad. Optimally sparse representation in general (nonorthogonal) dictionaries via ℓ_1 minimization. *Proc. Natl. Acad. Sci. USA*, 100(5), 2003.

[64] D. L. Donoho, V. Stodden, and Y. Tsaig. About SparseLab.

[65] D. L. Donoho and J. Tanner. Sparse Nonnegative Solution of Underdetermined Linear Equations by Linear Programming. *Proc. Natl. Acad. Sci. USA*, 102(27), 2005.

[66] D. L. Donoho and Y. Tsaig. Sparse Solution of Underdetermined Linear Equations by Stagewise Orthogonal Matching Pursuit. *IEEE Transf. Inf. Theory*, 58(2), 2006.

[67] D. L. Donoho and Y. Tsaig. Fast Solution of ℓ_1-norm Minimization Problems When the Solution May be Sparse. *IEEE Trans. Inf. Theory*, 54(11), 2008.

[68] J. Eckstein and D.P. Bertsekas. On the Douglas-Rachford Splitting Method and the Proximal Point Algorithm for Maximal Monotone Operators. *Math. Prog.*, 55(3), 1992.

[69] M. Edmunds, R.S. Laramee, G. Chen, N. Max, E. Zhang, and C. Ware. Surface-based flow visualization. *Computers and Graphics*, 2012.

[70] B. Efron, T. Hastie, I. Johnstone, and R. Tibshirani. Least Angle Regression. *Ann. Stat.*, 32, 2004.

[71] M. Elad and A.M. Bruckstein. A generalized uncertainty principle and sparse representation in pairs of bases. *IEEE Trans. Inf. Theory*, 48(9), 2002.

[72] T. Elfving. On Some Methods for Entropy Maximization and Matrix Scaling. *Linear Algebra Appl.*, 34(12), 1980.

[73] T. Elfving, T. Nikazad, and C. Hansen. Semi-convergence and relaxation parameters for a class of SIRT algorithms. *SIAM J. Imaging Sci.*, submitted.

[74] G. Elsinga, F. Scarano, B. Wieneke, and B. van Oudheusden. Tomographic particle image velocimetry. *Exp. Fluids*, 41(6), 2006.

[75] G. E. Elsinga. Complete removal of ghost particles in Tomographic-PIV. In *PIV*, 2013.

[76] G. E. Elsinga, F. Scarano, B. Wieneke, and B.W. Oudheusden. Assemenent of tomo-PIV for three-dimensional flows. In *PIV*, 2005.

[77] G. E. Elsinga, F. Scarano, B. Wieneke, and B.W. Oudheusden. Tomographic particle image velocimetry. In *PIV*, 2005.

[78] G. E. Elsinga, J. Westerweel, F. Scarano, and M. Novara. On the velocity of ghost particles and the bias errors Tomographic-PIV. *Exp. Fluids*, 50(4), 2010.

[79] G. E. Elsinga, B. Wieneke, F. Scarano, and A. Schröder. Tomographic 3D-PIV and applications. *Top. Appl. Phys.*, 112, 2008.

[80] T. Fahringer and B.S. Thurow. Tomographic Reconstruction of a 3-D Flow Field Using a Plenoptic Camera. In *AIAA Fluid Dynamics Conference*, 2012.

[81] M.A. Figueiredo, R.D. Nowak, and S.J. Wright. Gradient Projection for Sparse Reconstruction: Application to Compressed Sensing and Other Inverse Problems. *IEEE J. Sel. Top. Sign. Proces.*, 1(4), 2007.

[82] D. Fleet and Y. Weiss. Optical Flow Estimation. In *Handbook of Mathematical Models in Computer Vision*, chapter 15. Springer, 2006.

[83] A. Forsgren, P.E. Gill, and M.H. Wright. Interior Methods for Nonlinear Optimization. *SIAM Rev.*, 44(4), 2002.

[84] Y. Furukawa and J. Ponce. Dense 3D motion capture from synchronized video streams. *CVPR*, 2008.

[85] T. Georgiev. New results on the Plenoptic 2.0 camera. In *Asilomar*, 2009.

[86] D. German. Constrained restoration and the recovery of discontinuities. *IEEE Trans. Pattern Anal. Mach. Intell.*, 14(3), 1992.

[87] S. Ghaemi and F. Scarano. Multi-pass light amplification for tomographic particle image velocimetry applications. *Meas. Sci. Technol.*, 21(12), 2010.

[88] J.W. Goodman. *Introduction to Fourier Optics*. Roberts & Company Publishers, 2004.

[89] R. Gribonval and M. Nielsen. Sparse Representations in Unions of Bases. Technical report, INRIA, 2002.

[90] R.L. Grothe and D. Dabiri. An improved three-dimensional characterization of defocusing digital particle image velocimetry (DDPIV) based on a new imaging volume definition. *Meas. Sci. Technol.*, 19(6), 2008.

[91] C. Hansen and M. Saxild-Hansen. AIR Tools — A MATLAB package of algebraic iterative reconstruction methods. *J. Comput. Appl. Math.*, 236(8), 2012.

[92] P. Héas, É. Mémin, D. Heitz, and P.D. Mininni. Power laws and inverse motion modelling: application to turbulence measurements from satellite images. *Tellus A*, 64, 2012.

[93] E. Hecht. *Optics*. Addison Wesley, 2002.

[94] G. T. Herman. Applications of maximum entropy and Bayesian optimization methods to image reconstructions from projections. In Reidel, editor, *Maximum Entropy and Bayesian Methods in Inverse Problems*. C.P. Smith and W.T. Grandy, Jr., 1985.

[95] G. T. Herman and A. Lent. Iterative reconstruction algorithms. *Comput. Biol. Med.*, 6(4), 1976.

[96] G. T. Herman, A. Lent, and P.H. Lutz. Relaxation methods for image reconstruction. *Commun. ACM*, 21(2), 1978.

[97] G. T. Herman and L.B. Meyer. Algebraic reconstruction techniques can be made computationally efficient. *IEEE Trans. Med. Imag.*, 12(3), 1993.

[98] C. Herzet and A. Drémeau. Bayesian Pursuit Algorithms. In *EUSIPCO*, 2010.

[99] K.D. Hinsch. Three-dimensional particle velocimetry. *Meas. Sci. Technol.*, 6(6), 1995.

[100] K.D. Hinsch. Holographic particle image velocimetry. *MEAS SCI TECHNOL*, 2002.

[101] B. K. P. Horn and B. G. Schunck. Determining Optical Flow. *Artif. Intell.*, 17(1-3), 1981.

[102] P.J. Huber. Robust Estimation of a Location Parameter. *Annals of Statistics*, 53, 1964.

[103] M. Jiang and G. Wang. Convergence of the Simultaneous Algebraic Reconstruction Technique (SART). *IEEE Trans. Image Process.*, 12(8), 2003.

[104] S. Kaczmarz. Angenäherte Auflösung von Systemen Linearer Gleichungen. *J. Theor. Biol*, 35, 1937.

[105] S. Kadri Harouna. *Ondelettes pour la prise en compte de conditions aux limites en turbulence incompressible.* PhD thesis, Université de Grenoble, 2010.

[106] C. Kähler and J. Kompenhaus. Fundamentals of multiple plane stereo particle image velocimetry. *Exp. Fluids*, 29(1), 2000.

[107] C. Kähler, B. Sammler, and J. Kompenhaus. Generation and control of particle size distributions for optical velocity measurement techniques in fluid mechanics. In *PIV*, 2002.

[108] L. Kajitani and D. Dabiri. A full three-dimensional characterization of defocusing digital particle image velocimetry. *Meas. Sci. Technol.*, 16(3), 2005.

[109] N. Karmarkar. A new polynomial-time algorithm for linear programming. *Combinatorica*, 4, 1984.

[110] J. Kitzhofer, P. Westfeld, O. Pust, H.G. Nonn, and C. Brucker. Estimation of 3D deformation and rotation rate tensor from volumetric particle data via 3D least squares matching. In *SALTFM*, 2010.

[111] M. Kojima, N. Megiddo, and S. Mizuno. Theoretical convergence of large step primal-dual interior point algorithms for linear programming. *Math. Prog.*, 59, 1993.

[112] S. Kullback and R. Leibler. On information and sufficiency. *Ann. Math. Stat.*, 22, 1951.

[113] R.R. La Foy and P. Vlachos. Multi-Camera Plenoptic Particle Image Velocimetry. In *PIV*, 2013.

[114] Y. Le Sant, F. Champagnat, G. Besnerais, B. Jaubert, and B. Leclaire. Folki-3C : un algorithme d'extraction directe de champs 3C en PIV. In *CFM*, 2009.

[115] A. Lent and Y. Censor. The primal-dual algorithm as a constraint-set-manipulation device. *Math. Program.*, 50(1-3), 1991.

[116] B.D. Lucas and T. Kanade. An Iterative Image Registration Technique with an Application to Stereo Vision. In *Proc. Imaging Understanding Workshop*, 1981.

[117] K. Lynch and B.S. Thurow. Three-Dimensional Particle Image Velocimetry Using a Plenoptic Camera. In *AIAA Aerospace Sciences Meeting*, 2012.

[118] H.G. Maas, A. Gruen, and D. Papantoniou. Particle tracking velocimetry in three-dimensional flows. *Exp. Fluids*, 15(2), 1993.

[119] D.M. Maliatouv, M. Çetin, and A.S Willsky. Homotopy continuation for sparse signal representation. In *ICASSP*, 2005.

[120] S. Mallat and Z. Zhang. Matching Pursuit With Time-Frequency Dictionaries. *IEEE Trans. Sig. Proc.*, 41(12), 1993.

[121] C. Mätzler. MATLAB Functions for Mie Scattering and Absorbtion. Technical report, Institut für Angewandte Physik, 2002.

[122] N. Megiddo. Pathways to the optimal set in linear programming. In *Progress in Mathematical Programming: Interior Point and Related Methods*. Springer-Verlag, 1989.

[123] A. Melling. Tracer particles and seeding for particle image velocimetry. *Meas. Sci. Technol.*, 8(12), 1997.

[124] H. Meng, G. Pan, Y. Pu, and S.H. Woordward. Holographic particle image velocimetry: from film to digital recording. *Meas. Sci. Technol.*, 15(4), 2004.

[125] M. Merzkirch. *Techniques of Flow Visualization*. AGARD, Essen, 1987.

[126] R. Meynart. Digital image processing for speckle flow velocimetry. *Rev. Sci. Instrum.*, 29(35), 1982.

[127] R. Meynart. Speckle velocimetry: an application of image analysis techniques to the measurement of instantaneous velocity fields in unsteady flow. In *ICIASF*, 1983.

[128] A. Mitiche and P. Bouthemy. Computation and Analysis of Image Motion: A Synopsis of Current Problems and Methods. *Int. J Comput. Vision*, 19(1), 1996.

[129] R.D.C. Monteiro and I. Adler. Interior path following primal-dual algorithms. Part I: Linear Programming. *Math. Prog.*, 44, 1989.

[130] Y. Nakayama, W. A. Woods, and D. G. Clark. *Visualized Flow*. Begell House, New York, 1993.

[131] D. Needell and J.A. Tropp. CoSaMP :Iterative signal recovery from incomplete and inaccurate sample. *Appl. Comput. Harmon. Anal.*, 26(3), 2009.

[132] Y. Nesterov. A method for solving the convex programming problem with convergence rate $\mathcal{O}(\sqrt{(k)})$. *Dokl. Akad. Nauk. SSSR*, 269, 1986.

[133] M. Novara. *Advances in tomographic PIV*. PhD thesis, Technische Universiteit Delft, 2013.

[134] M. Novara, K. J. Batenburg, and F. Scarano. Motion tracking-enhanced MART for tomographic PIV. *Meas. Sci. Technol.*, 21(3), 2010.

[135] M. Osborne, B. Presnell, and B. Turlach. A new approach to variable selection in least squares problems. *IMA J. Numer. Anal.*, 20, 2000.

[136] N. Parikh and S.P. Boyd. Proximal Algorithms. *Found. Trends Optim.*, 2013.

[137] Y. C. Pati, R. Rezaiifar, and P. S. Krishnaprasad. Orthogonal Matching Pursuit: Recursive Function Approximation with Applications to Wavelet Decomposition. In *ASILOMAR*, 1993.

[138] F. Pereira, M. Gharib, D. Dabiri, and D. Modaress. Defocusing digital particle image velocimetry: a 3-component 3-dimensional DPIV measurement technique. Application to bubbly flows. *Exp. Fluids*, 29(1), 2000.

[139] S. Petra, C. Popa, and C. Schnörr. Enhancing Sparsity by Constraining Strategies: Constrained SIRT versus Spectral Projected Gradient Methods. In *VMM*, 2008.

[140] S. Petra, C. Popa, and C. Schnörr. Extended and Constrained Cimmino-type Algorithms with Applications in Tomographic Image Reconstruciton. *Int. J. Comput. Math.*, 2010.

[141] S. Petra and C. Schnörr. Average case recovery analysis of tomographic compressive sensing. *Special Issue on Sparse Approximate Solution of Linear Systems*, 441, 2013.

[142] S. Petra, C. Schnörr, F. Becker, and F. Lenzen. B-SMART: Bregman-Based First-Order Algorithms for Non-negative Compressed Sensing Problems. In *SSVM*, 2013.

[143] S. Petra, C. Schnörr, A. Schröder, and B. Wieneke. Tomographic Image Reconstruction in Experimental Fluid Dynamics: Synopsis and Problems. In *WMM*, 2007.

[144] S. Petra and Schnörr, C. TomoPIV meets Compressed Sensing. *Pure Math. Appl.*, 2009.

[145] S. Petra, A. Schröder, and C. Schnörr. 3D Tomography from Few Projections in Experimental Fluid Mechanics. In Nitsche, W. and Dobriloff, C., editor, *Imaging Measurement Methods for Flow Analysis*, volume 106. Springer, 2009.

[146] S. Petra, A. Schröder, and C. Schnörr. Critical parameter values and reconstruction properties of discrete tomography: Application to experimental fluid dynamics. *Fundamenta Informaticae*, 2013.

[147] S. Petra, A. Schröder, B. Wieneke, and C. Schnörr. On Sparsity Maximization in Tomographic Particle Image Reconstruction. In *Proceedings of the 30th DAGM Symposium on Pattern Recognition*, 2008.

[148] S. Petra, A. Schröder, B. Wieneke, and C. Schnörr. Tomography from Few Projections in Experimental Fluid Dynamics. In *Imaging Measurement Methods for Flow Analysis*, 2009.

[149] B.T. Phong. Illumination for Computer Generated Pictures. *COMMUN ACM*, 1975.

[150] J. Ponce and D.A. Forsyth. *Computer Vision: A Modern Approach*. Prentice Hall, 2003.

[151] C. Popa. Constrained Kaczmarz extended algorithm for image reconstruction. *Linear Algebra Appl.*, 429, 2008.

[152] F.A. Potra and S.J. Wright. Interior-Point Methods, 2000.

[153] M. Raffel, E. Christian, S. Wereley, and J. Kompenhaus. *Particle Image Velocimery – A Practical Guide*. Springer-Verlag, 2007.

[154] M. A. Saunders. PDCO: Primal-dual interior-point method for convex objectives. *Syst. Optim. Lab*, 2002.

[155] F Scarano. Recent Developments in time-resolved three dimensional velocity measurements in turbulent flows by high-speed tomographic PIV. In *FVR*, 2011.

[156] F. Scarano. Tomographic PIV: principles and practice. *Meas. Sci. Technol.*, 24(1), 2013.

[157] F. Scarano and B.W. Oudheusden. Planar velocity measurements of a two-dimensional compressible wake. *Exp. Fluids*, 34(3), 2003.

[158] F. Scarano and C. Poelma. Three-dimensional vorticity patterns of cylinder wakes. *Exp. Fluids*, 47(1), 2009.

[159] J.-P. Schäfer. *Implementierung und Anwendung analytischer und numerischer Verfahren zur Losung der Maxwellgleichungen fur die Untersuchung der Lichtausbreitung in biologischem Gewebe*. PhD thesis, Universität Ulm, 2011.

[160] L. Schäfer and A. Schröder. Comparison of Holographic and Tomographic Particle Image Velocimetry Turbulent Channel Flow Measurements. In *ETC*, 2013.

[161] D. Schanz, S. Gesemann, A. Schroder, B. Wieneke, and D. Michaelis. Tomographic reconstruction with non-uniform optical transfert functions (OTF). In *SALTFM*, 2010.

[162] D. Schanz, S. Gesemann, A. Schröder, B. Wieneke, and M. Novara. Non-uniform optical transfer functions in particle imaging: calibration and application to Tomographic reconstruction. *Meas. Sci. Technol.*, 24(2), 2013.

[163] A. Schröder, R. Geisler, G. E. Elsinga, F. Scarano, and U. Dierksheide. Investigation of a turbulent spot and a tripped turbulent boundary layer flow using time-resolved tomographic PIV . *Exp. Fluids*, 44(2), 2008.

[164] G.S. Settles, E.B. Hackett, J.D. Miller, and L.M Weinstein. Full-Scale Schlieren Flow Visualization. *Flow Visualization*, 1995.

[165] C.M. Silva, R. Baidya, and I. Marusic. Enhancing Tomo-PIV reconstruction quality by reducing ghost particles. *Meas. Sci. Technol.*, 24(2), 2012.

[166] K.D. Solf. *Fotografie: Grundlagen*. Fisher Taschenbuch Verlag, 1986.

[167] S.M. Soloff and R.J. Adrian. Distortion compensation for generalized stereoscopic particle image velocimetry. *Meas. Sci. Technol.*, 8(12), 1997.

[168] C. Soussen, J. Idier, D. Brie, and J. Duan. From Bernoulli–Gaussian Deconvolution to Sparse Signal Restoration. *IEEE Trans. Sig. Proc.*, 59(10), 2011.

[169] D. Suter. Motion estimation and vector splines. In *CCVPR*, 1994.

[170] L. Thomas, B. Tremblais, and L. David. Influence des paramètres de reconstruction sur la qualité des résultats de tomo-PIV. In *CTFL*, 2010.

[171] L. Thomas, R. Vernet, B. Tremblais, and L. David. Influence of geometric parameters and image preprocessing on tomo-piv results. In *SALTFM*, 2010.

[172] B.S. Thurow and T. Fahringer. Recent Development of Volumetric PIV with a Plenoptic Camera. In *PIV*, 2013.

[173] B. Triggs, P. McLauchlan, R. Hartley, and A. Fitzgibbon. Bundle Adjustment —A Modern Synthesis. *Vision Algorithms: Theory and Practice*, 2000.

[174] C. Tropea, A.L. Yarin, and J.F. Foss. *Springer Handbook of Experimental Fluid Mechanics*. Springer-Verlag, 2007.

[175] J.A. Tropp. Greed is good: Algorithmic results for sparse approximation. *J. Signal Process.*, 2004.

[176] J.A. Tropp and S.J. Wright. Computational Methods for Sparse Solution of Linear Inverse Problems. *Proc. IEEE*, 98(6), 2010.

[177] P. Tseng. On Accelerated Proximal Gradient Methods for Convex-Concave Optimization . *submitted to SIAM J. Optim.*, 2008.

[178] B. Turlach. On Algorithms for Solving Least Squares Problems under an ℓ_1 Penalty or an ℓ_1 Constraint. In *ASA Proc. Stat. Comput. Sec.*, 2005.

[179] H.C. van de Hulst. *Light scattering by small particles*. Dover Publications, Inc., 1957.

[180] Milton Van Dyke. *An album of fluid motion*. Parabolic Press Stanford, CA, 1982.

[181] S. Vedula, S. Baker, P. Rander, R. T. Collins, and T. Kanade. Three-Dimensional Scene Flow. In *ICCV*, 1999.

[182] C. Vogel. *Computation Methods for Inverse Problems*. Society for Industrial and Applied Mathematics Philadelphia, 2002.

[183] P. Westfeld, H.-G. Maas., O. Pust, J. Kitzhofer, and C. Brucker. 3-D least squares matching for volumetric velocimetry data processing. In *SALTFM*, 2010.

[184] B. Wieneke. Volume self-calibration for 3D particle image velocimetry. *Exp. Fluids*, 45(5), 2008.

[185] B. Wieneke. Iterative reconstruction of volumetric particle distribution. *Meas. Sci. Technol.*, 24(2), 2013.

[186] C.E. Willert. Stereoscopic digital particle image velocimetry for application in wind tunnel flows. *Meas. Sci. Technol.*, 8(12), 1997.

[187] C.E. Willert and M. Gharib. Digital particle image velocimetry. *Exp. Fluids*, 10(4), 1991.

[188] N. A. Worth and T. B. Nickels. Acceleration of Tomo-PIV by estimating the initial volume intensity distribution. *Exp. Fluids*, 45(5), 2008.

[189] T. Wriedt. A Review of Elastic Light Scattering Theories. *Part. Part. Syst. Charact.*, 1998.

[190] S.J. Wright. *Primal-Dual Interior-Point Methods*. SIAM, 1997.

[191] A.Y. Yang, A. Ganesh, Z. Zhou, and Y. Sastry, S.S. ang Ma. A Review of Fast ℓ_1-Minimization Algorithms for Robust Face Recognition. *CoRR*, 2010.

[192] Z. Zhang. Camera Calibration. In *Emerging Topics in Computer Vision*. Prentice Hall Professional Technical Reference, 2004.

Abstract

The challenge of the modern understanding of the 3D turbulent flows involves the need for *(i).* a reliable sensing technology *(ii).* the design of low-complexity estimation tools *(iii).* physically-sound priors. Novel techniques relying on processing image sequences have been advanced. Their methodology relies on conjugating approaches issued from the computer vision community with physical knowledge on fluid dynamics with the intent of designing an accurate motion estimator. Most of these procedures are formalized within a bidimensional framework, *i.e.*, they reconstruct a 2D motion field out of two consecutive 2D images, making them unsuitable for several fluid regimes with high 3D structures. Estimating the fluid motion within a 3D framework seems more pertinent. In related work, the velocity fields are most often retrieved from previously estimated volumetric densities. Recent contributions estimating the volumetric distribution with regard to the motion field that links them suggest a joint optimization approach as the appropriate modus operandi towards rigorous retrieval of turbulent fluid flow. In this thesis, we have proposed a novel joint solution to address the task of 3D fluid motion estimation out of multiple sequences of synchronized 2D images. The theoretical frame has been presented with connections to the computer vision and signal processing fields, as well as to the Tomographic PIV (tomoPIV) community. Our work can be divided into three main tasks: *(i).* the design of a physically sound model with respect to the nature of the visualized scene *(ii).* the devise of volume reconstruction algorithmic schemes with low complexity that take into account known priors on the physical signal and output a satisfying estimation within a few iterations *(iii).* the formalization of a velocity reconstruction scheme that accounts for noisy settings and for the linked structure between two instantaneous volume reconstructions. We evaluate the agility of our methods and highlight their performance throughout realistic numerical experiments mimicking the real-world tomoPIV signal.

Keywords: PIV Tomography, inverse problems, non-linear optimization, algorithms for sparse reconstruction, computer vision, 3D motion estimation

---

Résumé

L'analyse du mouvement en 3 dimensions (3D) des fluides turbulents à évolué vers un cadre nécessitant *(i).* un système de capteurs puissants *(ii).* le développement d'outils d'estimation de basse complexité *(iii).* des connaissances *a priori* issues de la physique du fluide. Des nouvelles techniques formulées dans ce contexte et s'appuyant sur le traitement d'images ont été proposées. Leur méthodologie repose sur la conjugaison du savoir propre à la communauté Vision par Ordinateur avec des modèles physiques de la dynamiques du fluide. Mais voilà, la plupart de ces procédures sont exprimées dans un cadre bidimensionnel (2D), dans le sens où elles reconstruisent un champ 2D à partir des deux images consécutives 2D ; dès lors, ces-dernières ne sont pas adaptées pour certains régimes du fluide. Récemment, des nouvelles contributions ont proposé l'estimation du champ 3D des fluides à partir des densités volumiques préalablement reconstruites. De plus, une amélioration de ces schémas classiques suggère un apport signifiant en netteté de la reconstruction dans un cadre joint d'estimation volume-mouvement. Motivés par ces développements, nous proposons dans cette étude une alternative au schéma joint déjà présent dans la littérature afin d'estimer la vitesse 3D des fluides à partir de plusieurs séquences synchronisées d'images 2D. Le cadre théorique de cette thèse a été présenté en connexion avec les communautés de la Vision par Ordianteur, du Traitement du Signal et de la Tomographie PIV. Notre travail peut être divisé en trois tâches majeures : *(i).* la formulation d'un modèle proche de la physique du système observé *(ii).* la conception des algorithmes de reconstruction volumique de basse complexité qui prennent en compte des particularités notables sur le système *(iii).* l'élaboration d'un schéma de reconstruction des champs de vitesse qui considère des scénarios bruités et la structure cohérente volumique entre deux instants. Nous évaluons les performances de nos méthodes sur des scènes réalistes représentant le signal de Tomographie PIV.

Mots-clés : Tomographie PIV, problèmes inverses, optimization non-linéaire, algorithmes pour la reconstruction parcimonieuse, estimation de la vitesse 3D